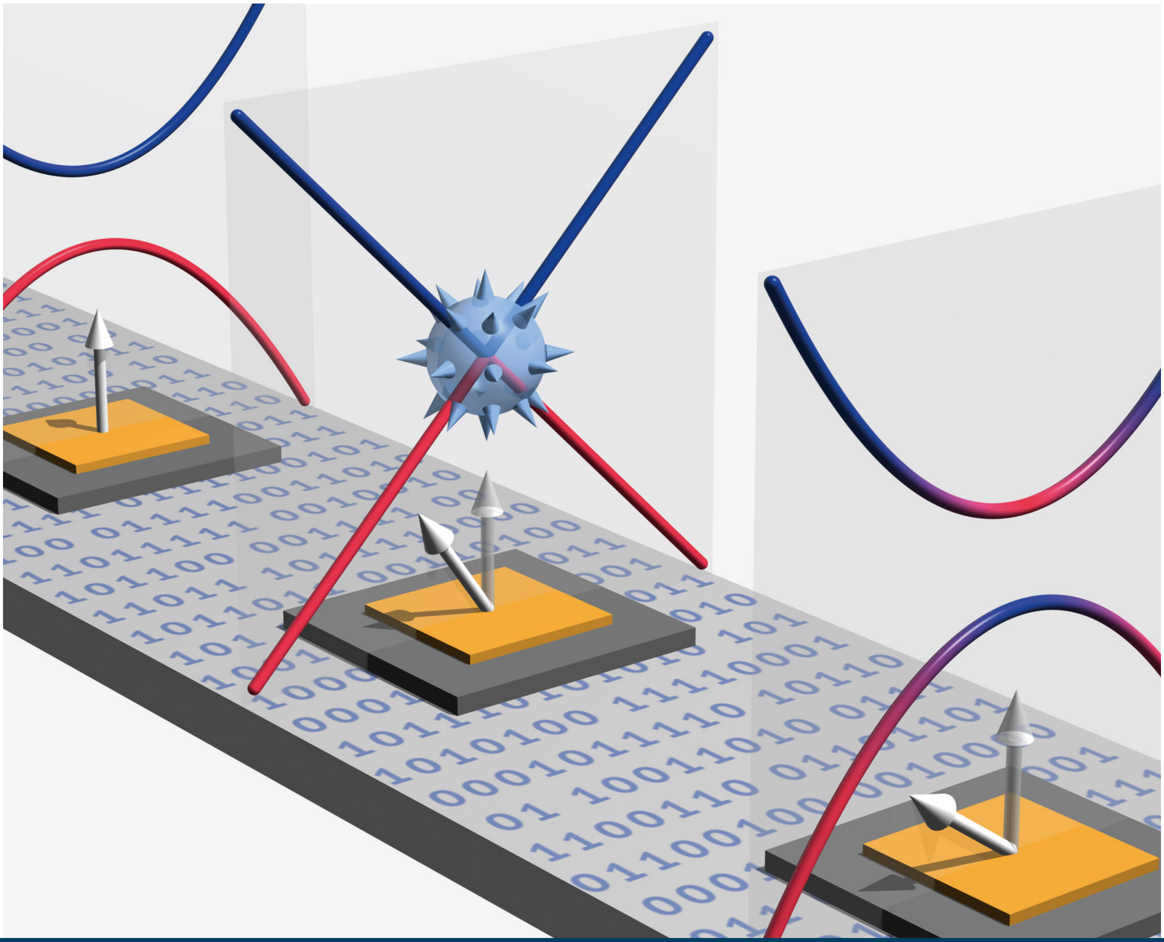

Topological properties of complex magnets from an advanced *ab-initio* Wannier description

Jan-Philipp Hanke

Schlüsseltechnologien / Key Technologies
Band / Volume 183
ISBN 978-3-95806-357-0

Mitglied der Helmholtz-Gemeinschaft

JÜLICH
Forschungszentrum

Schriften des Forschungszentrums Jülich
Reihe Schlüsseltechnologien / Key Technologies Band / Volume 183

Forschungszentrum Jülich GmbH
Peter Grünberg Institut (PGI)
Quanten-Theorie der Materialien (PGI-1 / IAS-1)

Topological properties of complex magnets from an advanced *ab-initio* Wannier description

Jan-Philipp Hanke

Schriften des Forschungszentrums Jülich
Reihe Schlüsseltechnologien / Key Technologies Band / Volume 183

ISSN 1866-1807 ISBN 978-3-95806-357-0

Bibliografische Information der Deutschen Nationalbibliothek.
Die Deutsche Nationalbibliothek verzeichnet diese Publikation in der
Deutschen Nationalbibliografie; detaillierte Bibliografische Daten
sind im Internet über http://dnb.d-nb.de abrufbar.

Herausgeber und Vertrieb:	Forschungszentrum Jülich GmbH Zentralbibliothek, Verlag 52425 Jülich Tel.: +49 2461 61-5368 Fax: +49 2461 61-6103 zb-publikation@fz-juelich.de www.fz-juelich.de/zb
Umschlaggestaltung:	Grafische Medien, Forschungszentrum Jülich GmbH
Druck:	Grafische Medien, Forschungszentrum Jülich GmbH
Copyright:	Forschungszentrum Jülich 2018

Schriften des Forschungszentrums Jülich
Reihe Schlüsseltechnologien / Key Technologies, Band / Volume 183

D 82 (Diss., RWTH Aachen University, 2018)

ISSN 1866-1807
ISBN 978-3-95806-357-0

Vollständig frei verfügbar über das Publikationsportal des Forschungszentrums Jülich (JuSER)
unter www.fz-juelich.de/zb/openaccess.

Abstract

Berry phases impart an elegant interpretation of fundamental condensed-matter phenomena as a direct consequence of the electrons' adiabatic evolution under the variation of control parameters. This thesis develops advanced *ab initio* methods based on density functional theory and applies them to investigate Berry phase effects in complex magnets, rooting in the global properties of two distinct types of phase spaces.

The non-trivial geometry of momentum space manifests in intrinsic contributions to the anomalous Hall effect as well as orbital magnetism in solids. While the former has been subject to intensive research in the past decades, our understanding of orbital magnetism in periodic systems is still at a rather premature stage. Even its quantum-mechanical description was elusive until the recent advent of a rigorous but involved Berry phase theory, the overall importance of which is unclear. To resolve this open question, we implement the modern theory of orbital magnetization within the full-potential linearized augmented-plane-wave method that is known for its high precision. By comparing to a commonly applied but simple local approximation, we uncover in this thesis that the Berry phase theory is crucial to predict reliably orbital magnetism in systems studied extensively in spintronics, including thin magnetic heterostructures and topological magnets. Remarkably, we demonstrate that the emergent magnetic field due to the chiral spin structure of non-coplanar antiferromagnets constitutes an efficient mechanism to lift the orbital degeneracy even in the absence of spin-orbit coupling. In a new class of materials to which we refer as topological orbital ferromagnets, the macroscopic magnetization originates solely from pronounced orbital magnetism due to non-local charge currents. We identify promising candidates of film and bulk systems that realize the predicted topological orbital magnetization, without any reference to correlation or spin-orbit effects.

Paving the road towards innovative device architectures, the burgeoning research field of spin-orbitronics exploits relativistic phenomena to control electrically magnetism by means of spin-orbit torques. Only recently, these torques and the related Dzyaloshinskii-Moriya interaction were recognized as innately geometrical effects that originate from the global properties of a *mixed* phase space entangling the crystal momentum with the magnetization direction. However, the efficient treatment of such complex higher-dimensional phase spaces sets a central challenge for *ab initio* theory, calling for advanced computational methods. This demand is met by a generalized Wannier interpolation that we develop here in order to describe Berry phase effects in generic parameter spaces precisely. Using the scheme for spin torques and chiral interactions in magnetic heterostructures, we correlate their microscopic origin with the electronic structure, and elucidate the role of chemical composition and disorder. In addition, the developed formalism enables us to evaluate efficiently the dependence of these phenomena on the magnetization direction, revealing large anisotropies in the studied systems. Considering the interplay of magnetism and topology, we uncover that magnetically induced band crossings manifest in prominent magneto-electric responses in magnetic insulators. We introduce the concept of mixed Weyl semimetals to establish novel guiding principles for engineering large spin-orbit torques in topologically complex ferromagnets. Moreover, we show that topological phase transitions in these materials are accompanied by drastic changes of the local orbital chemistry.

Kurzfassung

Berry-Phasen ermöglichen eine elegante Deutung physikalischer Effekte in Festkörpern basierend auf der adiabatischen Evolution der Elektronen, wenn Kontrollparameter variiert werden. Diese Arbeit entwickelt fortgeschrittene *ab initio* Methoden für die Dichtefunktionaltheorie, um Eigenschaften komplexer Magneten durch die geometrischen Merkmale von zwei unterschiedlichen Phasenräumen zu beschreiben.

Die Geometrie des Impulsraums manifestiert sich in intrinsischen Beiträgen zum anomalen Hall-Effekt und zur Orbitalmagnetisierung von Kristallen. Dabei ist im Gegensatz zum anomalen Transport das allgemeine Verständnis von Orbitalmagnetismus in periodischen Systemen unvollständig. Eine quantenmechanische Beschreibung des Phänomens fehlte sogar bis zur kürzlichen Entwicklung einer aufwendigen Berry-Phasen-Theorie, deren Relevanz jedoch unbekannt ist. Um diese offene Frage zu beantworten, implementieren wir die moderne Theorie der Orbitalmagnetisierung innerhalb der präzisen *full-potential linearized augmented-plane-wave* Methode. Durch den Vergleich mit einer häufig verwendeten Näherung zeigen wir, dass die Berry-Phasen-Theorie essentiell ist, um Orbitalmagnetismus in heutigen Materialien der Spintronik (z.B. dünne Heterostrukturen oder topologische Magneten) verlässlich vorherzusagen. Wir zeigen zudem, dass die chirale Spinstruktur nicht-koplanarer Antiferromagneten als emergentes magnetisches Feld wirkt und somit die orbitale Entartung effizient aufhebt, sogar in Abwesenheit der Spin-Bahn-Wechselwirkung. Durch diesen Mechanismus ist die makroskopische Magnetisierung in einer neuen Materialklasse, die wir als topologische Orbitalferromagneten bezeichnen, allein durch starken Orbitalmagnetismus infolge nicht-lokaler Ströme verursacht. Wir identifizieren vielversprechende Film- und Bulksysteme, die eine solche topologische Orbitalmagnetisierung aufweisen.

Das aufstrebende Forschungsfeld der Spin-Orbitronik eröffnet neue Möglichkeiten in der Konzeption magnetischer Bauelemente, da es relativistische Phänomene wie Spin-Orbit-Torques zur elektrischen Kontrolle von Magnetismus nutzt. Seit Kurzem werden diese Torques sowie die Dzyaloshinskii-Moriya-Wechselwirkung als geometrische Effekte eines gemischten Phasenraums aus Kristallimpuls und Magnetisierungsrichtung betrachtet. Jedoch stellt die effiziente Beschreibung von solchen komplexen Phasenräumen eine zentrale Herausforderung für die *ab initio* Theorie dar, was neuartige Methoden erfordert. Um entsprechende Berry-Phasen-Effekte präzise zu beschreiben, entwickeln wir in dieser Arbeit eine verallgemeinerte Wannier Interpolation. Wir wenden den Formalismus auf Spin-Orbit-Torques und die chirale Austauschwechselwirkung an, deren mikroskopischen Ursprung wir in magnetischen Filmen mit der Elektronenstruktur korrelieren und die Rolle von chemischer Zusammensetzung sowie Unordnung betrachten. Zudem ermöglicht die entwickelte Methode die effiziente Berechnung der teilweise deutlichen Anisotropie dieser Phänomene bezüglich der Magnetisierungsrichtung. Wir untersuchen ebenfalls das Zusammenspiel von Magnetismus und Topologie, wodurch magnetisch induzierten Kreuzungspunkten in der Bandstruktur von isolierenden Systemen eine starke magneto-elektrische Antwort zugeschrieben werden kann. Um dies als Leitfaden zur Erzeugung großer Spin-Orbit-Torques in topologischen Ferromagneten zu etablieren, führen wir das Konzept von *mixed Weyl semimetals* ein. Wir zeigen, dass entsprechende topologische Phasenübergänge von drastischen Veränderungen der orbitalen Chemie begleitet werden.

"The thing that doesn't fit is the thing that's the most interesting: the part that doesn't go according to what you expected."

– Richard P. Feynman

"You can't start a fire, you can't start a fire without a spark."

– Bruce Springsteen

Contents

Chapter 1

Introduction

All along in the history of mankind the ability to write, store, and read information has been an integral driving force for the development of human civilization. Starting from the very first simple picture drawings carved into rock during the premechanical age, information technology has evolved remarkably until today. Present-day devices utilize innately quantum-mechanical effects based on fundamental degrees of freedom of the electrons in order to process data. Especially, the discovery of the giant magnetoresistance (GMR) effect by Peter Grünberg *et al.* [1] and Albert Fert *et al.* [2] in 1988 revolutionized information technology and substantiated the fascinating research field of *spintronics* by uncovering the key role of the exchange interaction between spins. In heterostructures composed of alternating ferromagnetic and non-magnetic conductive layers, the GMR effect converts spin information to electrical signals as it manifests in a drastic change of the electrical resistance with the relative orientation of the magnetization in adjacent ferromagnetic layers. Soon after this seminal finding, standard electronics footing on the electric charge was advanced to encode information using the spin degree of freedom of the electrons as well. Being two of the technologically most important phenomena in spintronics, the GMR and the related tunneling magnetoresistance (TMR) effect [3–5] facilitated thereby the realization of magnetic storage media with prominently high data densities. Ever since, representing data based on the orientation of magnetic bits became a guiding principle for modern information technology that is implemented in present computer hard drives and non-volatile magnetoresistive random-access memories (MRAMs).

Controlling reliably the magnetization direction of single magnetic domains is absolutely vital in order to write information, *e.g.*, into MRAMs, which is typically achieved using magnetic fields created by applied electric currents. However, this process of magnetization reversal lacks generally efficiency, speed, and scalability owing to the large required current densities, which impedes recently progress towards improved magnetic storage devices. Exploiting the ideas of spintronics as laid out by the aforementioned magnetoresistive effects, a much more attractive mechanism for switching is the *spin-transfer torque (STT)* as anticipated by Slonczewski [6] and Berger [7]. That is, a spin-polarized current may transfer spin angular momentum between two adjacent ferromagnetic layers that are separated by a thin insulating layer in a magnetic tunnel junction. By coupling via the exchange interaction to the local magnetic moments, the spin current exerts a spin torque known as STT on the macroscopic magnetization of the free ferromagnet, which is eventually reversed if the current density exceeds a relatively low threshold. Therefore, the STT mechanism is perceived to hold bright promises for energy-efficient and fast magnetization switching, which is also beneficial for novel concepts of ultradense memory devices based on non-uniform magnetic textures [8]. In 2016, the first commercial MRAM chips that incorporate STT tunnel junctions as key units became available. On-going substantial efforts in theory and experiment are devoted to understanding and optimizing the material design of magnetic heterostructures in order to achieve large spin torques under minimal current densities. But even beyond their doubtless technological potential in non-volatile magnetic storage media [9–11], spin torques are of great scientific interest in basic research as they probe fundamental magnetic interactions and magnetization dynamics.

While classical spintronic devices utilize the exchange interaction to generate and detect spin-polarized currents, the burgeoning field of *spin-orbitronics* exploits instead the spin-orbit interaction in non-magnetic materials to manipulate adjacent nanomagnets through injected spin currents. Stemming from bulk or interfacial spin-orbit phenomena, these spin currents give rise to *spin-orbit torques (SOTs)* that were demonstrated only recently to mediate very efficient electrical control of magnetism in single ferromagnetic layers [12,13] and antiferromagnets [14]. Experiments distinguish between antidamping and field-like torques as two qualitatively different contributions to the SOT. Using the intrinsic spin-orbit coupling to create spin currents contrasts favorably from the STT mechanism in magnetic tunnel junctions as it renders the presence of a ferromagnetic polarizer unnecessary. In particular, this facilitates versatile switching geometries in devices with enhanced durability and easily separable lines for writing and reading. Intimately connected to the phenomenon of current-induced SOT is the Dzyaloshinskii-Moriya interaction (DMI) [15,16] that can stabilize localized chiral magnetic textures known as skyrmions in non-centrosymmetric bulk crystals or at surfaces. Realizing these topologically protected spin whirls and moving them on “racetracks” in innovative magnetic memories [17] by relativistic spin currents is a central motivation for extensive materials research in spin-orbitronics. Driven by striking advances in the synthesis of complex spin systems composed of diverse chemical elements, functionalized materials with unprecedented properties can be conceived and controlled experimentally at the nanoscale. Supplementing experiments fruitfully, electronic structure theory contributes essentially to the design of such functional devices as it provides a powerful means to uncover the microscopic origins of emergent phenomena rooting in the first-principles electronic structure.

Condensed matter physics experienced a revolutionary twist when topology as a branch of mathematics entered the stage, establishing an elegant interpretation of precisely quantized transport phenomena based on universal arguments (see, *e.g.*, Refs. [18,19]). These celebrated concepts have pioneered the theoretical classification of solids according to global properties of momentum space, as a consequence of which the transition between two topologically distinct phases of matter necessitates drastic changes of the electronic structure. The quest for realizing ever-new topological materials including quantum anomalous Hall insulators, Weyl and Dirac semimetals, certain photonic crystals, correlated Kitaev materials, and topological insulators opened up prosperous research fields at the frontline of science. In these topological phases, the fundamental interplay of symmetry, spin-orbit coupling, and exchange interaction manifests in characteristic hallmarks, *e.g.*, protected band crossings or perfectly conducting edge states. Exploiting such unique phenomena in future memory and logic devices may open up auspicious avenues towards green information technology that dissipates hardly any energy. For example, the peculiar spin-momentum locking of the robust surface states of topological insulators renders these systems efficient sources of spin currents, which can be injected into an adjacent ferromagnet to control its macroscopic magnetization by current-induced spin torques. Strikingly, Pancharatnam [20] and Berry [21] discovered in their groundbreaking works that the non-trivial geometrical properties of momentum space promote a “geometrical memory” of the electron as revealed by the so-called *Berry phase*, which is acquired upon quantum adiabatic transport under external forces. These gauge-invariant phases are physically relevant as they describe a plethora of Berry phase properties such as the intrinsic anomalous Hall effect, the electric polarization [22,23], and the phenomenon of orbital magnetization (OM) in its modern Berry phase framework [24–27]. Anti-damping spin torques as well as the closely related DMI originate analogously from the complex geometry of a mixed phase space that entangles the crystal momentum with the magnetization direction [28]. Emphasizing their geometrical nature, the corresponding Berry phase theory facilitates the efficient calculation of the latter effects based on the ferromagnetic electronic structure. In addition, it outlines bright prospects for using the ubiquitous arguments of topology to understand and design magneto-electric coupling phenomena in magnetic insulators.

The vital role of topology and geometry as unifying principles in spin-orbitronics has inspired this thesis to investigate anomalous transport, orbital magnetism and magneto-electric effects in periodic systems by theoretical means. In particular, computational *ab initio* methods are developed and applied in order to determine the electronic structure of complex solids based solely on the charges and positions of the nuclei, without any reference to adjustable parameters.

Owing to the exponentially increasing number of elements in the Hilbert space, the rigorous solution of the intricate many-body problem by quantum mechanics relies on feasible but accurate approximations. In this context, one of the most successful and widely pursued approaches is parameter-free density functional theory (DFT) as developed by Hohenberg and Kohn [29], and Kohn and Sham [30]. By replacing the many-body wave function with charge and spin densities, this theory maps the many-body problem onto effective single-particle ones where all of the complexity of the original many-electron system manifests in the exchange and correlation potential. While an exact form of the latter is still unknown, experience has shown that this potential is described surprisingly well by exchange and correlation effects in a homogeneous electron gas, rendering DFT practical even for large and complex systems. In addition, due to on-going developments of continually improved exchange and correlation functionals, material-specific DFT became a powerful computational tool for predicting qualitatively the electronic structure and derived phenomena. Therefore, first-principles theory can supplement and assist substantially the experimental efforts in functionality-inspired material design by advancing our understanding of the *structure-property relation.* Among the zoo of different DFT implementations, the full-potential linearized augmented-plane-wave (FLAPW) method used in this thesis is appreciated for its high precision that is accompanied, however, by heavy computational burden and conceptual complexity. Accounting for the full nuclear potential, this all-electron method is well-suited to describe bulk solids, surfaces and interfaces, one-dimensional wires, and open geometries formed by any chemical element of the periodic table. Realistic force calculations including the spin-orbit interaction support the structural optimization of the atomic positions. The method allows us further to study ferromagnetic and antiferromagnetic structures as well as complex magnetism.

Despite of mapping the many-body problem to effective single-particle ones, Kohn-Sham DFT remains computationally very demanding, which applies in particular to the FLAPW implementation that adopts no shape approximations for the potential. Due to this considerable intricacy, first-principles theory is supplemented routinely by an efficient tight-binding representation of the electronic structure based on Wannier functions [31], which facilitate an accurate interpolation of energy bands and transport phenomena. In contrast to the wave-like Bloch states, Wannier functions are localized in real space whereby they impart intuitive insights into the character of chemical bonds. This basis constitutes additionally an ideal starting point for constructing model Hamiltonians that aim at the description of correlated solid-state systems with prominent electron-electron interactions. Moreover, as the action of the position operator on the localized Wannier functions is well-defined, the quantum-mechanical theories of electric polarization and OM are formulated most naturally in this basis.

Being one of the most elementary quantum-mechanical phenomena in condensed matter, magnetism stems generally not only from the electrons' spin but also from circulating charge currents that manifest in an orbital moment. The latter effect is at the heart of the complex concurrence of spin-orbit interaction, electronic correlations, and crystal-field effects in periodic crystals. Since the magnitude of the quenched orbital moment is usually strongly overshadowed by the spin part, the overall relevance of orbital magnetism is debated vividly, even though fascinating phenomena such as the gyrotropic magnetic effect rely sensitively on the orbital moments at the Fermi surface. This controversy roots primarily in the yet premature understanding of orbital magnetism as compared to its spin counterpart, which can be ascribed partially to the lack of a rigorous quantum-mechanical description until the recent advent of the Berry phase theory of OM [24–27]. However, a clear justification for the involved first-principles methodology associated with this Berry phase theory has been missing so far. In this thesis, we implement an efficient Wannier scheme for interpolating the OM according to its modern Berry phase theory, and apply the developed computational method to bulk ferromagnets, heterostructures, and topological materials. By comparing to a commonly adopted local approximation, we clarify the crucial role of the truly quantum-mechanical treatment to describe reliably orbital magnetism in condensed matter. Our results emphasize the relevance of the Berry phase theory in order to link to experiments on extensively scrutinized systems in spintronics and spin-orbitronics. We further outline the intriguing concept of *topological orbital magnetism*, which is driven by chiral spin textures rather than the spin-orbit interaction. The corresponding unconventional orbital moments are demonstrated to amount to colossal values in non-collinear antiferromagnets, and promising material candidates are identified based on symmetry analysis.

Intrinsic antidamping SOTs and the DMI were recognized lately as innately geometric effects that originate from global properties of the higher-dimensional phase space entangling crystal momentum and magnetization direction. As a consequence, knowledge about the variation of the wave functions with respect to the magnetic orientation constitutes a key ingredient in the corresponding Berry phase theory [28]. Since such information is not readily available in current electronic structure codes, we develop and implement in this thesis the formalism of higher-dimensional Wannier functions (HDWFs), which provides efficiently the necessary ingredients. Our generic method is ideally suited to study anisotropic Berry phase properties based on the first-principles electronic structure of ferromagnetic systems. We verify the efficiency and correctness of this technique in predicting SOTs and DMI in magnetic heterostructures. In particular, we uncover the microscopic origin and the composition dependence of these effects in alloyed Co-based trilayers, where we identify characteristic sign changes of the DMI. Additionally, we investigate the anisotropy of spin torques with respect to the magnetization direction, which affects the dynamical properties of chiral magnetic textures. Ultimately, using the universal arguments of topology, we introduce the concept of *mixed Weyl semimetals* to explain unambiguously pronounced magneto-electric effects in magnetic insulators, where emergent monopoles close to the Fermi level are of central importance. Thereby, we bring the field of current-induced torques to the realm of topology, promoting novel guidelines for the design of large SOTs in insulating magnets. We identify from first principles the two examples of magnetically doped graphene and functionalized magnetic films as promising realizations of the class of mixed Weyl semimetals that reveal non-trivial Berry phase properties. Our results pave the road towards low-dissipation magnetization control by electric fields.

The thesis is organized as follows: in Chapters 2 and 3, we outline how to solve the quantum-mechanical many-body problem by density functional theory, and discuss the FLAPW method. Chapter 4 introduces the concept of Berry phases relating to solid-state phenomena that are currently under intensive scrutiny in spin-orbitronics. We describe in Chapter 5 the method of Wannier interpolation and present our implementation of the modern theory of orbital magnetism in the Jülich DFT code FLEUR. Applying this computational method, we present in Chapter 6 a comprehensive study on the relevance of the Berry phase theory for describing reliably orbital magnetism. Further, we elucidate the emergent phenomenon of topological orbital moments that originate solely from chiral non-coplanar spin textures. In Chapter 7, we develop the framework of HDWFs and motivate a generalized Wannier interpolation. Chapter 8 applies this technique to the efficient *ab initio* description of SOTs and DMI in metallic heterostructures. In Chapter 9, we explore the universal arguments of topology to understand and design magneto-electric coupling effects in topologically complex magnets. The thesis is concluded in Chapter 10.

Chapter 2

Density functional theory

Contents

In this chapter, we provide a concise introduction to the electronic-structure problem and its quantum-mechanical solution in terms of density functional theory. Starting from the interacting many-body Hamiltonian, we motivate the Born-Oppenheimer approximation and discuss approaches to the solution of the corresponding many-electron Schrödinger equation. The Thomas-Fermi model as a first example of a density-based method is reviewed, followed by the formulation of the two seminal theorems by Hohenberg and Kohn, which underlie modern density functional theory. Based on these theorems, we formulate the Kohn-Sham equations of effectively non-interacting particles in the case of non-magnetic, collinear, and non-collinear systems. Finally, we turn to the intricate treatment of exchange and correlation effects that render practical approximations obligatory.

2.1 Many-body problem in quantum mechanics

The predictive theoretical description of fundamental phenomena in condensed-matter systems relies substantially on using the rigorous machinery of quantum mechanics. Consequently, the complex many-body problem of mutually interacting nuclei and electrons forming the solid sets a central challenge for electronic structure theory. This key challenge amounts to solving an eigenvalue problem in terms of the stationary Schrödinger equation [32] to the Hamiltonian H, which reflects the quantum nature of the many-electron system:

$$H\Psi(\boldsymbol{r}_1,\ldots,\boldsymbol{r}_N,\boldsymbol{\tau}_1,\ldots,\boldsymbol{\tau}_M) = E\Psi(\boldsymbol{r}_1,\ldots,\boldsymbol{r}_N,\boldsymbol{\tau}_1,\ldots,\boldsymbol{\tau}_M)\,, \tag{2.1}$$

where the state of the system is represented by the many-body wave function Ψ that depends on the coordinates $\boldsymbol{r}_i$ of all N electrons as well as on the positions $\boldsymbol{\tau}_\mu$ of the M ions, and E is the corresponding energy of the system. In general, the many-body Hamiltonian entering the Schrödinger equation assumes in atomic coordinates the form

$$H = -\frac{1}{2}\sum_i \nabla_i^2 - \frac{1}{2}\sum_\mu \frac{1}{M_\mu}\nabla_\mu^2 - \sum_{i\mu}\frac{Z_\mu}{|\boldsymbol{\tau}_\mu - \boldsymbol{r}_i|} + \frac{1}{2}\sum_{ij}\frac{1}{|\boldsymbol{r}_i - \boldsymbol{r}_j|} + \frac{1}{2}\sum_{\mu\nu}\frac{Z_\mu Z_\nu}{|\boldsymbol{\tau}_\mu - \boldsymbol{\tau}_\nu|}\,. \tag{2.2}$$

Here, the first two terms track the kinetic energy of electrons and nuclei, respectively, the third contribution represents the attractive interaction between a nucleus of charge Z_μ at $\boldsymbol{\tau}_\mu$ and an electron at $\boldsymbol{r}_i$, and the two remaining parts correspond to the repulsion among electrons and nuclei, respectively.

Since the massive nuclei are much heavier than the light electrons, the kinetic energy of the nuclei in Eq. (2.2) can often be neglected, leading to an effective decoupling of electronic and ionic coordinates, and thus to an important simplification of the many-body problem. In this *Born-Oppenheimer approximation* [33], electronic properties can be evaluated while considering the nuclei fixed as the fast electrons adapt instantaneously to slow changes of the ionic positions. This leads to the electronic Schrödinger equation

$$\left[-\frac{1}{2}\sum_i \nabla_i^2 + \frac{1}{2}\sum_{ij}\frac{1}{|\boldsymbol{r}_i-\boldsymbol{r}_j|} - \sum_{i\mu}\frac{Z_\mu}{|\boldsymbol{\tau}_\mu-\boldsymbol{r}_i|}\right]\Psi(\boldsymbol{r}_1,\ldots,\boldsymbol{r}_N) = E\Psi(\boldsymbol{r}_1,\ldots,\boldsymbol{r}_N)\,, \tag{2.3}$$

where we suppress for sake of simplicity the parametric dependence of the electronic wave function on the fixed ionic positions. The atomic nuclei of the solid constitute an external potential with which the electrons interact. Other single-body effects arising from the interaction of electrons with electric or magnetic fields could easily be added to the above expression. Moreover, if spin-orbit coupling is included, the non-relativistic formulation (2.3) of the electronic problem becomes spin-dependent and its solutions are described by spinors.

It is remarkable that any electronic property can in principle be derived from solving the electronic Schrödinger equation, given just the (fixed) coordinates $\boldsymbol{\tau}_\mu$ and the charges Z_μ of the nuclei. However, the electronic problem is still of vast complexity due to the dramatically increasing size of the Hilbert space with the number of electrons[1], causing a direct solution of Eq. (2.3) to be impossible for many-electron systems. Besides, the long-range Coulomb interaction between two electrons renders the problem particularly intricate. As already pointed out by Dirac in the late 1920's [34], this makes further practical approximations indispensable in order to solve eventually the electronic structure problem. On one side, approximate many-body wave functions can be found by systematically expanding them in terms of *Slater determinants* [35,36] that describe the non-interacting system exactly[2]. For example, taking into account only a single Slater determinant as wave function of the fully-interacting system results in the so-called *Hartree-Fock approximation* [35, 37, 38]. Motivated by specific physical effects, one could alternatively approximate the many-body Hamiltonian to reduce complexity by keeping only the relevant ingredients of the Hamiltonian that govern the sought effects. This amounts usually to restricting the number of electrons, or to treating the long-range electron-electron interaction as local.

---

[1] If V is the system size and N is the number of electrons, the dimension of the Hilbert space of the wave functions $\Psi(\boldsymbol{r}_1,\ldots,\boldsymbol{r}_N)$ grows like V^N. Since frequently $V \propto N$, the dimension of the Hilbert space scales with N^N in this case.

[2] In absence of any electron-electron interactions, the Hamiltonian in Eq. (2.3) becomes a simple sum of single-particle terms such that the electronic many-body wave function is an antisymmetric linear combination of the corresponding single-particle solutions, which is known as Slater determinant.

In fact, the primary ambition of electronic structure methods is not the hunt for an exact wave function – which is anyhow not directly observable – but rather the reliable prediction of physical expectation values $\langle\Psi|\mathcal{O}|\Psi\rangle$ of quantum-mechanical operators $\mathcal{O}$. Using appropriate approximations as those discussed before, these methods aim at describing only information necessary for the accurate evaluation of expectation values while reducing the burden associated with the many-body problem. Establishing an effective single-particle description, a powerful method that follows this line of thought is density functional theory.

2.2 The Thomas-Fermi model

A first density-based approach to the electronic structure was developed by Thomas and Fermi [39–41] who found explicit expressions of the kinetic energy, the electron-electron interaction, and the nuclear potential in Eq. (2.3) in terms of the electronic many-body density $n(\boldsymbol{r})$. In the Thomas-Fermi model, the electrons are treated as independent particles with a purely electrostatic mutual interaction – known as *Hartree term* that reads

$$V_{\mathrm{H}}[n(\boldsymbol{r})] = \frac{1}{2}\iint \frac{n(\boldsymbol{r})n(\boldsymbol{r}')}{|\boldsymbol{r}-\boldsymbol{r}'|}\,\mathrm{d}^3r\mathrm{d}^3r' \,. \tag{2.4}$$

The external potential formed by the nuclei is easily written as functional of the density:

$$V_{\mathrm{ext}}[n(\boldsymbol{r})] = -\int \sum_{\mu} \frac{Z_\mu}{|\boldsymbol{\tau}_\mu - \boldsymbol{r}|} n(\boldsymbol{r})\,\mathrm{d}^3r \,. \tag{2.5}$$

Thomas and Fermi addressed the central challenge to obtain an adequate representation of the kinetic energy by considering a locally uniform electron gas of independent non-interacting particles. Within this local density approximation (LDA) [30, 42, 43], the kinetic energy density assumes the form $t[n(\boldsymbol{r})] = 3/10\,(3\pi^2)^{2/3} n^{2/3}(\boldsymbol{r})$ such that the kinetic energy functional is given by

$$T[n(\boldsymbol{r})] = \int t[n(\boldsymbol{r})]n(\boldsymbol{r})\,\mathrm{d}^3r = \frac{3}{10}(3\pi^2)^{\frac{2}{3}} \int n^{\frac{5}{3}}(\boldsymbol{r})\,\mathrm{d}^3r \,, \tag{2.6}$$

which completes the total energy functional $E[n(\boldsymbol{r})] = T[n(\boldsymbol{r})] + V_{\mathrm{ext}}[n(\boldsymbol{r})] + V_{\mathrm{H}}[n(\boldsymbol{r})]$ in the Thomas-Fermi model. Then, under the condition that the overall number of electrons $N = \int n(\boldsymbol{r})\,\mathrm{d}^3r$ remains constant, which is taken care of via the Lagrange multiplier λ, the total energy functional can be minimized to arrive at the Thomas-Fermi equation

$$\frac{1}{2}(3\pi^2)^{\frac{2}{3}} n^{\frac{2}{3}}(\boldsymbol{r}) + \int \frac{n(\boldsymbol{r}')}{|\boldsymbol{r}-\boldsymbol{r}'|}\,\mathrm{d}^3r' - \sum_{\mu} \frac{Z_\mu}{|\boldsymbol{\tau}_\mu - \boldsymbol{r}|} + \lambda = 0 \,. \tag{2.7}$$

To include, at least to some extent, exchange effects due to the Pauli exclusion principle, Dirac suggested later to add to Eq. (2.7) a correction term $W_{\mathrm{x}}[n(\boldsymbol{r})] \propto \int n^{4/3}(\boldsymbol{r})\,\mathrm{d}^3r$ originating from the exchange energy of a homogeneous electron liquid. Still, the Thomas-Fermi model suffers from the particularly poor representation of the kinetic energy[3], errors in the exchange energy, and neglecting completely any correlation effects. As a consequence, the Thomas-Fermi approach cannot predict the binding of molecules or solids, does not lead to an atomic shell structure, and never develops ferromagnetism. Irrespective of these drawbacks, the mathematically well-defined model was frequently studied since it becomes exact in the limit of $Z_\mu \to \infty$, and yields reasonable total energies for atoms.

2.3 The seminal theorems by Hohenberg and Kohn

The modern density functional theory (DFT) is based on two ground-breaking theorems by Hohenberg and Kohn [29] that provide the firm theoretical framework for substituting the many-body wave function with the electronic many-body density

$$n(\boldsymbol{r}) = \langle \Psi | \sum\nolimits_i \delta(\boldsymbol{r} - \boldsymbol{r}_i) | \Psi \rangle \tag{2.8}$$

in order to investigate quantum-mechanical systems. Here, we discuss first the case of a non-magnetic material with spin degeneracy but return to the extension to spin-polarized systems later.

When we consider the many-body Hamiltonian $H = T + V_\text{ext} + V_\text{ee}$ that contains the kinetic energy T, the external potential V_ext (*e.g.*, due to the nuclei), and the electron-electron interaction V_ee, the first theorem by Hohenberg and Kohn states that there exists a unique functional relation between the total energy and the electronic density of the many-body system.

Theorem 1 *The external potential V_ext is determined by the electronic many-body density $n(\boldsymbol{r})$ up to a trivial constant. As a consequence, the total energy of the system is a unique functional of the density:*

$$E[n(\boldsymbol{r})] = T[n(\boldsymbol{r})] + V_\text{ext}[n(\boldsymbol{r})] + V_\text{ee}[n(\boldsymbol{r})] \,. \tag{2.9}$$

The indirect proof by Hohenberg and Kohn is based on the assumption that two different external potentials lead to the very same density, which is then shown to contradict the Rayleigh-Ritz variational principle. Thus, different external potentials must give rise to different ground-state electronic densities. Since specifying the external potential also specifies the Hamiltonian, the many-body wave function[4] and any measurable quantity such as the total energy are unique functionals of the electronic density as well.

Exploiting this knowledge about the ground-state wave function and applying once again the variational principle, Hohenberg and Kohn were able to formulate their second theorem that is valuable from the viewpoint of practical DFT calculations.

---

[3] In sharp contrast, the predictive method by Kohn and Sham, which is discussed below, improves substantially the representation of the kinetic energy.

[4] The ground-state density fully determines the many-body Hamiltonian and thus not only the ground-state wave function but also excited states of the system.

Theorem 2 *The total energy functional $E[n(\boldsymbol{r})]$ is minimized for the exact ground-state density $n_0(\boldsymbol{r})$ under the constraint that the total number of electrons is kept fixed:*

$$E[n_0(\boldsymbol{r})] \leq E[n(\boldsymbol{r})]\,. \tag{2.10}$$

In principle, the electronic density $n_0(\boldsymbol{r})$ and the total energy $E[n_0(\boldsymbol{r})]$ of the many-body ground state are obtained by following the Hohenberg-Kohn theorems if the functional $E[n(\boldsymbol{r})]$ would be given. However, the explicit functional form of the total energy is unknown and thus has to be approximated in DFT calculations of the electronic structure.

2.4 Towards practical schemes: The Kohn-Sham equations

Based on the variational principle of the total energy functional, Kohn and Sham [30] proposed a set of single-particle Schrödinger-like equations of N non-interacting electrons propagating in an effective potential $V_{\text{eff}}(\boldsymbol{r})$, where the electronic density is forced to reproduce the one of the genuine many-body problem. In contrast to the Thomas-Fermi model, no explicit shape of the kinetic energy is assumed such that this formalism – which underlies most modern DFT implementations, and won Kohn and Sham the Nobel Prize in chemistry – has truly predictive power. As the Kohn-Sham reference system is non-interacting, the ground state is represented by a single Slater determinant of the set of single-particle wave functions ψ_i with $i = 1, \ldots, N$. Each of these single-particle states obeys a Schrödinger-like equation

$$\left[-\frac{1}{2}\nabla^2 + V_{\text{eff}}(\boldsymbol{r})\right]\psi_i(\boldsymbol{r}) = \mathcal{E}_i\psi_i(\boldsymbol{r})\,, \tag{2.11}$$

which are known as Kohn-Sham equations, the solutions ψ_i are the Kohn-Sham wave functions, and $\mathcal{E}_i$ are the Kohn-Sham eigenvalues. The corresponding ground-state density $n_{\text{KS}}(\boldsymbol{r})$ of the reference system is found by occupying the lowest-lying solutions of Eq. (2.11), which amounts to $n_{\text{KS}}(\boldsymbol{r}) = \sum_i |\psi_i(\boldsymbol{r})|^2$. The total energy functional reads in this case

$$E_{\text{KS}}[n_{\text{KS}}(\boldsymbol{r})] = T_{\text{KS}}[n_{\text{KS}}(\boldsymbol{r})] + \int V_{\text{eff}}(\boldsymbol{r})n_{\text{KS}}(\boldsymbol{r})\,\mathrm{d}^3r\,, \tag{2.12}$$

and provides an alternative approach to find the ground-state density of the Kohn-Sham reference system when following the variational principle[5].

The formalism by Kohn and Sham converts the intricate many-body problem of interacting electrons into simpler single-particle problems that are solvable (at least approximately) but still allow for the efficient calculation of the exact ground-state energy of the interacting system. However, in order to satisfy the bridging condition that the electronic densities of the two systems are the same, *i.e.*, $n(\boldsymbol{r}) = n_{\text{KS}}(\boldsymbol{r})$, the

---

[5] In fact, we can derive the set of single-particle Schrödinger equations (2.11) if we minimize the energy functional $E_{\text{KS}}[n_{\text{KS}}]$, where the constraint of a fixed number of electrons is accounted for by the Lagrange multipliers $\mathcal{E}_i$.

effective potential $V_{\mathrm{eff}}(\boldsymbol{r})$ of the non-interacting reference system has to be adjusted adequately. To proceed, we rewrite the total energy functional (2.10) of the complex many-body system as[6]

$$E[n(\boldsymbol{r})] = T_{\mathrm{KS}}[n(\boldsymbol{r})] + \int v_{\mathrm{ext}}(\boldsymbol{r})n(\boldsymbol{r})\,\mathrm{d}^3r + \frac{1}{2}\iint \frac{n(\boldsymbol{r})n(\boldsymbol{r}')}{|\boldsymbol{r}-\boldsymbol{r}'|}\mathrm{d}^3r\mathrm{d}^3r' + E_{\mathrm{xc}}[n(\boldsymbol{r})]\,, \tag{2.13}$$

where the third term on the right-hand side is the *Hartree term* V_{H} (known already from the Thomas-Fermi model) taking into account explicitly electrostatic interactions between the electrons, and the exchange-correlation functional

$$E_{\mathrm{xc}}[n(\boldsymbol{r})] = W[n(\boldsymbol{r})] + T[n(\boldsymbol{r})] - T_{\mathrm{KS}}[n(\boldsymbol{r})] \tag{2.14}$$

contains corrections to the kinetic energy as well as the remaining electron-electron interaction $W = V_{\mathrm{ee}} - V_{\mathrm{H}}$. While the first three contributions on the right-hand side of Eq. (2.13) can be calculated numerically, an exact expression for the exchange-correlation part remains elusive until now. Consequently, the complexity of the interacting many-body problem is mapped to finding reliable approximations to E_{xc} in the Kohn-Sham approach. The minimization of the energy functional (2.13) leads to a second set of Schrödinger-like equations, which becomes identical to Eq. (2.11) if the effective potential is chosen as

$$V_{\mathrm{eff}}(\boldsymbol{r}) = v_{\mathrm{ext}}(\boldsymbol{r}) + \iint \frac{n(\boldsymbol{r}')}{|\boldsymbol{r}-\boldsymbol{r}'|}\,\mathrm{d}^3r' + \frac{\delta E_{\mathrm{xc}}[n(\boldsymbol{r})]}{\delta n(\boldsymbol{r})}\,, \tag{2.15}$$

which establishes the equality of the ground-state densities of the non-interacting reference system and the interacting one.

Since the effective potential entering the Kohn-Sham equations depends on the electronic density, the equations (2.11), (2.15), and $n(\boldsymbol{r}) = \sum_i |\psi_i(\boldsymbol{r})|^2$ constitute a non-linear system of equations that need to be solved self-consistently (see also Fig. 2.1): Starting from an initial density, the effective potential is set up, followed by the solution of the Schrödinger-like equation (2.11), which serves to compute the new ground-state density. This output density – or possibly a mixture of input and output densities – is used to determine again the effective potential, and iterated until input and output densities are the same. By combining within the Kohn-Sham formalism the Eqs. (2.11), (2.13), and (2.15), we arrive at the sought ground-state total energy of the interacting many-body system:

$$E = \sum_i \mathcal{E}_i - \frac{1}{2}\iint \frac{n(\boldsymbol{r})n(\boldsymbol{r}')}{|\boldsymbol{r}-\boldsymbol{r}'|}\,\mathrm{d}^3r\mathrm{d}^3r' - \int \frac{\delta E_{\mathrm{xc}}}{\delta n(\boldsymbol{r})} n(\boldsymbol{r})\,\mathrm{d}^3r + E_{\mathrm{xc}}\,, \tag{2.16}$$

where the simple sum of the occupied Kohn-Sham eigenvalues $\mathcal{E}_i$ of the auxiliary reference system needs to be corrected for the double counting of the electron-electron interactions. Notably, it cannot be expected that the Kohn-Sham orbitals and energies have a direct physical meaning on their own as they form solutions to an ancillary single-particle problem[7]. Nevertheless, experience has shown that these eigenstates

---

[6] As the densities $n(\boldsymbol{r})$ and $n_{\mathrm{KS}}(\boldsymbol{r})$ are required to be the same, the subscript is suppressed in the following.

[7] An exception is the highest occupied Kohn-Sham eigenvalue, which determines the ionization potential.

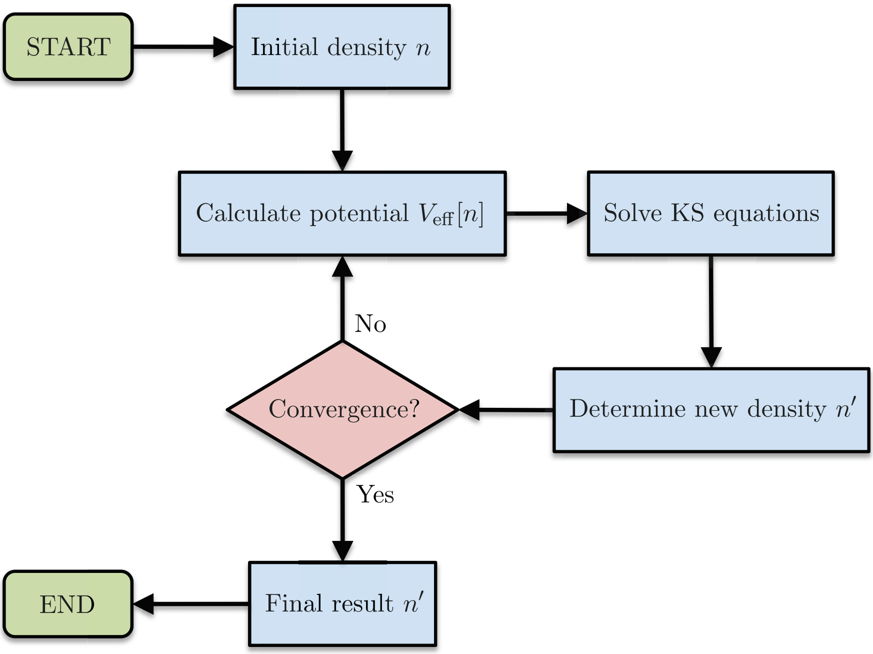

Figure 2.1: Self-consistency circle of density functional theory to determine the charge density $n(\boldsymbol{r})$ based on the Kohn-Sham approach (2.11).

and eigenvalues often describe the true electronic structure of the interacting many-electron system exceptionally well, which lends credibility to electronic band structure calculations based on the approach by Kohn and Sham. The ground-state Kohn-Sham wave functions can even serve as a starting point for advanced perturbative schemes aiming at the description of excitations.

2.5 Treatment of spin-polarized systems

Although it was originally introduced for non-magnetic systems, DFT can also be applied to spin-polarized systems [44] that may be subject to an external magnetic field $\boldsymbol{B}_{\text{ext}}$. By following an analogous reasoning, the total energy in the magnetic case can be proven to be a unique functional of both the electronic many-body density $n(\boldsymbol{r})$ and the spin, or, magnetization density $\boldsymbol{m}(\boldsymbol{r})$. Because of the additional magnetic field, the many-body Hamiltonian is modified as $H = T + U + V_{\text{ee}}$, where

$$U = \int \left[v_{\text{ext}}(\boldsymbol{r}) n(\boldsymbol{r}) - \boldsymbol{B}_{\text{ext}}(\boldsymbol{r}) \cdot \boldsymbol{m}(\boldsymbol{r}) \right] \mathrm{d}^3 r \,, \tag{2.17}$$

which represents the single-particle potential arising from the interaction of the electrons with the nuclear field v_{ext} and the magnetic field $\boldsymbol{B}_{\text{ext}}$. Based on the Rayleigh-Ritz variational principle, it follows by *reductio ad impossibilem* that two different external potentials U and U' lead to different densities $n(\boldsymbol{r}) \neq n'(\boldsymbol{r})$ and $\boldsymbol{m}(\boldsymbol{r}) \neq \boldsymbol{m}'(\boldsymbol{r})$. An equivalent formulation of DFT in spin-polarized systems is obtained by using instead of electronic and magnetization densities the 2×2 density matrix $\rho(\boldsymbol{r}) = \frac{1}{2}\left[n(\boldsymbol{r})I + \boldsymbol{m}(\boldsymbol{r}) \cdot \boldsymbol{\sigma}\right]$ as an alternative representation. Here, $\boldsymbol{\sigma}$ is the vector of Pauli matrices, and I denotes the unit matrix.

To generalize the Kohn-Sham equations (2.11), N occupied single-particle spinor wave functions $\boldsymbol{\psi}_i(\boldsymbol{r}) = (\psi_{i+}(\boldsymbol{r}), \psi_{i-}(\boldsymbol{r}))^{\mathrm{T}}$ are introduced such that the densities read

$$n(\boldsymbol{r}) = \sum_i \sum_{\alpha=\pm} |\psi_{i\alpha}(\boldsymbol{r})|^2 \,, \tag{2.18}$$

$$\boldsymbol{m}(\boldsymbol{r}) = \sum_i \boldsymbol{\psi}_i^\dagger(\boldsymbol{r})\boldsymbol{\sigma}\boldsymbol{\psi}_i(\boldsymbol{r}) \,. \tag{2.19}$$

If we apply the variational principle for the total energy functional $E[n(\boldsymbol{r}), \boldsymbol{m}(\boldsymbol{r})]$ in the spin-polarized case, we arrive at a set of Schrödinger-Pauli-like equations that describe the effective single-particle problem:

$$\left[-\frac{1}{2}\nabla^2 + V_{\mathrm{eff}}(\boldsymbol{r}) + \boldsymbol{\sigma} \cdot \boldsymbol{B}_{\mathrm{eff}}(\boldsymbol{r})\right] \boldsymbol{\psi}_i(\boldsymbol{r}) = \mathcal{E}_i \boldsymbol{\psi}_i(\boldsymbol{r}) \,. \tag{2.20}$$

The effective magnetic field $\boldsymbol{B}_{\mathrm{eff}} = \boldsymbol{B}_{\mathrm{ext}} + \boldsymbol{B}_{\mathrm{xc}}$ contains the external field as well as the so-called *exchange field*, which arises from the variation of the exchange-correlation term with the magnetization density:

$$\boldsymbol{B}_{\mathrm{xc}}(\boldsymbol{r}) = \frac{\delta E_{\mathrm{xc}}[n(\boldsymbol{r}), \boldsymbol{m}(\boldsymbol{r})]}{\delta \boldsymbol{m}(\boldsymbol{r})} \,. \tag{2.21}$$

Since effective potential and effective magnetic field in the Schrödinger-Pauli-like equations rely on spin and electron densities, Eq. (2.20) has to be solved iteratively until self-consistency is reached.

The spin-polarized Kohn-Sham equations in the general form (2.20) are well-suited to investigate *non-collinear magnetism*. In the case of *collinear magnetism*, for which the direction of the magnetic field is constant in space, *e.g.*, $\boldsymbol{B}_{\mathrm{eff}}(\boldsymbol{r}) = B_{\mathrm{eff}}(\boldsymbol{r})\hat{\boldsymbol{e}}_z$, the Schrödinger-Pauli-like equations decouple for the two spinor components into

$$\begin{aligned}\left[-\frac{1}{2}\nabla^2 + V_{\mathrm{eff}}(\boldsymbol{r}) + B_{\mathrm{eff}}(\boldsymbol{r})\right] \psi_{i+}(\boldsymbol{r}) &= \mathcal{E}_{i+}\psi_{i+}(\boldsymbol{r}) \,, \\ \left[-\frac{1}{2}\nabla^2 + V_{\mathrm{eff}}(\boldsymbol{r}) - B_{\mathrm{eff}}(\boldsymbol{r})\right] \psi_{i-}(\boldsymbol{r}) &= \mathcal{E}_{i-}\psi_{i-}(\boldsymbol{r}) \,,\end{aligned} \tag{2.22}$$

which can be solved independently for the two spin directions. As a result, observable quantities such as the total energy are functionals of the electronic density and the magnitude of the magnetization $m(\boldsymbol{r})$ rather than its direction. Therefore, an equivalent representation of the electronic structure problem in collinear magnets uses the densities of spin-up and spin-down electrons that read $n_+(\boldsymbol{r}) = \sum_i |\psi_{i+}(\boldsymbol{r})|^2$ and $n_-(\boldsymbol{r}) = \sum_i |\psi_{i-}(\boldsymbol{r})|^2$, respectively, from which the electron density $n(\boldsymbol{r}) = n_+(\boldsymbol{r}) + n_-(\boldsymbol{r})$ and the magnetization density $m(\boldsymbol{r}) = n_+(\boldsymbol{r}) - n_-(\boldsymbol{r})$ can be constructed. Most of the spin-polarized DFT calculations have been performed within this framework, where the effort of the collinear magnetic calculation (2.22) is twice that of a non-magnetic one.

2.6 Exchange and correlation effects

Remarkably, the above density-based formalism is an exact theory since it can reproduce in principle all ground-state properties of any interacting many-electron system if the exchange-correlation term $E_{\mathrm{xc}}[n(\boldsymbol{r}), \boldsymbol{m}(\boldsymbol{r})]$ was known. As this is not the case, however, approximations to account for exchange and correlation effects are obligatory. The great success of modern DFT for electronic structure calculations roots primarily in the observation that various elementary properties of interacting many-electron systems are described surprisingly well within relatively simple and thus practical approximations to the functional form of $E_{\mathrm{xc}}[n(\boldsymbol{r}), \boldsymbol{m}(\boldsymbol{r})]$.

One routinely applied example is the *local spin density approximation (LSDA)* [30, 43, 45–51], which is conceptually similar to the Thomas-Fermi approximation in replacing $E_{\mathrm{xc}}[n(\boldsymbol{r}), \boldsymbol{m}(\boldsymbol{r})]$ locally with the exchange-correlation energy of a homogeneous electron gas. Thus, the approximate functional assumes the form

$$E_{\mathrm{xc}}[n(\boldsymbol{r}), \boldsymbol{m}(\boldsymbol{r})] = \int \epsilon_{\mathrm{xc}}(n(\boldsymbol{r}), m(\boldsymbol{r}))n(\boldsymbol{r})\, \mathrm{d}^3 r\,, \tag{2.23}$$

where the exchange-correlation energy density ϵ_{xc} is just a function of the electron density and the magnitude $m(\boldsymbol{r})$ of the spin density. Due to this local definition, the exchange field is always aligned with the magnetization direction $\hat{\boldsymbol{m}}$ according to

$$\boldsymbol{B}_{\mathrm{xc}}(\boldsymbol{r}) = n(\boldsymbol{r})\frac{\partial \epsilon_{\mathrm{xc}}(n(\boldsymbol{r}), m(\boldsymbol{r}))}{\partial m(\boldsymbol{r})}\hat{\boldsymbol{m}}\,. \tag{2.24}$$

Accordingly, the Kohn-Sham equations in LSDA are simplified to the form of Hartree equations. While the exchange energy of the uniform electron liquid has been calculated by Dirac, the general correlation energy of this system is not known analytically. Therefore, the exchange-correlation density ϵ_{xc} is usually accounted for using specific parameterizations such as those given by von Barth and Hedin [45] based on the random phase approximation, by Vosko, Wilk and Nusair [48] rooting in quantum Monte-Carlo simulations, or by Perdew and Zunger [49] that mixes the latter two. Although the LSDA may be anticipated to be restricted to the case of slowly varying densities, it has been applied quite successfully even to inhomogeneous systems.

The *generalized gradient approximation (GGA)* denotes the next level of complexity in treating the unknown exchange-correlation term, which is expressed in this approach as

$$E_{\mathrm{xc}}[n_+, n_-] = \int f(n_+, n_-, \nabla n_+, \nabla n_-)\, \mathrm{d}^3 r\,. \tag{2.25}$$

In contrast to the LSDA, for which the basic ingredient $\epsilon_{\mathrm{xc}}(n_+, n_-)$ is directly related to the uniform electron liquid with spin densities n_+ and n_-, there is no such guiding principle to derive a unique function $f(n_+, n_-, \nabla n_+, \nabla n_-)$. As a result, a vast number of GGA exchange-correlation functionals exists, also termed semi-local functionals as they hinge on the gradient of the density. Among them is the parametrization by Perdew, Burke, and Ernzerhof (PBE), which is one of the most widely used semi-local functionals [52].

Particular many-body systems may call for the use of more specialized approximations beyond LSDA and GGA in order to describe ground-state properties reliably. For example, the latter two functional types tend to represent poorly the electronic structure of systems such as transition-metal oxides that comprise predominantly localized or strongly correlated electrons. An improved treatment of exchange-correlation effects in these systems is realized in the so-called self-interaction correction (SIC) [49] or the LDA+U method [53–56], which introduces an adjustable orbital-dependent interaction U in the calculations. Alternatively, the free parameter U can also be obtained self-consistently from DFT calculations [57–59]. Furthermore, the approach of exact exchange [60] is in order if spectral properties of insulators need to be determined to high precision.

Chapter 3

Full-potential linearized augmented-plane-wave method

Contents

We present the foundations of the full-potential linearized augmented-plane-wave (FLAPW) method that provides a suitable set of basis states for the solution of the electronic-structure problem laid out in the previous chapter. In the beginning, we highlight the origins of this framework rooting in augmented-plane-wave and linearized methods that typically employ shape approximations for the effective potential. Considering the full crystal potential, we formulate the generalized Kohn-Sham eigenvalue problem by constructing the Hamiltonian matrix in the non-orthogonal FLAPW basis, including possible contributions that arise from the adequate treatment of thin films and surfaces. Starting from the Dirac equation, we elaborate on how relativistic effects on valence electrons can be taken into account. Finally, the implementation of non-collinear magnetism within the FLAPW method is discussed.

3.1 Basis sets for density functional theory

3.1.1 Augmented plane-waves

The Kohn-Sham equations (2.11), or their general spin-polarized analog given by Eq. (2.20), can be solved following various strategies. A common approach is to expand the single-particle wave functions into suitable basis functions that adapt to the physical problem at hand. For example, the choice of an orthogonal plane-wave basis is convenient as these functions are simple, they diagonalize the kinetic energy term $-\frac{1}{2}\nabla^2$, and are suggested by the *Bloch theorem* as solutions of a periodic system [61].

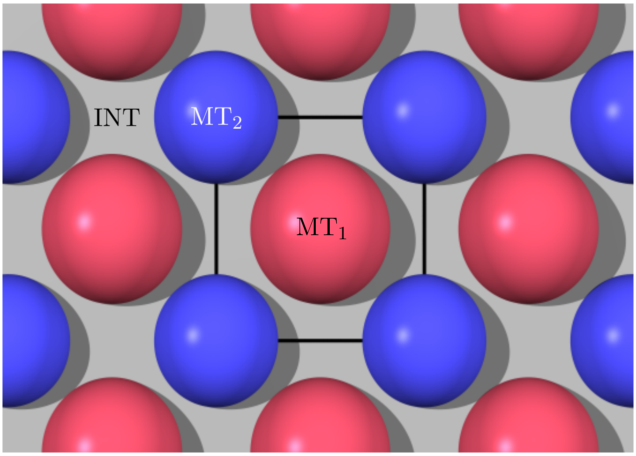

Figure 3.1: In the augmented-plane-wave method, the real space is partitioned into non-overlapping spheres (here MT$_1$ and MT$_2$) around the nuclei, known as muffin tins, and the interstitial region (INT). The different basis functions in these real-space regions are adapted to describe adequately the wave functions either near the nuclei or in between them. The unit cell of the depicted cubic lattice is indicated by black lines.

Owing to the translational invariance in solids, the Kohn-Sham wave functions may be written accordingly as *Bloch states* that read $\psi_{\boldsymbol{k}}(\boldsymbol{r}) = \mathrm{e}^{\mathrm{i}\boldsymbol{k}\cdot\boldsymbol{r}} u_{\boldsymbol{k}}(\boldsymbol{r})$ at any point $\boldsymbol{k}$ of the crystal-momentum Brillouin zone. The lattice-periodic functions $u_{\boldsymbol{k}}(\boldsymbol{r})$ are expanded into plane-waves with the reciprocal-lattice vector $\boldsymbol{G}$ as characteristic wave vector:

$$\psi_{\boldsymbol{k}}(\boldsymbol{r}) = \sum_{\boldsymbol{G}} c_{\boldsymbol{k}}^{\boldsymbol{G}}\, \phi_{\boldsymbol{k}}^{\boldsymbol{G}}(\boldsymbol{r}) \qquad \text{with} \qquad \phi_{\boldsymbol{k}}^{\boldsymbol{G}}(\boldsymbol{r}) = \frac{1}{\sqrt{V}}\, \mathrm{e}^{\mathrm{i}(\boldsymbol{k}+\boldsymbol{G})\cdot\boldsymbol{r}}\,, \tag{3.1}$$

where V is the unit-cell volume. In order to derive the expansion coefficients $c_{\boldsymbol{k}}^{\boldsymbol{G}}$, the eigenvalue problem of the single-particle Hamiltonian in the basis of the plane waves has to be formulated and solved.

Obviously, when aiming at the numerical solution of the Kohn-Sham problem, we need to restrict the size of the basis set in the plane-wave expansion (3.1) by taking into account only a finite but large enough number of vectors $\boldsymbol{G}$. Although this approach is successful in describing non-interacting electrons in a sufficiently smooth potential, it cannot capture rapid oscillations of charge density and wave functions that arise close to the ions. As an enormous amount of vectors $\boldsymbol{G}$ would be required for this to work, the use of a plane-wave basis is rendered highly inefficient in the light of the strong $1/r$-divergence of the Coulomb potential. This calls either for replacing the full nuclear field with an effective potential, also referred to as *pseudopotential*, that is smooth enough to be treated with a small number of plane waves, or for a better basis-set choice inspired by the underlying physics.

Along the latter line of reasoning, Slater proposed originally the augmented-plane-wave (APW) method [62], where real space is partitioned into muffin-tin spheres centered around the nuclei, and the remaining interstitial region in between the ions as shown in Fig. 3.1. Frequently, implementations of the APW method adopt so-called shape approximations by treating the potential inside the muffin tins as spherically symmetric, while the interstitial potential is set to a constant value. This suggests to use plane-wave basis functions in the interstitial region but spherical harmonics times a radial wave function for an expansion of the single-particle solutions within the muffin tins:

$$\phi_{\boldsymbol{k}}^{\boldsymbol{G}}(\boldsymbol{r}) = \begin{cases} \frac{1}{\sqrt{V}} \mathrm{e}^{\mathrm{i}(\boldsymbol{k}+\boldsymbol{G})\cdot\boldsymbol{r}} & \text{in interstitial} \\ \sum_{L} a_{L\boldsymbol{k}}^{\mu\boldsymbol{G}} u_l^{\mu}(r_\mu) Y_L(\hat{\boldsymbol{r}}_\mu) & \text{in muffin tin } \mu \end{cases}, \tag{3.2}$$

where $\boldsymbol{r}_\mu = r_\mu \hat{\boldsymbol{r}}_\mu = \boldsymbol{r} - \boldsymbol{\tau}_\mu$ is the position vector relative to the ionic position $\boldsymbol{\tau}_\mu$, and the angular-momentum quantum numbers are contained in $L = (l, m)$. The coefficients $a_{L\boldsymbol{k}}^{\mu\boldsymbol{G}}$ of the expansion into spherical harmonics have to be determined such that the wave functions at the muffin-tin boundary are continuous. Inside the muffin tin μ, the functions $u_l^\mu(r_\mu)$ are solutions of the radial Schrödinger equation[1]

$$\left[-\frac{1}{2}\frac{\partial^2}{\partial r_\mu^2} + \frac{1}{2}\frac{l(l+1)}{r_\mu^2} + V_\mu^0(r_\mu) - E_l^\mu\right] r_\mu u_l^\mu(r_\mu) = \left[H_{\mathrm{sph}}^\mu - E_l^\mu\right] r_\mu u_l^\mu(r_\mu) = 0 \tag{3.3}$$

to a given energy parameter E_l^μ, where $V_\mu^0(r_\mu)$ denotes the spherical part of the nuclear potential, and H_{sph}^μ is the spherical part of the non-relativistic Hamiltonian. Selecting the optimal energy parameters to obtain an adequate basis for the single-particle Hamiltonian is subtle: if these parameters are fixed during the construction of the basis, the electronic structure problem amounts to a generalized eigenvalue problem, which can be solved numerically. However, fixing E_l^μ strongly restricts the variational freedom of the APW basis (3.2) such that an accurate description is only recovered if the energy parameters are identical to the true (initially unknown) band energies. As the radial solutions hinge on the choice of E_l^μ, the electronic structure is not found from a simple diagonalization of the Hamiltonian matrix but invokes the iterative solution of a non-linear, computationally much more challenging problem.

Going beyond the shape approximation of a spherically symmetric potential inside the muffin tins makes this issue in the APW method even more intricate since the optimal energy parameters are not anymore the band energies in this case. In addition, the basis set (3.2) may suffer from the so-called asymptote problem if the radial functions $u_l^\mu(r_\mu)$ become tiny or vanish at the muffin-tin boundary, which renders the mentioned boundary conditions difficult to meet.

3.1.2 Linearized augmented-plane-waves

As the APW method does not offer enough variational freedom for fixed energy parameters and entails a non-linear energy dependence of the Hamiltonian for the optimal choice of E_l^μ, Andersen [63] as well as Koelling and Arbman [64] proposed the linearized augmented-plane-wave (LAPW) method. Here, additional variational freedom is introduced in the muffin tins by considering linear combinations of the radial functions and their energy derivatives $\dot{u}_l^\mu(r_\mu)$. In order to appreciate the inclusion of this additional contribution, a Taylor expansion of the radial functions around

---

[1] When including relativistic effects, the radial functions are found from solving the scalar relativistic Dirac equation (3.36) instead of the Schrödinger equation (3.3).

E_l^μ can be performed, which reads up to first order

$$u_l^\mu(r_\mu, \mathcal{E}) \approx u_l^\mu(r_\mu, E_l^\mu) + \dot{u}_l^\mu(r_\mu, E_l^\mu)(\mathcal{E} - E_l^\mu)\,, \tag{3.4}$$

where the dependence of the radial functions on the band energy $\mathcal{E}$ is written out explicitly, and $\dot{u}_l^\mu = \partial u_l^\mu / \partial \mathcal{E}$ is the energy derivative. This linearization introduces errors in the wave function that are quadratic with respect to the energy difference $\mathcal{E} - E_l^\mu$, which implies according to the variational principle an error on the order of $(\mathcal{E} - E_l^\mu)^4$ for the resulting band energies. Therefore, the LAPW method works usually very well even for a broad energy range of the valence bands[2].

The linearization motivates the use of the following LAPW basis states:

$$\phi_{\boldsymbol{k}}^{\boldsymbol{G}}(\boldsymbol{r}) = \begin{cases} \frac{1}{\sqrt{V}} \mathrm{e}^{\mathrm{i}(\boldsymbol{k}+\boldsymbol{G})\cdot\boldsymbol{r}} & \text{in interstitial} \\ \sum\limits_L \left[a_{L\boldsymbol{k}}^{\mu\boldsymbol{G}} u_l^\mu(r_\mu) + b_{L\boldsymbol{k}}^{\mu\boldsymbol{G}} \dot{u}_l^\mu(r_\mu) \right] Y_L(\hat{\boldsymbol{r}}_\mu) & \text{in muffin tin } \mu \end{cases}, \tag{3.5}$$

where the expansion coefficients $a_{L\boldsymbol{k}}^{\mu\boldsymbol{G}}$ and $b_{L\boldsymbol{k}}^{\mu\boldsymbol{G}}$ are determined via the constraint that the basis states and their first real-space derivatives are continuous at the muffin-tin boundary[3]. Typically, the normalization condition $\langle u_l^\mu | u_{l'}^\mu \rangle = \int_0^{R_\mu} u_l^\mu u_{l'}^\mu r_\mu^2 dr_\mu = \delta_{ll'}$ is adopted, where R_μ is the muffin-tin radius around the μth ion, which entails that the radial functions and their energy derivatives are mutually orthogonal, i.e., $\langle u_l^\mu | \dot{u}_{l'}^\mu \rangle = 0$. The latter states are proper solutions to a Schrödinger-like equation that is found by taking the derivative of Eq. (3.3) with respect to the energy parameter:

$$\left[-\frac{1}{2}\frac{\partial^2}{\partial r_\mu^2} + \frac{1}{2}\frac{l(l+1)}{r_\mu^2} + V_\mu^0(r_\mu) - E_l^\mu \right] r_\mu \dot{u}_l^\mu(r_\mu) = \left[H_{\mathrm{sph}}^\mu - E_l^\mu \right] r_\mu \dot{u}_l^\mu(r_\mu) = r_\mu u_l^\mu(r_\mu)\,. \tag{3.6}$$

Implementing the linearized basis states (3.5), the LAPW method overcomes the major drawbacks of the APW basis discussed before: first and foremost, an accurate treatment does not rely anymore on choosing the energy parameters E_l^μ as the band energies that are thus determined from a standard secular equation of the Hamiltonian. These linearized basis states also do not suffer from the asymptote problem as the radial and energy derivatives are often non-zero even if $u_l^\mu(r_\mu)$ vanishes at the muffin-tin boundary. And finally, the increased variational freedom in the muffin tins offers the powerful option to include rather easily potential contributions beyond the spherically symmetric one, which results in the full-potential linearized augmented-plane-wave (FLAPW) method.

However, we remark that the problem of the non-linear energy dependence of the Hamiltonian in the APW approach is avoided by the LAPW method at the cost of a larger number of plane waves to be taken into account in the interstitial region in order to realize eventually the extra variational freedom in the muffin tins. Although it might be surprising at first sight, this connection originates from the coupling of plane waves and muffin-tin basis functions mediated by the boundary conditions.

---

[2] While the use of a single set of energy parameters is typically sufficient, the energy range to be described could also be split into several energy windows with separate sets of energy parameters.

[3] Consequently, the LAPW basis set has to obey more constraints as compared to the APW one, where only the continuity of the basis states is required.

3.1.3 Extending the basis set by local orbitals

In order to improve the treatment of semi-core states such as the $3s$ and $3p$ orbitals in Ti, and thereby boost the convergence with respect to the number of basis functions, local orbitals (LOs) have been suggested [65–67] to supplement the above APW and LAPW basis sets. A given LO is restricted locally in space to the muffin-tin sphere of the particular atom the semi-core states of which it should represent. Inside the μth muffin tin, the basis states become linear combinations of radial semi-core solutions $u_l^{\mu\mathrm{LO}}$ of the Schrödinger-like equation to the energy parameter $E_l^{\mu\mathrm{LO}}$ and the functions u_l^μ and $\dot{u}_l^\mu$ that describe the valence electrons:

$$\phi_{\boldsymbol{k}}^{\mu\mathrm{LO}}(\boldsymbol{r}) = \sum_L \left[a_L^{\mu\mathrm{LO}} u_l^\mu(r_\mu) + b_L^{\mu\mathrm{LO}} \dot{u}_l^\mu(r_\mu) + c_L^{\mu\mathrm{LO}} u_l^{\mu\mathrm{LO}}(r_\mu)\right] Y_L(\hat{\boldsymbol{r}}_\mu)\,. \tag{3.7}$$

The expansion coefficients are chosen such that the basis functions and their radial derivatives vanish at the muffin-tin boundary.

3.1.4 Potential-shape approximations

Most of the calculations based on the APW and LAPW method adopt shape approximations for the external potential, in which the electrons move. For example, the potential in the unit cell $V(\boldsymbol{r})$ is often approximated by

$$V(\boldsymbol{r}) = \begin{cases} V_{\mathrm{int}}^0 = \text{const.} & \text{in interstitial} \\ V_\mu^0(r_\mu) & \text{in muffin tin } \mu \end{cases}, \tag{3.8}$$

which assumes the potential in the interstitial region to be constant but a spherically symmetric shape of the potential inside the muffin tins. Still, $V_\mu^0(r_\mu)$ is in principle specific to each muffin tin μ in order to account for the effect of different atom types. While using the shape approximation (3.8) could be motivated for simple metals with densely packed structure, the reliable prediction of electronic properties in complex solid-state systems such as perovskites or at surfaces would in general contradict the physical intuition.

A rigorous handling of the full potential without resorting to any shape approximation has been developed [68–70], and led in combination with an implementation of the total energy [71] to the FLAPW method. Dropping any shape approximation, this method extends the spherical muffin-tin potential by non-spherical contributions from $l > 0$, and it further includes the warped interstitial potential:

$$V(\boldsymbol{r}) = \begin{cases} \sum\limits_{\boldsymbol{G}} V_{\mathrm{int}}^{\boldsymbol{G}} \mathrm{e}^{\mathrm{i}\boldsymbol{G}\cdot\boldsymbol{r}} & \text{in interstitial} \\ \sum\limits_L V_\mu^L(r_\mu) Y_L(\hat{\boldsymbol{r}}) & \text{in muffin tin } \mu \end{cases}. \tag{3.9}$$

The charge density can be represented analogously. Apparently, Eq. (3.9) relies on accurate methods to determine the warping part $V_{\mathrm{int}}^{\boldsymbol{G}}$ and the non-spherical contribution $V_\mu^L(r_\mu)$ to the potential.

3.2 Construction of Hamiltonian matrix

3.2.1 Generalized eigenvalue problem

Since the plane waves in Eq. (3.5) are not defined for the whole space but are confined to the interstitial, they are not orthogonal when integrated over this region. In the muffin tins, the basis states exhibit a finite overlap due to the coupling to the plane-waves via the boundary conditions, even though the muffin-tin functions $u_l^\mu Y_L$ and $\dot{u}_l^\mu Y_L$ are mutually orthogonal. As a result, the electronic structure problem in the LAPW basis assumes the form of a generalized eigenvalue problem:

$$\left[H_{\boldsymbol{k}} - \mathcal{E}_{\boldsymbol{k}n} S_{\boldsymbol{k}}\right] \boldsymbol{c}_{\boldsymbol{k}n} = 0\,, \tag{3.10}$$

where $\boldsymbol{c}_{\boldsymbol{k}n}$ is the vector of coefficients in the expansion $\psi_{\boldsymbol{k}n}(\boldsymbol{r}) = \sum_{\boldsymbol{G}} c_{\boldsymbol{k}n}^{\boldsymbol{G}} \phi_{\boldsymbol{k}}^{\boldsymbol{G}}(\boldsymbol{r})$ of the nth eigenstate with the crystal momentum $\boldsymbol{k}$ in terms of non-orthogonal basis states $\phi_{\boldsymbol{k}}^{\boldsymbol{G}}(\boldsymbol{r})$. The Hamiltonian matrix $H_{\boldsymbol{k}}$ and the non-diagonal overlap matrix $S_{\boldsymbol{k}}$ in this basis are found from the expressions

$$H_{\boldsymbol{k}}^{\boldsymbol{G}\boldsymbol{G}'} = \langle \phi_{\boldsymbol{k}}^{\boldsymbol{G}} | H | \phi_{\boldsymbol{k}}^{\boldsymbol{G}'} \rangle = \int \phi_{\boldsymbol{k}}^{\boldsymbol{G}*}(\boldsymbol{r}) H \phi_{\boldsymbol{k}}^{\boldsymbol{G}'}(\boldsymbol{r})\, \mathrm{d}^3 r\,, \tag{3.11}$$

$$S_{\boldsymbol{k}}^{\boldsymbol{G}\boldsymbol{G}'} = \langle \phi_{\boldsymbol{k}}^{\boldsymbol{G}} | \phi_{\boldsymbol{k}}^{\boldsymbol{G}'} \rangle = \int \phi_{\boldsymbol{k}}^{\boldsymbol{G}*}(\boldsymbol{r}) \phi_{\boldsymbol{k}}^{\boldsymbol{G}'}(\boldsymbol{r})\, \mathrm{d}^3 r\,. \tag{3.12}$$

By using the Cholesky factorization of the Hermitian, positive-definite overlap matrix, the generalized eigenvalue problem (3.10) reduces to a standard eigenvalue problem, which can be solved efficiently.

3.2.2 Muffin-tin and interstitial contributions

Due to the augmentation of the LAPW basis states, the Hamiltonian consists of two separate parts originating from the muffin tins and the interstitial region, respectively. According to Eq. (3.3), the spherical term H_{sph}^μ of the full Hamiltonian in the μth muffin tin contains the kinetic energy $-\frac{1}{2}\frac{\partial^2}{\partial r_\mu^2}$, which has to be symmetrized by

$$-\frac{1}{2}\frac{\partial^2}{\partial r_\mu^2} \longrightarrow -\frac{1}{4}\left(\frac{\overset{\Leftarrow}{\partial}{}^2}{\partial r_\mu^2} + \frac{\overset{\Rightarrow}{\partial}{}^2}{\partial r_\mu^2}\right) \tag{3.13}$$

in order to arrive eventually at a Hermitian Hamiltonian matrix representation. Here, the double arrows indicate whether the derivative is acting to its right (as conventionally) or to its left. Thus, the matrix elements of the spherical Hamiltonian assume the form[4]

$$\begin{aligned} H_{\mathrm{sph}}^{\mu,\boldsymbol{G}\boldsymbol{G}'} &= \sum_L \int r_\mu^2 \left[a_L^{\mu\boldsymbol{G}} u_l^\mu + b_L^{\mu\boldsymbol{G}} \dot{u}_l^\mu\right]^* H_\mu^{\mathrm{sph}} \left[a_L^{\mu\boldsymbol{G}'} u_l^\mu + b_L^{\mu\boldsymbol{G}'} \dot{u}_l^\mu\right] \mathrm{d}r_\mu \\ &= \sum_L \left\{ \left(a_L^{\mu\boldsymbol{G}}\right)^* a_L^{\mu\boldsymbol{G}'} E_l^\mu + \frac{1}{2}\left[\left(a_L^{\mu\boldsymbol{G}}\right)^* b_L^{\mu\boldsymbol{G}'} + \left(b_L^{\mu\boldsymbol{G}}\right)^* a_L^{\mu\boldsymbol{G}'}\right] \left(b_L^{\mu\boldsymbol{G}}\right)^* b_L^{\mu\boldsymbol{G}'} E_l^\mu N_l^\mu \right\} \end{aligned} \tag{3.14}$$

---

[4] Here and in the following, we suppress the explicit $\boldsymbol{k}$-dependence of the expansion coefficients.

that follows from Eqs. (3.3), (3.6), and $\langle \dot{u}_l^\mu | \dot{u}_l^\mu \rangle = N_l^\mu$. Any spherically symmetric term in the Hamiltonian couples only spherical harmonics with the same angular momentum L.

The non-spherical part of the potential encompasses the remaining contributions from spherical harmonics with $l > 0$, which realizes a coupling between radial basis functions with different angular-momentum quantum numbers, in contrast to the spherically symmetric case. This manifests in the appearance of the so-called Gaunt coefficients $G(L, L', L'')$ when setting up the matrix elements of the non-spherical Hamiltonian that read

$$
\begin{aligned}
H_{\text{non}}^{\mu,\boldsymbol{G}\boldsymbol{G}'} &= \sum_{LL'L''} \int \left[a_L^{\mu\boldsymbol{G}} u_l^\mu + b_L^{\mu\boldsymbol{G}} \dot{u}_l^\mu \right]^* Y_L^* V_\mu^{L''} Y_{L''} \left[a_{L'}^{\mu\boldsymbol{G}'} u_{l'}^\mu + b_{L'}^{\mu\boldsymbol{G}'} \dot{u}_{l'}^\mu \right] Y_{L'} \, \mathrm{d}^3 r_\mu \\
&= \sum_{L,L'} \Big[\left(a_L^{\mu\boldsymbol{G}} \right)^* a_L^{\mu\boldsymbol{G}'} t_{LL'}^{\mu,uu} + \left(a_L^{\mu\boldsymbol{G}} \right)^* b_L^{\mu\boldsymbol{G}'} t_{LL'}^{\mu,u\dot{u}} \\
&\qquad + \left(b_L^{\mu\boldsymbol{G}} \right)^* a_L^{\mu\boldsymbol{G}'} t_{LL'}^{\mu,\dot{u}u} + \left(b_L^{\mu\boldsymbol{G}} \right)^* b_L^{\mu\boldsymbol{G}'} t_{LL'}^{\mu,\dot{u}\dot{u}} \Big] ,
\end{aligned}
\tag{3.15}
$$

where the coefficients

$$
\begin{aligned}
t_{LL'}^{\mu,uu} &= \sum_{L''} I_{ll'L''}^{\mu,uu} G(L, L', L'') , \\
t_{LL'}^{\mu,u\dot{u}} &= \sum_{L''} I_{ll'L''}^{\mu,u\dot{u}} G(L, L', L'') , \\
t_{LL'}^{\mu,\dot{u}u} &= \sum_{L''} I_{ll'L''}^{\mu,\dot{u}u} G(L, L', L'') , \\
t_{LL'}^{\mu,\dot{u}\dot{u}} &= \sum_{L''} I_{ll'L''}^{\mu,\dot{u}\dot{u}} G(L, L', L'')
\end{aligned}
\tag{3.16}
$$

are contractions of the Gaunt coefficients with integrals of the radial muffin-tin functions and the radial part of the non-spherical potential:

$$
\begin{aligned}
I_{ll'L''}^{\mu,uu} &= \int r_\mu^2 u_l^\mu(r_\mu) u_{l'}^\mu(r_\mu) V_\mu^{L''}(r_\mu) \, \mathrm{d}r_\mu , \\
I_{ll'L''}^{\mu,u\dot{u}} &= \int r_\mu^2 u_l^\mu(r_\mu) \dot{u}_{l'}^\mu(r_\mu) V_\mu^{L''}(r_\mu) \, \mathrm{d}r_\mu , \\
I_{ll'L''}^{\mu,\dot{u}u} &= \int r_\mu^2 \dot{u}_l^\mu(r_\mu) u_{l'}^\mu(r_\mu) V_\mu^{L''}(r_\mu) \, \mathrm{d}r_\mu , \\
I_{ll'L''}^{\mu,\dot{u}\dot{u}} &= \int r_\mu^2 \dot{u}_l^\mu(r_\mu) \dot{u}_{l'}^\mu(r_\mu) V_\mu^{L''}(r_\mu) \, \mathrm{d}r_\mu .
\end{aligned}
\tag{3.17}
$$

Because of the summations over additional sets of angular-momentum quantum numbers, the calculation of the matrix elements (3.15) of the non-spherical Hamiltonian are computationally more expensive as compared to the spherical contributions (3.14). While only matrix elements between LAPW basis functions are considered in Eqs. (3.14) and (3.15), the treatment of semi-core states by LOs yields further contributions LO-LO, LO-LAPW, and LAPW-LO, which are evaluated analogously to the LAPW-LAPW ones described above.

Setting up the Hamiltonian matrix in the interstitial region is straightforward due to the simple plane-wave basis. Once again, the kinetic energy in the Hamiltonian $-\frac{1}{2}\nabla^2 + V(\boldsymbol{r})$ is symmetrized such that the matrix elements are given by

$$\begin{aligned} H_{\text{int}}^{\boldsymbol{G}\boldsymbol{G}'} &= \frac{1}{V}\int_{\text{int}} \mathrm{e}^{-\mathrm{i}(\boldsymbol{G}+\boldsymbol{k})\cdot\boldsymbol{r}} \left[-\frac{1}{4}\overset{\Leftarrow}{\nabla}{}^2 - \frac{1}{4}\overset{\Rightarrow}{\nabla}{}^2 + V(\boldsymbol{r})\right] \mathrm{e}^{\mathrm{i}(\boldsymbol{G}'+\boldsymbol{k})\cdot\boldsymbol{r}}\,\mathrm{d}^3r \\ &= \frac{1}{4}\left[(\boldsymbol{G}+\boldsymbol{k})^2 + (\boldsymbol{G}'+\boldsymbol{k})^2\right]\Theta_{\boldsymbol{G}-\boldsymbol{G}'} + \sum_{\boldsymbol{G}''} V_{\text{int}}^{\boldsymbol{G}''}\,\Theta_{\boldsymbol{G}-\boldsymbol{G}'-\boldsymbol{G}''}\,, \end{aligned} \tag{3.18}$$

where $\Theta_{\boldsymbol{G}} = \int \Theta_{\text{int}}(\boldsymbol{r})\mathrm{e}^{\mathrm{i}\boldsymbol{G}\cdot\boldsymbol{r}}\mathrm{d}^3r$ is the Fourier transform of the real-space Heaviside step function that cuts out the interstitial region. The last term on the right-hand side is a convolution of the Fourier coefficients $V_{\text{int}}^{\boldsymbol{G}}$ of the warped potential with $\Theta_{\boldsymbol{G}}$.

To solve the generalized eigenvalue problem of the Hamiltonian matrix in the non-orthogonal LAPW basis, the overlap matrix S has to be constructed. Inside the μth muffin tin, the corresponding matrix elements read

$$S^{\mu,\boldsymbol{G}\boldsymbol{G}'} = \sum_{L}\left[\left(a_L^{\mu\boldsymbol{G}}\right)^* a_L^{\mu\boldsymbol{G}'} + \left(b_L^{\mu\boldsymbol{G}}\right)^* b_L^{\mu\boldsymbol{G}'} N_l^{\mu}\right]\,, \tag{3.19}$$

and the interstitial contribution amounts to

$$S_{\text{int}}^{\boldsymbol{G}\boldsymbol{G}'} = \frac{1}{V}\int_{\text{int}} \mathrm{e}^{-\mathrm{i}(\boldsymbol{G}-\boldsymbol{G}')\cdot\boldsymbol{r}}\,\mathrm{d}^3r = \Theta_{\boldsymbol{G}-\boldsymbol{G}'}\,. \tag{3.20}$$

3.2.3 Describing thin films and surfaces

Recently, thin films and surfaces came into focus of condensed-matter physics because of exotic properties originating partly from the reduced dimensionality of these systems. To predict such properties reliably from first principles without the increased computational burden associated with large super-cell calculations, Krakauer, Posternak, and Freeman [72] developed a truly two-dimensional version of the FLAPW method. In their approach, real space is partitioned into the muffin tins, the interstitial, and two vacuum regions above and below the film as shown in Fig. 3.2. Even though the translational symmetry is lost along the z-direction, i.e., perpendicular to the film plane, the muffin-tin basis functions are the same as before, and also the expansion of the interstitial wave-function into plane waves remains valid. While the interstitial region extends from $-D/2$ to $D/2$ in z-direction, the plane-wave vectors perpendicular to the film are defined in terms of the parameter $\tilde{D} > D$ to gain larger variational freedom[5]. As a consequence, the plane waves read

$$\phi_{\boldsymbol{k}_\parallel}^{\boldsymbol{G}_\parallel G_\perp}(\boldsymbol{r}) = \mathrm{e}^{\mathrm{i}\left(\boldsymbol{k}_\parallel+\boldsymbol{G}_\parallel\right)\cdot\boldsymbol{r}_\parallel}\mathrm{e}^{\mathrm{i}G_\perp z}\,, \tag{3.21}$$

where the wave vector $G_\perp$ perpendicular to the film is an integer multiple of $2\pi/\tilde{D}$, $\boldsymbol{G}_\parallel$ and $\boldsymbol{k}_\parallel$ are the two-dimensional reciprocal-lattice and Bloch vectors, and $\boldsymbol{r}_\parallel$ is the parallel component of $\boldsymbol{r}$.

---

[5] The interstitial wave-function that follows from this construction is usually non-zero at the boundary to the vacuum region, whereby a proper matching at $z = D$ is possible.

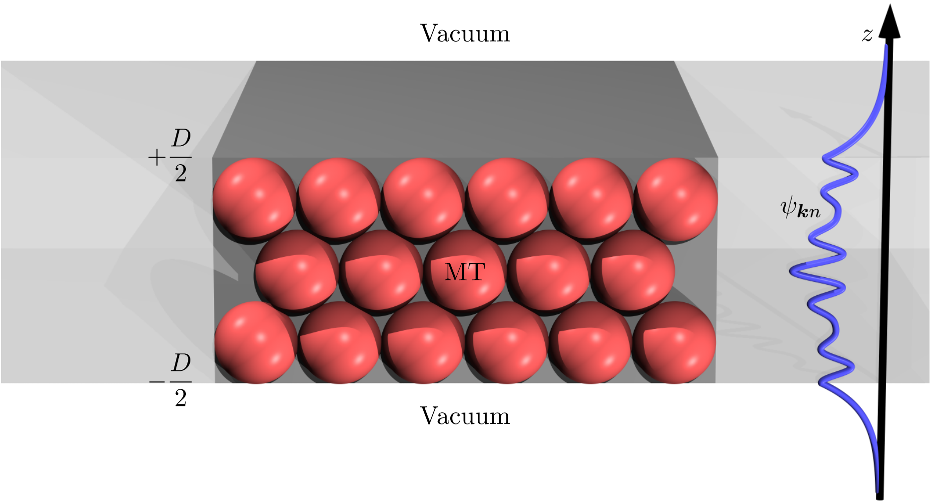

Figure 3.2: In addition to the muffin tins (MT) and the interstitial region, FLAPW calculations of truly two-dimensional geometries introduce vacuum regions for $|z| > D/2$, where z denotes the direction perpendicular to the film plane. The wave function $\psi_{\boldsymbol{k}n}$ of the illustrated three-layer system decays exponentially into the vacuum regions.

The basis in the newly introduced vacuum regions, which stretch from $\pm D/2$ to $\pm\infty$, is adapted ideally to describe the wave-function decay into the vacua. Inspired by the muffin-tin functions, the basis states in these regions consist of plane waves parallel to the film, and linear combinations of a z-dependent function $u(z)$ and its energy derivative $\dot{u}(z)$. These functions are solutions to one-dimensional Schrödinger-like equations:

$$\left[-\frac{1}{2}\frac{\partial^2}{\partial z^2} + V^0(z) - E_{\text{vac}} + \frac{\left(\boldsymbol{G}_\parallel + \boldsymbol{k}_\parallel\right)^2}{2}\right] u_{\boldsymbol{k}_\parallel}^{\boldsymbol{G}_\parallel}(z) = 0\,, \tag{3.22}$$

$$\left[-\frac{1}{2}\frac{\partial^2}{\partial z^2} + V^0(z) - E_{\text{vac}} + \frac{\left(\boldsymbol{G}_\parallel + \boldsymbol{k}_\parallel\right)^2}{2}\right] \dot{u}_{\boldsymbol{k}_\parallel}^{\boldsymbol{G}_\parallel}(z) = u_{\boldsymbol{k}_\parallel}^{\boldsymbol{G}_\parallel}(z)\,, \tag{3.23}$$

with the planar averaged part $V^0(z)$ of the vacuum potential, and E_{vac} is the vacuum energy parameter. In order to increase the variational freedom in treating the vacua, the energy parameter can be replaced with a series of $G_\perp$-dependent parameters $E_{\text{vac}} - \frac{1}{2}G_\perp^2$ if necessary. Thus, the basis for expanding the wave function in two-dimensional geometries assumes the form

$$\phi_{\boldsymbol{k}_\parallel}^{\boldsymbol{G}}(\boldsymbol{r}) = \begin{cases} \frac{1}{\sqrt{V}} \mathrm{e}^{\mathrm{i}(\boldsymbol{k}_\parallel + \boldsymbol{G}_\parallel)\cdot\boldsymbol{r}} \mathrm{e}^{\mathrm{i}G_\perp z} & \text{in interstitial} \\ \sum\limits_L \left[a_{L\boldsymbol{k}_\parallel}^{\mu\boldsymbol{G}} u_l^\mu(r_\mu) + b_{L\boldsymbol{k}_\parallel}^{\mu\boldsymbol{G}} \dot{u}_l^\mu(r_\mu)\right] Y_L(\hat{\boldsymbol{r}}_\mu) & \text{in muffin tin } \mu \\ \left[a_{\boldsymbol{k}_\parallel}^{\boldsymbol{G}} u_{\boldsymbol{k}_\parallel}^{\boldsymbol{G}_\parallel}(z) + b_{\boldsymbol{k}_\parallel}^{\boldsymbol{G}} \dot{u}_{\boldsymbol{k}_\parallel}^{\boldsymbol{G}_\parallel}(z)\right] \mathrm{e}^{\mathrm{i}\left(\boldsymbol{k}_\parallel + \boldsymbol{G}_\parallel\right)\cdot\boldsymbol{r}_\parallel} & \text{in vacuum} \end{cases} \tag{3.24}$$

where $\boldsymbol{G} = (\boldsymbol{G}_\parallel, G_\perp)^{\mathrm{T}}$.

The vacuum regions yield extra contributions to the elements of the Hamiltonian matrix, the form of which is reminiscent of their muffin-tin correspondents. As the basis functions in the vacuum diagonalize the non-corrugated planar averaged part of the Hamiltonian that contains the z-dependent potential and the (symmetrized) kinetic energy, the according matrix elements are given by

$$H_{\text{vac}}^{\boldsymbol{G}\boldsymbol{G}'} = \delta_{\boldsymbol{G}_\parallel \boldsymbol{G}'_\parallel} \left[a^{\boldsymbol{G}*} a^{\boldsymbol{G}'} E_{\text{vac}} + \frac{1}{2} \left(a^{\boldsymbol{G}*} b^{\boldsymbol{G}'} + b^{\boldsymbol{G}*} a^{\boldsymbol{G}'} \right) + b^{\boldsymbol{G}*} b^{\boldsymbol{G}'} E_{\text{vac}} N_{\text{vac}}^{\boldsymbol{G}_\parallel} \right] , \tag{3.25}$$

where $N_{\text{vac}}^{\boldsymbol{G}_\parallel} = \langle \dot{u}^{\boldsymbol{G}_\parallel} | \dot{u}^{\boldsymbol{G}_\parallel} \rangle_{\text{vac}}$, and the explicit dependence on $\boldsymbol{k}_\parallel$ is suppressed. In addition to the planar averaged part, the Hamiltonian contains the non-corrugated vacuum potential $V_{\text{co}}(\boldsymbol{r})$ that is expanded into z-dependent functions and plane waves within the film plane:

$$V_{\text{co}}(\boldsymbol{r}) = \sum_{\boldsymbol{G}_\parallel} V^{\boldsymbol{G}_\parallel}(z) \mathrm{e}^{\mathrm{i}\boldsymbol{G}_\parallel \cdot \boldsymbol{r}} . \tag{3.26}$$

Introducing the one-dimensional integrals

$$\begin{aligned}
I_{uu}^{\boldsymbol{G}_\parallel \boldsymbol{G}'_\parallel} &= \int_{\text{vac}} u^{\boldsymbol{G}_\parallel}(z) u^{\boldsymbol{G}'_\parallel}(z) V^{\boldsymbol{G}_\parallel - \boldsymbol{G}'_\parallel}(z) \, \mathrm{d}z , \\
I_{u\dot{u}}^{\boldsymbol{G}_\parallel \boldsymbol{G}'_\parallel} &= \int_{\text{vac}} u^{\boldsymbol{G}_\parallel}(z) \dot{u}^{\boldsymbol{G}'_\parallel}(z) V^{\boldsymbol{G}_\parallel - \boldsymbol{G}'_\parallel}(z) \, \mathrm{d}z , \\
I_{\dot{u}u}^{\boldsymbol{G}_\parallel \boldsymbol{G}'_\parallel} &= \int_{\text{vac}} \dot{u}^{\boldsymbol{G}_\parallel}(z) u^{\boldsymbol{G}'_\parallel}(z) V^{\boldsymbol{G}_\parallel - \boldsymbol{G}'_\parallel}(z) \, \mathrm{d}z , \\
I_{\dot{u}\dot{u}}^{\boldsymbol{G}_\parallel \boldsymbol{G}'_\parallel} &= \int_{\text{vac}} \dot{u}^{\boldsymbol{G}_\parallel}(z) \dot{u}^{\boldsymbol{G}'_\parallel}(z) V^{\boldsymbol{G}_\parallel - \boldsymbol{G}'_\parallel}(z) \, \mathrm{d}z
\end{aligned} \tag{3.27}$$

of the vacuum basis functions with the z-dependent non-corrugated potential over the respective vacuum region, the corresponding contribution to the Hamiltonian matrix assumes the form

$$H_{\text{vac,co}}^{\boldsymbol{G}\boldsymbol{G}'} = a^{\boldsymbol{G}*} a^{\boldsymbol{G}'} I_{uu}^{\boldsymbol{G}_\parallel \boldsymbol{G}'_\parallel} + a^{\boldsymbol{G}*} b^{\boldsymbol{G}'} I_{u\dot{u}}^{\boldsymbol{G}_\parallel \boldsymbol{G}'_\parallel} + b^{\boldsymbol{G}*} a^{\boldsymbol{G}'} I_{\dot{u}u}^{\boldsymbol{G}_\parallel \boldsymbol{G}'_\parallel} + b^{\boldsymbol{G}*} b^{\boldsymbol{G}'} I_{\dot{u}\dot{u}}^{\boldsymbol{G}_\parallel \boldsymbol{G}'_\parallel} . \tag{3.28}$$

Finally, the elements of the overlap matrix in the non-orthogonal vacuum basis read

$$S_{\text{vac}}^{\boldsymbol{G}\boldsymbol{G}'} = \delta_{\boldsymbol{G}_\parallel \boldsymbol{G}'_\parallel} \left[a^{\boldsymbol{G}*} a^{\boldsymbol{G}'} + b^{\boldsymbol{G}*} b^{\boldsymbol{G}'} N_{\text{vac}}^{\boldsymbol{G}_\parallel} \right] . \tag{3.29}$$

3.3 Relativistic calculations of valence electrons

A satisfactory description of core and valence electrons close to the nuclei relies on the correct treatment of relativistic effects as the kinetic energy becomes large in the vicinity of the ions, especially for heavy elements. While this affects essentially only the muffin-tin regions, a non-relativistic handling of interstitial and vacua is still reasonable[6]. Relativistic effects are particularly important to capture the coupling

---

[6] At the muffin-tin boundary, only the so-called large component of the four-component relativistic wave function will be matched to the (two-component) non-relativistic wave function outside of the muffin-tins. This approximation is reasonable as the small component is (i) overshadowed by the large one, and (ii) strongly suppressed at this distance from the nucleus.

between spin orientation and crystal lattice that is mediated by the so-called *spin-orbit interaction*, which also underlies conventionally other prominent phenomena such as orbital magnetism[7], spin-orbit torques, and Dzyaloshinskii-Moriya interaction. In a fully relativistic framework, also mass-velocity and Darwin terms are accounted for in addition to the spin-orbit interaction.

3.3.1 Kohn-Sham-Dirac equation

The fundamental Kohn-Sham wave equations of relativistic density functional theory have the form of massive-single-particle Dirac equations:

$$\left[c \sum_{i=1}^{3} \alpha_i p_i + (\beta - 1) m_0 c^2 + V_{\text{eff}}(\boldsymbol{r}) \right] \boldsymbol{\psi}(\boldsymbol{r}) = E \boldsymbol{\psi}(\boldsymbol{r}) \,, \tag{3.30}$$

where c is the speed of light, p_i is the ith Cartesian component of the electron's momentum, m_0 is its rest mass, and $V_{\text{eff}}(\boldsymbol{r})$ is the effective potential that comprises the attractive Coulomb interaction between electrons and ions, the electrostatic Hartree potential, and the exchange-correlation potential. The effective potential becomes spin-dependent for spin-polarized calculations. The 4×4-matrices α_i and β in the Dirac equation are given by

$$\alpha_i = \begin{pmatrix} 0 & \sigma_i \\ \sigma_i & 0 \end{pmatrix} \,, \qquad \beta = \begin{pmatrix} I & 0 \\ 0 & -I \end{pmatrix} \,, \tag{3.31}$$

where σ_i is the ith 2×2 Pauli matrix, and I denotes the 2×2 unit matrix. The relativistic solutions $\boldsymbol{\psi}(\boldsymbol{r})$ of Eq. (3.30) are four-component, or bi-spinor, wave functions.

However, solving the Kohn-Sham-Dirac equation is a delicate problem: if all four components of the relativistic wave function were expanded using the LAPW basis, four times as many basis functions would be necessary as compared to the non-relativistic treatment such that the overall computing time for diagonalizing the Hamiltonian would increase by a factor of $4^3 = 64$. This renders a direct approach usually unfeasible, and motivates the introduction of approximate methods for efficient relativistic calculations. For example, in the scalar relativistic approximation that is discussed below, the spin-orbit interaction – and with it any coupling between spin and spatial coordinates – is neglected, which leads to two separate matrices of half the original size, saving an overall factor of four in computing time during diagonalization.

3.3.2 Scalar relativistic approximation

Since the relativistic corrections are most prominent close to the nuclei, only the part of the electronic wave-function inside the muffin-tin spheres has to be treated relativistically, which sets the construction of the radial function as a first challenge. The starting point for this is the above Kohn-Sham-Dirac equation, where the effective

---

[7] We propose in Section 6.4 an alternative mechanism for orbital magnetism that does not root in the spin-orbit interaction but in the topology of chiral spin textures.

potential is replaced with its spherical average, i.e., $V_{\text{eff}}(\boldsymbol{r}) \to V(r)$ in Eq. (3.30). The solutions to the accordingly modified Dirac equation assume the form

$$\boldsymbol{\psi}_{\kappa\mu} = \begin{pmatrix} g_\kappa(r)\chi_{\kappa\mu} \\ \mathrm{i}f_\kappa(r)\chi_{-\kappa\mu} \end{pmatrix}\,, \tag{3.32}$$

where $g_\kappa(r)$ is the large component, and $f_\kappa(r)$ is the small component. The spinor $\chi_{\kappa\mu}$ is an eigenfunction of the projection j_z of the total angular momentum $\boldsymbol{j} = \boldsymbol{l} + \boldsymbol{s}$ and the operator $K = \beta(\boldsymbol{\sigma} \cdot \boldsymbol{l} + 1)$ with the eigenvalues μ and κ, respectively. As the spin operator $\boldsymbol{s}$ and the orbital angular momentum $\boldsymbol{l}$ do no longer provide valid quantum numbers because of spin-orbit coupling, the solutions (3.32) need to be labeled by κ and μ. The κ-dependent radial functions can be shown to obey coupled equations that read in matrix form [64]

$$\begin{pmatrix} -\frac{\kappa+1}{r} - \frac{\partial}{\partial r_\mu} & 2mc \\ \frac{V(r)-E_\kappa}{c} & \frac{\kappa-1}{r} - \frac{\partial}{\partial r} \end{pmatrix} \begin{pmatrix} g_\kappa(r) \\ f_\kappa(r) \end{pmatrix} = 0\,, \tag{3.33}$$

with the enhanced mass $m = m_0 + [E_\kappa - V(r)]/(2c^2)$ of the relativistic electrons moving in the spherically symmetric potential $V(r)$, and E_κ is the energy parameter.

In order to motivate the scalar relativistic approximation, Koelling and Harmon [64] proposed to rewrite the above equations by introducing the function

$$\omega_\kappa(r) = \frac{\kappa+1}{2mcr} g_\kappa(r) + f_\kappa(r) \tag{3.34}$$

such that Eq. (3.33) assumes the form

$$\begin{pmatrix} -\frac{\partial}{\partial r} & 2mc \\ \frac{\kappa(\kappa+1)}{2mcr^2} + \frac{V(r)-E_\kappa}{c} - \frac{\kappa+1}{2mcr}\left(\frac{\partial}{\partial r} - \frac{m'}{m}\right) & \frac{\kappa-1}{r} - \frac{\partial}{\partial r} \end{pmatrix} \begin{pmatrix} g_\kappa(r) \\ \omega_\kappa(r) \end{pmatrix} = 0\,, \tag{3.35}$$

where $m' = \partial m/\partial r$ stands for the radial derivative of m. Keeping in mind that κ is the eigenvalue of the operator $K \propto (\boldsymbol{l} \cdot \boldsymbol{\sigma} + 1)$, the term $(\kappa+1)m'/(2m^2cr)$ can be identified with the spin-orbit interaction. This is the only term that couples spin-up and spin-down contributions, and dropping it is the essence of the scalar relativistic approximation. Then, κ is replaced with l, and Eq. (3.35) can be rewritten as

$$H_{\text{sph}} \begin{pmatrix} g_l(r) \\ \omega_l(r) \end{pmatrix} = E_l \begin{pmatrix} g_l(r) \\ \omega_l(r) \end{pmatrix} \tag{3.36}$$

with the scalar relativistic Hamiltonian containing only the spherically averaged potential:

$$H_{\text{sph}} = \begin{pmatrix} \frac{l(l+1)}{2mr^2} + V(r) & -\frac{2c}{r} - c\frac{\partial}{\partial r} \\ c\frac{\partial}{\partial r} & -2m_0c^2 + V(r) \end{pmatrix}\,. \tag{3.37}$$

In the scalar relativistic approximation, spin-up and spin-down problems decouple and can thus be solved independently. The scalar relativistic LAPW basis set for each spin direction in the bulk case is

$$\phi_{\boldsymbol{k}}^{\boldsymbol{G}}(\boldsymbol{r}) = \begin{cases} \frac{1}{\sqrt{V}} \mathrm{e}^{\mathrm{i}(\boldsymbol{k}+\boldsymbol{G})\cdot\boldsymbol{r}} & \text{in interstitial} \\ \sum\limits_L a_{L\boldsymbol{k}}^{\mu\boldsymbol{G}} \begin{pmatrix} g_l(r_\mu) \\ \omega_l(r_\mu) \end{pmatrix} Y_L(\hat{\boldsymbol{r}}_\mu) + b_{L\boldsymbol{k}}^{\mu\boldsymbol{G}} \begin{pmatrix} \dot{g}_l(r_\mu) \\ \dot{\omega}_l(r_\mu) \end{pmatrix} Y_L(\hat{\boldsymbol{r}}_\mu) & \text{in muffin tin } \mu \end{cases}\,, \tag{3.38}$$

where the energy derivatives of the radial functions in the muffin tins are made to be orthogonal to the normalized radial functions. The energy derivatives $\dot{g}_l$ and $\dot{\omega}_l$ satisfy scalar relativistic equations that are found from the variation of Eq. (3.36) with energy. In general, a second-variation scheme [73] based on perturbation theory can be applied after a scalar relativistic calculation to still account for the spin-orbit interaction.

3.4 Non-collinear magnetism

In analogy to the representation of the density matrix in spin-polarized density functional theory (DFT) calculations, the potential of a non-collinear magnetic system can be written as

$$\mathcal{V}(\boldsymbol{r}) = \left[V(\boldsymbol{r})I + \bar{\boldsymbol{B}}(\boldsymbol{r}) \cdot \boldsymbol{\sigma}\right] = \begin{pmatrix} V(\boldsymbol{r}) + \bar{B}_z(\boldsymbol{r}) & \bar{B}_x(\boldsymbol{r}) - \mathrm{i}\bar{B}_y(\boldsymbol{r}) \\ \bar{B}_x(\boldsymbol{r}) + \mathrm{i}\bar{B}_y(\boldsymbol{r}) & V(\boldsymbol{r}) - \bar{B}_z(\boldsymbol{r}) \end{pmatrix}, \tag{3.39}$$

where $\bar{\boldsymbol{B}} = \mu_{\mathrm{B}} \left(\boldsymbol{B}_{\mathrm{xc}} + \boldsymbol{B}_{\mathrm{ext}}\right)$ comprises the exchange field and a possible external magnetic field times the Bohr magneton μ_{B}. The FLEUR computer program [74] implements an approximation of non-collinear magnetism by considering this full potential matrix only in the interstitial region, where the magnetization is treated as continuous vector field [75]. In a given muffin tin, however, the magnetization direction is not allowed to change and intra-atomic non-collinearity is neglected, which is motivated by the intuition that a well-defined magnetic moment is carried by each atom[8]. To represent the spin degrees of freedom inside the μth muffin tin, a local spin-coordinate frame is introduced such that the z-axis is parallel to the direction $\hat{\boldsymbol{e}}_\mu$ of the local magnetic moment. This allows for constructing the muffin-tin basis functions exactly the same way as in the collinear situation based on two potentials V_+ and V_-, which refer now to spin-up and spin-down components in the local frame. In other words, the exchange field inside the muffin tins is calculated using the collinear spin density $m_\mu(\boldsymbol{r}_\mu)$ found from projecting the full non-collinear spin density $\boldsymbol{m}(\boldsymbol{r})$ onto the local spin-quantization axis $\hat{\boldsymbol{e}}_\mu$:

$$m_\mu(\boldsymbol{r}_\mu) = \boldsymbol{m}(\boldsymbol{r}) \cdot \hat{\boldsymbol{e}}_\mu \,. \tag{3.40}$$

As the global spin-coordinate frame used in the interstitial region is generally different from the local one, changes come into play when matching the spinor wave functions at the muffin-tin boundary[9]. Notably, the approximation of neglecting the intra-atomic non-collinearity often renders the potential to be discontinuous at the boundary.

Vectors and spinors in the local frame of the μth muffin tin can be transformed into the global frame via the unitary rotation matrix $\mathcal{R}_\mu^{\mathrm{gl}}$ and the Hermitian matrix

---

[8] Nordström *et al.* [76] proposed the first approach that enables the magnetization to change magnitude and direction even within an atom, allowing them to study intra-atomic non-collinearity.

[9] Each component of the spinor in the interstitial region is matched to spin-up and spin-down basis functions in the muffin tin.

$\mathcal{U}_\mu^{\mathrm{gl}}$, respectively, that are given by

$$\mathcal{R}_\mu^{\mathrm{gl}} = \begin{pmatrix} \cos\varphi\cos\theta & -\sin\varphi & \cos\varphi\sin\theta \\ \sin\varphi\cos\theta & \cos\varphi & \sin\varphi\sin\theta \\ -\sin\theta & 0 & \cos\theta \end{pmatrix} , \tag{3.41}$$

$$\mathcal{U}_\mu^{\mathrm{gl}} = \begin{pmatrix} \mathrm{e}^{-\mathrm{i}\frac{\varphi}{2}}\cos\frac{\theta}{2} & -\mathrm{e}^{-\mathrm{i}\frac{\varphi}{2}}\sin\frac{\theta}{2} \\ \mathrm{e}^{\mathrm{i}\frac{\varphi}{2}}\sin\frac{\theta}{2} & \mathrm{e}^{\mathrm{i}\frac{\varphi}{2}}\cos\frac{\theta}{2} \end{pmatrix} , \tag{3.42}$$

where the local spin-quantization axis $\hat{\boldsymbol{e}}_\mu = (\cos\varphi\sin\theta, \sin\varphi\sin\theta, \cos\theta)$ is specified by the azimuthal angle φ and the polar angle θ, which vary generally for different muffin tins. Determined by the transpose and adjoint, respectively, the inverse operations $\mathcal{R}_\mu^{\mathrm{lg}}$ and $\mathcal{U}_\mu^{\mathrm{lg}}$ transform from global coordinates into the local-coordinate frame:

$$\mathcal{R}_\mu^{\mathrm{lg}} = \begin{pmatrix} \cos\varphi\cos\theta & \sin\varphi\cos\theta & -\sin\theta \\ -\sin\varphi & \cos\varphi & 0 \\ \cos\varphi\sin\theta & \sin\varphi\sin\theta & \cos\theta \end{pmatrix} , \tag{3.43}$$

$$\mathcal{U}_\mu^{\mathrm{lg}} = \begin{pmatrix} \mathrm{e}^{\mathrm{i}\frac{\varphi}{2}}\cos\frac{\theta}{2} & \mathrm{e}^{-\mathrm{i}\frac{\varphi}{2}}\sin\frac{\theta}{2} \\ -\mathrm{e}^{\mathrm{i}\frac{\varphi}{2}}\sin\frac{\theta}{2} & \mathrm{e}^{-\mathrm{i}\frac{\varphi}{2}}\cos\frac{\theta}{2} \end{pmatrix} . \tag{3.44}$$

Chapter 4

Berry phase effects in complex magnets

Contents

In this chapter, we introduce the celebrated concept of Berry phases that caused a true revolution of our understanding of many elementary properties in periodic solids, and has initiated ever-growing interest in predicting and exploiting new topological states of matter. Following the classic derivations by Berry, we motivate the emergence of these geometric phases as a direct consequence of an adiabatic Hamiltonian evolution, and provide several educational examples of non-trivial phase-space topology. We elaborate on the universal role of Berry phases for electronic properties such as (quantum) anomalous Hall effect and orbital magnetism in metallic and insulating systems. Furthermore, we demonstrate that the geometry of the "mixed" phase space of crystal momentum and magnetization direction governs the phenomenon of spin-orbit torques (SOTs) as well as the Dzyaloshinskii-Moriya interaction (DMI). Finally, we introduce the material class of chiral magnets as an ideal playground to realize all of these geometric effects at once.

4.1 What is the Berry phase?

4.1.1 Adiabatic time evolution

Although the geometric, or, Berry phase [20, 21, 77, 78] surely is the most prominent concept that underlies the evolution of Bloch electrons in topological band theory, it was originally discussed by Berry to elucidate how the wave function of a particle may change under quantum adiabatic transport in slowly varying fields [21]. In this context, the Hamiltonian $H(\boldsymbol{\lambda})$ is said to depend on a set of tunable abstract parameters $\boldsymbol{\lambda} = (\lambda_1, \lambda_2, \ldots)$, which mediate the coupling of the isolated system to its environment, for example, due to electric or magnetic fields. Aiming at the adiabatic evolution of the system, we consider the time-dependent parameters $\boldsymbol{\lambda} = \boldsymbol{\lambda}(t)$ to vary slowly along a path $\mathcal{C}$, and seek for instantaneous basis states of the Hamiltonian at each fixed point on that path by solving the Schrödinger equation

$$H(\boldsymbol{\lambda})|n\boldsymbol{\lambda}\rangle = \mathcal{E}_n(\boldsymbol{\lambda})|n\boldsymbol{\lambda}\rangle\,, \tag{4.1}$$

where the normalized instantaneous solutions $|n\boldsymbol{\lambda}\rangle$ are specified up to a phase due to the gauge freedom. While it is convenient to choose the phase to be smooth and single-valued along $\mathcal{C}$, this is not always possible[1] and requires typically to divide the path into overlapping segments or patches, on each of which a smooth and single-valued gauge can be defined.

The time evolution of the system in the state $|\psi(t)\rangle$ is given by the time-dependent Schrödinger equation

$$H(\boldsymbol{\lambda}(t))|\psi(t)\rangle = \mathrm{i}\hbar\partial_t|\psi(t)\rangle\,, \tag{4.2}$$

where $\partial_t = \partial/\partial t$ is the time derivative. The solution of the above equation can be expanded generally in terms of the instantaneous basis, $|\psi(t)\rangle = \sum_m c_m(t)|m\boldsymbol{\lambda}(t)\rangle$, where $c_m(t)$ are time-dependent expansion coefficients. Substituting this into Eq. (4.2) and multiplying from the left by $\langle n\boldsymbol{\lambda}(t)|$ yields a set of coupled equations that determine these coefficients:

$$\partial_t c_n(t) = -\mathrm{i}\frac{1}{\hbar}\mathcal{E}_n(\boldsymbol{\lambda}(t))c_n(t) - c_n(t)\langle n\boldsymbol{\lambda}(t)|\partial_t|n\boldsymbol{\lambda}(t)\rangle - \sum_{m\neq n} c_m(t)\Gamma^{-1}_{mn}(t)\,, \tag{4.3}$$

where we introduced the transition rate Γ^{-1}_{mn} from the instantaneous solution $|m\boldsymbol{\lambda}(t)\rangle$ to the state $|n\boldsymbol{\lambda}(t)\rangle$. In absence of degeneracies in the eigenspectrum of the Hamiltonian at any point along the parameter path[2], the transition rate can be expressed as

$$\Gamma^{-1}_{mn}(t) = \langle n\boldsymbol{\lambda}(t)|\partial_t|m\boldsymbol{\lambda}(t)\rangle = \frac{\langle n\boldsymbol{\lambda}(t)|\partial_t H(t)|m\boldsymbol{\lambda}(t)\rangle}{\mathcal{E}_m(t) - \mathcal{E}_n(t)}\,. \tag{4.4}$$

After the system has been prepared in an initial state $|n\boldsymbol{\lambda}(0)\rangle$, which corresponds to setting all but the expansion coefficient $c_n(0)$ to zero, the system stays always in the instantaneous eigenstate of the Hamiltonian under an adiabatic evolution in time, *i.e.*, $|\psi(t)\rangle = c_n(t)|n\boldsymbol{\lambda}(t)\rangle$. According to Eqs. (4.3) and (4.4), this notion of adiabatic transport along a certain parameter path is valid for states that are well-separated in energy and for Hamiltonians that vary slower in time than the intrinsic time-scale set by quantum transitions between the states. If the adiabatic transport is assumed, Eq. (4.3) is decoupled and can be solved easily by integration:

$$\begin{aligned} c_n(t) &= \exp\left(-\frac{\mathrm{i}}{\hbar}\int_0^t \mathcal{E}_n(\tau)\,\mathrm{d}\tau\right)\exp\left(\mathrm{i}\int_0^t \mathrm{i}\langle n\boldsymbol{\lambda}(\tau)|\partial_\tau|n\boldsymbol{\lambda}(\tau)\rangle\,\mathrm{d}\tau\right) \\ &= \exp(-\mathrm{i}\alpha_{\mathrm{dyn}}(t))\exp(\mathrm{i}\gamma_n(t))\,, \end{aligned} \tag{4.5}$$

---

[1] For instance, systems with a non-zero first Chern number constitute examples for which the phase cannot be defined globally as a smooth and single-valued function in the whole Brillouin zone.

[2] The presence of degeneracies would lead to the concept of the *non-Abelian* Berry phase, or, Wilczek-Zee phase [79], which we do not discuss here however. Importantly, the Berry connection (4.7) becomes a matrix in the degenerate subspace.

where the wave function acquires in addition to the well-known dynamical phase $\alpha_{\mathrm{dyn}}(t)$ the so-called geometric, or, Berry phase $\gamma_n(t)$:

$$\gamma_n(t) = \int_0^t \mathrm{i}\langle n\boldsymbol{\lambda}(\tau)|\partial_\tau|n\boldsymbol{\lambda}(\tau)\rangle \, \mathrm{d}\tau = \int_{\mathcal{C}} \mathrm{i}\langle n\boldsymbol{\lambda}|\nabla_{\boldsymbol{\lambda}}|n\boldsymbol{\lambda}\rangle \cdot \mathrm{d}\boldsymbol{\lambda}\,, \tag{4.6}$$

which is a real number defined modulo 2π since the basis states are normalized. The Berry phase is a direct consequence of the coupling to the environment through slowly varying parameters and accounts for changes in the wave function during the respective evolution of the system under external “forces”. In 1986, Tomita *et al.* [80] confirmed experimentally the manifestation of Berry phases in the rotation of linearly polarized light in an optical fiber. A classical analogue of the geometric phase, known as Hannay’s angle [81], is the Foucault pendulum, whose plane of rotation undergoes parallel transport due to the Earth’s rotation [77]. The parallel transport of a tangent vector on the sphere, which is illustrated in Fig. 4.1, is a closely related example.

4.1.2 Handbook of geometric quantities

In the last step in Eq. (4.6), we removed the explicit time dependence and recast the expression into a purely geometrical representation based on the *Berry connection*, or, *Berry vector potential* along the path $\mathcal{C}$:

$$\boldsymbol{A}^n(\boldsymbol{\lambda}) = \mathrm{i}\langle n\boldsymbol{\lambda}|\nabla_{\boldsymbol{\lambda}}|n\boldsymbol{\lambda}\rangle\,. \tag{4.7}$$

Similarly to its analog in electromagnetism, the real-valued Berry connection depends on the gauge choice in such a way that the gauge transformation[3] $|n\boldsymbol{\lambda}\rangle \to \mathrm{e}^{\mathrm{i}\xi(\boldsymbol{\lambda})}|n\boldsymbol{\lambda}\rangle$ results in the new vector potential $\boldsymbol{A}^{n\prime}(\boldsymbol{\lambda}) = \boldsymbol{A}^n(\boldsymbol{\lambda}) - \nabla_{\boldsymbol{\lambda}}\xi(\boldsymbol{\lambda})$. Until the paramount work of Berry, people were eager to conclude that the geometric phase (4.6) could be canceled by a clever choice of the gauge $\xi(\boldsymbol{\lambda})$, which is however not true. If a closed path in the parameter space is considered, the deep *geometrical* origin of the Berry phase manifests in the fact that $\gamma_n(\mathcal{C})$ is a purely gauge-invariant property measuring the local geometry along the closed loop $\mathcal{C}$:

$$\gamma_n'(\mathcal{C}) = \oint_{\mathcal{C}} \boldsymbol{A}^{n\prime} \cdot \mathrm{d}\boldsymbol{\lambda} = \oint_{\mathcal{C}} \boldsymbol{A}^{n} \cdot \mathrm{d}\boldsymbol{\lambda} - \oint_{\mathcal{C}} \nabla_{\boldsymbol{\lambda}}\xi(\boldsymbol{\lambda}) \cdot \mathrm{d}\boldsymbol{\lambda} = \gamma_n(\mathcal{C})\,. \tag{4.8}$$

where $\oint_{\mathcal{C}} \nabla_{\boldsymbol{\lambda}}\xi(\boldsymbol{\lambda}) \cdot \mathrm{d}\boldsymbol{\lambda} = \xi(\boldsymbol{\lambda}_f) - \xi(\boldsymbol{\lambda}_i) = 0$ since the final parameters $\boldsymbol{\lambda}_f$ are the same as the initial ones $\boldsymbol{\lambda}_i$. Therefore, the Berry phase of a closed path cannot be canceled by a smart gauge choice, which can be shown to hold also for more general gauge transformations. Remarkably, there exist many situations where the Berry phase $\gamma_n(\mathcal{C})$ is unchanged under smooth deformations of the closed loop $\mathcal{C}$, *i.e.*, the path may be distorted but not cut open at any point. In this case, the gauge-invariant Berry phase is of *topological* nature.

---

[3] We assume for sake of simplicity that a single patch is sufficient to define a proper gauge but the drawn conclusions can be shown to hold in more general situations as well.

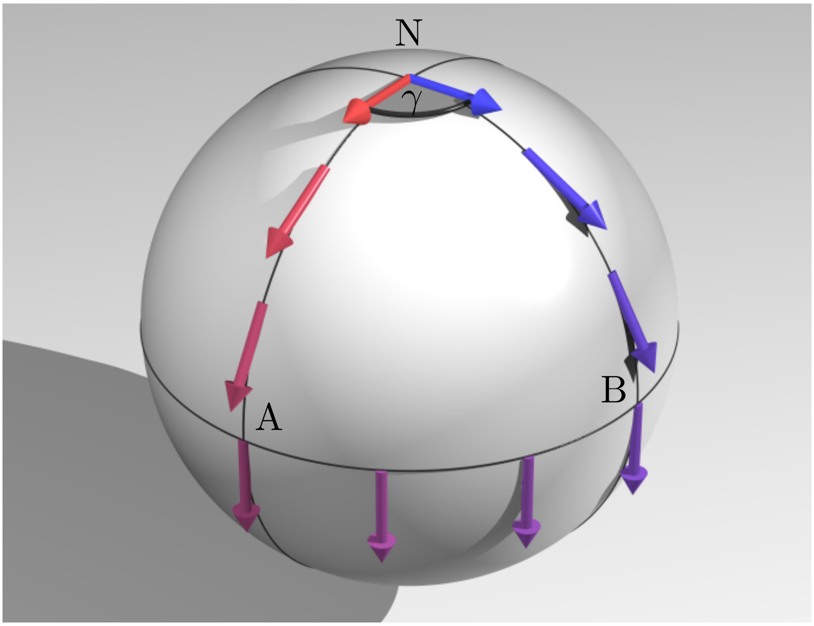

Figure 4.1: The parallel transport of a tangent vector on the sphere along a closed path from the north pole N over A and B and back to N results in a misalignment between original (dark red) and transported (dark blue) vector, owing to the non-trivial curvature on the sphere. The opening angle γ can be viewed as a geometric phase that manifests under parallel transport.

Stokes' theorem can be applied to rewrite the integral (4.6) along the closed path $\mathcal{C}$ as an integral over the surface S that the loop $\mathcal{C}$ encompasses[4]:

$$\gamma_n(\mathcal{C}) = \oint_{\mathcal{C}} \boldsymbol{A}^n(\boldsymbol{\lambda}) \cdot \mathrm{d}\boldsymbol{\lambda} = \int_S \boldsymbol{\Omega}^n(\boldsymbol{\lambda}) \cdot \mathrm{d}\boldsymbol{S}\,, \tag{4.9}$$

where we introduced an effective "magnetic field" $\boldsymbol{\Omega}^n = \nabla_{\boldsymbol{\lambda}} \times \boldsymbol{A}^n$ that is in the spirit of electromagnetics given by the curl of the Berry vector potential. This "magnetic field" is known as the *Berry curvature*, or more precisely, the *Berry curvature field.* Clearly, the Berry curvature field is identically zero everywhere on the manifold S if the Berry vector potential is the gradient field of a smooth and unique function. As a consequence of this so-called pure gauge, the Berry phase vanishes, indicating trivial geometrical properties of the underlying parameter space. More interestingly and in the focus of this thesis are situations in which the pure gauge does not apply such that non-trivial geometrical or even topological phases may manifest. Equation (4.9) provides a clear interpretation of the Berry phase as the flux of the Berry curvature field through the surface S.

Commonly, the Berry curvature is expressed as an antisymmetric rank-2 tensor –

---

[4] In differential geometry Stokes' theorem states that the integral of the Berry connection (a differential 1-form) over the boundary $\mathcal{C} = \partial S$ of an orientable manifold S is equal to the integral of the corresponding Berry curvature (a differential 2-form) over the whole manifold S.

known as *Berry curvature tensor* – with the components

$$\Omega^n_{ij}(\boldsymbol{\lambda}) = \frac{\partial}{\partial\lambda_i}A^n_j(\boldsymbol{\lambda}) - \frac{\partial}{\partial\lambda_j}A^n_i(\boldsymbol{\lambda}) = -2\mathrm{Im}\left\langle \frac{\partial}{\partial\lambda_i}n\boldsymbol{\lambda}\middle|\frac{\partial}{\partial\lambda_j}n\boldsymbol{\lambda}\right\rangle , \tag{4.10}$$

where the indices i and j refer to Cartesian coordinates. If the parameter space is three-dimensional, the ith component of the Berry curvature field $\boldsymbol{\Omega}^n$ can be obtained from the tensor elements (4.10) via $[\boldsymbol{\Omega}^n]_i = (1/2)\sum_{jk}\epsilon_{ijk}\Omega^n_{jk}$ with the antisymmetric Levi-Civita symbol ϵ_{ijk}. Adopting the so-called parallel transport gauge[5] is particularly useful to evaluate locally gauge-invariant objects in differential geometry such as the elements (4.10) of the Berry curvature tensor. Based on the resulting perturbation-theory expression for the derivative of the wave functions

$$\partial_{\lambda_i}|n\boldsymbol{\lambda}\rangle = \sum_{m\neq n}\frac{\langle m\boldsymbol{\lambda}|\partial_{\lambda_i}H(\boldsymbol{\lambda})|n\boldsymbol{\lambda}\rangle}{\mathcal{E}_n(\boldsymbol{\lambda}) - \mathcal{E}_m(\boldsymbol{\lambda})}|m\boldsymbol{\lambda}\rangle , \tag{4.11}$$

the following expression is recovered:

$$\Omega^n_{ij}(\boldsymbol{\lambda}) = -2\mathrm{Im}\sum_{m\neq n}\frac{\langle n\boldsymbol{\lambda}|\partial_{\lambda_i}H(\boldsymbol{\lambda})|m\boldsymbol{\lambda}\rangle\langle m\boldsymbol{\lambda}|\partial_{\lambda_j}H(\boldsymbol{\lambda})|n\boldsymbol{\lambda}\rangle}{(\mathcal{E}_n - \mathcal{E}_m)^2} , \tag{4.12}$$

which is notably valuable for practical Berry-phase calculations independent of the specific gauge since the derivatives have been moved from the wave functions to the Hamiltonian. In other words, Eq. (4.12) can be evaluated using any eigenstates that a computer code produces, regardless of whether the corresponding phases are single-valued and smooth over the parameter manifold or not. Additionally, the importance of band degeneracies as sources or drains [82] of the Berry curvature in their vicinity becomes evident from Eq. (4.12), which also highlights that the Berry phase γ_n can be viewed as an effect of transitions of the state $|n\boldsymbol{\lambda}\rangle$ to all other states $|m\boldsymbol{\lambda}\rangle$ mediated by the adiabatic interaction $\nabla_{\boldsymbol{\lambda}}H$.

4.1.3 Example 1: Spin-1/2 and magnetic monopoles

Berry himself [21] considered an educational but relevant example of geometric phases in quantum physics, which is the problem of a spin-1/2 particle in a slowly varying magnetic field [83]:

$$H(\hat{\boldsymbol{n}})|\pm\hat{\boldsymbol{n}}\rangle = B\boldsymbol{\sigma}\cdot\hat{\boldsymbol{n}}|\pm\hat{\boldsymbol{n}}\rangle = \mathcal{E}_\pm|\pm\hat{\boldsymbol{n}}\rangle , \tag{4.13}$$

where B is the fixed magnitude of the magnetic field with direction $\hat{\boldsymbol{n}}$ that takes the role of the external parameter in the Hamiltonian. The spin follows adiabatically the direction of the field, which is represented in spherical coordinates as $\hat{\boldsymbol{n}} = (\cos\varphi\sin\theta, \sin\varphi\sin\theta, \cos\theta)$ using the polar angle θ and the azimuthal angle φ. The eigenvalues of the two-level system are $\mathcal{E}_\pm = \pm B$, and the instantaneous eigenstates $|\pm\hat{\boldsymbol{n}}\rangle$ are easily found by solving the problem first in local coordinates,

---

[5] Although the Berry phase is physical and gauge-invariant, it can be removed along segments of the closed path $\mathcal{C}$ via the parallel transport gauge $\langle n\boldsymbol{\lambda}|\nabla_{\boldsymbol{\lambda}}|n\boldsymbol{\lambda}\rangle = 0$.

where the local z-axis coincides with $\hat{\boldsymbol{n}}$, followed by a rotation of the two spinors to the global frame using the transformation matrix

$$U(\theta,\varphi) = \mathrm{e}^{-\mathrm{i}\varphi\sigma_z/2}\mathrm{e}^{-\mathrm{i}\theta\sigma_y/2}\mathrm{e}^{\mathrm{i}\varphi\sigma_z/2} = \begin{pmatrix} \cos\frac{\theta}{2} & \mathrm{e}^{-\mathrm{i}\varphi}\sin\frac{\theta}{2} \\ -\mathrm{e}^{\mathrm{i}\varphi}\sin\frac{\theta}{2} & \cos\frac{\theta}{2} \end{pmatrix} , \tag{4.14}$$

which yields the solutions

$$|+\hat{\boldsymbol{n}}\rangle = \begin{pmatrix} \cos\frac{\theta}{2} \\ -\mathrm{e}^{\mathrm{i}\varphi}\sin\frac{\theta}{2} \end{pmatrix} , \qquad |-\hat{\boldsymbol{n}}\rangle = \begin{pmatrix} \mathrm{e}^{-\mathrm{i}\varphi}\sin\frac{\theta}{2} \\ \cos\frac{\theta}{2} \end{pmatrix} . \tag{4.15}$$

Obviously, every quantum state in the Hilbert space of the two-level system is in one-to-one correspondence with a point on the sphere S^2. Since the above eigenstates are smooth and single-valued for any parameter $\hat{\boldsymbol{n}}$ but not at the south pole $\theta = \pi$, the gauge transformation $|\pm\hat{\boldsymbol{n}}\rangle \to \mathrm{e}^{\mp\mathrm{i}\varphi}|\pm\hat{\boldsymbol{n}}\rangle$ has to be applied in order to cure the problem at that point. However, this second gauge is not well-behaved at the north pole $\theta = 0$, which leads to the general conclusion that at least two patches are required to define a smooth gauge for the entire parameter manifold of the Hamiltonian (4.13).

The only non-vanishing component of the Berry connection on the first patch reads

$$A_\varphi^\pm = \mathrm{i}\langle\pm\hat{\boldsymbol{n}}|\partial_\varphi|\pm\hat{\boldsymbol{n}}\rangle = \mp\frac{1-\cos\theta}{2} , \tag{4.16}$$

and accordingly $A_\varphi^\pm \to A_\varphi^\pm \pm 1$ for the above gauge transformation on the second patch. As the Berry curvature tensor is locally gauge-invariant, its non-trivial element

$$\Omega_{\theta\varphi}^\pm = \partial_\theta A_\varphi^\pm = \mp\frac{\sin\theta}{2} \tag{4.17}$$

is the same for both patches. Using the well-known expressions for gradient and curl in spherical coordinates, we arrive at the following vector quantities in three-dimensional space in which the parameter space of $H(\hat{\boldsymbol{n}})$ is naturally embedded:

$$\boldsymbol{A}^\pm = \mp\frac{1-\cos\theta}{2r\sin\theta}\hat{\boldsymbol{e}}_\varphi , \tag{4.18}$$

$$\boldsymbol{\Omega}^\pm = \pm\frac{1}{2r^2}\hat{\boldsymbol{e}}_r , \tag{4.19}$$

where $\hat{\boldsymbol{e}}_\varphi$ and $\hat{\boldsymbol{e}}_r$ denote unit vectors in the spherical coordinate system, and r is the radial distance (which is fixed since the magnitude of the field is constant). The Berry phase of the spin-1/2 problem amounts to

$$\gamma_\pm(\mathcal{C}) = \pm\frac{1}{2}\omega(\mathcal{C}) , \tag{4.20}$$

which is not of topological but of geometrical nature as the phase is determined by the solid angle $\omega(\mathcal{C})$ that the magnetic field direction $\hat{\boldsymbol{n}}$ describes along the closed parameter path $\mathcal{C}$ during the Hamiltonian evolution of the two-level system. Interestingly, the Berry phase (4.20) depends on the projection of the spin onto $\hat{\boldsymbol{n}}$ (given by $\pm 1/2$) rather than on the magnitude of the spin itself.

In order to elucidate the perception of sources and drains of the Berry curvature as condensed-matter realizations of magnetic point charges, we draw an analogy with the magnetic field of a so-called *Dirac monopole.* This amounts to solving the modified Maxwell's equation $\nabla \cdot \boldsymbol{B} = 4\pi g \delta(\boldsymbol{r})$ that contains a fictitious source term due to a magnetic point charge of magnitude g located at the origin. The form of the resulting magnetic field $\boldsymbol{B} = (g/r^2)\hat{\boldsymbol{e}}_r$ is identical to the Berry curvature field (4.19) if $g = \pm 1/2$, that is, if the magnetic charge is quantized[6]. Just like the magnetic monopole field is singular at the location of the point charge, the Berry curvature diverges at the origin since the eigenvalues $\mathcal{E}_-$ and $\mathcal{E}_+$ would become degenerate for $r = 0$. Acting as a source of the Berry curvature around it, this degeneracy is formally equivalent to a magnetic monopole that manifests eventually in the magnetic field $\boldsymbol{B}$.

4.1.4 Example 2: Aharonov-Bohm effect and topology

The prominent Aharonov-Bohm effect [85] arises for charged particles that envelop during their propagation in a strictly field-free region an infinitely long flux tube that carries the magnetic flux Φ. Berry provided a geometrical interpretation of this effect [21] by considering electrons that are confined to a box, which in turn is dragged around the tube if the position parameter $\boldsymbol{R}$ of the box is tuned, see Fig. 4.2. Consequently, the parameter space is equal to the real space without the region of the flux tube, rendering the parameter manifold multiply connected. While the magnetic field $\boldsymbol{B}$ is restricted to the inside of the tube, the vector potential $\boldsymbol{A}$ is generally non-zero at the electron's position such that the following Schrödinger equation has to be solved:

$$\frac{1}{2}\left(\mathrm{i}\hbar\nabla - e\boldsymbol{A}(\boldsymbol{r})\right)^2 |n\boldsymbol{R}\rangle = \mathcal{E}_n |n\boldsymbol{R}\rangle\,, \tag{4.21}$$

where $\nabla = \nabla_{\boldsymbol{r}}$ denotes the gradient with respect to the electronic coordinates $\boldsymbol{r}$, and e is the elementary positive charge. A standard approach to this problem is to rewrite the solutions $|n\boldsymbol{R}\rangle$ of the full system in terms of normalized wave functions $|\psi_n^0\rangle$ in absence of the vector potential:

$$\langle \boldsymbol{r}|n\boldsymbol{R}\rangle = \exp\left(-\mathrm{i}\frac{e}{\hbar}\int_{\boldsymbol{R}}^{\boldsymbol{r}} \boldsymbol{A}(\boldsymbol{r}')\cdot \mathrm{d}\boldsymbol{r}'\right)\psi_n^0(\boldsymbol{r}-\boldsymbol{R}) = \exp(\mathrm{i}g(\boldsymbol{r}))\psi_n^0(\boldsymbol{r}-\boldsymbol{R})\,, \tag{4.22}$$

where the integration is performed along a path inside the box, and the unperturbed states satisfy the free-particle Schrödinger equation[7] $-(\hbar^2/2)\nabla^2\psi_n^0(\boldsymbol{r}) = \mathcal{E}_n\psi_n^0(\boldsymbol{r})$, which motivates why the eigenvalues in Eq. (4.21) do not depend on $\boldsymbol{R}$. In addition, the eigenvalues are independent of the vector potential since the latter can always be made to vanish within finite regions of space such as the box containing the electrons by a clever gauge choice although the vector potential cannot be removed globally.

As the expectation value of $\nabla_{\boldsymbol{R}}$ vanishes in the free system, it follows that

$$\boldsymbol{A}^n(\boldsymbol{R}) = \mathrm{i}\langle n\boldsymbol{R}|\nabla_{\boldsymbol{R}}|n\boldsymbol{R}\rangle = -\frac{e}{\hbar}\boldsymbol{A}(\boldsymbol{R})\,, \tag{4.23}$$

$$\boldsymbol{\Omega}^n(\boldsymbol{R}) = \nabla_{\boldsymbol{R}} \times \boldsymbol{A}^n(\boldsymbol{R}) = -\frac{e}{\hbar}\boldsymbol{B}(\boldsymbol{R})\,, \tag{4.24}$$

---

[6] Dirac derived a quantization condition [84] that relates the electric charge to any yet to be observed magnetic charge. In fact, $g = \pm 1/2$ is the minimal non-trivial solution of this constraint. This logic can also be turned around to derive Dirac's constraint from the Berry phase calculated over two physically equivalent surfaces excluding either north or south pole.

[7] This follows from $[\mathrm{i}\hbar\nabla - e\boldsymbol{A}(\boldsymbol{r})]\,\langle \boldsymbol{r}|n\boldsymbol{R}\rangle = \mathrm{i}\exp(\mathrm{i}g(\boldsymbol{r}))\nabla\psi_n^0(\boldsymbol{r}-\boldsymbol{R})$ according to the ansatz (4.22).

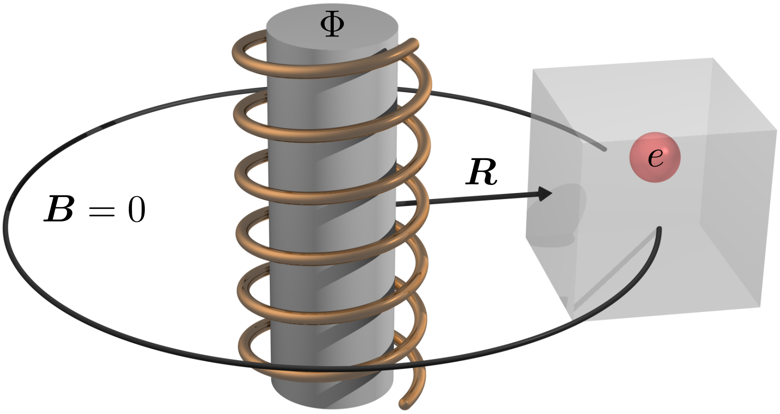

Figure 4.2: Setup for the Aharonov-Bohm effect. The magnetic field is restricted in real space to an infinitely long solenoid around which the box of the electrons (red sphere) is dragged. Due to the magnetic flux Φ piercing the encompassed region, a topological Berry phase manifests in the electronic wave function.

which means that the Berry connection $\boldsymbol{A}^n$ and the Berry curvature field $\boldsymbol{\Omega}^n$ are determined by the vector potential $\boldsymbol{A}$ and the physical magnetic field $\boldsymbol{B}$, respectively. Since the latter is confined to the tube region, the Berry curvature field is zero everywhere outside of the tube. The Berry phase describing Aharonov-Bohm interference effects due to the magnetic flux Φ is given by

$$\gamma_n(\mathcal{C}) = \oint_{\mathcal{C}} \boldsymbol{A}^n(\boldsymbol{R}) \cdot \mathrm{d}\boldsymbol{R} = -N(\mathcal{C})\frac{e}{\hbar}\Phi\,, \tag{4.25}$$

where $N(\mathcal{C})$ is the winding number that counts how often the closed path $\mathcal{C}$ winds around the flux tube. In this example, the Berry phase does not depend on n, and is topological as it is independent of the path if only loops that envelop the flux tube the same number of times are compared. If the electrons do not move in a strictly field-free region but the magnetic field is allowed to be present everywhere in space, the Berry phase returns to its geometric nature $\gamma_n(\mathcal{C}) = -(e/\hbar)\Phi(\mathcal{C})$, where $\Phi(\mathcal{C})$ is the path-dependent magnetic flux through the surface enclosed by the loop $\mathcal{C}$.

Finally, we point out that since $\langle n\boldsymbol{R}|\nabla_{\boldsymbol{R}}|m\boldsymbol{R}\rangle = 0$ for any $n \neq m$, the adiabatic assumption that reads $\Gamma_{nm}^{-1} \ll 1$, where Γ_{nm}^{-1} is defined by Eq. (4.4), is always satisfied here [86], irrespective of how fast the electrons' box is dragged around the flux tube.

4.2 Geometric effects due to momentum-space curvature

4.2.1 Berry curvature in momentum space

In general, the Berry phase manifests as a consequence of the Hamiltonian evolution under slow variations of a set of universal parameters $\boldsymbol{\lambda} = (\lambda_1, \lambda_2, \ldots)$. If electrons move now in the periodic potential of a solid, the role of these abstract parameters is played by the crystal momentum $\boldsymbol{k}$, the variation of which can be ascribed to external "forces" facilitated by, for example, electric and magnetic fields or other perturbations. The generic instantaneous solutions entering the above mathematical framework of quantum adiabatic transport are identified in this case with the lattice-periodic Bloch functions $|u_{\boldsymbol{k}n}\rangle$ that satisfy the Schrödinger equation of the Hamiltonian $H_{\boldsymbol{k}}$ for a given crystal momentum:

$$H_{\boldsymbol{k}}|u_{\boldsymbol{k}n}\rangle = \mathrm{e}^{-\mathrm{i}\boldsymbol{k}\cdot\boldsymbol{r}} H \mathrm{e}^{\mathrm{i}\boldsymbol{k}\cdot\boldsymbol{r}}|u_{\boldsymbol{k}n}\rangle = \mathcal{E}_{\boldsymbol{k}n}|u_{\boldsymbol{k}n}\rangle \, . \tag{4.26}$$

Typically, the Hamiltonian $H_{\boldsymbol{k}} = \mathrm{e}^{-\mathrm{i}\boldsymbol{k}\cdot\boldsymbol{r}} H \mathrm{e}^{\mathrm{i}\boldsymbol{k}\cdot\boldsymbol{r}}$ is referred to as *crystal-momentum representation* of H, which allows us to exactly apply the machinery of Berry phases that was developed in the previous section. When translating the abstract definitions of the Berry connection and the Berry curvature tensor to the situation of Bloch electrons where $\boldsymbol{\lambda} = \boldsymbol{k}$, we arrive at the following realizations of Eqs. (4.7) and (4.10):

$$\boldsymbol{A}^n(\boldsymbol{k}) = \mathrm{i}\langle u_{\boldsymbol{k}n}|\nabla_{\boldsymbol{k}} u_{\boldsymbol{k}n}\rangle \, , \tag{4.27}$$

as well as

$$\Omega^n_{ij}(\boldsymbol{k}) = -2\mathrm{Im}\left\langle \frac{\partial}{\partial k_i} u_{\boldsymbol{k}n} \middle| \frac{\partial}{\partial k_j} u_{\boldsymbol{k}n} \right\rangle = -2\mathrm{Im}\sum_{m\neq n} \frac{\langle u_{\boldsymbol{k}n}|\partial_{k_i} H_{\boldsymbol{k}}|u_{\boldsymbol{k}m}\rangle\langle u_{\boldsymbol{k}m}|\partial_{k_j} H_{\boldsymbol{k}}|u_{\boldsymbol{k}n}\rangle}{(\mathcal{E}_{\boldsymbol{k}n} - \mathcal{E}_{\boldsymbol{k}m})^2} \, . \tag{4.28}$$

Numerous fascinating phenomena in condensed matter root in the non-trivial nature of the momentum-space Berry curvature (4.28), promoting the deep connection between physical response effects and genuinely geometrical properties of the underlying phase space. Before turning to such geometric solid-state phenomena, we comment briefly on the symmetry properties of the Berry curvature in momentum space: while $\Omega^n_{ij}(\boldsymbol{k}) = \Omega^n_{ij}(-\boldsymbol{k})$ holds in the presence of spatial inversion symmetry, the Berry curvature is an odd function of $\boldsymbol{k}$ if time-reversal symmetry is preserved[8], *i.e.*, $\Omega^n_{ij}(\boldsymbol{k}) = -\Omega^n_{ij}(-\boldsymbol{k})$. Consequently, the Berry curvature vanishes everywhere in the Brillouin zone if the solid is symmetric with respect to both spatial and time inversions, which underlines that breaking at least one of the two symmetries is crucial for a non-trivial Berry curvature to emerge. Finally, the overall shape of the rank-2 Berry curvature tensor composed out of the individual elements (4.28) is determined typically by the (magnetic) point group of the system.

4.2.2 Hall effects

In 1879, Edwin Hall measured a transverse voltage drop as a response to longitudinal electric currents flowing in conducting samples that are subject to an external magnetic field [87]. This so-called *ordinary Hall effect* originates from the Lorentz force $-e\boldsymbol{v} \times \boldsymbol{B}$, which acts on charged particles moving with velocity $\boldsymbol{v}$ in the magnetic field $\boldsymbol{B}$, leading thereby to an asymmetric charge distribution at the opposite sample edges, which builds up an electric field that obstructs the migration of further charges and establishes eventually a steady electric potential. The phenomenon is

---

[8] This is easily verified by recalling that (i) time reversal transforms $|u_{\boldsymbol{k}n}\rangle$ into $(|u_{-\boldsymbol{k}n}\rangle)^*$, and (ii) spatial inversion symmetry relates $|u_{\boldsymbol{k}n}\rangle$ and $|u_{-\boldsymbol{k}n}\rangle$.

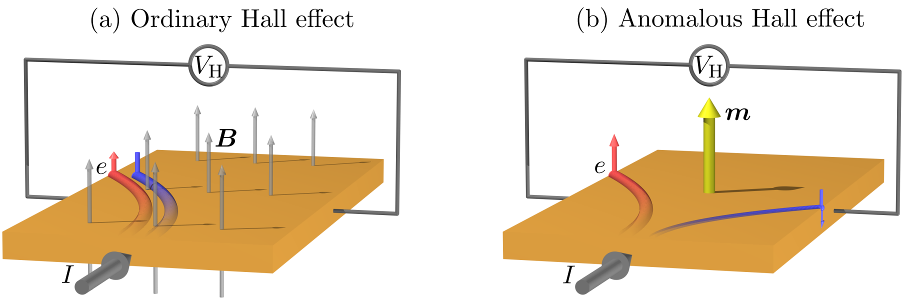

Figure 4.3: (a) Ordinary and (b) anomalous Hall effect due to the charge current I. While the transverse Hall voltage V_H in (a) originates from the applied magnetic field $\boldsymbol{B}$, the magnetization $\boldsymbol{m}$ of a ferromagnet drives the anomalous Hall effect in (b). In the latter case, the resulting asymmetric charge distribution at the sample edges is accompanied by a finite spin polarization due to spin-dependent scattering processes.

characterized by the ratio of induced electric field and applied magnetic field times current density, which is also known as Hall coefficient that depends on material-specific parameters like type and density of the charge carriers. At low temperatures and potent magnetic fields that give rise to discrete Landau levels, two-dimensional systems exhibit exactly *quantized* plateaus [88–90] of the Hall conductance

$$\frac{I}{V_\mathrm{H}} = \nu \frac{e^2}{h} \,, \tag{4.29}$$

where I is the longitudinal charge current, V_H is the transverse Hall voltage drop across the sample, and the filling factor ν takes integer (or certain fractional[9]) values.

While the ordinary Hall effect relies fundamentally on the application of a magnetic field, which breaks time-reversal symmetry, it has been realized already in 1881 by Hall [92] that the magnetization in ferromagnets like Fe mediates an *anomalous Hall effect* independent of any external magnetic field. Footing on the combination of magnetic polarization and relativistic spin-orbit interaction, this extraordinary phenomenon overshadows frequently the ordinary Hall effect by one to two orders of magnitude [92]. Remarkably, the anomalous Hall effect can be decomposed into (i) an intrinsic contribution that roots solely in the geometry of reciprocal space [19,93–95], and (ii) extrinsic parts termed side-jump and skew-scattering, which take into consideration the spin-dependent scattering of the charge carriers [96], and are therefore characteristic to the type and strength of disorder in the studied material. A detailed discussion of the intricate first-principles treatment of the extrinsic effects is provided in Refs. [97,98].

In order to motivate the deep connection between momentum-space geometry and intrinsic anomalous Hall effect, we consider the explicit expression for the velocity of Bloch electrons in an electric field $\boldsymbol{E} = -\partial_t \boldsymbol{A}$ that is written as variation of the time-dependent vector potential $\boldsymbol{A}$ with time t. Effectively, the electric field shifts the

---

[9] The *fractional* Hall effect stems from repulsive electron-electron interactions and can be interpreted as quantum Hall effect of so-called composite fermions (see, for example, the classic Ref. [91]).

crystal momentum that enters the Hamiltonian according to $\boldsymbol{k} = -\mathrm{i}\nabla + (e/\hbar)\boldsymbol{A}$ such that $\partial_t \boldsymbol{k} = -(e/\hbar)\boldsymbol{E}$. Going beyond the simple adiabatic assumption by including first order corrections in the time-evoluted wave functions, we arrive eventually at an equation for the electron's velocity in the nth band [99]:

$$\boldsymbol{v}^n(\boldsymbol{k}) = \langle \tilde{\psi}_{\boldsymbol{k}n} | \boldsymbol{v} | \tilde{\psi}_{\boldsymbol{k}n} \rangle = \frac{1}{\hbar} \langle u_{\boldsymbol{k}n} | \nabla_{\boldsymbol{k}} H_{\boldsymbol{k}} | u_{\boldsymbol{k}n} \rangle = \frac{1}{\hbar} \nabla_{\boldsymbol{k}} \mathcal{E}_{\boldsymbol{k}n} - \frac{e}{\hbar} \boldsymbol{E} \times \boldsymbol{\Omega}^n(\boldsymbol{k}) \,, \tag{4.30}$$

where the wave functions $|\tilde{\psi}_{\boldsymbol{k}n}\rangle$ are obtained from evolving the instantaneous solutions $|u_{\boldsymbol{k}n}\rangle$ in time. In addition to the usual group velocity relating to the gradient of the dispersion, obviously, the Bloch electrons acquire an *anomalous velocity* [100] transverse to the electric field if the Berry curvature field $\boldsymbol{\Omega}^n$ is finite. Recalling that crystal momentum, velocity, and electric field change sign under inversion symmetry whereas time reversal inverts only the first two, we can confirm the previously motivated symmetries of the Berry curvature in momentum space using Eq. (4.30).

The *intrinsic anomalous Hall effect* describes the linear response to an applied electric field in terms of an induced current $\boldsymbol{J} = -e \int \sum_n^{\mathrm{occ}} \boldsymbol{v}^n(\boldsymbol{k}) \, \mathrm{d}^d k/(2\pi)^d$ that roots purely in the geometrical properties of the d-dimensional phase space as encoded in the Berry curvature (4.28):

$$\boldsymbol{J} = \sigma \boldsymbol{E} \qquad \text{with} \qquad \sigma_{ij} = \frac{e^2}{\hbar} \int \sum_n^{\mathrm{occ}} \Omega_{ij}^n(\boldsymbol{k}) \, \frac{\mathrm{d}^d k}{(2\pi)^d} \,. \tag{4.31}$$

Here, the response matrix is the anomalous Hall conductivity, the components σ_{ij} of which are antisymmetric with respect to the Cartesian indices i and j. Analogously to the ordinary transport phenomenon, the anomalous Hall effect relies on broken time-reversal symmetry since the integral in Eq. (4.31) of the Berry curvature over the whole Brillouin zone vanishes otherwise. If the magnetization of a ferromagnet is reversed, the response σ_{ij} changes sign. As an intriguing consequence of its beautiful geometric origin, the anomalous Hall conductivity (4.31) is a genuine bulk property of the periodic crystal without any boundaries, even though the relevant physical processes that support the intrinsic anomalous Hall effect are inherent to the surface.

Theoretical predictions (see Refs. [19, 101, 102] among many others) of an exotic topological variant of the anomalous Hall effect in two-dimensional insulators have triggered tremendous experimental efforts devoted to uncovering such a phase in real materials. Only recently, this *quantum anomalous Hall effect* was discovered experimentally at cryogenic temperatures [103]. One hallmark of this topological phase is the precise quantization of the transport coefficient σ_{xy} in magnetic insulators [18]:

$$\sigma_{xy} = \frac{e^2}{h} \mathcal{C} \,, \tag{4.32}$$

where $\mathcal{C} = \sum_n^{\mathrm{occ}} \mathcal{C}_n = 1/(2\pi) \sum_n^{\mathrm{occ}} \int \Omega_{xy}^n \, \mathrm{d}k_x \mathrm{d}k_y$ is the Chern number, which is guaranteed to be an integer if the unoccupied and occupied states are separated by a finite energy gap. Thus, the Chern number may only change if the global band gap closes and the system becomes metallic. From a mathematical point of view, the Chern number $\mathcal{C}_n$ of the nth band is a topological invariant over the two-dimensional Brillouin zone, which is a well-behaved compact manifold without boundaries. Since the Chern number does not vanish whenever at least two gauge patches are required, we may interpret $\mathcal{C}$ as a hindrance from choosing a smooth and single-valued gauge over the entire parameter manifold[10]. Insulating materials with a non-vanishing Chern number of the occupied states are given the name *Chern insulators* as they display fascinating properties such as the quantization (4.32) that roots in the non-trivial topology of momentum space. The quantum anomalous Hall effect is accompanied by the appearance of perfectly conducting edge states that cross the bulk band gap in the case of a Chern insulator of finite sample size. Because of their topological protection from scattering, these robust states are believed to hold great prospects for energy-efficient spintronic applications. However, promising material candidates suffer so far from either small band gaps or too low Curie temperatures, both of which obstruct the desirable operation of spintronic devices at room temperature.

Finally, we mention only briefly that another member of the family of Hall effects – referred to as the *spin Hall effect* – was suggested by Dyakonov and Perel [104,105], who predicted in 1971 the spin accumulation along the edges of current-carrying paramagnets[11] due to the spin-orbit interaction. A topical overview of this charge-to-spin current conversion is provided in Ref. [107]. In particular, the *quantum spin Hall effect* receives substantial attention as it constitutes a unique response characteristic of topological insulators, where it manifests in helical edge states that are protected from scattering off non-magnetic impurities. Similarly to the anomalous Hall effect, the non-trivial topology of the underlying momentum phase space gives rise to an intrinsic contribution to the spin Hall effect that is driven by the "spin" Berry curvature, where one of the velocities in Eq. (4.12) is replaced with the spin current density, *i.e.*, the anticommutator of velocity and spin operators.

4.2.3 Orbital magnetism

Being one of the most fundamental quantum-mechanical phenomena in solids, magnetism is typically decomposed into the intrinsic spin magnetic moment of electrons and an orbital contribution mediated by circulating electric currents. While the concept and understanding of the spin magnetization, which is the spin magnetic moment per unit volume, has been advanced substantially during the course of the past decades, the overall relevance of orbital magnetism in periodic systems is vividly debated these days. In part, this controversy arises from the fact that the spin moment usually overshadows its orbital counterpart by far due to the quenching of the orbital moment. Orbital magnetism is generally ascribed to either correlation effects that result in orbital moments following Hund's second rule of atomic physics, or the spin-orbit interaction if electron correlations are negligible or not taken into account. Although spin-orbit coupling lifts partially the exact degeneracy of left- and right-propagating currents in the crystal field, Fig. 4.4, this mechanism is rather inefficient in generating a large net orbital moment in most solids as is shown in Chapter 6.

Nevertheless, in particular systems the orbital magnetization (OM) becomes as important as the spin contribution, which can even lead to a spin-orbital compensa-

---

[10] In the spin-1/2 problem, where two gauge patches are necessary, the Chern number amounts to $\mathcal{C}_\pm = \pm 1$ when integrating the curvature (4.19) over the entire parameter manifold of θ and φ.

[11] In general, also systems with broken time-reversal symmetry can host the spin Hall effect if the combined action of time inversion and another crystalline symmetry restores Kramer's degeneracy. For example, this is the case for an antiferromagnetic texture on the square lattice [106].

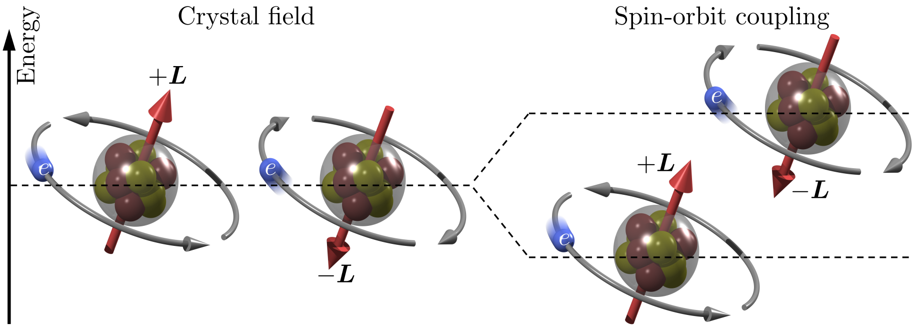

Figure 4.4: If electrons circulate with a certain rotational sense around the nucleus, an orbital angular momentum $+\boldsymbol{L}$ emerges. In the crystal field, however, this state is energetically equivalent to the situation with the opposite rotational sense, which leads to a cancellation and no net orbital moment. Only when coupling the spin degrees of freedom to the crystal lattice via the spin-orbit interaction, we break this orbital degeneracy such that a finite orbital moment may manifest.

tion of the total macroscopic magnetization [108–110]. Apart from these rather rare instances, its general influence on spin-dependent transport [111–114], magnetic susceptibility and magneto-electric response [114–117], magnetic anisotropy [118], and Dzyaloshinskii-Moriya interaction (DMI) [15, 16] renders the OM crucial for understanding basic properties of complex magnets. Consequently, deeper insight into the orbital magnetism of solids is deemed to be of outstanding relevance. However, as we shall see below, the rigorous description of orbital magnetism sets a surprisingly formidable challenge for theory and has remained elusive until only recently. In contrast to theory, experimental techniques to distinguish the individual spin and orbital contributions to the overall magnetization of crystals are readily available since several decades [119–122]. Among these probing methods, X-ray magnetic circular dichroism (XMCD) measurements in terms of the difference in the absorption spectra under left- and right-circularly polarized light in a magnetic field are particularly popular to extract information on the magnetic properties. In transition metals, such X-ray absorption spectra are conventionally taken at the so-called L_2 and L_3 edges[12] where photons excite, for example, $2p$ electrons of Fe into the $3d$ states that define the magnetic attributes of the considered material.

From the viewpoint of theory, the phenomenon of orbital magnetism has remained difficult to grasp primarily due to the subtle theoretical treatment of the orbital angular momentum operator $\boldsymbol{L} = \boldsymbol{r} \times \boldsymbol{p}$ in condensed-matter systems. As the position operator is unbounded in crystals, applying $\boldsymbol{r}$ to any Bloch wave function takes us outside of the Hilbert space. Consequently, the vast majority of previous first-principles calculations assessing the role of orbital magnetism took advantage of an *atom-centered approximation (ACA)* which tames the position operator by lo-

---

[12] In XMCD, the X-ray absorption edge reports the orbital of the electron that absorbs the photon. For example, the atomic orbitals $2p_{1/2}$ and $2p_{3/2}$ are identified with the L_2 and L_3 absorption edge, respectively.

cally restricting the evaluation of the operator $\boldsymbol{L}$ to finite spherical regions around the atoms. Within the full-potential linearized augmented-plane-wave (FLAPW) method, these regions in real space are naturally identified with the muffin tins such that $\boldsymbol{m}^{\mu}_{\boldsymbol{k}n} = -\frac{e}{2m_0}\langle\psi_{\boldsymbol{k}n}|\boldsymbol{r}_\mu \times \boldsymbol{p}|\psi_{\boldsymbol{k}n}\rangle_\mu$ denotes the local orbital moment associated with the state $|\psi_{\boldsymbol{k}n}\rangle$ in the μth muffin tin, and $e > 0$ is the positive elementary charge of the electron with mass m_0. Based on the ACA, the OM amounts to summing up the individual contributions over all occupied states and atoms in the unit cell, and dividing subsequently by the unit cell volume V:

$$\boldsymbol{m}^{\text{aca}} = \frac{1}{N_{\boldsymbol{k}}V}\sum_{\boldsymbol{k}n}^{\text{occ}}\sum_{\mu}\boldsymbol{m}^{\mu}_{\boldsymbol{k}n}\,, \tag{4.33}$$

where $N_{\boldsymbol{k}}$ is the number of $\boldsymbol{k}$-points. However, it is *a priori* unclear whether this approach captures the physically relevant contributions to the orbital magnetism when neglecting strictly all regions of real space but the muffin tins. Especially, non-local currents circulating around several atoms are not fully accounted for.

Only recently, a complete theory aiming at the proper description of orbital magnetism was established through three independent approaches [24–27]. (i) A fruitful way to circumvent the problematic definition of $\boldsymbol{r}$ for extended Bloch states is to use localized Wannier functions (see Chapter 5) instead. Starting from finite samples, it was proven that the magnetization comprises a "local circulation" of bulk-like Wannier functions and an "itinerant circulation" that stems from a net current carried by Wannier functions near the surface [24, 25]. Although the gauge-invariant sum converges in the thermodynamic limit to a boundary-insensitive property involving a Brillouin zone integral of the Bloch states, we emphasize that the itinerant circulation is non-negligible even in the bulk case. (ii) Alternatively, a semiclassical picture of Bloch electrons modeled by wave packets can be used to derive a semiclassical formula for the OM [26]. Here, the intrinsic orbital moment $\langle\nabla_{\boldsymbol{k}}u_{\boldsymbol{k}n}| \times (H_{\boldsymbol{k}} - \mathcal{E}_{\boldsymbol{k}n})|\nabla_{\boldsymbol{k}}u_{\boldsymbol{k}n}\rangle$ due to the rotation of the nth wave packet around its center of mass is complemented with a term that originates from variations of the density of states with magnetic field. (iii) Finally, a full quantum-mechanical derivation based on perturbation theory in the external magnetic field can be performed to uncover additionally the explicit temperature dependence of the OM [27]. All three approaches result in the Berry phase theory of orbital magnetism [99, 123–125], which is also referred to as *modern theory* in analogy to the corresponding framework for calculating the electric polarization in inversion-asymmetric crystals [22, 23, 124]. The OM in the modern theory amounts to a genuine bulk property that is evaluated from the ground-state wave functions:

$$\boldsymbol{m} = \frac{e}{2\hbar}\,\text{Im}\sum_{n}^{\text{occ}}\int[\text{d}k]\,\langle\nabla_{\boldsymbol{k}}u_{\boldsymbol{k}n}|\times\left(H_{\boldsymbol{k}} + \mathcal{E}_{\boldsymbol{k}n} - 2\mathcal{E}_{\text{F}}\right)|\nabla_{\boldsymbol{k}}u_{\boldsymbol{k}n}\rangle\,, \tag{4.34}$$

where $\boldsymbol{k}$ is the crystal momentum, $[\text{d}k]$ stands for $\text{d}\boldsymbol{k}/(2\pi)^3$ in three dimensions, $|u_{\boldsymbol{k}n}\rangle$ is an eigenstate of the lattice-periodic Hamiltonian $H_{\boldsymbol{k}}$ to the band energy $\mathcal{E}_{\boldsymbol{k}n}$, and $\mathcal{E}_{\text{F}}$ is the Fermi energy. Since we are interested in the behavior at zero temperature, the summation has been restricted to all occupied states below the Fermi energy. Note that both $H_{\boldsymbol{k}}$ and $\mathcal{E}_{\boldsymbol{k}n}$ enter Eq. (4.34) with the same sign in contrast to the semiclassical expression for the orbital moment of a wave packet given before.

As compared to the rather crude approximation discussed before, Eq. (4.34) accounts naturally and unambiguously also for contributions to the OM from non-local electric currents [126], however, at the expense of a much more challenging computation. Moreover, the physically intuitive real-space resolution of local orbital moments as provided by Eq. (4.33) is abandoned in the Berry phase theory of OM. In order to connect to experiments on orbital magnetism, we write $\boldsymbol{m} = \boldsymbol{m}_{\mathrm{lc}} + \boldsymbol{m}_{\mathrm{ic}}$ with

$$\boldsymbol{m}_{\mathrm{lc}} = \frac{e}{2\hbar}\,\mathrm{Im}\sum_n^{\mathrm{occ}}\int[\mathrm{d}k]\,\langle\nabla_{\boldsymbol{k}}u_{\boldsymbol{k}n}|\times(H_{\boldsymbol{k}}-\mathcal{E}_{\mathrm{F}})\,|\nabla_{\boldsymbol{k}}u_{\boldsymbol{k}n}\rangle\,, \tag{4.35}$$

$$\boldsymbol{m}_{\mathrm{ic}} = \frac{e}{2\hbar}\,\mathrm{Im}\sum_n^{\mathrm{occ}}\int[\mathrm{d}k]\,\langle\nabla_{\boldsymbol{k}}u_{\boldsymbol{k}n}|\times(\mathcal{E}_{\boldsymbol{k}n}-\mathcal{E}_{\mathrm{F}})\,|\nabla_{\boldsymbol{k}}u_{\boldsymbol{k}n}\rangle\,, \tag{4.36}$$

referring to the aforementioned local and itinerant circulation[13], respectively. On the other hand, XMCD measurements endeavor conventionally the dichroic f-sum rule to disentangle spin and orbital contributions from the differential absorption spectrum. Based on this sum rule, the XMCD spectrum can be shown [127] to probe not all contributions to orbital magnetism but only one specific part of it that links to the integral of $\langle\nabla_{\boldsymbol{k}}u_{\boldsymbol{k}n}|\times(H_{\boldsymbol{k}}-\mathcal{E}_{\boldsymbol{k}n})|\nabla_{\boldsymbol{k}}u_{\boldsymbol{k}n}\rangle$, missing thus the term $2\boldsymbol{m}_{\mathrm{ic}}$ associated with the itinerant circulation. The quantitative relevance of the latter contribution is largely unexplored and debated in the electronic-structure community [124].

Remarkably, the Berry phase expression (4.34) comprises a geometric motive of orbital magnetism, which motivates us to perceive this phenomenon at least partly as a geometric effect stemming from the Berry curvature in momentum space. For example, if we consider the variation of the non-vanishing component m_z with the Fermi level in a two-dimensional insulator[14], this fact becomes even more explicit:

$$\frac{\partial m_z}{\partial\mathcal{E}_{\mathrm{F}}} = \frac{e}{h}\frac{1}{2\pi}\left(-2\mathrm{Im}\sum_n^{\mathrm{occ}}\int\left\langle\frac{\partial u_{\boldsymbol{k}n}}{\partial k_x}\middle|\frac{\partial u_{\boldsymbol{k}n}}{\partial k_y}\right\rangle\mathrm{d}k_x\mathrm{d}k_y\right) = \frac{e}{h}\,\mathcal{C}\,, \tag{4.37}$$

which means that the z-component of the OM changes linearly with energy throughout the band gap of Chern insulators, and the according (positive or negative) slope is determined by the integer Chern number $\mathcal{C}$ of all occupied valence bands. In other words, Eq. (4.37) correlates the emergence of conducting edge states in topologically non-trivial insulators with the orbital magnetism in these systems. Apparently, the OM stays constant within energy regions of trivial band gaps for which $\mathcal{C} = 0$.

It is commonly known that derivatives of the total magnetization $\boldsymbol{M}$ can determine characteristic physical properties such as the magnetic susceptibility [114], which signalizes variations $\partial M_i/\partial B_j$ of the magnetization with an external magnetic field $\boldsymbol{B}$, or the magneto-electric polarizability $\partial M_i/\partial E_j$ [115–117], which specifies the induced magnetization due to an electric field $\boldsymbol{E}$ in insulators with broken time-reversal and inversion symmetries[15]. Therefore, since the total magnetization contains the orbital contribution $\boldsymbol{m}$, derivatives of the latter quantity can be substantial to describe the

---

[13] It should be kept in mind that the difference between the simple ACA and the modern theory is not just the itinerant circulation as pointed out in Ref. [126].

[14] In metals, the derivative of the step-like Fermi distribution provides an extra Fermi-surface term, which supplements the integral of the Berry curvature over the whole Brillouin zone [124].

[15] Based on Maxwell's relations, the induced magnetization due to an applied electric field can be viewed alternatively as the response of the electric polarization to an external magnetic field.

previously mentioned response effects although the magnitude of the orbital magnetization itself might be negligible as compared to the spin counterpart. In addition, the orbital magnetic moment is of crucial importance for other response phenomena such as the gyrotropic magnetic effect [128], current-induced OM [129], and orbital Hall effects [130, 131]. Consequently, as we demonstrate in Chapter 6, advancing our yet premature understanding of orbital magnetism by employing the predictive Berry phase theory is fundamental to accomplish a qualitative and quantitative description of relevant electronic and magnetic effects in condensed-matter systems.

4.3 Geometric effects due to mixed-space curvature

4.3.1 Berry curvature in mixed space

The momentum-space curvature that rules the previously discussed geometric phenomena of anomalous Hall effect and orbital magnetism is only one component of a more general Berry curvature tensor $\boldsymbol{\Omega}$ [26, 132], which assumes in the presence of the crystal momentum $\boldsymbol{k}$ and additional tunable parameters $\boldsymbol{\lambda}$ the form

$$\boldsymbol{\Omega} = \begin{pmatrix} \Omega^{\boldsymbol{kk}} & \Omega^{\boldsymbol{k\lambda}} \\ \Omega^{\boldsymbol{\lambda k}} & \Omega^{\boldsymbol{\lambda\lambda}} \end{pmatrix} . \tag{4.38}$$

Here, $\Omega^{\boldsymbol{kk}}$ corresponds to the Berry curvature tensor of all occupied states in momentum space, $\Omega^{\boldsymbol{k\lambda}}$ and $\Omega^{\boldsymbol{\lambda k}}$ denote *mixed Berry curvatures* that entangle the usual reciprocal space with the abstract $\boldsymbol{\lambda}$-manifold, and $\Omega^{\boldsymbol{\lambda\lambda}}$ describes the curvature originating purely from the parameter space of $\boldsymbol{\lambda}$ (see also Fig. 4.5(b)). Depending on the choice of the nature of $\boldsymbol{\lambda}$, different physical effects can be understood from the underlying phase-space geometry mediated by Eq. (4.38).

The present thesis has its focus on situations in which the role of the additional parameter is played by the magnetization direction $\hat{\boldsymbol{m}} = (\cos\varphi\sin\theta, \sin\varphi\sin\theta, \cos\theta)$, which is represented in spherical coordinates using the polar angle θ and the azimuthal angle φ as illustrated in Fig. 4.5(a). As will be shown below, such a setting enables us to interpret antidamping spin-orbit torques (SOTs) and the Dzyaloshinskii-Moriya interaction (DMI) in inversion-asymmetric magnets as geometric phenomena that root in the mixed Berry curvature tensor $\Omega^{\hat{\boldsymbol{m}}\boldsymbol{k}}$. This quantity intertwines the phase spaces of crystal momentum and magnetization direction in the following way [28]:

$$\begin{aligned} \Omega_{ij}^{\hat{\boldsymbol{m}}\boldsymbol{k}} &= -2\mathrm{Im}\sum_n^{\mathrm{occ}} \hat{\boldsymbol{e}}_i \cdot \left(\hat{\boldsymbol{m}} \times \left\langle \frac{\partial u_{\boldsymbol{k}n}}{\partial \hat{\boldsymbol{m}}} \middle| \frac{\partial u_{\boldsymbol{k}n}}{\partial k_j} \right\rangle \right) \\ &= -2\mathrm{Im}\sum_n^{\mathrm{occ}} \hat{\boldsymbol{e}}_i \cdot \left(\hat{\boldsymbol{e}}_\varphi \left\langle \frac{\partial u_{\boldsymbol{k}n}}{\partial \theta} \middle| \frac{\partial u_{\boldsymbol{k}n}}{\partial k_j} \right\rangle - \frac{1}{\sin\theta} \hat{\boldsymbol{e}}_\theta \left\langle \frac{\partial u_{\boldsymbol{k}n}}{\partial \varphi} \middle| \frac{\partial u_{\boldsymbol{k}n}}{\partial k_j} \right\rangle \right) , \end{aligned} \tag{4.39}$$

where the explicit magnetization dependence of the wave functions $|u_{\boldsymbol{k}n}\rangle$ is suppressed to simplify the notation. To arrive at the second line, we expressed the gradient in spherical coordinates using the unit vectors $\hat{\boldsymbol{e}}_\varphi = (1/\sin\theta)\partial\hat{\boldsymbol{m}}/\partial\varphi = (-\sin\varphi, \cos\varphi, 0)$ and $\hat{\boldsymbol{e}}_\theta = \partial\hat{\boldsymbol{m}}/\partial\theta = (\cos\varphi\cos\theta, \sin\varphi\cos\theta, -\sin\theta)$. Based on first order perturbation theory, Eq. (4.39) can be recast into a numerically advantageous

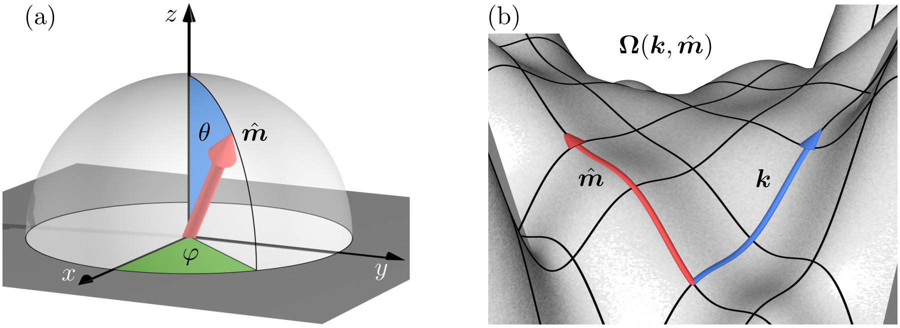

Figure 4.5: (a) The magnetization direction $\hat{\boldsymbol{m}}$ can be represented in spherical coordinates using the polar angle θ (blue) and the azimuthal angle φ (green). (b) Illustration of the complex phase space that entangles the crystal momentum $\boldsymbol{k}$ with the dynamical magnetization direction $\hat{\boldsymbol{m}}$, resulting eventually in a non-trivial general Berry curvature $\boldsymbol{\Omega}(\boldsymbol{k},\hat{\boldsymbol{m}})$.

shape that may be evaluated under an arbitrary gauge of the wave functions. In addition to the usual velocity operator $\hbar\boldsymbol{v}(\boldsymbol{k}) = \nabla_{\boldsymbol{k}} H_{\boldsymbol{k}}$ given by Eq. (4.30), we employ for this purpose the torque operator

$$\boldsymbol{\mathcal{T}} = \hat{\boldsymbol{m}} \times \boldsymbol{B}_{\text{xc}} = \hat{\boldsymbol{m}} \times \frac{\partial H}{\partial \hat{\boldsymbol{m}}} = \frac{\partial H}{\partial \theta}\hat{\boldsymbol{e}}_{\varphi} - \frac{1}{\sin\theta}\frac{\partial H}{\partial \varphi}\hat{\boldsymbol{e}}_{\theta}\,, \tag{4.40}$$

where $\boldsymbol{B}_{\text{xc}}$ stands for the exchange field. An equivalent formulation of the torque operator $\boldsymbol{\mathcal{T}}$ is obtained by replacing H in the above equation with the crystal-momentum representation $H_{\boldsymbol{k}}$. Then, the mixed Berry curvature assumes the form

$$\Omega_{ij}^{\hat{\boldsymbol{m}}\boldsymbol{k}} = -2\text{Im}\sum_{n}^{\text{occ}}\sum_{m\neq n}\frac{\langle u_{\boldsymbol{k}n}|\mathcal{T}_i|u_{\boldsymbol{k}m}\rangle\langle u_{\boldsymbol{k}m}|\hbar v_j(\boldsymbol{k})|u_{\boldsymbol{k}n}\rangle}{(\mathcal{E}_{\boldsymbol{k}n}-\mathcal{E}_{\boldsymbol{k}m})^2}\,, \tag{4.41}$$

where $\mathcal{T}_i$ and $v_j(\boldsymbol{k})$ refer to the ith and jth Cartesian component of torque operator and velocity operator, respectively.

As compared to the Berry curvature $\Omega^{\boldsymbol{kk}}$ in momentum space, Eq. (4.28), which correlates two polar vectors (velocities), the geometry of the mixed phase space is measured by the coupling of the axial vector $\boldsymbol{\mathcal{T}}$ to the polar vector $\boldsymbol{v}(\boldsymbol{k})$, as a consequence of which the symmetry properties of the mixed Berry curvature are thoroughly distinct from $\Omega^{\boldsymbol{kk}}$. Notably, the axial and polar vectors may only couple if the inversion symmetry is broken. Moreover, the mixed Berry curvature is even under magnetization reversal in contrast to the pure curvature in momentum space. While the antisymmetric tensor shape in the latter case is due to the Onsager reciprocity relations, the structure of the mixed curvature tensor roots solely in the allowed symmetry operations in the considered system. For instance, in perpendicularly magnetized films such as Mn/W(001) and Co/Pt(111) [133], the existence of a rotational symmetry $C_n^{\perp}$ with $n > 2$ around the axis perpendicular to the film plane dictates an antisymmetric tensor shape, *i.e.*, $\Omega_{ij}^{\hat{\boldsymbol{m}}\boldsymbol{k}} = -\Omega_{ji}^{\hat{\boldsymbol{m}}\boldsymbol{k}}$. However, this relation does not hold anymore once the magnetization is rotated away from the out-of-plane direction.

4.3.2 Spin-orbit torques

Controlling and manipulating the magnetization of magnetic materials is of utter relevance for the innovative design of future high-speed, non-volatile, energy-efficient, and scalable spintronic devices. Since the involved currents are much smaller, magnetization switching of nanomagnets due to injected (spin-polarized) charge currents or applied electric fields is perceived as highly promising and contrasts favorably from utilizing external magnetic fields to set the magnetic state. Thus, the electrical control via *spin torques* acting on the macroscopic magnetization opens bright technological perspectives for the integration and miniaturization of functionalized magnetic units in electronic circuits such as novel random-access memories [9–11].

Slonczewski [6] and Berger [7] were the first in 1996 to formulate independently the physical principle of exploiting spin-polarized currents to exert torques on the magnetization. These so-called *spin-transfer torques (STTs)* drive non-uniform magnetic textures like domain walls [134] and facilitate the switching of free ferromagnetic layers in spin valves and magnetic tunnel junctions. A charge current that flows perpendicular to the film plane of a spin valve, for example, becomes spin-polarized in the first ferromagnetic layer due to the spin-filtering effect[16] before entering the nonmagnetic spacer. At the interface between the spacer and the second magnetic layer with local magnetization $\boldsymbol{m}$, a non-equilibrium spin polarization $\delta\boldsymbol{s}$ accumulates due to the different conductivities for spin-up and spin-down electrons in the ferromagnet. As a consequence of the exchange interaction $\boldsymbol{m}\cdot\delta\boldsymbol{s}$ of the local magnetization with this accumulated spin polarization at the interface, spin angular momentum is transferred between the spin current and the macroscopic magnetization if $\delta\boldsymbol{s}$ is misaligned with $\boldsymbol{m}$. If the magnitude of the local ferromagnetic moment is assumed to remain constant, only the perpendicular contribution $\delta\boldsymbol{s}_\perp = a\boldsymbol{m}\times\delta\boldsymbol{s} + b(\boldsymbol{m}\times\delta\boldsymbol{s})\times\boldsymbol{m}$ of the spin current manifests in a torque, where the parameters a and b carry distinct dependencies on the applied current density, the relative angle between $\boldsymbol{m}$ and $\delta\boldsymbol{s}$, and details of the interface geometry. The time rate of change of spin angular momentum is then quantified by the spin-transfer torque acting on $\boldsymbol{m}$, *i.e.*, the cross product of the macroscopic magnetization with the effective exchange field mediated by the non-equilibrium spin polarization [135, 136]:

$$\boldsymbol{T} \propto \boldsymbol{m}\times\delta\boldsymbol{s}_\perp = a\boldsymbol{m}\times(\boldsymbol{m}\times\delta\boldsymbol{s}) + b\boldsymbol{m}\times\delta\boldsymbol{s}\,. \tag{4.42}$$

While the out-of-plane *field-like torque* ($b\boldsymbol{m}\times\delta\boldsymbol{s}$) causes the magnetization to precess around the effective exchange field, the in-plane *antidamping torque* ($a\boldsymbol{m}\times(\boldsymbol{m}\times\delta\boldsymbol{s})$) rotates the magnetization towards $\delta\boldsymbol{s}$ due to the absorption of the transverse part of the spin current, switching eventually the magnetization if the applied current is large enough. In typical spin-transfer torque geometries, the critical current densities necessary for magnetization reversal amount to about 10^8 A/cm^2.

The magnetization dynamics is described by the Landau-Lifshitz-Gilbert equation

$$\dot{\boldsymbol{m}} = -\gamma\boldsymbol{m}\times\boldsymbol{H}_{\text{eff}} + \frac{\alpha}{m}\boldsymbol{m}\times\dot{\boldsymbol{m}} + \eta_{\text{ad}}\boldsymbol{m}\times(\boldsymbol{m}\times\delta\boldsymbol{s})\,, \tag{4.43}$$

where $\dot{\boldsymbol{m}} = \partial\boldsymbol{m}/\partial t$ is the variation of $\boldsymbol{m} = m\hat{\boldsymbol{m}}$ with time, γ characterizes the precession around the effective field $\boldsymbol{H}_{\text{eff}}$ consisting of external magnetic and intrinsic

---

[16] The spin-filtering effect originates from the difference in transmission and reflection for spin-up and spin-down electrons in typical ferromagnets.

exchange fields, α is the Gilbert damping parameter, and the importance of the antidamping torque is controlled by η_{ad}, which hinges on the applied current magnitude. In order to achieve magnetization switching, the antidamping torque has to overcome the magnetic damping. Remarkably, while spin torques describe the phenomenon of spin-polarized currents rotating the magnetization, exciting externally the dynamics of the magnetization induces spin currents because of the inverse effect known as *spin pumping* [137–140]. Since magnetic damping dissipates during the magnetization dynamics spin angular momentum into the conduction electrons, a spin current is pumped out of a ferromagnet like permalloy into an adjacent non-magnetic conductor such as Pt.

Albeit the spin-transfer torque offers an exciting prospect to orient the free layer in spin valves and magnetic tunnel junctions, practical technology that foots on this effect is limited by the wear-out, or, dielectric breakdown from which these magnetic heterostructures suffer. Spin valves and magnetic tunnel junctions might be damaged if large currents flow across the device, which is, however, necessary to switch the magnetization. Additionally, reading out the magnetic information reliably in the spin-transfer torque geometries without inducing any switching requires particular care. Facing these challenges, we elucidate in the following an advantageous mechanism based on fundamental relativistic phenomena to generate spin-polarized currents and thereby exert so-called *spin-orbit torques (SOTs)* on the magnetization.

The SOTs are ascribed to two contributing effects that usually coexist in the studied systems [141]: (i) When an in-plane current is passed through a heavy-metal film like Pt, the strong spin-orbit coupling converts the charge current into a transverse spin current via the spin Hall effect, whereby a non-equilibrium spin accumulation at the interface to an adjacent ferromagnet such as Co is generated. This spatially nonuniform spin polarization interacts with the magnetization of the ferromagnet and exerts a spin torque on the local magnetic moment. (ii) In general, the spin-orbit interaction can be represented as $H_{\mathrm{so}}(\boldsymbol{k}) = -\boldsymbol{m}\cdot\boldsymbol{B}_{\mathrm{so}}(\boldsymbol{k})$ using the spin-orbit effective magnetic field $\boldsymbol{B}_{\mathrm{so}}(\boldsymbol{k})$. If crystals with broken spatial inversion symmetry are subject to a charge current, the states with $\boldsymbol{k}$ and $-\boldsymbol{k}$ are populated unevenly, leading to a net average of the spin-orbit field. It manifests in the *inverse spin galvanic effect*, or, *Edelstein effect* by creating through the exchange interaction with the spin of the conduction electrons a homogeneous spin polarization, which eventually reorients the local magnetic moment in a ferromagnet. In this case, the current-induced spin torque inherits the symmetries associated with the spin-orbit field that is occasionally but not necessarily of Rashba or Dresselhaus type.

Overall, the phenomenon of SOTs offers a highly efficient means of electrical control of the magnetization in crystals that combine broken spatial inversion symmetry and strong spin-orbit coupling[17] [133, 142–145], and facilitates to separate write and read lines in spin valves and magnetic tunnel junctions. These spin torques were demonstrated to enable switching of single ferromagnetic layers [12, 13] and even antiferromagnets [14] via the transfer of orbital angular momentum from the lattice to the spin system. Experiments on ferromagnetic trilayers have identified to lowest

---

[17] In Chapter 9 we uncover an intriguing mechanism for large magneto-electric effects that roots not in the spin-orbit interaction itself but in the global topology of the mixed phase space.

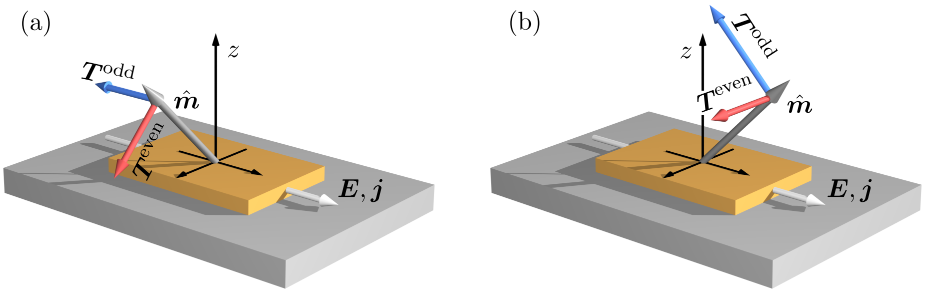

Figure 4.6: If an electric field $\boldsymbol{E}$ (or, equivalently, a charge current $\boldsymbol{j}$) is applied to an inversion-asymmetric magnetic heterostructure, the magnetization reorients its direction $\hat{\boldsymbol{m}}$ as a response to the resulting spin-orbit torques. These torques can be decomposed into an antidamping (even) and a field-like (odd) contribution according to Eqs. (4.44) and (4.45).

order in $\hat{\boldsymbol{m}}$ two qualitatively distinct torques acting on the magnetization[18]:

$$\boldsymbol{T}^{\mathrm{even}} = t^{\mathrm{even}} \hat{\boldsymbol{m}} \times \left[(\hat{\boldsymbol{e}}_z \times \boldsymbol{E}) \times \hat{\boldsymbol{m}} \right] , \tag{4.44}$$

$$\boldsymbol{T}^{\mathrm{odd}} = t^{\mathrm{odd}} (\hat{\boldsymbol{e}}_z \times \boldsymbol{E}) \times \hat{\boldsymbol{m}} , \tag{4.45}$$

where $\boldsymbol{E}$ is an in-plane electric field, t^{even} and t^{odd} are $\hat{\boldsymbol{m}}$-independent constants, and $\hat{\boldsymbol{e}}_z$ is the unit vector perpendicular to the film (see Fig. 4.6). While the antidamping torque $\boldsymbol{T}^{\mathrm{even}}$ is even under magnetization reversal, the field-like torque $\boldsymbol{T}^{\mathrm{odd}}$ is an odd function of $\hat{\boldsymbol{m}}$.

From the viewpoint of theory, the torque $\boldsymbol{T}$ due to spin-polarized currents is naturally described as a linear response to the applied electric field $\boldsymbol{E}$:

$$\boldsymbol{T} = \tau \boldsymbol{E} , \tag{4.46}$$

where the so-called *torkance tensor* τ mediates the electric-field response of the system [133]. Here we restrict ourselves to the case of ferromagnets that are characterized by a position-independent magnetization direction. Within the Kubo formalism, the torkance tensor relates to the imaginary part of the retarded torque-velocity correlation function, which can be calculated conveniently by the Matsubara technique of analytical continuation [146]. This yields a Green function representation of the energy-resolved torkance tensor that assumes at zero temperature the form [133]

$$\begin{aligned} \vartheta_{ij}(\mathcal{E}) = {} & \frac{e}{h} \delta(\mathcal{E} - \mathcal{E}_{\mathrm{F}}) \mathrm{Tr} \langle \mathcal{T}_i G^{\mathrm{R}}(\mathcal{E}) v_j G^{\mathrm{A}}(\mathcal{E}) \rangle - \frac{e}{h} \delta(\mathcal{E} - \mathcal{E}_{\mathrm{F}}) \mathrm{Re} \mathrm{Tr} \langle \mathcal{T}_i G^{\mathrm{R}}(\mathcal{E}) v_j G^{\mathrm{R}}(\mathcal{E}) \rangle \\ & + \frac{e}{h} \theta(\mathcal{E}_{\mathrm{F}} - \mathcal{E}) \mathrm{Re} \mathrm{Tr} \left\langle \mathcal{T}_i G^{\mathrm{R}}(\mathcal{E}) v_j \frac{\mathrm{d} G^{\mathrm{R}}(\mathcal{E})}{\mathrm{d}\mathcal{E}} - \mathcal{T}_i \frac{\mathrm{d} G^{\mathrm{R}}(\mathcal{E})}{\mathrm{d}\mathcal{E}} v_j G^{\mathrm{R}}(\mathcal{E}) \right\rangle , \end{aligned} \tag{4.47}$$

where $G^{\mathrm{R}}(\mathcal{E}) = \hbar [\mathcal{E} - H + \mathrm{i}\eta]^{-1}$ and $G^{\mathrm{A}}(\mathcal{E}) = \hbar [\mathcal{E} - H - \mathrm{i}\eta]^{-1}$ denote the retarded and the advanced Green function, respectively, H is the single-particle Hamiltonian, and

---

[18] In AlO_x/Co/Pt corrections by terms of higher order in $\hat{\boldsymbol{m}}$ are relevant to account for the anisotropy of the SOTs with magnetization direction [145].

$\eta > 0$ originates from the Matsubara construction. When integrating $\vartheta_{ij}(\mathcal{E})$ over the full energy range, we find the element τ_{ij} of the torkance tensor entering Eq. (4.46):

$$\tau_{ij} = \int \vartheta_{ij}(\mathcal{E})\,\mathrm{d}\mathcal{E}\,, \tag{4.48}$$

which comprises in general contributions from both Fermi surface and Fermi sea according to Eq. (4.47). Remarkably, the Bastin equation [147] for the conductivity tensor (derived from the current-current correlation) provides a formally equivalent expression if the current density operator $-ev_i/V$ is replaced therein with $-\mathcal{T}_i$.

Although the limit of zero temperature is considered here, the presumably most dominant effect of disorder-induced smearing of the energy bands can still be modeled. For this purpose, we introduce a constant broadening Γ of the bands[19] in the eigenstate representation of the Green functions, *e.g.*, $\langle u_{\boldsymbol{k}n}|G^{\mathrm{R}}(\mathcal{E})|u_{\boldsymbol{k}n}\rangle = \hbar[\mathcal{E} - \mathcal{E}_{\boldsymbol{k}n} + \mathrm{i}\Gamma]^{-1}$. Plugging this into Eq. (4.48) and grouping those parts that hinge either on the real part or on the imaginary part of $\langle u_{\boldsymbol{k}n}|\mathcal{T}_i|u_{\boldsymbol{k}m}\rangle\langle u_{\boldsymbol{k}m}|v_j(\boldsymbol{k})|u_{\boldsymbol{k}n}\rangle$, we recover the decomposition of the torkance into an even term

$$\begin{aligned}\tau_{ij}^{\text{even}} = \frac{e\hbar}{2\pi N_{\boldsymbol{k}}} \sum_{\boldsymbol{k}n}\sum_{m\neq n} & \operatorname{Im}(\langle u_{\boldsymbol{k}n}|\mathcal{T}_i|u_{\boldsymbol{k}m}\rangle\langle u_{\boldsymbol{k}m}|v_j(\boldsymbol{k})|u_{\boldsymbol{k}n}\rangle) \\ & \times \left\{ \frac{\Gamma(\mathcal{E}_{\boldsymbol{k}m} - \mathcal{E}_{\boldsymbol{k}n})}{[(\mathcal{E}_{\mathrm{F}} - \mathcal{E}_{\boldsymbol{k}n})^2 + \Gamma^2][(\mathcal{E}_{\mathrm{F}} - \mathcal{E}_{\boldsymbol{k}m})^2 + \Gamma^2]} \right. \\ & + \frac{2\Gamma}{(\mathcal{E}_{\boldsymbol{k}n} - \mathcal{E}_{\boldsymbol{k}m})[(\mathcal{E}_{\mathrm{F}} - \mathcal{E}_{\boldsymbol{k}m})^2 + \Gamma^2]} \\ & \left. + \frac{2}{(\mathcal{E}_{\boldsymbol{k}n} - \mathcal{E}_{\boldsymbol{k}m})^2} \operatorname{Im}\ln\frac{\mathcal{E}_{\boldsymbol{k}m} - \mathcal{E}_{\mathrm{F}} - \mathrm{i}\Gamma}{\mathcal{E}_{\boldsymbol{k}n} - \mathcal{E}_{\mathrm{F}} - \mathrm{i}\Gamma} \right\},\end{aligned} \tag{4.49}$$

and into an odd contribution that changes sign under magnetization reversal:

$$\tau_{ij}^{\text{odd}} = \frac{e\hbar}{\pi N_{\boldsymbol{k}}} \sum_{\boldsymbol{k}n}\sum_{m} \frac{\Gamma^2 \operatorname{Re}(\langle u_{\boldsymbol{k}n}|\mathcal{T}_i|u_{\boldsymbol{k}m}\rangle\langle u_{\boldsymbol{k}m}|v_j(\boldsymbol{k})|u_{\boldsymbol{k}n}\rangle)}{[(\mathcal{E}_{\mathrm{F}} - \mathcal{E}_{\boldsymbol{k}n})^2 + \Gamma^2][(\mathcal{E}_{\mathrm{F}} - \mathcal{E}_{\boldsymbol{k}m})^2 + \Gamma^2]}\,. \tag{4.50}$$

While the odd torkance that characterizes the field-like SOT is purely due to the Fermi surface terms in Eq. (4.47), the antidamping torque as represented by the even torkance originates from both the Fermi surface and the Fermi sea. Equations (4.49) and (4.50) can be used to evaluate based on the electronic structure the SOTs as an electric-field response in (disordered) inversion-asymmetric systems. As the torkance tensor τ roots in the coupling of the axial vector $\boldsymbol{\mathcal{T}}$ and the polar vector $\boldsymbol{v}(\boldsymbol{k})$, its shape is not determined by Onsager reciprocity relations but by the crystal symmetries.

In the limit of vanishing disorder $\Gamma \to 0$, *i.e.*, in clean samples, the odd torkance diverges like $1/\Gamma$:

$$\tau_{ij}^{\text{odd}} = \frac{e\hbar}{2\Gamma N_{\boldsymbol{k}}} \sum_{\boldsymbol{k}n} \langle u_{\boldsymbol{k}n}|\mathcal{T}_i|u_{\boldsymbol{k}n}\rangle\langle u_{\boldsymbol{k}n}|v_j(\boldsymbol{k})|u_{\boldsymbol{k}n}\rangle\delta(\mathcal{E}_{\mathrm{F}} - \mathcal{E}_{\boldsymbol{k}n})\,. \tag{4.51}$$

---

[19] A more sophisticated approach towards treating disorder coherently, *e.g.*, within the Gaussian disorder model, requires the evaluation of so-called vertex corrections.

However, the even torkance assumes a scattering-independent value for $\Gamma \to 0$:

$$\begin{aligned} \mathcal{T}_{ij}^{\text{even}} &= \frac{2e\hbar}{N_{\boldsymbol{k}}} \sum_{\boldsymbol{k}n}^{\text{occ}} \sum_{m\neq n} \operatorname{Im} \frac{\langle u_{\boldsymbol{k}n}|\mathcal{T}_i|u_{\boldsymbol{k}m}\rangle\langle u_{\boldsymbol{k}m}|v_j(\boldsymbol{k})|u_{\boldsymbol{k}n}\rangle}{(\mathcal{E}_{\boldsymbol{k}n}-\mathcal{E}_{\boldsymbol{k}m})^2} \\ &= -\frac{e}{N_{\boldsymbol{k}}} \sum_{\boldsymbol{k}} \Omega_{ij}^{\hat{\boldsymbol{m}}\boldsymbol{k}}(\boldsymbol{k})\,, \end{aligned} \tag{4.52}$$

which is determined by the integral of the mixed Berry curvature (4.41) of all occupied states over the Brillouin zone. Consequently, the latter intrinsic contribution to the antidamping SOT in clean samples reveals strong formal analogies to the anomalous Hall conductivity (4.31), which motivates us to interpret antidamping SOTs as manifestly geometric phenomena that are governed by the non-trivial properties of the combined phase space of crystal momentum and magnetization direction.

4.3.3 Dzyaloshinskii-Moriya interaction

The exchange interaction between two indistinguishable electrons comprises an *antisymmetric* part referred to as Dzyaloshinskii-Moriya interaction (DMI) [15,16], which gains recently ever-growing attention as it stabilizes fascinating chiral spin structures [148]. This interaction is particularly important for the condensed-matter realization of localized soliton solutions known as magnetic skyrmions [132,149–151] that are topologically protected magnetic whirls. Moreover, the DMI manifests in chiral magnetic domain walls, which are perceived to hold promises for novel memory devices as they can be driven very efficiently by current-induced spin torques [152–156]. Originating from the interplay between spin-orbit coupling and broken inversion symmetry in non-centrosymmetric bulk crystals or at interfaces, the antisymmetric exchange energy $\boldsymbol{\mathcal{D}}_{ij}\cdot(\boldsymbol{S}_i\times\boldsymbol{S}_j)$ between the two spins $\boldsymbol{S}_i$ and $\boldsymbol{S}_j$ favors a canting of these magnetic moments. This amounts to the formation of a non-collinear spin structure with a particular handedness, or, chirality that is determined by the DMI vectors $\boldsymbol{\mathcal{D}}_{ij}$, which are constrained by the crystal symmetries.

One of the common approaches to predict from *ab initio* the vectors $\boldsymbol{\mathcal{D}}_{ij}$ mediating the DMI is to perform non-collinear calculations of spin spirals with finite wave vectors $\boldsymbol{q}$, where spin-orbit coupling is added as a small perturbation [157–161]. As a consequence, the chiral interaction manifests in the $\boldsymbol{q}$-linear contribution to the dispersion $E(\boldsymbol{q})$, *i.e.*, the total energy as a function of the spin-spiral wave vector. Alternative computational techniques extract the DMI from derivatives of the spin correlation function [162], intrinsic spin currents [163], a tight-binding representation of the energy bands [164], or from multiple-scattering theory [165]. A subset of these methods employs computationally demanding frameworks associated either with the calculation of non-collinear spin structures[20] or with the full-relativistic Kohn-Korringa-Rostoker (KKR) method. In addition, some of the approaches rely on restrictive assumptions on the magnitude of exchange and spin-orbit interactions, which renders the accuracy of such methods in particular for materials that contain heavy metals

---

[20] As the Hamiltonian is block-diagonal in the collinear case, the diagonalization scales like $2n^3$, where n is the dimension of a single spin block. In the non-collinear case, however, the diagonalization is more expensive and scales like $(2n)^3$ since the spin-up and spin-down problems become coupled.

with strong spin-orbit coupling controversial. In contrast, a Berry phase theory was developed in Ref. [28] that evaluates the DMI from the electronic structure of the collinear ferromagnetic ground state with self-consistent spin-orbit coupling.

Within the latter Berry phase theory, the pairwise DMI vectors $\boldsymbol{\mathcal{D}}_{ij}$ are replaced with the micromagnetic *spiralization tensor* D, which relates to the atomistic quantities via [161]

$$D = \frac{2\pi}{V} \sum_i \boldsymbol{\mathcal{D}}_{0i} \otimes \boldsymbol{R}_i \,, \tag{4.53}$$

where $\boldsymbol{R}_i$ is the ith lattice vector, and the outer product "$\otimes$" illustrates the tensorial nature of the 3×3 spiralization matrix D. Equivalently, the micromagnetic D can be represented by the outer product of the rotation vector of a spin spiral and the gradient of the total energy with respect to the spin-spiral wave vector [161].

Quantifying the DMI, the spiralization tensor D reflects the change of the micromagnetic free energy density F as a response to chiral perturbations $\partial\hat{\boldsymbol{m}}/\partial r_j$. This energy change assumes up to first order in gradients of the magnetization direction $\hat{\boldsymbol{m}}$ the form [28]

$$\delta F(\boldsymbol{r}) = \sum_{ij} D_{ij}(\hat{\boldsymbol{m}})\hat{\boldsymbol{e}}_i \cdot \left(\hat{\boldsymbol{m}}(\boldsymbol{r}) \times \frac{\partial \hat{\boldsymbol{m}}(\boldsymbol{r})}{\partial r_j} \right) \,, \tag{4.54}$$

where $\hat{\boldsymbol{e}}_i$ denotes the ith Cartesian unit vector, D_{ij} is an element of the 3×3 spiralization tensor, and $\boldsymbol{r}$ is the position. In the present work, we focus on the DMI in ferromagnetic systems, for which the magnetization direction $\hat{\boldsymbol{m}}$ depends only weakly on the position $\boldsymbol{r}$ in real space. Consequently, an explicit expression for the matrix elements of the spiralization tensor is obtained if the free energy change due to small spatial oscillations of the magnetization direction is equated with the free energy change according to Eq. (4.54).

We employ in the following the torque operator $\boldsymbol{\mathcal{T}} = \hat{\boldsymbol{m}} \times \boldsymbol{B}_{\mathrm{xc}}$ with the exchange field $\boldsymbol{B}_{\mathrm{xc}}$, and the velocity operator in crystal momentum representation, $\hbar\boldsymbol{v}(\boldsymbol{k}) = \partial_{\boldsymbol{k}}(e^{-i\boldsymbol{k}\cdot\boldsymbol{r}} H e^{i\boldsymbol{k}\cdot\boldsymbol{r}})$, where H is the single-particle Hamiltonian of the ferromagnetic system. Following the detailed derivations given in Ref. [28], we arrive at an expression for the spiralization at finite temperatures T:

$$D_{ij} = \frac{1}{N_{\boldsymbol{k}} V} \sum_{\boldsymbol{k}n} \left[f(\mathcal{E}_{\boldsymbol{k}n}) A^n_{ij}(\boldsymbol{k}) + \frac{1}{\beta} \ln\left(1 + e^{-\beta(\mathcal{E}_{\boldsymbol{k}n}-\mu)}\right) B^n_{ij}(\boldsymbol{k}) \right] , \tag{4.55}$$

where V is the unit cell volume, $f(\mathcal{E}_{\boldsymbol{k}n})$ is the Fermi distribution function with the band energy $\mathcal{E}_{\boldsymbol{k}n}$, $\beta = 1/(k_{\mathrm{B}}T)$, and μ is the chemical potential. The intrinsic scattering-independent nature of Eq. (4.55) is encoded in the $\boldsymbol{k}$-dependent quantities A^n_{ij} and B^n_{ij} that hinge on matrix elements of the torque and velocity operators:

$$A^n_{ij}(\boldsymbol{k}) = -\mathrm{Im} \sum_{m \neq n} \frac{\langle u_{\boldsymbol{k}n} | \mathcal{T}_i | u_{\boldsymbol{k}m} \rangle \langle u_{\boldsymbol{k}m} | \hbar v_j(\boldsymbol{k}) | u_{\boldsymbol{k}n} \rangle}{\mathcal{E}_{\boldsymbol{k}n} - \mathcal{E}_{\boldsymbol{k}m}} \,, \tag{4.56}$$

and

$$B^n_{ij}(\boldsymbol{k}) = -2\mathrm{Im} \sum_{m \neq n} \frac{\langle u_{\boldsymbol{k}n} | \mathcal{T}_i | u_{\boldsymbol{k}m} \rangle \langle u_{\boldsymbol{k}m} | \hbar v_j(\boldsymbol{k}) | u_{\boldsymbol{k}n} \rangle}{(\mathcal{E}_{\boldsymbol{k}n} - \mathcal{E}_{\boldsymbol{k}m})^2} \,, \tag{4.57}$$

which is the momentum- and band-resolved mixed Berry curvature.

In order to elucidate the deep geometric origin of Eq. (4.55), we rewrite again the torque operator as gradient of the Hamiltonian with respect to the magnetization direction, *i.e.*, $\boldsymbol{\mathcal{T}} = \hat{\boldsymbol{m}} \times (\partial H/\partial \hat{\boldsymbol{m}})$, and represent the magnetization direction as $\hat{\boldsymbol{m}} = (\cos\varphi \sin\theta, \sin\varphi \sin\theta, \cos\theta)$ using the azimuthal angle φ and the polar angle θ shown in Fig. 4.5. Based on these definitions, we obtain at zero temperature an alternative formulation of the spiralization in terms of derivatives of the wave functions with respect to the crystal momentum and the magnetization direction:

$$\begin{aligned} D_{ij} &= \frac{1}{N_{\boldsymbol{k}} V} \sum_{\boldsymbol{k}n}^{\text{occ}} \left[A_{ij}^n(\boldsymbol{k}) - (\mathcal{E}_{\boldsymbol{k}n} - \mathcal{E}_{\mathrm{F}}) B_{ij}^n(\boldsymbol{k}) \right] \\ &= \frac{\hat{\boldsymbol{e}}_i}{N_{\boldsymbol{k}} V} \cdot \operatorname{Im} \sum_{\boldsymbol{k}n}^{\text{occ}} \left[\hat{\boldsymbol{m}} \times \left\langle \frac{\partial u_{\boldsymbol{k}n}}{\partial \hat{\boldsymbol{m}}} \middle| H_{\boldsymbol{k}} + \mathcal{E}_{\boldsymbol{k}n} - 2\mathcal{E}_{\mathrm{F}} \middle| \frac{\partial u_{\boldsymbol{k}n}}{\partial k_j} \right\rangle \right] \\ &= \frac{\hat{\boldsymbol{e}}_i}{N_{\boldsymbol{k}} V} \cdot \operatorname{Im} \sum_{\boldsymbol{k}n}^{\text{occ}} \left[\hat{\boldsymbol{e}}_\varphi \left\langle \frac{\partial u_{\boldsymbol{k}n}}{\partial \theta} \middle| h_{\boldsymbol{k}n} \middle| \frac{\partial u_{\boldsymbol{k}n}}{\partial k_j} \right\rangle - \frac{\hat{\boldsymbol{e}}_\theta}{\sin\theta} \left\langle \frac{\partial u_{\boldsymbol{k}n}}{\partial \varphi} \middle| h_{\boldsymbol{k}n} \middle| \frac{\partial u_{\boldsymbol{k}n}}{\partial k_j} \right\rangle \right] , \end{aligned} \tag{4.58}$$

where the sum is restricted to all occupied states, μ was replaced with the Fermi level $\mathcal{E}_{\mathrm{F}}$, and $h_{\boldsymbol{k}n} = (H_{\boldsymbol{k}} + \mathcal{E}_{\boldsymbol{k}n} - 2\mathcal{E}_{\mathrm{F}})$. Obviously, the DMI spiralization tensor exhibits a manifestly geometric contribution originating from the adiabatic Hamiltonian evolution of the ferromagnetic system under slow variations of the crystal momentum and the magnetization direction. Notably, the Berry phase expression (4.58) is strongly reminiscent of Eq. (4.34) that lays out the modern theory of orbital magnetization, leading us to refer analogously to the above formalism as the *modern theory* of DMI. However, as compared to Eq. (4.34), one of the momentum derivatives was substituted with the derivative of the wave function with respect to the magnetization direction.

In passing, we note that antidamping torkance and DMI spiralization are mutually connected via the non-trivial geometry of the mixed phase space of $\boldsymbol{k}$ and $\hat{\boldsymbol{m}}$ just like intrinsic anomalous Hall conductivity and orbital magnetization are related.

Using the energy-resolved torkance $\vartheta_{ij}(\mathcal{E})$ given by Eq. (4.47), we may express the spiralization tensor at zero temperature in Kubo linear-response theory as [28]

$$D_{ij} = \frac{1}{eV} \int (\mathcal{E} - \mathcal{E}_{\mathrm{F}}) \vartheta_{ij}(\mathcal{E}) \, \mathrm{d}\mathcal{E} \, , \tag{4.59}$$

which underlines the intimate correlation with (parts of) the torkance tensor that is given in the Kubo formalism by Eq. (4.48). Due to the prefactor $(\mathcal{E} - \mathcal{E}_{\mathrm{F}})$ the Fermi surface terms in the energy-resolved torkance do not contribute, and we are left with

$$D_{ij} = \frac{1}{hV} \int_{-\infty}^{\mathcal{E}_{\mathrm{F}}} (\mathcal{E} - \mathcal{E}_{\mathrm{F}}) \operatorname{Re} \operatorname{Tr} \left\langle \mathcal{T}_i G^{\mathrm{R}}(\mathcal{E}) v_j \frac{\mathrm{d}G^{\mathrm{R}}(\mathcal{E})}{\mathrm{d}\mathcal{E}} - \mathcal{T}_i \frac{\mathrm{d}G^{\mathrm{R}}(\mathcal{E})}{\mathrm{d}\mathcal{E}} v_j G^{\mathrm{R}}(\mathcal{E}) \right\rangle \mathrm{d}\mathcal{E} \, . \tag{4.60}$$

To model the effect of disorder, we extend this Kubo expression of the spiralization tensor in the clean limit such that the eigenstate representation of the retarded Green function G^{R} includes a constant band broadening Γ. This yields the following formula describing the disorder dependence of the DMI spiralization (see Appendix B):

$$
\begin{aligned}
D_{ij} = \frac{\hbar}{2\pi N_{\boldsymbol{k}} V} \sum_{\boldsymbol{k}n} \sum_{m\neq n} \operatorname{Im} \left[\langle u_{\boldsymbol{k}n} | \mathcal{T}_i | u_{\boldsymbol{k}m} \rangle \langle u_{\boldsymbol{k}m} | v_j(\boldsymbol{k}) | u_{\boldsymbol{k}n} \rangle \right] \\
\times \left[\frac{\mathcal{E}_{\boldsymbol{k}n} + \mathcal{E}_{\boldsymbol{k}m} - 2\mathcal{E}_{\mathrm{F}}}{(\mathcal{E}_{\boldsymbol{k}n} - \mathcal{E}_{\boldsymbol{k}m})^2} \operatorname{Im} \log \frac{\mathcal{E}_{\boldsymbol{k}m} - \mathcal{E}_{\mathrm{F}} - i\Gamma}{\mathcal{E}_{\boldsymbol{k}n} - \mathcal{E}_{\mathrm{F}} - i\Gamma} - \frac{2\Gamma}{(\mathcal{E}_{\boldsymbol{k}n} - \mathcal{E}_{\boldsymbol{k}m})^2} \operatorname{Re} \log \frac{\mathcal{E}_{\boldsymbol{k}m} - \mathcal{E}_{\mathrm{F}} - i\Gamma}{\mathcal{E}_{\boldsymbol{k}n} - \mathcal{E}_{\mathrm{F}} - i\Gamma} \right],
\end{aligned}
\tag{4.61}
$$

where the summation is not restricted to the occupied manifold but has to be performed in principle over all electronic states. In the clean limit of $\Gamma \to 0^+$, the second term in Eq. (4.61) vanishes as a consequence of which the scattering-independent Berry phase expression (4.58) is recovered as proven in Appendix B. Since time reversal inverts not only the magnetization but transforms also $\langle u_{\boldsymbol{k}n} | \mathcal{T}_i | u_{\boldsymbol{k}m} \rangle$ into $(\langle u_{\boldsymbol{k}n} | \mathcal{T}_i | u_{\boldsymbol{k}m} \rangle)^*$ and $\langle u_{\boldsymbol{k}m} | v_j(\boldsymbol{k}) | u_{\boldsymbol{k}n} \rangle$ into $-(\langle u_{\boldsymbol{k}m} | v_j(\boldsymbol{k}) | u_{\boldsymbol{k}n} \rangle)^*$, the DMI spiralization tensor is even in the magnetization direction just like the antidamping torkance $\tau_{ij}^{\mathrm{even}}$.

4.4 Geometric effects due to real-space curvature

Time reversal and spatial inversion constitute generally the two primary symmetry operations that govern the emergence of the relativistic phenomena introduced in this chapter. Hence, non-centrosymmetric bulk magnets and thin magnetic heterostructures are ideal candidates to study anomalous charge or spin transport, orbital magnetism, current-induced magnetization switching, and chiral exchange interactions in a single system. These crystals are prototypical representatives of the material class of *chiral magnets* that lack both time and spatial inversions, resulting often in twisted magnetic textures in real space (*e.g.*, spin spirals or magnetic skyrmions), which emanate from non-zero chiral interactions. As a consequence, chiral magnets feature naturally real-space Berry phases that root in the curvature $\Omega^{\boldsymbol{rr}}$ of the underlying complex phase space and manifest ultimately in unique texture-driven transport properties of chiral magnets such as the *topological Hall effect* [150,166,167].

For example, when an electron propagates through the slowly varying magnetic structure of a large skyrmion in a thin magnetic film, its spin follows adiabatically the local magnetization of the texture if the exchange coupling is strong enough. Effectively, the impact of the non-collinear magnetic structure can be represented as an emergent magnetic field that affects the electron's dynamics and changes the electrical response of the system. To achieve such a mapping onto an effective problem in electrodynamics, the topological charge or skyrmion winding number is conventionally employed:

$$
n_{\mathrm{sk}} = \frac{1}{4\pi} \int \hat{\boldsymbol{m}}(\boldsymbol{r}) \cdot \left[\frac{\partial \hat{\boldsymbol{m}}(\boldsymbol{r})}{\partial x} \times \frac{\partial \hat{\boldsymbol{m}}(\boldsymbol{r})}{\partial y} \right] \mathrm{d}x \mathrm{d}y \,, \tag{4.62}
$$

where $\hat{\boldsymbol{m}}(\boldsymbol{r})$ is the spatially varying magnetization direction of the texture, and the integration is performed in the xy film plane. Using Eq. (4.62), one can predict the magnitude of the fictitious magnetic field originating from the smooth magnetic structure as well as the induced topological Hall signal. In Chapter 6, we follow analogous ideas to interpret unconventional orbital magnetism based on the emergent magnetic field of chiral magnetic structures but on a discrete lattice.

Chapter 5

Wannier functions

Contents

In this chapter, we present an alternative and practical representation of the electronic structure in terms of so-called Wannier functions (WFs) that enable us to determine efficiently the electronic structure at any point in the phase space of crystal momentum. Emphasizing the mutual influence of gauge choice of the Bloch states and real-space localization of WFs, we discuss the Marzari-Vanderbilt algorithm to obtain maximally-localized Wannier functions (MLWFs), and outline a routinely employed implementation of this scheme. Finally, we motivate the accurate interpolation of the electronic structure as well as of transport and magnetic properties based on the constructed MLWFs.

5.1 Basic definition and properties

The electronic structure of periodic crystals is commonly represented by single-particle Bloch waves $|\psi_{\boldsymbol{k}n}\rangle = \mathrm{e}^{\mathrm{i}\boldsymbol{k}\cdot\boldsymbol{r}}|u_{\boldsymbol{k}n}\rangle$ that diagonalize the Hamiltonian and the lattice translation operators simultaneously [61]. As a consequence of their delocalized wave character in real space, however, Bloch states obstruct the development of an intuitive picture of local chemical and physical processes that underlie, for example, the nature of crystal bonding. In addition, Bloch waves are not well-suited to describe efficiently phenomena that originate from local electron correlations or other spatially localized entities such as impurities.

In contrast to the Bloch representation of the electronic structure, localized Wannier functions (WFs) as introduced by Gregory Wannier [31] are a conceptual extension of orthogonal atomic orbitals to the case of solids, which allows us to grasp the chemist's notion of atomic bonds in the context of condensed-matter physics. Likewise, the concept of electric polarization, which relates to the Berry phase in the language of Bloch states, acquires a transparent interpretation based on the displacement of the centers of WFs. From a more technical perspective, WFs are attractive since they are adapted ideally to describe rapidly decaying interactions in real space[1], and

---

[1] For example, screened short-ranged electron-electron interactions can be represented efficiently using the localized WFs, resulting in sparse matrices as compared to the Bloch basis.

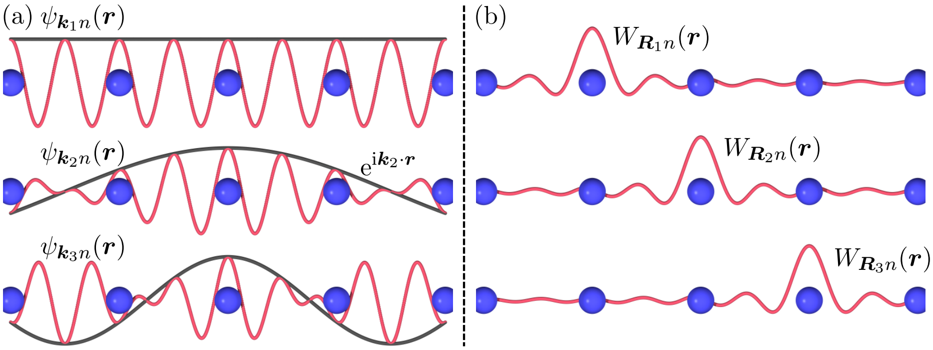

Figure 5.1: Real-space representation of the electronic structure of a periodic crystal in terms of (a) Bloch functions $\psi_{\boldsymbol{k}n}(\boldsymbol{r})$ and (b) Wannier functions $W_{\boldsymbol{R}n}(\boldsymbol{r})$ for various values of the crystal momentum $\boldsymbol{k}$ and the direct lattice vector $\boldsymbol{R}$. While the Bloch states are delocalized in real space, the localized Wannier functions exhibit well-defined centers. The black lines in (a) indicate the phase factor $e^{i\boldsymbol{k}\cdot\boldsymbol{r}}$ of the Bloch functions. Figure inspired by [168].

thereby enable us to efficiently formulate the electronic structure problem in such a situation. Figure 5.1 compares schematically the fundamentally different behavior of Bloch states and WFs in real space. The WF $|W_{\boldsymbol{R}n}\rangle$ of the nth isolated energy band is a discrete Fourier transformation of the according Bloch state:

$$W_{\boldsymbol{R}n}(\boldsymbol{r}) = \frac{1}{N_{\boldsymbol{k}}} \sum_{\boldsymbol{k}} e^{-i\boldsymbol{k}\cdot\boldsymbol{R}} \psi_{\boldsymbol{k}n}(\boldsymbol{r})\,, \tag{5.1}$$

where $\boldsymbol{R}$ is a real-space lattice vector, the summation runs over crystal momenta from the first Brillouin zone, and $N_{\boldsymbol{k}}$ denotes the number of $\boldsymbol{k}$-points.

Several remarks regarding the properties of these functions are in order. While the Bloch states are normalized with respect to the unit cell, the WFs form an orthonormal basis over the so-called *super cell*, which has the volume $N_{\boldsymbol{k}}V$ of $N_{\boldsymbol{k}}$ unit cells:

$$\langle W_{\boldsymbol{R}n} | W_{\boldsymbol{R}'m}\rangle = \int_{N_{\boldsymbol{k}}V} W^*_{\boldsymbol{R}n}(\boldsymbol{r}) W_{\boldsymbol{R}'m}(\boldsymbol{r})\, d^3r = \delta_{\boldsymbol{R}\boldsymbol{R}'}\delta_{nm}\,, \tag{5.2}$$

which is beneficial for expressing the Hamiltonian in the Wannier basis. Already Gregory Wannier was well aware of the importance of the orthogonality to represent the electronic structure: “It would no doubt be more satisfactory for insulating crystals, to discuss the Hamiltonian using atomic functions. But this line of attack has been hampered by the fact that atomic functions are not orthogonal” [31]. Furthermore, WFs inherit their real-space periodicity from the Bloch states, *i.e.*, if $|W_{\boldsymbol{R}n}\rangle$ is translated by the super-cell vector $\boldsymbol{L}$, its functional form is unaffected:

$$\mathcal{T}_{\boldsymbol{L}} W_{\boldsymbol{R}n}(\boldsymbol{r}) = W_{\boldsymbol{R}n}(\boldsymbol{r}+\boldsymbol{L}) = W_{\boldsymbol{R}n}(\boldsymbol{r})\,, \tag{5.3}$$

where the action of the translation operator $\mathcal{T}_{\boldsymbol{L}}$ shifts the position argument of the WF. Since the Wannier basis is a unitary transformation of the Bloch states, it is easy to show that $\langle \boldsymbol{r}|W_{\boldsymbol{R}n}\rangle$ can be interpreted as the translated reference WF $\langle \boldsymbol{r}+\boldsymbol{R}|W_{\boldsymbol{0}n}\rangle$:

$$\mathcal{T}_{\boldsymbol{R}} W_{\boldsymbol{0}n}(\boldsymbol{r}) = W_{\boldsymbol{0}n}(\boldsymbol{r}+\boldsymbol{R}) = W_{\boldsymbol{R}n}(\boldsymbol{r})\,. \tag{5.4}$$

At the core of the efficient description of the electronic structure is the presumably most striking property of WFs, that is, their localization in a certain unit cell as indicated by the real-space label $\boldsymbol{R}$. Starting with the seminal work by Kohn [169] on solutions of the one-dimensional Schrödinger equation, studies of these localization properties [170–173] have proven the existence of exponentially localized WFs in topologically trivial insulators[2], for which the Bloch states evolve smoothly in reciprocal space. This statement about the Wannier basis can be formalized as $\lim_{r\to\infty} W_{\mathbf{0}n}(\boldsymbol{r})\mathrm{e}^{\alpha r} = 0$, where α is a strictly positive constant. In metallic systems and insulators with non-zero Chern number, however, the optimally localized WFs of the group of occupied bands display only a polynomial decay with the distance r due to topological obstructions [173].

As the Bloch states of isolated energy bands are only defined up to an arbitrary phase, Eq. (5.1) does not provide a unique set of WFs. In fact, while no physical effects are altered when multiplying the Bloch states by the phase $\mathrm{e}^{\mathrm{i}\varphi_{\boldsymbol{k}}}$, where $\varphi_{\boldsymbol{k}}$ is an analytic real-valued function of the crystal momentum, the localization properties of the Wannier basis are usually affected drastically by this *gauge transformation.* In the case of an isolated group of M energy bands – also called composite band – the gauge transformation of the Bloch states is mediated by the unitary $M \times M$ matrix $U^{(\boldsymbol{k})}$ such that Eq. (5.1) generalizes to

$$W_{\boldsymbol{R}n}(\boldsymbol{r}) = \frac{1}{N_{\boldsymbol{k}}} \sum_{\boldsymbol{k}} \sum_{m=1}^{M} \mathrm{e}^{-\mathrm{i}\boldsymbol{k}\cdot\boldsymbol{R}} U^{(\boldsymbol{k})}_{mn} \psi_{\boldsymbol{k}m}(\boldsymbol{r})\,. \tag{5.5}$$

In the case of entangled energy bands that do not form an isolated group, the transformation matrix $U^{(\boldsymbol{k})}$ becomes in general rectangular (and thus non-unitary) since the number of Bloch states at $\boldsymbol{k}$ can be larger than the target number of WFs. Choosing a smoother gauge for the Bloch states in reciprocal space implies that the WFs become more localized in real space due to fundamental properties of the Fourier transformation.

5.2 Maximally-localized Wannier functions

Despite the mathematically proven and widely accepted existence of strongly localized WFs, they were hardly used in practice to support electronic structure theory as systematic methods to construct a unique Wannier basis with good localization properties were elusive until the late 1990's. Only then, tremendous progress towards practical applications of WFs was made by Marzari and Vanderbilt [174], who developed the notion of maximally-localized Wannier functions (MLWFs). In order to treat not only composite but also entangled energy bands adequately, the notion of MLWFs was later extended by Souza, Marzari and Vanderbilt [175]. Leading to a unique Wannier basis set, the imposed constraint of maximal localization fixes an optimally smooth gauge for the Bloch states. The spatial extent, or, spread of the

---

[2] In these systems, the exponentially localized WFs are real-valued (expect for a global phase) if the Hamiltonian is real, *e.g.*, in absence of spin-orbit coupling.

WFs is given by the sum of their second moments

$$\Omega = \sum_n \left[\langle W_{\mathbf{0}n}|\boldsymbol{r}^2|W_{\mathbf{0}n}\rangle - \langle W_{\mathbf{0}n}|\boldsymbol{r}|W_{\mathbf{0}n}\rangle^2\right] = \sum_n \left[\langle \boldsymbol{r}^2\rangle_n - \langle \boldsymbol{r}\rangle_n^2\right] , \tag{5.6}$$

where $\langle\cdot\rangle_n = \langle W_{\mathbf{0}n}| \cdot |W_{\mathbf{0}n}\rangle$ is the expectation value with respect to the nth reference WF, and the sum runs over all Wannier orbitals that are constructed from the considered group of energy bands. While the spatial extent (5.6) depends on the gauge transformation $U^{(\boldsymbol{k})}$ via Eq. (5.5), the sum of the Wannier centers $\langle \boldsymbol{r}\rangle_n$ is gauge-invariant modulo a lattice translation in the case of an isolated manifold of Bloch bands. The optimal gauge choice is obtained by minimizing the spread of the WFs, which reveals remarkable equivalence to the definition of Boy's localized orbitals known in quantum chemistry [176, 177].

The iterative minimization algorithm proposed by Marzari and Vanderbilt translates the real-space spread (5.6) into an expression in reciprocal space using the identities [174, 178]

$$\langle W_{\boldsymbol{R}n}|\boldsymbol{r}|W_{\mathbf{0}m}\rangle = \mathrm{i}\frac{V}{(2\pi)^3}\int_{\mathrm{BZ}} \mathrm{e}^{\mathrm{i}\boldsymbol{k}\cdot\boldsymbol{R}}\langle u^{(\mathrm{W})}_{\boldsymbol{k}n}|\nabla_{\boldsymbol{k}} u^{(\mathrm{W})}_{\boldsymbol{k}m}\rangle \,\mathrm{d}^3k\,, \tag{5.7}$$

$$\langle W_{\boldsymbol{R}n}|\boldsymbol{r}^2|W_{\mathbf{0}m}\rangle = -\frac{V}{(2\pi)^3}\int_{\mathrm{BZ}} \mathrm{e}^{\mathrm{i}\boldsymbol{k}\cdot\boldsymbol{R}}\langle u^{(\mathrm{W})}_{\boldsymbol{k}n}|\nabla^2_{\boldsymbol{k}} u^{(\mathrm{W})}_{\boldsymbol{k}m}\rangle \,\mathrm{d}^3k\,, \tag{5.8}$$

where the integration is over the whole Brillouin zone, and $|u^{(\mathrm{W})}_{\boldsymbol{k}n}\rangle = \sum_m U^{(\boldsymbol{k})}_{mn}|u_{\boldsymbol{k}m}\rangle$ stands for the evolution of the lattice-periodic part of the Bloch state during the iterative refinement of the gauge transformation. While these identities hold in the continuum-limit, in practice, relations for uniform but discrete $\boldsymbol{k}$-meshes are needed. This is achieved by replacing the gradients in Eqs. (5.7) and (5.8) with finite-difference expressions [174], which result in practical identities that rely on the overlaps between the lattice-periodic parts of the Bloch states at nearest-neighboring points $\boldsymbol{k}$ and $\boldsymbol{k}+\boldsymbol{b}$:

$$M^{(\boldsymbol{k},\boldsymbol{b})}_{mn} = \langle u_{\boldsymbol{k}m}|u_{\boldsymbol{k}+\boldsymbol{b}n}\rangle\,. \tag{5.9}$$

Based on these overlaps, which are an input provided by first-principles methods, the key ingredients in Eq. (5.6) evaluate to[3]

$$\langle \boldsymbol{r}\rangle_n = -\frac{1}{N_{\boldsymbol{k}}}\sum_{\boldsymbol{k}\boldsymbol{b}} w_b \boldsymbol{b}\,\mathrm{Im}\ln \tilde{M}^{(\boldsymbol{k},\boldsymbol{b})}_{nn}\,, \tag{5.10}$$

and

$$\langle \boldsymbol{r}^2\rangle_n = \frac{1}{N_{\boldsymbol{k}}}\sum_{\boldsymbol{k}\boldsymbol{b}} w_b \left[1 - \left|\tilde{M}^{(\boldsymbol{k},\boldsymbol{b})}_{nn}\right|^2 + \left(\mathrm{Im}\ln \tilde{M}^{(\boldsymbol{k},\boldsymbol{b})}_{nn}\right)^2\right] , \tag{5.11}$$

---

[3] Although the expressions are non-unique as many finite-difference formulas approximate the gradient $\nabla_{\boldsymbol{k}}$ correctly up to first order in $\boldsymbol{b}$, the ones used here display desirable transformation properties when shifting the WFs [174]. To render the finite differences precise to first order, the bond weights w_b need to satisfy the condition $\sum_{\boldsymbol{b}} w_b b_\alpha b_\beta = \delta_{\alpha\beta}$, which accounts for the underlying lattice structure.

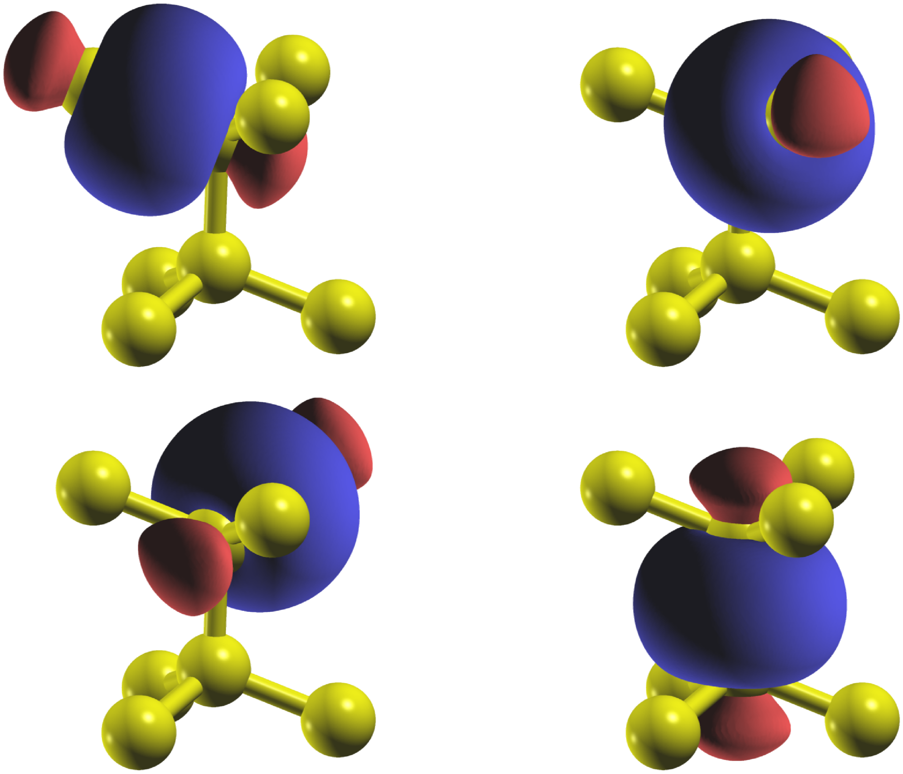

Figure 5.2: The maximally-localized Wannier functions extracted from the four valence bands of diamond reveal the covalent nature of the chemical bonding between the carbon atoms (yellow spheres). Red and blue colors denote positive and negative isosurface values, respectively.

where the bond weight w_b associated with $\boldsymbol{b} = b\hat{\boldsymbol{b}}$ originates from the finite-difference approximation of the gradient $\nabla_{\boldsymbol{k}}$, and the overlap matrix is updated during the iterative minimization process according to

$$\tilde{M}^{(\boldsymbol{k},\boldsymbol{b})}_{mn} = \sum_{m'n'} \left[U^{(\boldsymbol{k})}_{m'm} \right]^{*} M^{(\boldsymbol{k},\boldsymbol{b})}_{m'n'} U^{(\boldsymbol{k})}_{n'n} \, . \tag{5.12}$$

The efficient procedure suggested by Marzari and Vanderbilt is implemented in the scientific computer code WANNIER90 [179] that uses a steepest-descent algorithm to minimize the spread (5.6). In this thesis, the FLEUR interface [180] with WANNIER90 is employed to obtain the necessary input for the minimization process. Besides the overlaps $M^{(\boldsymbol{k},\boldsymbol{b})}_{mn}$, the WANNIER90 program expects as an input the projections $A^{(\boldsymbol{k})}_{mn} = \langle \Psi_{\boldsymbol{k}m} | g_n \rangle$ of the Bloch states onto localized trial orbitals $|g_n\rangle$, which are essential to construct so-called first-guess WFs as a starting point for the optimization process. Based on these projections, the Löwdin transformations of the reference states $\sum_m A^{(\boldsymbol{k})}_{mn} |\psi_{\boldsymbol{k}m}\rangle$ are plugged into Eq. (5.1) to set up an initial set of WFs. Usually, the trial orbitals are chosen as atomic-like orbitals centered around the ionic positions. Although the first-guess Wannier basis hinges on the trial orbitals, it converges ideally to the unique set of MLWFs during the steepest descent, irrespective of the initial choice for $|g_n\rangle$. Instead of arriving at the global spread minimum, however, the localization procedure may get trapped in local minima if the first-guess WFs are not optimal. To improve the convergence and reduce the effort in finding the global minimum considerably, the trial orbitals should be chosen deliberately to be as close as possible to the expected MLWFs. Figure 5.2 illustrates as an example the covalent MLWFs of diamond that originate from the four valence energy bands.

Finally, we remark that after the maximal localization procedure has been carried out with the WANNIER90 code, the resulting MLWFs might not exhibit all of the crystal symmetries. While this originates from the implemented minimization algorithm rather than physical effects and has frequently no severe consequences, it can manifest in a more involved analysis of electronic properties in certain systems, *e.g.*, in topological insulators. An approach to overcome this numerical problem is to reinstate the full crystal symmetries via so-called symmetry-adapted Wannier functions [181].

5.3 Wannier interpolation

5.3.1 Band structure

The Wannier interpolation, Fig. 5.3, is a classic technique to extract efficiently single-particle operators such as the Hamiltonian at any desired point in reciprocal space, even though the key ingredients of this scheme – namely, the MLWFs – are constructed only from a coarse sampling of the Brillouin zone. To motivate the seemingly miraculous performance of this interpolation, it is rewarding to scrutinize the relation between Eq. (5.1) and its extension to the continuum limit, which assumes the form

$$\mathcal{W}_{\boldsymbol{R}n}(\boldsymbol{r}) = \frac{V}{(2\pi)^3} \int_{\mathrm{BZ}} \mathrm{e}^{-\mathrm{i}\boldsymbol{k}\cdot\boldsymbol{R}} \psi^{(\mathrm{W})}_{\boldsymbol{k}n}(\boldsymbol{r})\, \mathrm{d}^3 k\,, \tag{5.13}$$

where the integration is performed over the first Brillouin zone of the crystal, and the superscript “W” is used to indicate that the gauge transformation is hidden in $|\psi^{(\mathrm{W})}_{\boldsymbol{k}n}\rangle$. As the Fourier transformation is invertible, the Bloch state can be determined at any $\boldsymbol{k}$-point once the “true” orbital $|\mathcal{W}_{\boldsymbol{R}n}\rangle$ is known, by using the inverse of Eq. (5.13):

$$\psi^{(\mathrm{W})}_{\boldsymbol{k}n}(\boldsymbol{r}) = \sum_{\boldsymbol{R}} \mathrm{e}^{\mathrm{i}\boldsymbol{k}\cdot\boldsymbol{R}} \mathcal{W}_{\boldsymbol{R}n}(\boldsymbol{r})\,, \tag{5.14}$$

with the infinite sum running over all lattice vectors $\boldsymbol{R}$. The surprising performance of the Wannier interpolation roots now in the central observation that the shape of the Wannier orbital $|W_{\boldsymbol{R}n}\rangle$ defined by Eq. (5.1) converges rapidly to the “true” function (5.13) with an increasing but discrete number of $\boldsymbol{k}$-points entering in the construction of $|W_{\boldsymbol{R}n}\rangle$. Since the function $|\mathcal{W}_{\boldsymbol{R}n}\rangle$ is approximated excellently by its little sister $|W_{\boldsymbol{R}n}\rangle$, the Bloch state in Eq. (5.14) can be obtained in principle at any $\boldsymbol{k}$-point based just on the electronic-structure information known on the coarse mesh. However, a minor difference between the two types of orbitals $|\mathcal{W}_{\boldsymbol{R}n}\rangle$ and $|W_{\boldsymbol{R}n}\rangle$ is that the latter functions display by construction spurious periodic images (see Eq. (5.3)). In order to establish the equivalence with the “true” functions, these well-separated

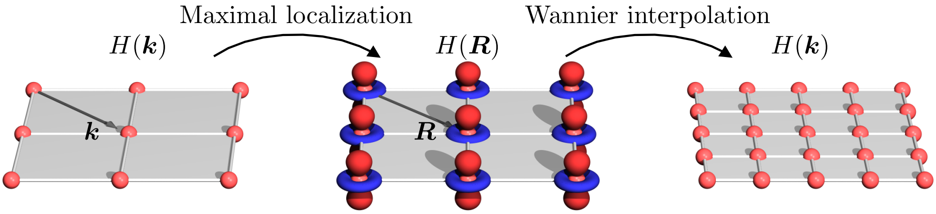

Figure 5.3: Illustration of the Wannier interpolation scheme. Starting from the electronic structure as encoded in the Hamiltonian $H(\boldsymbol{k})$ on a coarse $\boldsymbol{k}$-grid, we construct Wannier functions that are localized in real space at the positions $\boldsymbol{R}$. Using these functions to represent efficiently the electronic structure in terms of the hoppings $H(\boldsymbol{R})$, we obtain ultimately the Hamiltonian on a much denser mesh of $\boldsymbol{k}$-points via an inverse Fourier transformation. Figure inspired by [168].

images need to be cut away in practice, for example, by setting $|W_{\boldsymbol{R}n}\rangle$ to zero in all but one super cell.

Starting from the Kohn-Sham eigenvalues $\mathcal{E}_{\boldsymbol{k}n}$ that are known on the coarse first-principles mesh, we can deduce the single-particle Hamiltonian on an ultra-dense interpolation mesh via the Wannier interpolation. The matrix elements of the Hamiltonian in the Wannier basis, which are also referred to as *hoppings*[4], read

$$H_{nm}(\boldsymbol{R}) = \langle W_{\boldsymbol{0}n}|H|W_{\boldsymbol{R}m}\rangle = \frac{1}{N_{\boldsymbol{k}}}\sum_{\boldsymbol{k}} \mathrm{e}^{-\mathrm{i}\boldsymbol{k}\cdot\boldsymbol{R}} \left[U^{(\boldsymbol{k})}_{n'n}\right]^* \mathcal{E}_{\boldsymbol{k}n'} U^{(\boldsymbol{k})}_{n'm}\,, \tag{5.15}$$

where $U^{(\boldsymbol{k})}$ carries the maximal-localization gauge, and the sum runs over the coarse grid that samples the Brillouin zone. As a consequence of the translational symmetry of the system, the hoppings depend only on the distance vector $\boldsymbol{R}$, which separates the two Wannier orbitals. With increasing distance $|\boldsymbol{R}|$, the matrix elements (5.15) decay swiftly since the MLWFs are strongly localized in real space and do not overlap appreciably. By applying an inverse Fourier transformation, we arrive at

$$H^{(\mathrm{W})}_{nm}(\boldsymbol{k}) = \langle u^{(\mathrm{W})}_{\boldsymbol{k}n}|H_{\boldsymbol{k}}|u^{(\mathrm{W})}_{\boldsymbol{k}m}\rangle = \sum_{\boldsymbol{R}} \mathrm{e}^{\mathrm{i}\boldsymbol{k}\cdot\boldsymbol{R}} H_{nm}(\boldsymbol{R})\,, \tag{5.16}$$

which interpolates the single-particle Hamiltonian for any arbitrary point $\boldsymbol{k}$ even if this point is not contained in the original coarse mesh used to construct the MLWFs. Although the finite sum in Eq. (5.16) takes into consideration all lattice vectors, it can be performed even more efficiently by keeping in mind that the hoppings decay rapidly with distance. The sought interpolated band energies $\mathcal{E}_{\boldsymbol{k}n}$ are found by diagonalization of the Hamiltonian:

$$\langle u^{(\mathrm{H})}_{\boldsymbol{k}n}|H_{\boldsymbol{k}}|u^{(\mathrm{H})}_{\boldsymbol{k}m}\rangle = \left[V^{(\boldsymbol{k})\dagger} H^{(\mathrm{W})}(\boldsymbol{k}) V^{(\boldsymbol{k})}\right]_{nm} = \mathcal{E}_{\boldsymbol{k}n}\delta_{nm}\,, \tag{5.17}$$

where $V^{(\boldsymbol{k})}$ is the unitary matrix of eigenstates $|u^{(\mathrm{H})}_{\boldsymbol{k}n}\rangle = \sum_m |u^{(\mathrm{W})}_{\boldsymbol{k}m}\rangle V^{(\boldsymbol{k})}_{mn}$. The interpolation is guaranteed to reproduce exactly the Kohn-Sham eigenvalues at all points

---

[4] The explicit tight-binding formulation $H = \sum_{\boldsymbol{R}\boldsymbol{R}'}\sum_{nn'} H_{nn'}(\boldsymbol{R}-\boldsymbol{R}')|W_{\boldsymbol{R}n}\rangle\langle W_{\boldsymbol{R}'n'}|$ of the Hamiltonian emphasizes the role of Eq. (5.15) as hopping integral between localized orbitals.

contained in the original coarse mesh. If this initial mesh is fine enough, for example, an $8 \times 8 \times 8$ grid of $\boldsymbol{k}$-points, then the Wannier interpolation is very accurate. As the technique represents the Hamiltonian with a strongly reduced number of basis functions as compared to the complete full-potential linearized augmented-plane-wave (FLAPW) basis set, this method is profoundly efficient: in fact, the Wannier interpolation can provide the electronic structure with an accuracy of first-principles methods at the computational cost of a tight-binding approach.

The Wannier interpolation emphasizes the fundamental role of nearest-neighbor interactions for the electronic structure in a spirit similar to the Slater-Koster interpolation that is based on the linear combination of atomic orbitals (LCAO) method [182]. However, in sharp contrast to the Wannier interpolation, the approach by Slater and Koster resorts to disposable parameters[5] to approximate the most relevant hopping integrals.

5.3.2 Intrinsic anomalous Hall conductivity

Apart from an interpolation of the single-particle Hamiltonian, the Wannier method facilitates the calculation of transport properties since it provides an efficient means to extract analytically the gradient of the interpolated Hamiltonian, Eq. (5.16), with respect to the crystal momentum:

$$\nabla_{\boldsymbol{k}} H^{(\mathrm{W})}_{nm}(\boldsymbol{k}) = \sum_{\boldsymbol{R}} \mathrm{i}\boldsymbol{R}\mathrm{e}^{\mathrm{i}\boldsymbol{k}\cdot\boldsymbol{R}} H_{nm}(\boldsymbol{R})\,. \tag{5.18}$$

By supplementing this information with matrix elements of the position operator in the Wannier basis, we can compute the velocity operator properly and thereby access geometric properties of the underlying momentum phase space as determined by Eq. (4.28). Consequently, it is not surprising that a scheme to evaluate efficiently the pure Berry curvature $\Omega^{\boldsymbol{kk}}_{ij}$ of all occupied states as well as the scattering-independent contribution to the anomalous Hall conductivity σ_{ij} has been suggested [183, 184]. The computation of these quantities foots primarily on the *ab initio* band energies and the overlaps $M^{(\boldsymbol{k},\boldsymbol{b})}_{mn}$ that enter already in the construction of MLWFs. As we review the proposed scheme later in Section 7.4 against a much broader background, we remark at this stage only that the Wannier technique is particularly valuable as it achieves easily an ultradense sampling of the Brillouin zone, which is desirable when integrating the Berry curvature in Eq. (4.31).

5.3.3 Orbital magnetization

Clearly, the same benefits apply as well to the Wannier interpolation of the orbital magnetization (OM) in the modern theory, Eq. (4.34), for which an according computational machinery has been established in Ref. [184]. While we generalize this framework explicitly to the chiral exchange interaction in Section 7.4, we briefly point out here the origins of the scheme and the main ingredients that are required

---

[5] The Slater-Koster parameters are adjusted by fitting the first-principles bands at high-symmetry points or determined from group theory, revealing an at least to some extent universal character of these parameters.

to calculate the OM from first-principles theory. For this purpose, we start from the definitions $\mathcal{P}(\boldsymbol{k}) = \sum_n^{\mathrm{occ}} |u_{\boldsymbol{k}n}\rangle\langle u_{\boldsymbol{k}n}|$ and $\mathcal{Q}(\boldsymbol{k}) = \sum_n^{\mathrm{unocc}} |u_{\boldsymbol{k}n}\rangle\langle u_{\boldsymbol{k}n}|$ of the projection operators onto the occupied and unoccupied manifold of the electronic Hilbert space, respectively. Constituting a complete basis set (which implies that $\mathcal{P} + \mathcal{Q} = 1$), the lattice-periodic states $|u_{\boldsymbol{k}n}\rangle$ satisfy the relation

$$\mathrm{Im}\sum_n^{\mathrm{occ}}\sum_m \langle\partial_i u_{\boldsymbol{k}n}|u_{\boldsymbol{k}m}\rangle\langle u_{\boldsymbol{k}m}|\partial_j u_{\boldsymbol{k}n}\rangle = \mathrm{Im}\sum_n^{\mathrm{occ}}\sum_m^{\mathrm{unocc}} \langle\partial_i u_{\boldsymbol{k}n}|u_{\boldsymbol{k}m}\rangle\langle u_{\boldsymbol{k}m}|\partial_j u_{\boldsymbol{k}n}\rangle\,, \tag{5.19}$$

where $\partial_i = \partial/\partial k_i$. Following the derivations in Refs. [25,184], we can rewrite thus the momentum Berry curvature of the occupied states as well as Eqs. (4.35) and (4.36) for the OM to arrive at

$$\Omega_{ij}^{\boldsymbol{kk}} = -2\mathrm{Im}\sum_n^{\mathrm{occ}}\langle\partial_i u_{\boldsymbol{k}n}|\partial_j u_{\boldsymbol{k}n}\rangle = -2\mathrm{Im}\mathcal{F}_{ij}\,, \tag{5.20}$$

$$\boldsymbol{m}_{\mathrm{lc}} = -\frac{e}{2\hbar}\int[\mathrm{d}k]\;[-2\mathrm{Im}(\mathcal{G}_{ij} - \mathcal{E}_{\mathrm{F}}\mathcal{F}_{ij})]\,, \tag{5.21}$$

$$\boldsymbol{m}_{\mathrm{ic}} = -\frac{e}{2\hbar}\int[\mathrm{d}k]\;[-2\mathrm{Im}(\mathcal{H}_{ij} - \mathcal{E}_{\mathrm{F}}\mathcal{F}_{ij})]\,. \tag{5.22}$$

Here, we introduced the $\boldsymbol{k}$-dependent and antisymmetric tensors $\mathcal{F}_{ij}$, $\mathcal{G}_{ij}$, and $\mathcal{H}_{ij}$ that are further gauge-invariant as they are given by the trace of the projection operators and the Hamiltonian over the full Hilbert space of electronic wave functions:

$$\mathcal{F}_{ij} = \mathrm{Tr}\left[(\partial_i\mathcal{P})\mathcal{Q}(\partial_j\mathcal{P})\right]\,, \tag{5.23}$$

$$\mathcal{G}_{ij} = \mathrm{Tr}\left[(\partial_i\mathcal{P})\mathcal{Q}H_{\boldsymbol{k}}\mathcal{Q}(\partial_j\mathcal{P})\right]\,, \tag{5.24}$$

$$\mathcal{H}_{ij} = \mathrm{Tr}\left[H_{\boldsymbol{k}}(\partial_i\mathcal{P})\mathcal{Q}(\partial_j\mathcal{P})\right]\,. \tag{5.25}$$

Although these equations are manifestly invariant with respect to the gauge choice, it is particularly convenient to evaluate them in the Wannier gauge of non-orthogonal states $|u_{\boldsymbol{k}n}^{(\mathrm{W})}\rangle$. The resulting expressions [184] are formally identical to those in Chapter 7 for the chiral exchange interaction, Eqs. (7.69)–(7.71), and allow for investigating orbital magnetism by means of the efficient Wannier scheme. While the interpolation of the anomalous Hall effect reckons on band energies and wave-function overlaps as the main input from *ab initio*, the Wannier interpolation of the OM relies on additional matrix elements that need to be provided by the first-principles code:

$$\langle u_{\boldsymbol{k}+\boldsymbol{b}_1 n}|H_{\boldsymbol{k}}|u_{\boldsymbol{k}+\boldsymbol{b}_2 m}\rangle\,, \tag{5.26}$$

where the Hamiltonian at $\boldsymbol{k}$ is sandwiched between wave functions at different neighboring points $\boldsymbol{k}+\boldsymbol{b}_1$ and $\boldsymbol{k}+\boldsymbol{b}_2$. The following subsection presents the computationally demanding FLAPW implementation of these important quantities that underlie the interpolation of the Berry phase theory of orbital magnetism in periodic solids, which is achieved accurately only if the ingredients (5.26) are accounted for.

5.3.4 Orbital magnetism within FLAPW

We elucidate the FLAPW implementation of the matrix elements $\langle u_{\boldsymbol{k}+\boldsymbol{b}_1 n}|H_{\boldsymbol{k}}|u_{\boldsymbol{k}+\boldsymbol{b}_2 m}\rangle$ that are necessary ingredients to interpolate the OM according to its modern Berry phase theory. The lattice-periodic states $|u_{\boldsymbol{k}n}\rangle$ are eigenstates of $H_{\boldsymbol{k}} = \mathrm{e}^{-\mathrm{i}\boldsymbol{k}\cdot\boldsymbol{r}} H \mathrm{e}^{\mathrm{i}\boldsymbol{k}\cdot\boldsymbol{r}}$, where H is the first-principles Hamiltonian of the considered system, and $\boldsymbol{k}+\boldsymbol{b}_1$ and $\boldsymbol{k}+\boldsymbol{b}_2$ are neighboring points of $\boldsymbol{k}$. Already at this stage, we stress that it is not sufficient for the accurate computation of the above matrix elements to resort to the eigenstate representation $H_{\boldsymbol{k}} = \sum_n \mathcal{E}_{\boldsymbol{k}n} |u_{\boldsymbol{k}n}\rangle\langle u_{\boldsymbol{k}n}|$, where $\mathcal{E}_{\boldsymbol{k}n}$ are the band energies. Since the computationally accessible set of states $|u_{\boldsymbol{k}n}\rangle$ is only of finite size, a projection error would inevitably be the consequence of using this approach in setting up the overlaps. In order to overcome this challenge, we derive in the following explicit computational expressions for the matrix elements that assume in the basis of the Bloch states $|\psi_{\boldsymbol{k}n}\rangle = \mathrm{e}^{\mathrm{i}\boldsymbol{k}\cdot\boldsymbol{r}}|u_{\boldsymbol{k}n}\rangle$ the form

$$\langle u_{\boldsymbol{k}+\boldsymbol{b}_1 n}|H_{\boldsymbol{k}}|u_{\boldsymbol{k}+\boldsymbol{b}_2 m}\rangle = \langle \psi_{[\boldsymbol{k}+\boldsymbol{b}_1]n}|\mathrm{e}^{\mathrm{i}\boldsymbol{b}_1\cdot\boldsymbol{r}} H \mathrm{e}^{-\mathrm{i}\boldsymbol{b}_2\cdot\boldsymbol{r}}|\psi_{[\boldsymbol{k}+\boldsymbol{b}_2]m}\rangle\,, \tag{5.27}$$

where $[\boldsymbol{k}] = \boldsymbol{k} - \boldsymbol{G}(\boldsymbol{k})$ and $\boldsymbol{G}(\boldsymbol{k})$ folds back $\boldsymbol{k}$ to the first Brillouin zone. According to the FLAPW methodology, different regions in real space contribute to Eq. (5.27).

Interstitial region The Hamiltonian consists of the symmetrized kinetic energy and the potential $V(\boldsymbol{r})$ in the interstitial region:

$$H(\boldsymbol{r}) = -\frac{1}{4}\left(\overset{\Leftarrow}{\Delta} + \overset{\Rightarrow}{\Delta}\right) + V(\boldsymbol{r})\,, \tag{5.28}$$

where the Laplacians $\overset{\Leftarrow}{\Delta}$ and $\overset{\Rightarrow}{\Delta}$ act to the left and to the right, respectively. Adapted to the physics in the interstitial region, the wave functions can be expanded into plane waves with wave vector $\boldsymbol{G}$ and expansion coefficients $c^{\boldsymbol{G}}_{\boldsymbol{k}n}$:

$$\psi_{\boldsymbol{k}n}(\boldsymbol{r}) = \frac{1}{\sqrt{V}} \sum_{\boldsymbol{G}} c^{\boldsymbol{G}}_{\boldsymbol{k}n} \mathrm{e}^{\mathrm{i}(\boldsymbol{k}+\boldsymbol{G})\cdot\boldsymbol{r}}\,. \tag{5.29}$$

After introducing the abbreviations $\boldsymbol{\mathcal{K}} = \boldsymbol{k}+\boldsymbol{G}-\boldsymbol{G}(\boldsymbol{k}+\boldsymbol{b}_1)$, $\boldsymbol{\mathcal{K}}' = \boldsymbol{k}+\boldsymbol{G}'-\boldsymbol{G}(\boldsymbol{k}+\boldsymbol{b}_2)$, and $\boldsymbol{\mathcal{G}} = \boldsymbol{\mathcal{K}}' - \boldsymbol{\mathcal{K}}$, we arrive at a suitable computational expression for the interstitial contribution to Eq. (5.27):

$$\begin{aligned}\langle u_{\boldsymbol{k}+\boldsymbol{b}_1\,n}|H_{\boldsymbol{k}}|u_{\boldsymbol{k}+\boldsymbol{b}_2\,m}\rangle &= \frac{1}{V}\sum_{\boldsymbol{G}\boldsymbol{G}'} \left(c^{\boldsymbol{G}}_{\boldsymbol{k}+\boldsymbol{b}_1 n}\right)^* c^{\boldsymbol{G}'}_{\boldsymbol{k}+\boldsymbol{b}_2 m} \int_{\mathrm{int}} \mathrm{e}^{-\mathrm{i}\boldsymbol{\mathcal{K}}\cdot\boldsymbol{r}} H(\boldsymbol{r})\, \mathrm{e}^{\mathrm{i}\boldsymbol{\mathcal{K}}'\cdot\boldsymbol{r}}\,\mathrm{d}\boldsymbol{r} \\ &= \sum_{\boldsymbol{G}\boldsymbol{G}'} \left(c^{\boldsymbol{G}}_{\boldsymbol{k}+\boldsymbol{b}_1 n}\right)^* c^{\boldsymbol{G}'}_{\boldsymbol{k}+\boldsymbol{b}_2 m} \left\{\frac{\boldsymbol{\mathcal{K}}^2 + \boldsymbol{\mathcal{K}}'^2}{4}\Theta(\boldsymbol{\mathcal{G}}) + V(\boldsymbol{\mathcal{G}})\right\}\,. \end{aligned} \tag{5.30}$$

Here, $V(\boldsymbol{\mathcal{G}})$ and $\Theta(\boldsymbol{\mathcal{G}})$ are the Fourier transformations of the interstitial potential and the step function that cuts out the interstitial region, respectively:

$$V(\boldsymbol{\mathcal{G}}) = \frac{1}{V}\int_{\mathrm{int}} \mathrm{e}^{\mathrm{i}\boldsymbol{\mathcal{G}}\cdot\boldsymbol{r}}\, V(\boldsymbol{r})\,\mathrm{d}\boldsymbol{r}\,, \qquad \Theta(\boldsymbol{\mathcal{G}}) = \frac{1}{V}\int_{\mathrm{int}} \mathrm{e}^{\mathrm{i}\boldsymbol{\mathcal{G}}\cdot\boldsymbol{r}}\,\mathrm{d}\boldsymbol{r}\,, \tag{5.31}$$

with the integration over real space restricted to the interstitial.

Muffin tins In the muffin-tin spheres, the wave functions are given by

$$\psi_{\boldsymbol{k}n}(\boldsymbol{r}) = \sum_{L\mu} \left[A^{\mu}_{Ln}(\boldsymbol{k}) u^{\mu}_{l}(r_\mu) + B^{\mu}_{Ln}(\boldsymbol{k}) \dot{u}^{\mu}_{l}(r_\mu)\right] Y_L(\hat{\boldsymbol{r}}_\mu)\,, \tag{5.32}$$

where L stands for the angular momentum quantum numbers (l, m), and $\boldsymbol{r}_\mu$ is the position vector relative to the μth muffin tin. The wave functions u^μ_l are chosen as eigenstates of the spherical term of the muffin-tin Hamiltonian, and $\dot{u}^\mu_l$ is the energy derivative of u^μ_l. In total, the muffin-tin Hamiltonian H consists of a spherical part with $l = 0$ (including the kinetic energy), the non-spherical potential (terms with $l \neq 0$), and the spin-orbit interaction that corresponds formally also to $l = 0$. In the following paragraphs, we consider each of these individual contributions to the overlaps $\langle u_{\boldsymbol{k}+\boldsymbol{b}_1 n}|H_{\boldsymbol{k}}|u_{\boldsymbol{k}+\boldsymbol{b}_2 m}\rangle$. But before, we write down the general expressions for these matrix elements in the muffin tins:

$$\begin{aligned}\langle u_{\boldsymbol{k}+\boldsymbol{b}_1 n}|H_{\boldsymbol{k}}|u_{\boldsymbol{k}+\boldsymbol{b}_2 m}\rangle = \sum_{LL'}\sum_{\mu}\Big\{ & \left(A^\mu_{Ln}(\boldsymbol{k}+\boldsymbol{b}_1)\right)^* A^\mu_{L'm}(\boldsymbol{k}+\boldsymbol{b}_2) I^{\mu,uu}_{LL'}(\boldsymbol{b}_1,\boldsymbol{b}_2) \\ & + \left(A^\mu_{Ln}(\boldsymbol{k}+\boldsymbol{b}_1)\right)^* B^\mu_{L'm}(\boldsymbol{k}+\boldsymbol{b}_2) I^{\mu,u\dot{u}}_{LL'}(\boldsymbol{b}_1,\boldsymbol{b}_2) \\ & + \left(B^\mu_{Ln}(\boldsymbol{k}+\boldsymbol{b}_1)\right)^* A^\mu_{L'm}(\boldsymbol{k}+\boldsymbol{b}_2) I^{\mu,\dot{u}u}_{LL'}(\boldsymbol{b}_1,\boldsymbol{b}_2) \\ & + \left(B^\mu_{Ln}(\boldsymbol{k}+\boldsymbol{b}_1)\right)^* B^\mu_{L'm}(\boldsymbol{k}+\boldsymbol{b}_2) I^{\mu,\dot{u}\dot{u}}_{LL'}(\boldsymbol{b}_1,\boldsymbol{b}_2)\Big\}\,,\end{aligned} \tag{5.33}$$

where

$$I^{\mu,uu}_{LL'}(\boldsymbol{b}_1,\boldsymbol{b}_2) = \int Y^*_L(\hat{\boldsymbol{r}}_\mu) \mathrm{e}^{\mathrm{i}\boldsymbol{b}_1\cdot\boldsymbol{r}} u^\mu_l(r_\mu) H(\boldsymbol{r}_\mu) Y_{L'}(\hat{\boldsymbol{r}}_\mu) \mathrm{e}^{-\mathrm{i}\boldsymbol{b}_2\cdot\boldsymbol{r}} u^\mu_{l'}(r_\mu)\,\mathrm{d}\boldsymbol{r}_\mu\,, \tag{5.34}$$

$$I^{\mu,u\dot{u}}_{LL'}(\boldsymbol{b}_1,\boldsymbol{b}_2) = \int Y^*_L(\hat{\boldsymbol{r}}_\mu) \mathrm{e}^{\mathrm{i}\boldsymbol{b}_1\cdot\boldsymbol{r}} u^\mu_l(r_\mu) H(\boldsymbol{r}_\mu) Y_{L'}(\hat{\boldsymbol{r}}_\mu) \mathrm{e}^{-\mathrm{i}\boldsymbol{b}_2\cdot\boldsymbol{r}} \dot{u}^\mu_{l'}(r_\mu)\,\mathrm{d}\boldsymbol{r}_\mu\,, \tag{5.35}$$

with the muffin-tin Hamiltonian H, the spherical harmonic Y_L, and analogously for the other I-coefficients. To evaluate explicitly the above integrals, we use the well-known Rayleigh expansion[6] for the plane-wave factors $\mathrm{e}^{\mathrm{i}\boldsymbol{b}_1\cdot\boldsymbol{r}}$ and $\mathrm{e}^{-\mathrm{i}\boldsymbol{b}_2\cdot\boldsymbol{r}}$ that yields, *e.g.*, for the coefficient $I^{\mu,uu}$ the following:

$$\begin{aligned}I^{\mu,uu}_{LL'}(\boldsymbol{b}_1,\boldsymbol{b}_2) = {} & (4\pi)^2 \mathrm{e}^{\mathrm{i}(\boldsymbol{b}_1-\boldsymbol{b}_2)\cdot\boldsymbol{\tau}_\mu} \sum_{\bar{L}\bar{L}'} (-1)^{\bar{l}'} \mathrm{i}^{\bar{l}+\bar{l}'} Y_{\bar{L}}(\hat{\boldsymbol{b}}_1) Y_{\bar{L}'}(\hat{\boldsymbol{b}}_2) \\ & \times \int Y^*_L(\hat{\boldsymbol{r}}_\mu) Y^*_{\bar{L}}(\hat{\boldsymbol{r}}_\mu) u^\mu_l(r_\mu) j_{\bar{l}}(b_1 r_\mu) H(\boldsymbol{r}_\mu) Y_{L'}(\hat{\boldsymbol{r}}_\mu) Y^*_{\bar{L}'}(\hat{\boldsymbol{r}}_\mu) u^\mu_{l'}(r_\mu) j_{\bar{l}'}(b_2 r_\mu)\,\mathrm{d}\boldsymbol{r}_\mu\,,\end{aligned} \tag{5.36}$$

where j_l is the spherical Bessel function, and $\boldsymbol{\tau}_\mu$ is the position of the μth ion. When introducing the so-called Gaunt coefficients $G_{L_1L_2L_3} = \int Y^*_{L_1} Y_{L_2} Y_{L_3} \mathrm{d}\Omega$ as the angular integral of three spherical harmonics, we can recast the product of Y_{L_2} and Y_{L_3} using the spherical harmonic Y_{L_1}:

$$\begin{aligned}I^{\mu,uu}_{LL'}(\boldsymbol{b}_1,\boldsymbol{b}_2) = {} & (4\pi)^2 \mathrm{e}^{\mathrm{i}(\boldsymbol{b}_1-\boldsymbol{b}_2)\cdot\boldsymbol{\tau}_\mu} \sum_{\bar{L}\bar{L}'} (-1)^{\bar{l}'} \mathrm{i}^{\bar{l}+\bar{l}'} Y_{\bar{L}}(\hat{\boldsymbol{b}}_1) Y_{\bar{L}'}(\hat{\boldsymbol{b}}_2) \sum_{\mathcal{L}\mathcal{L}'} G_{\mathcal{L}L\bar{L}} G_{L'\bar{L}'\mathcal{L}'} \\ & \times \int Y^*_{\mathcal{L}}(\hat{\boldsymbol{r}}_\mu) u^\mu_l(r_\mu) j_{\bar{l}}(b_1 r_\mu) H(\boldsymbol{r}_\mu) Y_{\mathcal{L}'}(\hat{\boldsymbol{r}}_\mu) u^\mu_{l'}(r_\mu) j_{\bar{l}'}(b_2 r_\mu)\,\mathrm{d}\boldsymbol{r}_\mu\,,\end{aligned} \tag{5.37}$$

and similar expressions follow for the other I-coefficients. We note that the above formula contains summations with respect to the four angular momentum variables

---

[6] The Rayleigh expansion reads $\mathrm{e}^{\mp\mathrm{i}\boldsymbol{b}\cdot\boldsymbol{r}} = 4\pi\mathrm{e}^{\mp\mathrm{i}\boldsymbol{b}\cdot\boldsymbol{\tau}_\mu}\sum_L(\mp1)^l\mathrm{i}^l j_l(r_\mu b) Y_L(\hat{\boldsymbol{b}})\left(Y_L(\hat{\boldsymbol{r}}_\mu)\right)^*$, where $\boldsymbol{\tau}_\mu$ is the position of the μth atom and j_l is the spherical Bessel function.

$\bar{L}$, $\bar{L}'$, $\mathcal{L}$, and $\mathcal{L}'$, which renders the evaluation of the muffin-tin contribution to Eq. (5.27) computationally demanding. Consequently, exploiting the constraints on these quantum numbers set by the Gaunt coefficients is crucial.

Spherical muffin-tin Hamiltonian Computing the integrals I for the spherical part of the Hamiltonian H would be straightforward if both $\boldsymbol{b}_1$ and $\boldsymbol{b}_2$ were zero since the wave functions u_l are eigenstates of the spherical Hamiltonian. However, the integration contains in general also the spherical Bessel functions that stem from finite $\boldsymbol{b}_1$ and $\boldsymbol{b}_2$. Therefore, we need to calculate explicitly the necessary matrix elements in the scalar-relativistic approximation, in which the spherical Hamiltonian assumes the form (see also Section 3.3)

$$H_{\mathrm{sph}} u_l = H_l u_l = \begin{pmatrix} \frac{1}{2m}\frac{l(l+1)}{r_\mu^2} + V(r_\mu) & -\frac{2c}{r_\mu} - c\frac{\partial}{\partial r_\mu} \\ c\frac{\partial}{\partial r_\mu} & -2m_0c^2 + V(r_\mu) \end{pmatrix} \begin{pmatrix} f_l \\ g_l \end{pmatrix} . \tag{5.38}$$

Here, f_l and g_l are the large and small component of the wave function u_l, respectively, $V(r_\mu)$ is the spherically averaged potential, $m = m_0 + (E_l - V(r_\mu))/(2c^2)$, $c \approx 1/137$, and $m_0 = 1$. Since the spherical term may only couple spherical harmonics to the very same angular momentum, it follows that

$$\begin{aligned} I^{\mu,uu}_{LL'}(\boldsymbol{b}_1, \boldsymbol{b}_2) = (4\pi)^2 \mathrm{e}^{\mathrm{i}(\boldsymbol{b}_1 - \boldsymbol{b}_2)\cdot\boldsymbol{\tau}_\mu} \sum_{\bar{L}\bar{L}'} (-1)^{\bar{l}'} \mathrm{i}^{\bar{l}+\bar{l}'} Y_{\bar{L}}(\hat{\boldsymbol{b}_1}) Y_{\bar{L}'}(\hat{\boldsymbol{b}_2}) \sum_{\mathcal{L}} G_{\mathcal{L}L\bar{L}} G_{L'\bar{L}'\mathcal{L}} \\ \times \int r_\mu^2\, u^\mu_l(r_\mu) j_{\bar{l}}(b_1 r_\mu) H_\ell(r_\mu) u^\mu_{l'}(r_\mu) j_{\bar{l}'}(b_2 r_\mu)\, \mathrm{d}r_\mu \, , \end{aligned} \tag{5.39}$$

where ℓ is one of the quantum numbers grouped in $\mathcal{L}$. Since the scalar-relativistic Hamiltonian is not symmetric in the above formulation, we explicitly symmetrize the corresponding radial integrals as follows. The matrix elements (5.27) need to satisfy the conjugation rule $\langle u_n | H_{\boldsymbol{k}} | u_m \rangle = (\langle u_m | H_{\boldsymbol{k}} | u_n \rangle)^*$, which directly implies that

$$I^{\mu,\alpha\beta}_{LL'}(\boldsymbol{b}_1, \boldsymbol{b}_2) = \left(I^{\mu,\beta\alpha}_{L'L}(\boldsymbol{b}_2, \boldsymbol{b}_1) \right)^* , \tag{5.40}$$

where α and β represent u and $\dot{u}$. To guarantee that this relation is satisfied, we explicitly symmetrize the scalar-relativistic Hamiltonian by applying half of it to the right hand-side and half of it to the left hand-side in the radial integrals in Eq. (5.39).

Non-spherical muffin-tin Hamiltonian In the muffin tins, the non-spherical part of the Hamiltonian with $l \neq 0$ assumes the form

$$H_{\mathrm{non}}(\boldsymbol{r}_\mu) = \sum_L^{l\neq 0} V_l(r_\mu) Y_L(\hat{\boldsymbol{r}}_\mu) \, , \tag{5.41}$$

which has to be substituted into Eq. (5.37) to obtain the corresponding contribution to the matrix elements (5.27). As a consequence, the spherical harmonics $Y_{\mathcal{L}}$ and $Y_{\mathcal{L}'}$ to different angular momenta are now coupled in Eq. (5.37), which manifests in a substantially increased computational effort as compared to the spherical term. This becomes also obvious from the final expression that contains three Gaunt coefficients:

$$I^{\mu,uu}_{LL'}(\boldsymbol{b}_1,\boldsymbol{b}_2) = (4\pi)^2 \mathrm{e}^{\mathrm{i}(\boldsymbol{b}_1-\boldsymbol{b}_2)\cdot\boldsymbol{\tau}_\mu} \sum_{\bar{L}\bar{L}'} (-1)^{\bar{l}'} \mathrm{i}^{\bar{l}+\bar{l}'} Y_{\bar{L}}(\hat{\boldsymbol{b}_1}) Y_{\bar{L}'}(\hat{\boldsymbol{b}_2}) \sum_{\mathcal{L}\mathcal{L}'} \sum_{\tilde{L}}^{\tilde{l}\neq 0} G_{\mathcal{L}L\bar{L}} G_{L'\bar{L}'\mathcal{L}'} G_{\mathcal{L}\mathcal{L}'\tilde{L}} \\ \times \int r_\mu^2\, u^\mu_l(r_\mu) j_{\bar{l}}(b_1 r_\mu) V_{\tilde{l}}(r_\mu) u^\mu_{l'}(r_\mu) j_{\bar{l}'}(b_2 r_\mu)\, \mathrm{d}r_\mu\,. \tag{5.42}$$

Contribution from the spin-orbit interaction The overall shape of the spin-orbit Hamiltonian is formally equivalent to the spherical term in coupling only spherical harmonics with the same angular momentum l:

$$H_{\mathrm{so}}(\boldsymbol{r}_\mu) = H_{\mathrm{so}}(r_\mu) = V_{\mathrm{so}}(r_\mu)\boldsymbol{L}\cdot\boldsymbol{S}\,. \tag{5.43}$$

Substituting this Hamiltonian into Eq. (5.37) leads to the spin-orbit contribution to the matrix elements that underlie the interpolation of orbital magnetism:

$$I^{\mu,uu}_{LL'}(\boldsymbol{b}_1,\boldsymbol{b}_2) = (4\pi)^2 \mathrm{e}^{\mathrm{i}(\boldsymbol{b}_1-\boldsymbol{b}_2)\cdot\boldsymbol{\tau}_\mu} \sum_{\bar{L}\bar{L}'} (-1)^{\bar{l}'} \mathrm{i}^{\bar{l}+\bar{l}'} Y_{\bar{L}}(\hat{\boldsymbol{b}_1}) Y_{\bar{L}'}(\hat{\boldsymbol{b}_2}) \sum_{\mathcal{L}\mathcal{L}'} G_{\mathcal{L}L\bar{L}} G_{L'\bar{L}'\mathcal{L}'} \left[\boldsymbol{L}\cdot\boldsymbol{S}\right]^{\sigma\sigma'}_{\mathcal{L}\mathcal{L}'} \\ \times \int r_\mu^2\, u^\mu_l(r_\mu) j_{\bar{l}}(b_1 r_\mu) V_{\mathrm{so}}(r_\mu) u^\mu_{l'}(r_\mu) j_{\bar{l}'}(b_2 r_\mu)\, \mathrm{d}r_\mu\,, \tag{5.44}$$

where σ and σ' refer to the spin[7] of u_l and $u_{l'}$, respectively, and $[\boldsymbol{L}\cdot\boldsymbol{S}]^{\sigma\sigma'}_{\mathcal{L}\mathcal{L}'}$ stands for the matrix elements $\langle\mathcal{L}\sigma|\boldsymbol{L}\cdot\boldsymbol{S}|\mathcal{L}'\sigma'\rangle$ of the spin-orbit interaction between spin and angular momentum eigenstates $|\mathcal{L}\sigma\rangle$. Thus, the sets of quantum numbers $\mathcal{L}$ and $\mathcal{L}'$ can only differ in their magnetic quantum number (*e.g.*, m and m') but not in the angular momentum ℓ.

Vacuum contribution in film calculations When treating truly two-dimensional geometries, additional vacua are introduced that contribute also the the matrix elements (5.27). The corresponding wave functions assume the form (see also Section 3.2)

$$\psi_{\boldsymbol{k}+\boldsymbol{b}n}(\boldsymbol{r}) = \sum_{\boldsymbol{G}} \left(a^{\boldsymbol{G}n}_{\boldsymbol{k}+\boldsymbol{b}} u^{\boldsymbol{G}_\parallel}_{\boldsymbol{k}+\boldsymbol{b}}(z) + b^{\boldsymbol{G}n}_{\boldsymbol{k}+\boldsymbol{b}} \dot{u}^{\boldsymbol{G}_\parallel}_{\boldsymbol{k}+\boldsymbol{b}}(z) \right) \mathrm{e}^{\mathrm{i}(\boldsymbol{k}+\boldsymbol{b}_\parallel+\boldsymbol{G}_\parallel)\cdot\boldsymbol{x}_\parallel} \mathrm{e}^{\mathrm{i}b_z z} \tag{5.45}$$

where $\boldsymbol{k} = (k_x, k_y, 0)$ is the crystal momentum, and $\boldsymbol{b} = (b_x, b_y, b_z) = (\boldsymbol{b}_\parallel, b_z)$. In the vacuum region, the Hamiltonian is given by

$$H(\boldsymbol{r}) = h(z) + \sum_{\boldsymbol{G}_\parallel \neq \boldsymbol{0}} V_{\boldsymbol{G}_\parallel}(z) \mathrm{e}^{\mathrm{i}\boldsymbol{G}_\parallel\cdot\boldsymbol{x}_\parallel}\,, \tag{5.46}$$

which consists of a non-warping, planar averaged part h and a warping term that relates to $V_{\boldsymbol{G}_\parallel}$. The functions $u^{\boldsymbol{G}_\parallel}_{\boldsymbol{k}}$ are eigenstates of the non-corrugated part that includes the z-dependent potential to $\boldsymbol{G}_\parallel = \boldsymbol{0}$ and the kinetic energy, *i.e.*,

$$h(z) u^{\boldsymbol{G}_\parallel}_{\boldsymbol{k}}(z) = \left[-\frac{1}{2}\frac{\partial^2}{\partial z^2} + V_{\boldsymbol{G}_\parallel=\boldsymbol{0}}(z) + \frac{1}{2}\left(\boldsymbol{G}_\parallel + \boldsymbol{k}\right)^2 \right] = E_{\mathrm{vac}} u^{\boldsymbol{G}_\parallel}_{\boldsymbol{k}}(z)\,, \tag{5.47}$$

---

[7] Note that we suppressed for sake of clarity the dependence of the I-coefficients on the spin indices σ and σ' of the two participating wave functions u^μ_l and $u^\mu_{l'}$ (or their energy derivatives).

and analogously for the energy derivative $\dot{u}_{\boldsymbol{k}}^{\boldsymbol{G}_\parallel}$. Before evaluating the vacuum contribution to the matrix elements (5.27), we symmetrize the action of h such that

$$h(z) \longrightarrow \left[-\frac{1}{4}\left(\overset{\Leftarrow}{\partial}{}_z^2 + \overset{\Rightarrow}{\partial}{}_z^2 \right) + V_{\boldsymbol{G}_\parallel=\boldsymbol{0}}(z) + \frac{1}{4}\left(\boldsymbol{G}_\parallel + \boldsymbol{k} + \boldsymbol{b}_{1\parallel}\right)^2 + \frac{1}{4}\left(\boldsymbol{G}_\parallel + \boldsymbol{k} + \boldsymbol{b}_{2\parallel}\right)^2 \right] . \tag{5.48}$$

Then, the matrix elements (5.27) can be expressed as

$$\begin{aligned} \langle u_{\boldsymbol{k}+\boldsymbol{b}_1 n} | H_{\boldsymbol{k}} | u_{\boldsymbol{k}+\boldsymbol{b}_2 m} \rangle = \sum_{\boldsymbol{G}\boldsymbol{G}'} & \left(a_{\boldsymbol{k}+\boldsymbol{b}_1}^{\boldsymbol{G}n}\right)^* a_{\boldsymbol{k}+\boldsymbol{b}_2}^{\boldsymbol{G}'m} \mathcal{I}^{uu}_{\boldsymbol{G}_\parallel \boldsymbol{G}'_\parallel}(\boldsymbol{b}_1, \boldsymbol{b}_2) + \left(a_{\boldsymbol{k}+\boldsymbol{b}_1}^{\boldsymbol{G}n}\right)^* b_{\boldsymbol{k}+\boldsymbol{b}_2}^{\boldsymbol{G}'m} \mathcal{I}^{u\dot{u}}_{\boldsymbol{G}_\parallel \boldsymbol{G}'_\parallel}(\boldsymbol{b}_1, \boldsymbol{b}_2) \\ & + \left(b_{\boldsymbol{k}+\boldsymbol{b}_1}^{\boldsymbol{G}n}\right)^* a_{\boldsymbol{k}+\boldsymbol{b}_2}^{\boldsymbol{G}'m} \mathcal{I}^{\dot{u}u}_{\boldsymbol{G}_\parallel \boldsymbol{G}'_\parallel}(\boldsymbol{b}_1, \boldsymbol{b}_2) + \left(b_{\boldsymbol{k}+\boldsymbol{b}_1}^{\boldsymbol{G}n}\right)^* b_{\boldsymbol{k}+\boldsymbol{b}_2}^{\boldsymbol{G}'m} \mathcal{I}^{\dot{u}\dot{u}}_{\boldsymbol{G}_\parallel \boldsymbol{G}'_\parallel}(\boldsymbol{b}_1, \boldsymbol{b}_2) , \end{aligned} \tag{5.49}$$

where we introduced the abbreviation

$$\mathcal{I}^{uu}_{\boldsymbol{G}_\parallel \boldsymbol{G}'_\parallel}(\boldsymbol{b}_1, \boldsymbol{b}_2) = S_\parallel \left[\delta_{\boldsymbol{g}_\parallel \boldsymbol{g}'_\parallel} I_1^{uu} + I_2^{uu} \right] , \tag{5.50}$$

and analogously for the other $\mathcal{I}$-coefficients. Here, $S_\parallel$ is the area of the in-plane unit cell, $\boldsymbol{g}_\parallel = \boldsymbol{G}_\parallel + \boldsymbol{k} - \boldsymbol{G}_\parallel(\boldsymbol{k} + \boldsymbol{b}_1)$, and $\boldsymbol{g}'_\parallel = \boldsymbol{G}'_\parallel + \boldsymbol{k} - \boldsymbol{G}_\parallel(\boldsymbol{k} + \boldsymbol{b}_2)$. The important ingredients I_1 and I_2 are defined by integrals of the vacuum Hamiltonian and the wave functions with additional phases that originate from finite $\boldsymbol{b}_1$ and $\boldsymbol{b}_2$:

$$I_1^{uu} = \int_{\pm D/2}^{\pm\infty} u_{\boldsymbol{G}_\parallel}(\boldsymbol{k} + \boldsymbol{b}_1, z) \mathrm{e}^{\mathrm{i}G_z(\boldsymbol{k}+\boldsymbol{b}_1)z} h(z) u_{\boldsymbol{G}'_\parallel}(\boldsymbol{k} + \boldsymbol{b}_2, z) \mathrm{e}^{-\mathrm{i}G_z(\boldsymbol{k}+\boldsymbol{b}_2)z} \,\mathrm{d}z , \tag{5.51}$$

$$I_2^{uu} = \int_{\pm D/2}^{\pm\infty} u_{\boldsymbol{G}_\parallel}(\boldsymbol{k} + \boldsymbol{b}_1, z) \mathrm{e}^{\mathrm{i}G_z(\boldsymbol{k}+\boldsymbol{b}_1)z} V_{\boldsymbol{g}_z - \boldsymbol{g}'_z}(z) u_{\boldsymbol{G}'_\parallel}(\boldsymbol{k} + \boldsymbol{b}_2, z) \mathrm{e}^{-\mathrm{i}G_z(\boldsymbol{k}+\boldsymbol{b}_2)z} \,\mathrm{d}z , \tag{5.52}$$

where the integration is performed in both vacuum regions above and below the film. Obviously, I_1 relates to the planar averaged Hamiltonian while I_2 roots in the warping part of the potential in the vacuum. Finally, we point out that the treatment of truly one-dimensional geometries in the FLAPW method [185] results in similar computational expressions for the necessary matrix elements (5.27).

Chapter 6

Orbital magnetism in periodic crystals

Contents

Using density functional theory calculations of the electronic structure, we uncover in this chapter the crucial role of the Berry phase theory for a satisfactory description of orbital magnetism in general periodic systems. We compare first a widely applied atom-centered approximation (ACA) to the Berry phase theory in elementary ferromagnets, where the latter formalism improves agreement with experiment. Next, we investigate orbital magnetism in a heterostructure of a manganese monolayer on a tungsten (001) substrate as example of structurally and chemically complex systems, for which using the Berry phase theory is indispensable for a predictive theoretical treatment of orbital magnetism. Approaching the field of topological condensed matter, we reveal then the intimate relation between orbital magnetism and Chern number in topologically non-trivial insulators of magnetically doped Graphene. Ultimately, we discover and elucidate a thoroughly distinct type of orbital magnetism that roots in the emergent field associated with chiral spin textures rather than the conventional spin-orbit mechanism. As an intriguing consequence, we predict the manifestation of giant "topological" orbital ferromagnetism in non-coplanar spin structures without any reference to spin-orbit coupling or strong correlation effects. We conclude with identifying promising material candidates on the basis of symmetry arguments.

The results presented in this chapter have already been published:

J.-P. Hanke, F. Freimuth, A. K. Nandy, H. Zhang, S. Blügel, and Y. Mokrousov
Physical Review B **94**, *121114(R) (2016)*

J.-P. Hanke, F. Freimuth, S. Blügel, and Y. Mokrousov
Scientific Reports **7**, *41078 (2017)*

6.1 Elementary ferromagnets Fe, Co, and Ni

To assess the importance of the modern theory of orbital magnetization (OM) in materials that are relevant to spintronics and spin-orbitronics, we start off with the three elementary bulk ferromagnets bcc Fe, hcp Co, and fcc Ni. In all cases, the magnetization direction is oriented along the experimentally verified easy axis of the system, which is [001] in bcc Fe, [0001] in hcp Co, and [111] in fcc Ni (see Appendix A.1

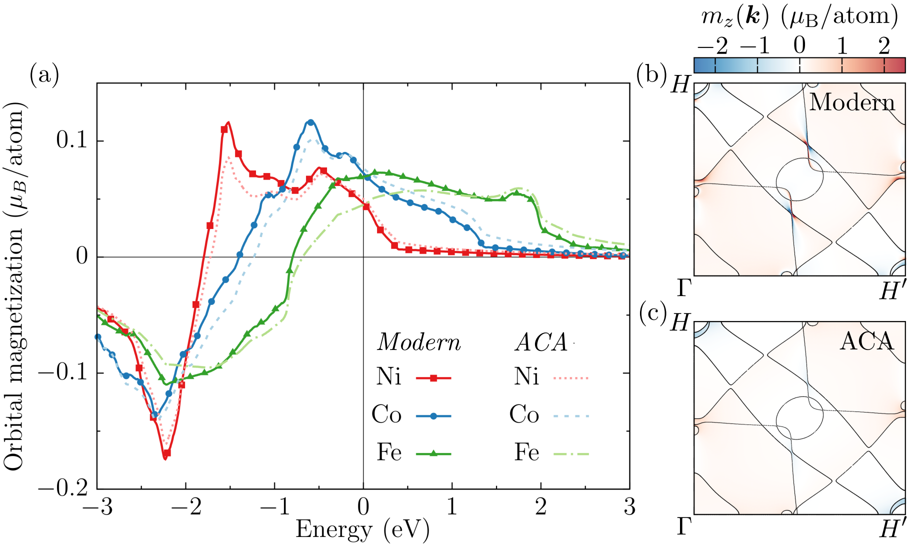

Figure 6.1: (a) Easy-axis orbital magnetization (OM) in the elementary bulk ferromagnets fcc Ni, hcp Co, and bcc Fe, either according to the modern theory (solid lines) or according to the atom-centered approximation (ACA, dashed lines). The OM is given in units of Bohr magneton per atom, and the shift of the Fermi level is measured with respect to the true Fermi energy. (b,c) Distribution of the $\boldsymbol{k}$-resolved OM $m_z(\boldsymbol{k})$ in bcc Fe based on the modern theory and the ACA, where the plane of $k_x = 0$ is considered, and $\Gamma = (000)$, $H = (001)$, and $H'(010)$ in units of 2π over lattice constant.

for comprehensive computational details). We compare in Fig. 6.1 the OM that is obtained from the modern theory to results based on the simple atom-centered approximation (ACA) for varying values of the Fermi level. Among all systems, the quantitative agreement between the two different approaches is rather good, although we notice deviations in Fe that are manifest in the vicinity of the true Fermi level. These discrepancies could possibly be attributed to a larger degree of delocalization of the Bloch wave functions in Fe, the nearly half-filled $3d$ shell of which comprises one electron less than Co and two electrons less than Ni. Thus, non-local orbital currents that are not fully accounted for by the ACA may be expected to yield important contributions to the OM, which gives rise to visible deviations between the ACA and the rigorous Berry phase theory. This indicates that the predictive power of the simple yet routinely employed ACA is limited, and an adequate description of orbital magnetism in solids calls for the modern theory.

Exactly at the Fermi energy of the respective material, the OM along the easy axis amounts to the values shown in Table 6.1. Indeed, applying the Berry phase formalism leads to an improved agreement between the theoretical predictions and experimental values [119] extracted from X-ray magnetic circular dichroism (XMCD) measurements. In particular, the ACA result of $0.045\,\mu_\mathrm{B}$ per Fe atom is corrected by more than 50% in the modern theory to $0.069\,\mu_\mathrm{B}$/atom, which is substantially closer to the

	Easy axis	ACA	Modern theory	Ref. [184]	Experiment [119]
Fe	[001]	0.045	0.069	0.076	0.081
Co	[0001]	0.077	0.073	0.084	0.133
Ni	[111]	0.050	0.046	0.047	0.053

Table 6.1: Orbital magnetization in the elementary bulk ferromagnets bcc Fe, hcp Co, and fcc Ni with the magnetization aligned along the easy axis. Our FLAPW results obtained either in the atom-centered approximation (ACA) or in the modern theory are compared to the Berry phase results based on pseudo potentials [184] as well as to XMCD experiments [119]. All values are given in units of Bohr magneton per atom.

experimental result of $0.081\,\mu_\mathrm{B}$ per Fe atom[1]. As evident from Fig. 6.1(b,c), also the distribution of the momentum-resolved OM in the Brillouin zone (shown here for the plane with $k_x = 0$ of Fe) reflects clear differences between the two approaches. Since the integrated values that we obtain within the full-potential linearized augmented-plane-wave (FLAPW) method agree well for all systems with theoretical calculations that rely on pseudo potentials [184], we are confident that our FLAPW implementation of the Berry phase theory of OM works properly. Nevertheless, the general relevance of the rigorous Berry phase theory for orbital magnetism in solids is still questionable at this stage as the predicted orbital moments on the order of less than $0.08\,\mu_\mathrm{B}$ are largely overshadowed by the spin magnetic moments in the considered ferromagnets, which amount to $2.1\,\mu_\mathrm{B}$ in Fe, $1.5\,\mu_\mathrm{B}$ in Co, and $0.6\,\mu_\mathrm{B}$ in Ni.

6.2 Structurally and chemically complex systems

After studying pristine bulk ferromagnets, we turn now to condensed-matter systems that are heterogeneous with respect to their crystal structure or their chemical composition. In such heterostructures as thin magnetic films, which are perceived to be promising candidates for implementing basic spintronic concepts, the local orbital moments can vary strongly in real space. That is, the orbital moments of adjacent atomic layers can differ drastically or may even compensate each other. Since local contributions to orbital magnetism become small, non-local effects are expected to play a more significant role for the OM in these heterogeneous systems, suggesting that a treatment based on the Berry phase is needed. In order to confirm this intuition, we consider as a prime example of a heterogeneous two-dimensional material the chiral magnet Mn/W(001), which is an inversion-asymmetric slab of a Mn monolayer deposited on nine atomic layers of bcc W. We adopt the computational parameters presented in Appendix A.2, and study orbital magnetism in the collinear ferromagnetic case with magnetization perpendicular to the film plane although Mn/W(001) hosts in reality a long-wavelength chiral spin texture [158].

In sharp contrast to the previously discussed bulk ferromagnets, our first-principles calculations of the out-of-plane OM m_z in Mn/W(001), Fig. 6.2, reveal profound

---

[1] Recall that the technique of XMCD probes the magnetic properties only locally. As we discussed in Chapter 4, it is not sensitive to the itinerant circulation of the OM wherefore deviations between theory and experiment are not surprising.

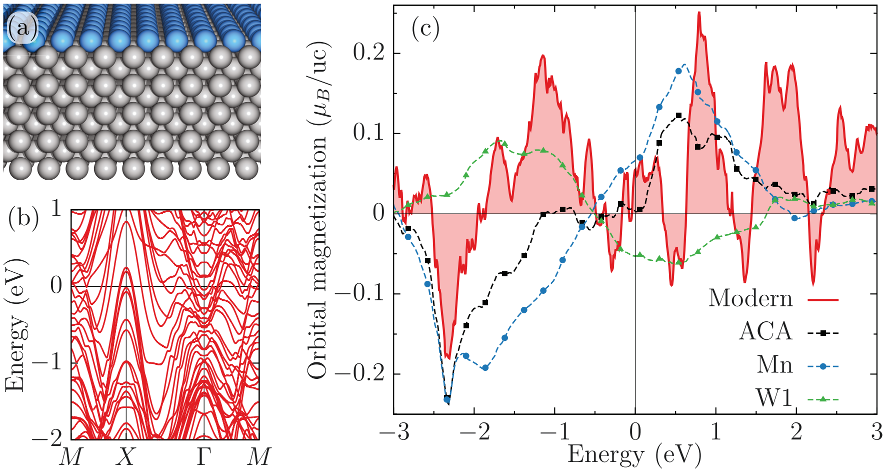

Figure 6.2: (a) Crystal structure and (b) band structure of a Mn monolayer on nine atomic layers of W(001). (c) Orbital magnetization perpendicular to the film plane of Mn/W(001). The dependence of m_z on the position of the Fermi level is presented within the modern theory (red solid line) and the atom-centered approximation (ACA, black squares), where the orbital magnetization is given in units of Bohr magneton per in-plane unit cell. In addition, the local orbital moments in the muffin tins of Mn and the W at the interface (W1) are indicated by blue circles and green triangles, respectively.

discrepancies between the modern theory and the localized picture that is provided by the ACA. Beyond just altering the magnitude of the computed OM, the modern theory predicts even the opposite sign as compared to the ACA over wide regions of energy. Figure 6.2 shows additionally the local orbital moments in the first two layers, *i.e.*, the Mn overlayer and the first layer of W, which dominate the total orbital moment in the ACA. As these local moments nearly cancel, the simple ACA typically underestimates the magnitude of the orbital magnetism in the heterogeneous system. Notably, this oversight is pronounced near the Fermi level where the OM is anticipated to be thoroughly diminished by one order of magnitude as compared to its value in the full Berry phase theory. Still, the OM in the latter approach amounts to a rather small value of merely $0.04\,\mu_\mathrm{B}$ per in-plane unit cell. While magnetism originates primarily from the Mn atoms[2], it is W that grants strong spin-orbit coupling as necessary ingredient to lift the orbital degeneracy in the crystal field. Therefore, contributions from non-local effects become important in order to describe orbital magnetism in Mn/W(001) correctly, as a consequence of which the ACA performs particularly poorly with respect to the Berry phase theory. Finally, we remark that the non-trivial and rapidly oscillating energy dependence of the OM in the modern theory is well known from transport properties that are driven by the Berry curvature in momentum phase space. Such a manifestly complex behavior of the orbital magnetism in magnetic multilayers calls for revisiting our understanding of orbital physics at interfaces and surfaces in general.

---

[2] The magnitude of the magnetic moment induced in W falls off rapidly away from the interface.

6.3 Chern insulators

To continue with our exploration of orbital magnetism in periodic solids, in the following, we reach out to topological states of matter, the hallmarks of which we uncover in the OM. Working towards this ultimate goal, we evaluate first the significance of the modern theory for describing orbital magnetism in two-dimensional Chern insulators that feature topologically non-trivial band gaps in their spectrum. The nature of these gaps is characterized by the integer Chern number $\mathcal{C} = 1/(2\pi) \int \Omega^{\boldsymbol{kk}}_{xy}\, \mathrm{d}k_x \mathrm{d}k_y$, where $\Omega^{\boldsymbol{kk}}_{xy}$ denotes the momentum Berry curvature of all occupied states below the respective gap. It has been shown in previous works [186] that graphene decorated with $5d$ transition-metal adatoms supports strong magneto-electric responses and Chern insulator characteristics due to the spin-orbit interaction. Following these ideas, we consider here the example of ferromagnetically coupled W adatoms with a resulting spin moment of $1.6\,\mu_\mathrm{B}$ deposited in a 4×4 supercell geometry on graphene. Using the computational parameters from Appendix A.3, we place the W adatoms at the hollow sites of free-standing graphene, with the magnetization oriented perpendicular to the film plane, *i.e.*, along the z-axis. The complex hybridization between the d states of W and the p states of graphene induces a global band gap directly at the Fermi level as well as approximately $0.27\,\mathrm{eV}$ below it, both of which arise from the prominent spin-orbit coupling. The topological origin of these gaps manifests in the finite Chern numbers $\mathcal{C} = +2$ and $\mathcal{C} = -2$, respectively, and the corresponding (quantized) anomalous Hall conductivity amounts to $\sigma_{xy} = (e^2/h)\mathcal{C}$. As we discussed earlier in Chapter 4, the out-of-plane component m_z of the OM is expected to satisfy the relation $\mathrm{d}m_z/\mathrm{d}\mathcal{E}_F = (e/h)\mathcal{C}$ in a Chern insulator [123].

Figure 6.3 presents the performance of the Berry phase theory of OM with respect to the simple ACA, where our initial focus lies on the shaded areas that highlight the topologically non-trivial gaps of the Chern insulator. In the modern theory, the out-of-plane OM varies indeed linearly with the Fermi energy, where the slope is determined by the finite Chern number of the corresponding band gap. Remarkably, this even manifests in a characteristic sign change of m_z around the true Fermi level as shown in Fig. 6.3(b). On the other hand, the local probe of ACA fails completely as it anticipates the OM to remain constant throughout the band gaps with non-zero Chern numbers. When replacing the W adatoms with other $5d$ transition metals, for instance Ir, we note that this breakdown of the ACA is not specific to a particular material realization but persists for the band gaps of any Chern insulator, Fig. 6.3(c). Due to the poor predictive power of the ACA as compared to the modern theory, the microscopic distribution of the OM $m_z(\boldsymbol{k})$ in the Brillouin zone is fundamentally distinct within the two approaches as shown in Fig. 6.3(d,e) for the case of W adatoms.

Aside from the topologically non-trivial gaps in the spectrum of these systems, the dependence of m_z on the Fermi level reveals that the local approximation is inferior to the rigorous Berry phase theory over a broad energy range. Similar to the thin magnetic films in the previous section, the ACA tends to underestimate generally the magnitude of orbital magnetism, which amounts to as much as $1.2\,\mu_\mathrm{B}$ per in-plane unit cell in the modern theory. Although spin magnetism and strong spin-orbit coupling originate from the very same species of atoms (here W), non-local effects are still important, especially in the vicinity of the topologically non-trivial gaps as the latter form due to strong mutual interactions between the states of graphene and W.

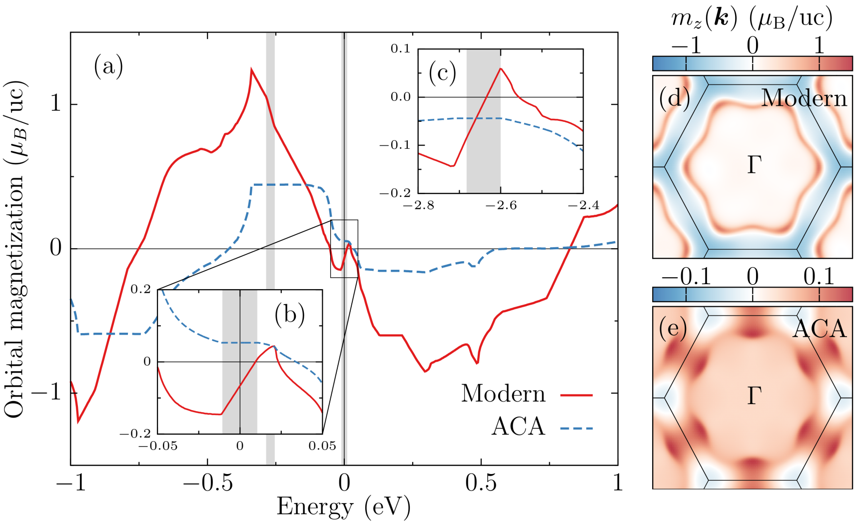

Figure 6.3: (a) Energy dependence of the out-of-plane orbital magnetization m_z in magnetically doped graphene with W adatoms. Red solid lines and blue dashed lines indicate the results based on the modern theory and the atom-centered approximation (ACA), respectively. The gray shaded areas highlight the band gaps with the non-zero Chern numbers $\mathcal{C} = \pm 2$. (b) Zoom to the marked region around the Fermi level. (c) The behavior of m_z for Ir adatoms deposited in 2×2 geometry on graphene reveals unique fingerprints of the topologically complex band gap with $\mathcal{C} = +2$ about 2.65 eV below the Fermi level. (d,e) Distribution of $m_z(\boldsymbol{k})$ in momentum space according to the modern theory and the ACA in the case of W adatoms. Note the different color scales.

Finally, while the Chern number connects orbital magnetism and anomalous Hall effect within band gaps of Chern insulators, we remark that the behavior of OM and anomalous Hall conductivity outside of these energy regions is overall not correlated in the considered realizations of magnetically doped graphene.

6.4 Topological orbital ferromagnetism

In all of the systems discussed so far, the orbital magnetism develops as a direct consequence of the spin-orbit interaction that lifts at least partially the quenching of the orbital moment. On the evidence of the tiny magnitude of the resulting orbital magnetism as compared to the spin magnetism, however, the spin-orbit coupling presents obviously not an efficient mechanism to break the orbital degeneracy in these materials. To realize large orbital moments that can even exceed the spin magnetic moments, we consider in the following magnetic systems with a chiral spin texture, the effect of which can be ascribed to a fictitious magnetic field influencing electrons that propagate through the structure [187,188]. If an electron hops between different lattice sites, its spin follows adiabatically the local direction determined by the underlying spin structure, which can be interpreted as local magnetic fields acting on the electron's spin. As we demonstrate below, depending on the symmetries of the crystal, these local fields either cancel over the unit cell or add up to a net magnetic field. Without referring to the spin-orbit interaction or any electron correlations, this magnetic field may manifest in a *topological orbital moment* by coupling to the orbital degrees of freedom and lifting thereby the orbital degeneracy. Consequently, the resulting topological orbital moment roots purely in the non-trivial spin arrangement in real space [189–191]. In order to quantify the emergent magnetic field and the corresponding *topological orbital magnetism*, we utilize the scalar spin chirality [188]

$$\chi_{ijk} = \boldsymbol{S}_i \cdot (\boldsymbol{S}_j \times \boldsymbol{S}_k) \ , \tag{6.1}$$

which correlates three neighboring spins $\boldsymbol{S}_i$, $\boldsymbol{S}_j$, and $\boldsymbol{S}_k$. If these three spins do not lie in a single plane, *i.e.*, if the spin texture is non-coplanar, the scalar spin chirality χ_{ijk} associated with the spin triangle is finite as well as the local magnetic field

$$\boldsymbol{b}_{ijk} \propto t_{ij} t_{jk} t_{ki} \chi_{ijk} \hat{\boldsymbol{n}}_{ijk} \ , \tag{6.2}$$

where t_{ij} is the hopping amplitude between the ith and jth site, and $\hat{\boldsymbol{n}}_{ijk}$ is the unit vector perpendicular to the plane spanned by the lattice sites i, j, and k, with the orientation of the plane being consistent with the ordering of the spins in Eq. (6.1). Rooting in the non-coplanarity of the neighboring spins, the presence of such an emergent magnetic field plays also a crucial role in the interpretation of transport effects in chiral magnetic skyrmions [150,151,166,167,192,193] as outlined at the end of Chapter 4.

At this point, it is natural to envisage prototypical materials in which this unconventional type of orbital magnetism could be realized and investigated comprehensively. Hosting diverse complex spin textures in real space, non-collinear bulk antiferromagnets such as $\mathrm{Mn_5S_3}$ [194–196], Nd [197–200], $\mathrm{Mn_3GaN}$ [201, 202], $\mathrm{Mn_3Ir}$ [203], and $\mathrm{Mn_3Ge}$ [204] provide generally an exciting and rich playground to study unique electronic phenomena. Especially, the antiferromagnetic compounds $\mathrm{Mn_3X}$ came recently into prominence since band crossings in the electronic structure affect the transport and thermal properties of these systems [205–207]. As the non-collinear texture in the latter compounds is coplanar, however, the scalar spin chirality χ_{ijk} cannot give rise to a topological orbital moment. On the other hand, a spin state that potentially manifests in topological orbital magnetism based on the emergent magnetic field is the $3\boldsymbol{Q}$ spin structure illustrated in Fig. 6.4, which forms due to the linear combination of three spiral spin-density waves with distinct wave vectors $\boldsymbol{Q}$. Thus, bulk and film systems that exhibit the chiral and non-coplanar $3\boldsymbol{Q}$ spin texture in real space are ideal candidates to study the nature and the magnitude of the sought unconventional orbital magnetism.

6.4.1 Monolayer of Mn on Cu(111) substrate

We begin with considering the two-dimensional system Mn/Cu(111) that refers to a magnetic Mn monolayer deposited on a Cu(111) substrate, for which the chiral spin structure of the ground state is indeed the above $3\boldsymbol{Q}$ texture [208]. While chiral magnetic structures in interfacial systems with spin-orbit coupling are usually mediated by the Dzyaloshinskii-Moriya interaction (DMI) [15, 16], the non-coplanar $3\boldsymbol{Q}$ magnetic texture originates here not from the DMI but from the competition of isotropic higher-order exchange interactions. As a consequence, the frustrated spin structure of

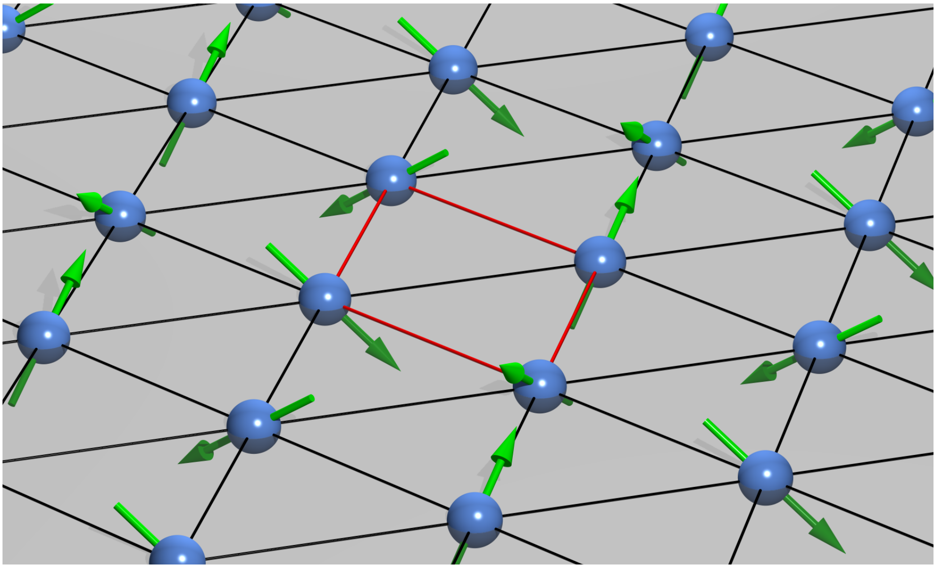

Figure 6.4: Non-coplanar $3\boldsymbol{Q}$ spin texture on the triangular lattice formed by Mn atoms (blue balls) on a Cu(111) substrate (not shown). The red parallelogram denotes the magnetic unit cell of four atoms, and green arrows indicate the individual spin moments, which compensate over the entire unit cell.

Mn/Cu(111) is hardly altered[3] upon including the spin-orbit interaction. Figure 6.4 visualizes that the total spin magnetization in the unit cell containing four Mn atoms vanishes for the $3\boldsymbol{Q}$ structure. If the orbital moment is assumed to follow locally the direction of the spin moment, which is reasonable in the presence of spin-orbit coupling, also the total OM is expected to be zero. However, we demonstrate below that this naive picture is not realized as a sizable topological orbital moment perpendicular to the film plane arises.

Since the electronic structure of Cu near the Fermi level is predominantly due to the s electrons, and the $3d$-$3d$ hybridization between the magnetic overlayer and the Cu substrate is negligible, we model the considered system as an unsupported Mn monolayer at the lattice constant of Cu(111). Appendix A.4 provides the computational details of the first-principles calculation. Taking into account also the Cu substrate, we generally find that our qualitative conclusions are completely unaffected even though the magnitude of the predicted effects is slightly diminished. We present in Fig. 6.5 the first-principles results for the energy dependence of the only non-vanishing component of the OM, which is normal to the Mn plane. Most strikingly, the direction of the orbital moment is not required to coincide with the direction of the spin magnetic moment, but its orientation is determined by the symmetry of the two-dimensional material. Comparing the two different approaches to calculate orbital magnetism in solids, we note that the ACA serves as a particularly crude approximation to the OM in that large differences to the modern theory become evident

---

[3] In Mn/Cu(111), the constituents are light atoms, which renders the electronic structure rather insensitive to the presence of the weak spin-orbit interaction.

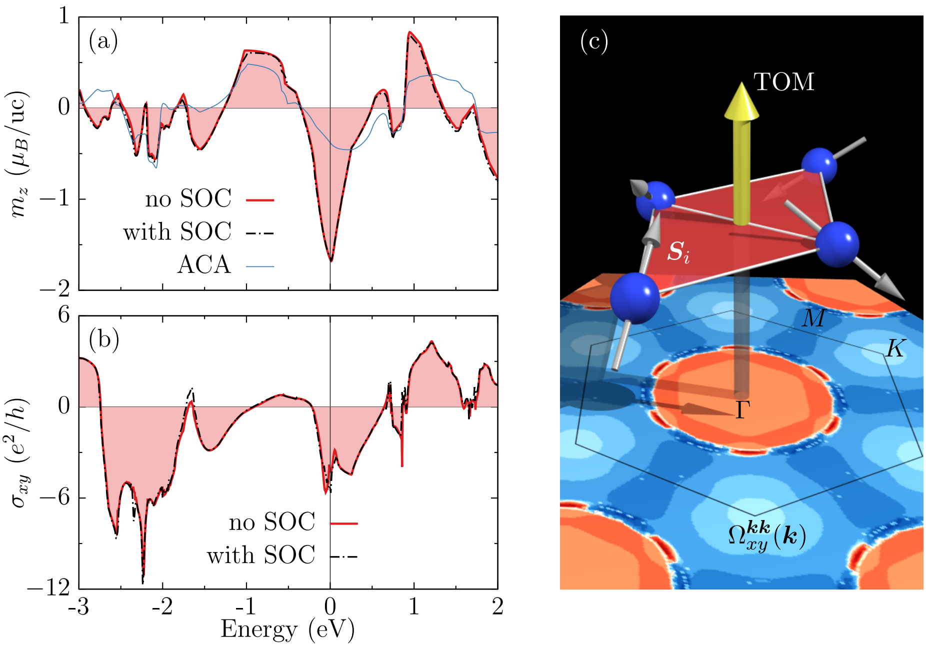

Figure 6.5: (a) Out-of-plane orbital magnetization m_z and (b) anomalous Hall conductivity σ_{xy} of the unsupported Mn monolayer in the $3\boldsymbol{Q}$ state. The calculations were performed without (red solid line) and with (black dashed line) including the effect of spin-orbit coupling (SOC). The blue thin line refers to the atom-centered approximation (ACA). (c) Emergence of a topological orbital moment (TOM) that roots solely in the complex phase-space geometry as revealed by the distribution of the Berry curvature $\Omega^{\boldsymbol{kk}}_{xy}$. The latter quantity ranges from large positive (dark red) to large negative (dark blue) values.

in Fig. 6.5. Especially close to the Fermi energy, the ACA largely underestimates the orbital magnetism in Mn/Cu(111) by predicting an OM that is four times smaller as compared to the full Berry phase theory that anticipates an extraordinarily large OM of $-1.5\,\mu_{\mathrm{B}}$ per unit cell. Moreover, as opposed to the ferromagnetic systems discussed before, we observe that the energy dependence of the out-of-plane OM in this non-coplanar magnet is much stronger correlated with that of the anomalous Hall conductivity.

While anomalous Hall effect and orbital magnetism are phenomena that are conventionally ascribed to the spin-orbit interaction, remarkably, we demonstrate in Fig. 6.5 that both properties do not at all rely on this relativistic effect but stem purely from the non-coplanar chiral spin texture of the $3\boldsymbol{Q}$ state in Mn/Cu(111). In contrast to the previously reported spin lattice of Fe/Ir(001) [190], for which a fraction of the OM is also present without spin-orbit coupling, we observe that the spin-orbit interaction has hardly any visible influence on the orbital magnetism and the anomalous Hall conductivity. Even though the chiral $3\boldsymbol{Q}$ spin texture is a topologically trivial structure as compared to, e.g, a magnetic skyrmion, we may still identify the transverse Hall effect in the system as a purely topological Hall effect [166, 190, 204] since it springs from the real-space configuration of the spin magnetic moments. As such it also manifests in a non-trivial distribution of the Berry curvature $\Omega_{xy}^{\boldsymbol{kk}}$ in the momentum phase space (see Fig. 6.5(c)). Despite the lack of a topological protection of the spin structure, we refer similarly to the accompanying texture-driven orbital magnetism as topological orbital magnetism. Exceptionally, the overall net magnetization is determined by the non-zero topological OM since the spin magnetization vanishes in the considered antiferromagnet Mn/Cu(111), which renders the system a representative of a new class of materials to which we refer as *topological orbital ferromagnets*, Fig. 6.5(c). In these ferromagnets, the macroscopic magnetization is solely arising from orbital magnetism originating explicitly from the non-trivial topology of the spin distribution in real space rather than the spin-orbit interaction. Stemming from manifestly non-local circulating currents, the topological orbital magnetism in this class of complex spin structures, but also orbital magnetism in multi-$\boldsymbol{Q}$ states and skyrmions in general, calls for a proper description based on the rigorous Berry phase theory.

As orbital moments couple to external magnetic fields, optical perturbations, and orbital currents, the predicted ferromagnetic ordering in terms of a large topological orbital moment in these spin-antiferromagnets opens an intriguing path to new physics. For example, we expect that the long-range ferromagnetism in topological orbital ferromagnets can survive above the spin-ordering temperature since chiral correlations in the *spin nematic phase* as mediated by order parameters comprising multiple spins are known to be particularly stable with respect to fluctuations [209, 210]. Moreover, our discovery of prominent topological orbital magnetism in non-collinear antiferromagnets implies that effective spin Hamiltonians that aim at describing the phase diagrams of these materials in an external magnetic field need to be amended by a Zeeman energy arising from the interaction of the emergent orbital moment with this field. Due to the direct correlation between the scalar spin chirality and the topological orbital moment, coupling to the orbital degrees of freedom by external means provides an interesting opportunity to control the chirality of the spin texture. Strikingly, this interplay could also be useful for detecting and characterizing efficiently complex magnetic structures (*e.g.*, skyrmions) as set apart by their unique signature imprinted on orbital magnetism [191].

6.4.2 Bulk antiferromagnet γ-FeMn

Neutron diffraction experiments [211, 212] and first-principles calculations of the electronic structure [213–215] suggest that the disordered bulk compound γ-Fe$_x$Mn$_{1-x}$ has a $3\boldsymbol{Q}$ ground state[4] over a wide range of composition ratios x (see Fig. 6.6). Revealing a non-coplanar spin texture, these alloys serve to assess the efficiency of the emergent magnetic field originating from the scalar spin chirality as an alternative mechanism that breaks the orbital degeneracy. For this purpose, we study topological contributions to the Berry phase theory of orbital magnetism and its transport companion, namely, the anomalous Hall effect.

---

[4] In the case of γ-FeMn with simple cubic unit cell containing four atoms as shown in Fig. 6.6, the corresponding wave vectors are $\boldsymbol{Q}_1 = (2\pi/a, 0, 0)$, $\boldsymbol{Q}_2 = (0, 2\pi/a, 0)$, and $\boldsymbol{Q}_3 = (0, 0, 2\pi/a)$, where a is the lattice constant.

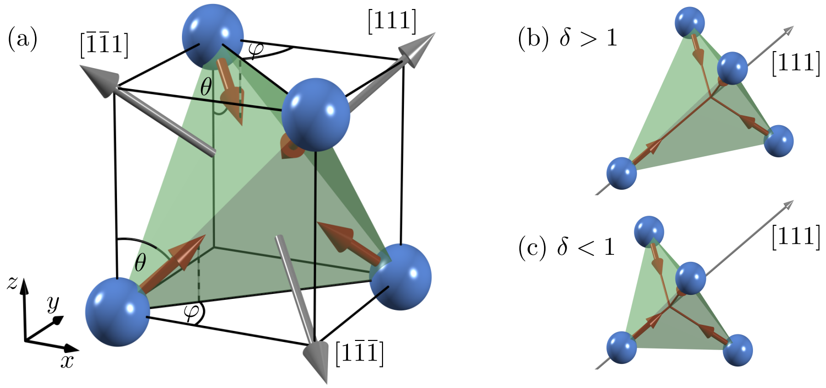

Figure 6.6: (a) Unit cell of the fcc compound γ-FeMn. The non-coplanar $3\boldsymbol{Q}$ spin texture is indicated by red arrows pointing towards the center of the green transparent tetrahedron, the faces of which highlight equivalent planes of the undistorted lattice. Gray arrows orthogonal to these planes mark the directions [$\bar{1}\bar{1}1$], [$1\bar{1}\bar{1}$], and [111], respectively. We use the polar angle θ and the azimuthal angle φ to represent the antiferromagnetic spin structure in spherical coordinates. The depicted $3\boldsymbol{Q}$ structure is realized if $\varphi = 45°$ and θ amounts to half of the tetrahedral angle, *i.e.*, $\theta \approx 54.7°$. If (b) tensile or (c) compressive strain is applied, the distance between adjacent (111) planes changes.

While the spin structure of the $3\boldsymbol{Q}$ state gives rise to a finite scalar spin chirality $\chi_{ijk} = \pm\chi_0$ between any three neighboring spins $\boldsymbol{S}_i$, $\boldsymbol{S}_j$, and $\boldsymbol{S}_k$ as can be understood from Fig. 6.6, the individual fictitious magnetic fields $\boldsymbol{b}_{ijk}$ cancel over the magnetic unit cell of four atoms. Since the net emergent field is zero, the cubic FeMn alloys display no topological orbital magnetism in the absence of spin-orbit coupling. This is consistent with the symmetries of the $3\boldsymbol{Q}$ state on the fcc lattice forming the *magnetic point group* m-3m′, which obstructs the system from showing any macroscopic magnetization. Consequently, texture-driven contributions to orbital magnetism and anomalous Hall effect cannot develop unless the crystal symmetries are reduced, for example, by applying strain along the [111] direction of the cube [189]. Lacking some of the mirror operations, the magnetic point group -3m′ in the strained case is *admissible*[5] and supports the formation of a net magnetic moment.

In practice, we use the ratio $\delta = d'/d$ to characterize such deformations of the crystal, where d and d' correspond to the distance between adjacent (111) planes in the undistorted and distorted structure, respectively (see Fig. 6.6). As the imposed spin texture is kept fixed in our calculations, the only effect of δ is to tune the intra-layer hopping between different (111) planes that manifests ultimately in a net magnetic field $\boldsymbol{B}_{\mathrm{em}}$ under strain, which we estimate as

$$\boldsymbol{B}_{\mathrm{em}} = \sum_{\langle ijk\rangle} \boldsymbol{b}_{ijk} \propto \chi_0 t^3 \left[1 - \frac{1}{\delta}\right] \begin{pmatrix} 1 \\ 1 \\ 1 \end{pmatrix} , \tag{6.3}$$

---

[5] While only 31 out of 122 magnetic point groups are admissible and thus allow for ferromagnetism, the remaining groups forbid any net (spin or orbital) magnetization.

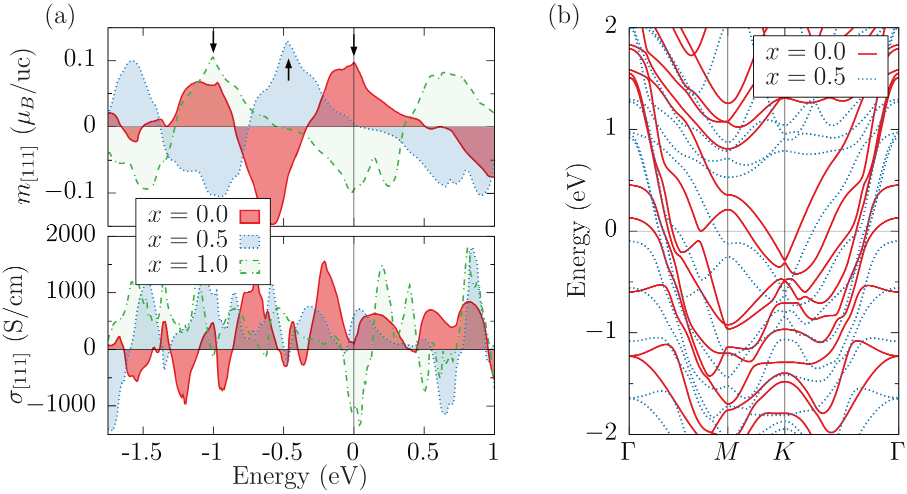

Figure 6.7: Transport and magnetic properties in strained γ-Fe$_x$Mn$_{1-x}$ with $\delta = 0.95$ and non-collinear $3\boldsymbol{Q}$ spin structure. (a) Dependence of the orbital magnetization and the anomalous Hall conductivity on the position of the Fermi level in various alloys. Characteristic features that shift towards lower energies with increasing x are marked by black arrows. The magnetic in-plane unit cell of four atoms is denoted by "uc". (b) The band structures for the two concentrations $x = 0.0$ and $x = 0.5$ reveal strong correlations due to the similar electron configuration of Fe and Mn. Spin-orbit coupling was not taken into account in (a) and (b).

where the sum is over all four spin triangles in the magnetic unit cell, χ_0 is the scalar spin chirality, and t denotes the inter-layer hopping. To arrive at the simple estimate (6.3) for the net field, we assumed additionally that the intra-layer hopping is given by t/δ. While the emergent field $\boldsymbol{B}_{\text{em}}$ indeed vanishes in the unstrained cubic case with $\delta = 1$, finite strain along the [111] direction generates effectively a net magnetic field that roots in the chiral spin texture and is opposite in sign for compressive and tensile strain. Thus, in strained FeMn alloys we expect the emergence of a topological orbital moment, the orientation of which is determined purely by the symmetries of the magnetic system.

Using moderate compressive strain as characterized by the parameter $\delta = 0.95$, we present in Fig. 6.7(a) the calculated energy dependence of OM (in the modern theory) and anomalous Hall conductivity in selected antiferromagnetic γ-Fe$_x$Mn$_{1-x}$ alloys in absence of any spin-orbit coupling. The computational details that underlie the first-principles calculations are discussed in Appendix A.5. If the alloy composition x is varied from pure Mn over Fe$_{0.5}$Mn$_{0.5}$ to pure Fe, the dependence of the OM on the Fermi energy is qualitatively not altered apart from a global shift towards lower energies as can be seen from the marked peaks in Fig. 6.7(a). As the electron configurations of Fe and Mn atoms greatly resemble each other, the electronic structures of the corresponding γ-Fe$_x$Mn$_{1-x}$ alloys are quite similar, in particular within the used method of virtual crystal approximation (VCA). Thus, it is not surprising that the band structures of the various systems shown in Fig. 6.7(b) match each other very well except for a global shift in energy. Although the Berry phase theory links orbital magnetism and anomalous Hall effect intimately via the Berry curvature in momentum phase space, we find that the variations of OM and anomalous Hall conductivity with the position of the Fermi level are not at all correlated in these disordered bulk antiferromagnets, Fig. 6.7(a). As compared to the orbital magnetism, the anomalous Hall effect reveals a more vivid energy dependence with non-trivial oscillations, emphasizing its strong sensitivity to the electronic structure. Notably, the different curves in Fig. 6.7(a) for the anomalous Hall conductivity at various alloy compositions are not mapped onto a single curve by a plain energy shift. Finally, we stress that the values of both OM and transverse conductivity, shown in Fig. 6.7(a), have been verified to be faintly affected by including the spin-orbit interaction in our calculations.

Figure 6.8(a) presents the variation of OM and transverse conductivity evaluated at the actual Fermi energy of γ-Fe$_x$Mn$_{1-x}$ when changing the composition ratio x of the compound. In the case of moderate compressive strain with $\delta = 0.95$, the net emergent magnetic field in the pure Mn crystal generates an OM of $0.1\,\mu_B$ per unit cell of four atoms, which gradually decreases with increasing Fe concentration, changes sign around $x \approx 0.5 - 0.6$, and eventually amounts to a value of about $-0.1\,\mu_B$ per unit cell in the case of pure Fe. Remarkably, this overall behavior is reversed qualitatively if we expand the lattice ($\delta > 1$) instead of contracting it, whereby the emergent magnetic field flips its sign according to the simple estimate (6.3). In the experimentally confirmed region of concentrations that lead to the $3\boldsymbol{Q}$ ground state in cubic γ-FeMn (see dashed lines in Fig. 6.8(a)), depending on the applied strain the OM ranges from -0.05 to $0.1\,\mu_B$ per unit cell, which is comparable to the magnitude of orbital magnetism in elementary bulk ferromagnets. Reinforcing the emergent magnetic field by using stronger compressive or tensile strain, or in other words, increasing the degree of symmetry-breaking along the [111] direction, we generally observe that both the OM and the anomalous Hall conductivity are enhanced.

In particular for tensile strain, the anomalous Hall effect follows in its dependence on the concentration x qualitatively the trend set by the orbital magnetism. The magnitude of the transverse conductivity in the antiferromagnetic bulk materials amounts to striking values of up to 1000 S/cm in the experimentally confirmed region of the $3\boldsymbol{Q}$ spin state, and even higher values are reached in the pure systems. Such anomalous Hall effect of outstanding magnitude in a spin-compensated material is remarkable, and we motivate experimental studies aimed at its detection. Again, we verified that OM and anomalous Hall conductivity shown in Fig. 6.8(a) are hardly influenced by the spin-orbit interaction, which promotes the non-coplanarity of the chiral spin texture as driving mechanism for these phenomena in the bulk antiferromagnet γ-FeMn.

Focusing on the (111) plane including the Γ-point, Figure 6.8(c) depicts the momentum distribution of OM and Berry curvature of all occupied bands for the case of the pure Mn compound in the $3\boldsymbol{Q}$ state under compressive strain ($\delta = 0.95$). These $\boldsymbol{k}$-resolved properties carry distinct sharp features due to the Fermi surface lines (see Fig. 6.7(b)), and both reveal further the six-fold rotational symmetry that is associated with the considered plane of the distorted lattice. While large negative contributions to the OM (circle around the Γ-point) root in the group of parabolic bands that intersect the Fermi level close to Γ along the paths ΓM and ΓK in Fig. 6.7(b), large areas of the Brillouin zone provide small but positive contributions to the net positive

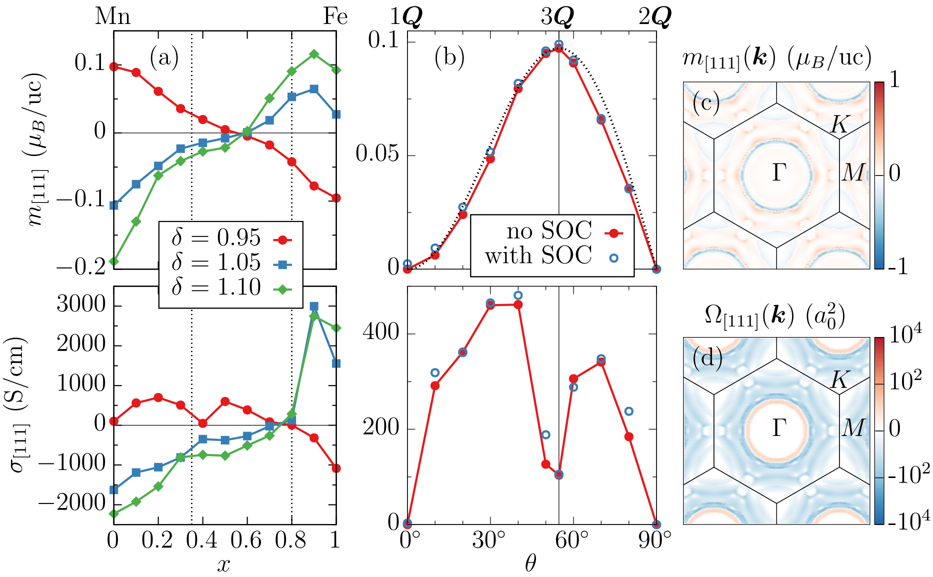

Figure 6.8: Effect of composition ratio and spin texture in strained γ-Fe$_x$Mn$_{1-x}$ without spin-orbit coupling (SOC). (a) Orbital magnetization $m_{[111]}$ and anomalous Hall conductivity $\sigma_{[111]}$ for varying composition ratio x and several choices of the strain δ. The imposed 3$\boldsymbol{Q}$ state is experimentally confirmed to arise in the unstrained compounds within the region bounded by dotted vertical lines. (b) Dependence of $m_{[111]}$ and $\sigma_{[111]}$ on the polar angle θ that characterizes the antiferromagnetic spin texture, for $x = 0$ and $\delta = 0.95$. Additionally, the spin-orbit interaction was included in the case of the blue open circles, and the black dotted line marks the angular dependence of the scalar spin chirality, Eq. (6.4). (c,d) Distribution of the $\boldsymbol{k}$-resolved orbital magnetization and the Berry curvature in momentum space for the 3$\boldsymbol{Q}$ state without spin-orbit coupling. Note the logarithmic color scale used for the Berry curvature.

OM. Similarly to the energy dependence discussed above, the Berry curvature reveals generally a richer and more complex distribution in momentum space as compared to the $\boldsymbol{k}$-resolved OM.

Finally, we scrutinize unambiguously the key role of the non-zero scalar spin chirality of the antiferromagnetic texture for orbital magnetism and anomalous Hall effect. While keeping the angle φ of the spin structure fixed to 45° as in the calculations reported above, we vary the other characteristic angle θ (see Fig. 6.6), which enables us to effectively control the value of the scalar spin chirality. The latter quantity depends on θ according to the following relation:

$$\chi_0(\theta) \propto \cos\theta \sin^2\theta \,. \tag{6.4}$$

As shown by the dotted line in Fig. 6.8(b), obviously, the chirality $\chi_0(\theta)$ vanishes for the coplanar cases of $\theta = 0°$, which is known as the 1$\boldsymbol{Q}$ state, and $\theta = 90°$, also known as the 2$\boldsymbol{Q}$ state, but it becomes maximal for $\theta = 54.74°$ in the 3$\boldsymbol{Q}$ structure. Figure 6.8(b) presents additionally the dependence of the OM and the anomalous Hall conductivity on θ, or alternatively, on the scalar spin chirality for the pure Mn system under compressive strain ($\delta = 0.95$). Reaching its decent maximum of about $0.1\,\mu_B$ per unit cell in the $3\boldsymbol{Q}$ state, the predicted θ-dependence of the OM matches almost perfectly the curve of $\chi_0(\theta)$, where we ascribe the remaining tiny differences to changes of fine details of the electronic structure as the antiferromagnetic spin texture is varied. The remarkable correlation between the OM and $\chi_0(\theta)$ in γ-FeMn clearly suggests that the orbital magnetism in this class of compounds is directly proportional to the net emergent magnetic field rooting in the scalar spin chirality, where the constant of proportionality can be viewed as a *topological orbital susceptibility.* Variations of the anomalous Hall effect with the polar angle θ, however, do not mirror directly the simple angular dependence of $\chi_0(\theta)$ but originate rather from higher-order terms that manifest in a more complex behavior. In particular, the anomalous Hall conductivity has a local minimum for the $3\boldsymbol{Q}$ spin structure, which is contrary to the OM that is maximized at that point. In order to substantiate that both orbital magnetism and anomalous Hall effect are purely driven by the spin arrangement in real space, we perform calculations including the effect of spin-orbit coupling. Our calculations uncover that the OM barely varies when considering the spin-orbit interaction, and similarly the anticipated changes of the anomalous Hall conductivity due to the effect of spin-orbit coupling on the electronic structure are insignificant, see Fig. 6.8(b).

While the θ-dependence of the anomalous Hall effect relates to higher-order terms, the correlation between the topological OM and the scalar spin chirality is particularly intimate, which motivates us to speculate that an inverse effect could be observable in terms of an enhanced magneto-structural coupling in non-coplanar antiferromagnets [216, 217]. That is, we propose that materials of the present type may be subject to a striking *topological orbital magnetostriction* mediated by the interaction of the topological orbital moment with an external magnetic field, resulting in changes of the crystallographic structure such as to maximize the energy gain due to this interaction. In particular, owing to the opposite sign of the topological orbital moment with respect to either compressive or tensile strain along the [111] direction in γ-FeMn, it could be possible to expand or compress the crystal along the [111] axis by reverting the applied magnetic field along this axis.

In resemblance to the previous system Mn/Cu(111), our results truly identify the non-coplanar bulk antiferromagnet γ-FeMn as a prototypical topological orbital ferromagnet. The spin-orbit interaction is completely replaced with the emergent magnetic field associated with the $3\boldsymbol{Q}$ spin texture as efficient mechanism lifting the orbital degeneracy. In the discussed type of topological orbital ferromagnets, non-vanishing orbital and charge currents arise from the scalar spin chirality in the distorted crystal that results in thoroughly topological contributions to the orbital magnetism and the anomalous Hall effect. Analogously, we anticipate non-coplanar magnets to display a *topological spin Hall effect* (see also Ref. [218]) owing to the non-trivial geometry of the spin structure, without referring to the spin-orbit interaction.

Topological orbital ferromagnets constitute a distinct class of materials as the non-trivial orbital magnetism originates directly from the complex spin configuration in real space. As a consequence, the properties of these materials are tunable by modifying the spin distribution, for instance, by means of electrically induced spin torques [14] or by altering the strength of the spin-spin interactions. Despite the smaller OM in γ-FeMn as compared to Mn/Cu(111), our calculations demonstrate that magnitude and sign of the topological orbital magnetism can be controlled via adequate electronic-structure engineering through alloy composition or strain. To outline the role of orbital magnetism in a broader context, we emphasize that the orbital degrees of freedom offer higher flexibility as to their internal structure and the size of the resulting orbital moments in contrast to the spin of the electrons. As such, orbital moments in general can be envisioned as versatile operational building blocks and information carriers in the burgeoning field of *orbitronics*.

6.4.3 Material candidates and experimental verification

Despite of the developed theoretical understanding of topological orbital moments that are linked explicitly to the chiral spin texture, an experimental verification of the phenomenon can be expected to set an intricate challenge. In order to assist experiments in detecting the effect, we summarize at this stage the key requirements for a net fictitious magnetic field to manifest, provide a list of promising material candidates that reveal potentially topological orbital magnetism, and propose ideas how to measure the phenomenon in experiment.

Clearly, the scalar spin chirality $\chi_{ijk} = \boldsymbol{S}_i \cdot (\boldsymbol{S}_j \times \boldsymbol{S}_k)$ is only finite if the involved spins do not lie in a single plane, which promotes the non-coplanarity of the spin structure as a necessary ingredient to realize texture-driven orbital magnetism. As we unraveled in the analysis of γ-FeMn, however, this is not a sufficient condition since the local emergent fields that originate from a finite χ_{ijk} might compensate depending on the symmetries of the system, which renders the adequate crystal symmetry an additional prerequisite. In fact, a net orbital moment in absence of spin-orbit coupling may develop only in non-coplanar magnetic structures that are characterized by one of the 31 admissible magnetic point groups. In particular, this excludes (amid others) all chiral magnetic materials that have cubic symmetry.

Equipped with these two constraints, we screened a crystallographic database of magnetic structures [219–221] to identify plausible candidate systems, a selection of which we collect in Table 6.2. Besides frustrated chiral antiferromagnets that constitute the presumably most promising class of materials to detect topological orbital ferromagnetism, also ferro- and ferrimagnetic systems with complex non-collinear spin textures are likely to show the anticipated effect. However, in the latter materials a prominent spin magnetization could overshadow the unconventional orbital moment and hamper its detection. Many of the systems shown in Table 6.2 are experimentally readily available such as the antiferromagnet $\mathrm{Mn_5Si_3}$ [195], the compound $\mathrm{MgCr_2O_4}$ that reveals a $3\boldsymbol{Q}$ spin structure [222], and the weak ferromagnet $\mathrm{Mn_3CuN}$, whose transition temperature of 143 K [223] is one of the highest among the materials in Table 6.2. The list is complemented by the layered insulator $\mathrm{K_{0.5}RhO_2}$, which was already predicted based on density functional theory to host a quantized topological Hall effect driven by a complex spin configuration in real space [224]. Although non-collinear but coplanar antiferromagnets (*e.g.*, $\mathrm{Mn_3Ir}$) are missing in Table 6.2, these systems have the potential to display topological orbital magnetism as well if an external magnetic field is used to tilt the spins out of the plane (see, for instance, the discussion in Ref. [225]).

In theory, one can distinguish rather easily the usual orbital magnetism from its topological cousin either (i) by comparing the cases with and without taking into account the spin-orbit interaction, or (ii) by performing two calculations but with

Candidate	FM/AFM	magnetic point group	Reference
Mn_5Si_3	AFM	admissible	[194, 195]
$K_{0.5}RhO_2$	AFM	admissible	[224]
$HoNiO_3$	AFM	2	[226]
$MgCr_2O_4$	AFM	-42′m′	[222]
$Nd_2Mo_2O_7$	FM	admissible	[188]
Nd_2NaRuO_6	FM	2/m	[227]
NiN_2O_6	FM	-3	[228]
U_3As_4	FM	3m′	[229]
MnV_2O_4	FM	4/m	[230]
Mn_3CuN	FM	4/m	[223]
$Ho_2Ru_2O_7$	FM	4/mm′m′	[231]

Table 6.2: Candidate systems with non-coplanar spin structure and proper crystal symmetries, allowing possibly for the experimental observation of topological orbital ferromagnetism in real materials. The list encompasses both antiferromagnets (AFM) and systems with a finite spin magnetization (FM). We provide the admissible magnetic point group of the system as well as the reference that predicts (theoretically or experimentally) a complex spin texture.

the emergent magnetic field reversed in the second run, *e.g.*, by modifying the spin structure adequately. On the other hand, tracing the experimental fingerprints of texture-driven orbital magnetism in XMCD measurements[6] poses a highly non-trivial problem and requires careful analysis. When following similar ideas as in theory, one might try to correlate two XMCD data sets taken on the very same sample but with opposite emergent magnetic fields, and thereby extract the signal of the topological orbital magnetism that reverses sign correspondingly. To invert the emergent field, a straightforward but practical approach would be to rotate the sample properly. An even more promising path towards uncovering topological orbital moments would be to monitor their stability upon heating the sample beyond the spin-ordering temperature. Originating from the three-spin correlation function $\boldsymbol{S}_i \cdot (\boldsymbol{S}_j \times \boldsymbol{S}_k)$, the phenomenon of topological orbital magnetism should be still detectable above the Curie temperature, where the signal of the spin texture itself is paramagnetic.

---

[6] Although XMCD probes the magnetic properties only locally and might thus underestimate the topological orbital moments (like the ACA in theory), this experimental technique should still allow for capturing signatures of the predicted unconventional orbital magnetism.

Chapter 7

Higher-dimensional Wannier functions

Contents

Building onto the framework laid out in Chapter 5, here, we generalize systematically the Wannier representation to describe higher-dimensional phase spaces that comprise not only the crystal momentum but also additional abstract parameters. We motivate that this situation is frequently met in the description of various condensed-matter phenomena, which renders our extension particularly valuable. Starting initially from an orthogonality problem, we derive the concept of higher-dimensional Wannier functions (HDWFs). The localization of these functions is achieved using a generalized algorithm to minimize iteratively the spread in the composite real space. In close analogy to the usual Wannier interpolation, we develop ultimately an interpolation technique based on HDWFs that is ideally suited to study efficiently the electronic structure in complex phase spaces. Consequently, this method enables us to investigate on an equal footing the anisotropy of transport phenomena, magneto-electric coupling effects, and the Dzyaloshinskii-Moriya interaction (DMI) in magnetic materials.

The concepts presented in this chapter have already been published:

J.-P. Hanke, F. Freimuth, S. Blügel, and Y. Mokrousov
Physical Review B **91**, *184413 (2015), Editor's suggestion*

J.-P. Hanke, F. Freimuth, S. Blügel, and Y. Mokrousov
J. Phys. Soc. Jpn. **87**, *041010 (2018)*

7.1 Why to go beyond Wannier functions?

Although the usual Wannier interpolation grants efficient access to such Berry phase properties as anomalous Hall conductivity and orbital magnetization, this technique is restricted to describe phenomena that root in the variation of the wave functions with the crystal momentum. As we have seen in Chapter 4, the non-trivial geometry of the higher-dimensional phase space of the crystal momentum and additional abstract parameters $\boldsymbol{\lambda}$ can give rise to further fascinating effects, for example, current-induced spin torques and chiral exchange interactions. To account for these phenomena, the response of the wave functions to changes in $\boldsymbol{\lambda}$ has to be known, which is, however, generally not available in any standard first-principles scheme so far. Therefore, the computation of geometric properties of complex phase spaces would benefit considerably from a generalized technique beyond the usual Wannier interpolation that provides the multiparameter Hamiltonian $H^{(\boldsymbol{k},\boldsymbol{\lambda})}$ at any point $(\boldsymbol{k},\boldsymbol{\lambda})$. With this aim, we develop below the concept of higher-dimensional Wannier functions (HDWFs) by performing Fourier transformations with respect to both $\boldsymbol{k}$ and $\boldsymbol{\lambda}$. After constructing such HDWFs from the electronic structure known on a coarse $(\boldsymbol{k},\boldsymbol{\lambda})$-grid, we represent the Hamiltonian by means of short-ranged hoppings, which enable us to interpolate $H^{(\boldsymbol{k},\boldsymbol{\lambda})}$ at any desired point $(\boldsymbol{k},\boldsymbol{\lambda})$ of the higher-dimensional phase space.

Rather than starting *in medias res* with the mathematical derivations, we highlight first the conceptual value of such a generalized technique. Depending on the particular nature of the additional parameter, a wide range of possible physical situations where the approach could be notably rewarding may be anticipated: (i) While the anomalous Hall effect is routinely extracted from maximally-localized Wannier functions (MLWFs), evaluating its dependence on the magnetization direction $\hat{\boldsymbol{m}}$ [232] can be time-consuming since it relies on the construction of individual sets of MLWFs for every considered direction. In contrast, using the generalized interpolation with $\boldsymbol{\lambda} = \hat{\boldsymbol{m}}$, we could obtain the complete anisotropy information simply from a single set of HDWFs. (ii) Likewise, the accurate prediction of Heisenberg exchange constants based on derivatives of the dispersion $E(\boldsymbol{q})$ render many non-collinear calculations of spin spirals with different wave vectors $\boldsymbol{q}$ necessary [233]. The tremendous computational burden associated with the *ab initio* calculation of exchange constants could be reduced when applying the technique of HDWFs to interpolate $E(\boldsymbol{q})$ and its derivatives with respect to the spin-spiral wave vector $\boldsymbol{\lambda} = \boldsymbol{q}$. (iii) Mixed Berry curvatures in position and momentum space are perceived to be of crucial quantitative importance in chiral magnets like MnSi, where they manifest in stable magnetic structures with finite electric charge [132]. As the generalized technique is ideally suited to study the geometry of complex phase spaces, the technique might trace fingerprints of generic Berry curvatures in transport properties, and thereby contribute to the topological characterization of non-trivial magnetic textures. (iv) Along this line, originating from the response of the wave functions upon changing the crystal momentum and the magnetization direction $\hat{\boldsymbol{m}}$ [28], the phenomena of spin-orbit torques (SOTs) and Dzyaloshinskii-Moriya interaction (DMI) could be described efficiently based on the higher-dimensional interpolation with $\boldsymbol{\lambda} = \hat{\boldsymbol{m}}$. (v) Ultimately, the formalism of HDWFs could provide an alternative tool for force calculations in first-principles methods or for calculating the ferroelectric polarization [22, 23, 234], where the parameter $\boldsymbol{\lambda}$ would describe the atomic displacements in both cases. (vi) Considering the composition ratio x as a parameter, finally, we anticipate that the generalized Wannier interpolation could allow for an unambiguous treatment of alloys like $\mathrm{Fe}_x\mathrm{Co}_{1-x}$ (same period in periodic table) or even $\mathrm{Bi}_x\mathrm{Sb}_{1-x}$ (same group in periodic table) within the so-called virtual crystal approximation (VCA) [235].

7.2 Orthogonality problem and its solution

In the presence of an additional periodic[1] parameter $\boldsymbol{\lambda}$, we assume the translationally invariant system to be characterized by a whole set of Hamiltonians, where each member $H^{(\boldsymbol{\lambda})}$ of this family represents the electronic structure for a particular value of $\boldsymbol{\lambda}$. As usual, the eigenstates of $H^{(\boldsymbol{\lambda})}$ are Bloch states $|\psi_{\boldsymbol{k}\boldsymbol{\lambda}n}\rangle$ carrying an explicit dependence on $\boldsymbol{\lambda}$:

$$H^{(\boldsymbol{\lambda})}(\boldsymbol{r})\psi_{\boldsymbol{k}\boldsymbol{\lambda}n}(\boldsymbol{r}) = \mathcal{E}_{\boldsymbol{k}\boldsymbol{\lambda}n}\psi_{\boldsymbol{k}\boldsymbol{\lambda}n}(\boldsymbol{r})\,, \tag{7.1}$$

where $\mathcal{E}_{\boldsymbol{k}\boldsymbol{\lambda}n}$ is the energy dispersion of the nth band. Since the Hamiltonians $H^{(\boldsymbol{\lambda})}$ and $H^{(\boldsymbol{\lambda}')}$ at different values of the parameter are often completely independent, the eigenstates at $\boldsymbol{\lambda}$ and $\boldsymbol{\lambda}'$ are not at all guaranteed to be orthogonal, which amounts to

$$\langle\psi_{\boldsymbol{k}\boldsymbol{\lambda}n}|\psi_{\boldsymbol{k}'\boldsymbol{\lambda}'m}\rangle \neq N_{\boldsymbol{k}}\delta_{\boldsymbol{k}\boldsymbol{k}'}\delta_{\boldsymbol{\lambda}\boldsymbol{\lambda}'}\delta_{nm}\,. \tag{7.2}$$

Only if the two Bloch states are eigenstates of the very same Hamiltonian $H^{(\boldsymbol{\lambda})}$ the conventional orthogonality with respect to the crystal momentum is present, *i.e.*, $\langle\psi_{\boldsymbol{k}\boldsymbol{\lambda}n}|\psi_{\boldsymbol{k}'\boldsymbol{\lambda}m}\rangle = N_{\boldsymbol{k}}\delta_{\boldsymbol{k}\boldsymbol{k}'}\delta_{nm}$. As a consequence of Eq. (7.2), it is not sufficient to perform discrete Fourier transformations of these Bloch states with respect to $\boldsymbol{k}$ and $\boldsymbol{\lambda}$ in analogy to the case of MLWFs since this procedure would not lead to orthonormal Wannier functions (WFs). On one side, non-orthogonal WFs can of course be defined [236] and may even be advantageous from the viewpoint of a stronger real-space localization [172]. On the other side, in the setup considered here already the Bloch states are not orthogonal for different parameters $\boldsymbol{\lambda}$ and $\boldsymbol{\lambda}'$, which results in conceptual complications when extending the definition of WFs. Especially, if we attempt to generalize the hoppings (5.15) to the case of these non-orthogonal WFs, we encounter formally matrix elements $\langle\psi_{\boldsymbol{k}\boldsymbol{\lambda}n}|H|\psi_{\boldsymbol{k}\boldsymbol{\lambda}'m}\rangle$. As it is not obvious which member of the family of Hamiltonians to consider, the handling of these elements is ambiguous for $\boldsymbol{\lambda} \neq \boldsymbol{\lambda}'$.

7.2.1 Transition to higher dimensions

In order to resolve these conceptual difficulties and to obtain well-localized orthonormal HDWFs, we introduce an *auxiliary space* $\boldsymbol{\xi}$ as the reciprocal of the $\boldsymbol{\lambda}$-space. Instead of taking the usual Bloch states in the construction of HDWFs, we consider orthogonal states $\Phi_{\boldsymbol{k}\boldsymbol{\lambda}n}(\boldsymbol{r},\boldsymbol{\xi})$ in the higher-dimensional real space $(\boldsymbol{r},\boldsymbol{\xi})$. Being key ingredients in the construction, the states $\Phi_{\boldsymbol{k}\boldsymbol{\lambda}n}(\boldsymbol{r},\boldsymbol{\xi})$ are defined as the products of the physical Bloch states and *auxiliary orbitals* $\zeta_{\boldsymbol{\lambda}}(\boldsymbol{\xi})$ that mediate the orthogonality:

$$\Phi_{\boldsymbol{k}\boldsymbol{\lambda}n}(\boldsymbol{r},\boldsymbol{\xi}) = \psi_{\boldsymbol{k}\boldsymbol{\lambda}n}(\boldsymbol{r})\zeta_{\boldsymbol{\lambda}}(\boldsymbol{\xi}) \qquad \text{or} \qquad |\Phi_{\boldsymbol{k}\boldsymbol{\lambda}n}\rangle = |\psi_{\boldsymbol{k}\boldsymbol{\lambda}n}\rangle \otimes |\zeta_{\boldsymbol{\lambda}}\rangle\,. \tag{7.3}$$

---

[1] As will become obvious below, the Bloch states need to be periodic functions of the parameter $\boldsymbol{\lambda}$ such that Fourier transformations of these states with respect to $\boldsymbol{\lambda}$ are well defined.

Obviously, the Bloch states and the auxiliary orbitals act individually on distinct real spaces. We enforce the necessary orthogonality of the product states by choosing the auxiliary orbitals as an orthogonal basis, *i.e.*, $\langle \zeta_{\boldsymbol{\lambda}} | \zeta_{\boldsymbol{\lambda}'} \rangle = N_{\boldsymbol{\lambda}} \delta_{\boldsymbol{\lambda}\boldsymbol{\lambda}'}$, where $N_{\boldsymbol{\lambda}}$ denotes the number of $\boldsymbol{\lambda}$-points on a coarse grid.

When constructing explicitly the auxiliary orbitals, we consider them to be solutions of the Schrödinger equation with a periodic potential in the auxiliary space, which is schematically shown in Fig. 7.1. That is, the auxiliary orbitals $|\zeta_{\boldsymbol{\lambda}}\rangle$ are chosen to be the lowest-energy eigenstates of a corresponding Hamiltonian $\bar{H}$:

$$\bar{H}(\boldsymbol{\xi})\zeta_{\boldsymbol{\lambda}}(\boldsymbol{\xi}) = \bar{\mathcal{E}}_{\boldsymbol{\lambda}}\zeta_{\boldsymbol{\lambda}}(\boldsymbol{\xi}) \,, \tag{7.4}$$

where $\bar{\mathcal{E}}_{\boldsymbol{\lambda}}$ represents the lowest energy band dispersing with $\boldsymbol{\lambda}$. Based on the imposed translational invariance in the auxiliary real space, one of the most natural and convenient choices for the shape of the auxiliary orbitals are Bloch waves:

$$\zeta_{\boldsymbol{\lambda}}(\boldsymbol{\xi}) = \mathrm{e}^{\mathrm{i}\boldsymbol{\lambda}\cdot\boldsymbol{\xi}}\rho_{\boldsymbol{\lambda}}(\boldsymbol{\xi}) \,, \tag{7.5}$$

where $\rho_{\boldsymbol{\lambda}}(\boldsymbol{\xi}) = \langle \boldsymbol{\xi} | \rho_{\boldsymbol{\lambda}} \rangle$ are lattice-periodic functions that are normalized to the unit cell in the auxiliary real space: $\langle \rho_{\boldsymbol{\lambda}} | \rho_{\boldsymbol{\lambda}'} \rangle = \delta_{\boldsymbol{\lambda}\boldsymbol{\lambda}'}$. By construction, it follows that the resulting auxiliary orbitals are indeed orthogonal, *i.e.*, $\langle \zeta_{\boldsymbol{\lambda}} | \zeta_{\boldsymbol{\lambda}'} \rangle = N_{\boldsymbol{\lambda}} \delta_{\boldsymbol{\lambda}\boldsymbol{\lambda}'}$, where the integration is performed in a supercell of $N_{\boldsymbol{\lambda}}$ unit cells in the auxiliary space.

As depicted in Fig. 7.1, the regular lattice in the auxiliary space is modeled using a series of potential wells of finite depth $\bar{V}_0$. Since an extension to higher dimensions is straightforward, we restrict the following discussion to the case of a one-dimensional lattice as described in atomic units by the single-particle Hamiltonian

$$\bar{H}(\xi) = -\frac{1}{2}\frac{\mathrm{d}^2}{\mathrm{d}\xi^2} - \bar{V}_0 \sum_{\Xi} \left[\Theta\left(\xi - \Xi + \bar{b}/2\right) - \Theta\left(\xi - \Xi_j - \bar{b}/2\right)\right] . \tag{7.6}$$

Here, the scalar ξ is the auxiliary real-space position in one dimension, and the combination of Heaviside step functions Θ cuts out the potential-well region of width $\bar{b}$ centered around the position Ξ, where the coordinate $\Xi = n\bar{a}$ is defined by the lattice constant $\bar{a}$ measured along the chain axis and an integer n. We can solve numerically the one-dimensional Schrödinger equation of the effective Hamiltonian (7.6) for the auxiliary orbital ζ_λ using a plane-wave basis, with the potential depth $\bar{V}_0$ chosen to suppress strongly any tunneling between different wells. Alternatively, we can also arrive analytically at the expression for the lowest-energy eigenstate of (7.6) in the deep-well limit $\bar{V}_0 \to \infty$ by starting from the solution of the problem of a single potential well at the origin, which assumes the form

$$w(\xi) = \begin{cases} \sqrt{\dfrac{2}{\bar{b}}}\cos\dfrac{\pi\xi}{\bar{b}} & \text{, if } |\xi| < \bar{b}/2 \\ 0 & \text{, else} \end{cases} . \tag{7.7}$$

Then, the auxiliary orbital is obtained as the inverse Fourier transformation of the Wannier-like function $w(\xi)$ with respect to the lattice positions Ξ. Building onto the expected Bloch shape, we find that the lattice-periodic part in Eq. (7.5) is given by

$$\rho_\lambda(\xi) = \mathrm{e}^{-\mathrm{i}\lambda\xi}\sum_{\Xi}\mathrm{e}^{\mathrm{i}\lambda\Xi}w(\xi - \Xi) \,. \tag{7.8}$$

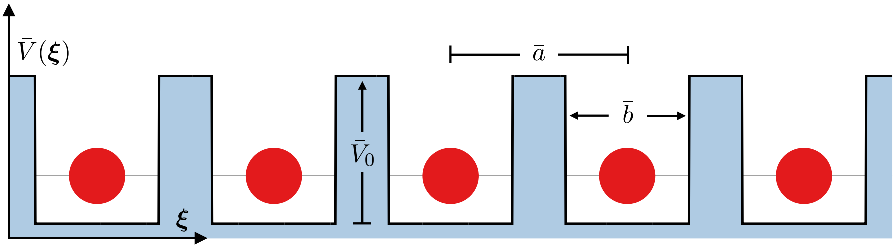

Figure 7.1: Periodic potential $\bar{V}(\boldsymbol{\xi})$ in the auxiliary real space $\boldsymbol{\xi}$. As discussed in the main text, the potential landscape of the one-dimensional chain of virtual atoms (red balls) is defined as series of finite potential wells of depth $\bar{V}_0$, well width $\bar{b}$, and lattice constant $\bar{a}$.

As will be shown below, the overlaps between these lattice-periodic functions at different values λ and $\lambda+\beta$ of the additional parameter are some of the key ingredients for constructing the sought HDWFs. Thus, we note for later reference that

$$\langle \rho_\lambda | \rho_{\lambda+\beta} \rangle = 8\pi^2 \frac{\sin\left(\beta\bar{b}/2\right)}{\beta\bar{b}(4\pi^2 - \beta^2\bar{b}^2)} = 1 + \frac{\beta^2\bar{b}^2}{24\pi^2}(6-\pi^2) + \mathcal{O}(\beta^4)\,, \tag{7.9}$$

where the integration is performed over one unit cell in the auxiliary real space, and β plays a similar role like the vector $\boldsymbol{b}$ in Eq. (5.9) connecting neighboring grid points. Remarkably, while the overlaps (7.9) hinge explicitly on β, they are independent of the parameter λ itself. Moreover, it follows from the above Taylor expansion of the overlaps that $\langle \rho_\lambda | \partial_\lambda \rho_\lambda \rangle = 0$ and $\langle \rho_\lambda | \partial_\lambda^2 \rho_\lambda \rangle = (6-\pi^2)\bar{b}^2/(12\pi^2)$, which we use at a later stage in the expressions for the centers of HDWFs.

7.2.2 Product states and composite Hamiltonian

Before defining eventually generalized tight-binding functions, we turn now to the higher-dimensional product states $|\Phi_{\boldsymbol{k}\boldsymbol{\lambda}n}\rangle$ given by the usual Bloch states and the auxiliary orbitals that we elucidated earlier. Exploiting Eq. (7.5), we rewrite the product states in Eq. (7.3) as

$$\Phi_{\boldsymbol{k}\boldsymbol{\lambda}n}(\boldsymbol{r},\boldsymbol{\xi}) = \mathrm{e}^{\mathrm{i}\boldsymbol{k}\cdot\boldsymbol{r}}\mathrm{e}^{\mathrm{i}\boldsymbol{\lambda}\cdot\boldsymbol{\xi}}\phi_{\boldsymbol{k}\boldsymbol{\lambda}n}(\boldsymbol{r},\boldsymbol{\xi})\,, \tag{7.10}$$

where

$$\phi_{\boldsymbol{k}\boldsymbol{\lambda}n}(\boldsymbol{r},\boldsymbol{\xi}) = u_{\boldsymbol{k}\boldsymbol{\lambda}n}(\boldsymbol{r})\rho_{\boldsymbol{\lambda}}(\boldsymbol{\xi}) \qquad \text{or} \qquad |\phi_{\boldsymbol{k}\boldsymbol{\lambda}n}\rangle = |u_{\boldsymbol{k}\boldsymbol{\lambda}n}\rangle \otimes |\rho_{\boldsymbol{\lambda}}\rangle \tag{7.11}$$

denotes a lattice-periodic function in the higher-dimensional real space $(\boldsymbol{r},\boldsymbol{\xi})$. Owing to the introduced auxiliary orbitals, the product states are guaranteed to be orthogonal in $\boldsymbol{k}$, in $\boldsymbol{\lambda}$, and in the band index: $\langle \Phi_{\boldsymbol{k}\boldsymbol{\lambda}n} | \Phi_{\boldsymbol{k}'\boldsymbol{\lambda}'m} \rangle = N_{\boldsymbol{k}} N_{\boldsymbol{\lambda}} \delta_{\boldsymbol{k}\boldsymbol{k}'} \delta_{\boldsymbol{\lambda}\boldsymbol{\lambda}'} \delta_{nm}$. In addition, these functions are periodic with respect to both the crystal momentum and the abstract parameter $\boldsymbol{\lambda}$.

At this point the logical question arises to which Hamiltonian $\mathcal{H}$ the product states (7.10) are eigenstates in the higher-dimensional real space. Clearly, due to the product shape of these functions, the sought Hamiltonian decomposes into two additive terms. If $\bar{H}$ stands for the single-particle Hamiltonian in the auxiliary space (see Eq. (7.4)), the corresponding operator of the full system is given by

$$\mathcal{H}(\boldsymbol{r},\boldsymbol{\xi}) = H(\boldsymbol{r}) + \bar{H}(\boldsymbol{\xi}) \qquad \text{or} \qquad \mathcal{H} = H \oplus \bar{H} \,. \tag{7.12}$$

Here, the Hamiltonian H that carries no explicit dependence on the abstract parameter $\boldsymbol{\lambda}$ can formally be expressed based on the individual members $H^{(\boldsymbol{\lambda})}$ as

$$H(\boldsymbol{r}) = \int H^{(\boldsymbol{\lambda})}(\boldsymbol{r})\delta(\hat{\boldsymbol{\lambda}} - \boldsymbol{\lambda})\,\mathrm{d}\boldsymbol{\lambda}\,, \tag{7.13}$$

where $\hat{\boldsymbol{\lambda}}|\psi_{\boldsymbol{k\lambda}n}\rangle = \boldsymbol{\lambda}|\psi_{\boldsymbol{k\lambda}n}\rangle$. Upon acting with this Hamiltonian on the usual Bloch state $|\psi_{\boldsymbol{k\lambda}n}\rangle$, the Delta function selects from the family of Hamiltonians the member $H^{(\boldsymbol{\lambda})}$ that corresponds to the particular parameter value of the Bloch state. Consequently, it follows from Eq. (7.1) that $H|\psi_{\boldsymbol{k\lambda}n}\rangle = \mathcal{E}_{\boldsymbol{k\lambda}n}|\psi_{\boldsymbol{k\lambda}n}\rangle$, meaning that the Bloch states are eigenstates of H. The product states satisfy therefore the equation

$$\mathcal{H}(\boldsymbol{r},\boldsymbol{\xi})\Phi_{\boldsymbol{k\lambda}n}(\boldsymbol{r},\boldsymbol{\xi}) = \left(\mathcal{E}_{\boldsymbol{k\lambda}n} + \bar{\mathcal{E}}_{\boldsymbol{\lambda}}\right)\Phi_{\boldsymbol{k\lambda}n}(\boldsymbol{r},\boldsymbol{\xi})\,, \tag{7.14}$$

with $\bar{\mathcal{E}}_{\boldsymbol{\lambda}}$ representing the energy of the auxiliary orbital at the parameter value $\boldsymbol{\lambda}$. Due to the additional energy dispersion $\bar{\mathcal{E}}_{\boldsymbol{\lambda}}$ entering in Eq. (7.14), the eigenvalues of the higher-dimensional Hamiltonian $\mathcal{H} = H \oplus \bar{H}$ differ generally from the *ab initio* band energies, which we would like to interpolate ultimately. In order to achieve the identity between the two sets of eigenvalues, we study the deep-well limit for the Hamiltonian $\bar{H}$, in the case of which the energy level $\bar{\mathcal{E}}_{\boldsymbol{\lambda}}$ becomes independent of $\boldsymbol{\lambda}$. Thus, by choosing the zero of energy properly, we can render $\bar{\mathcal{E}}_{\boldsymbol{\lambda}}$ drop out of Eq. (7.14) such that

$$\mathcal{H}(\boldsymbol{r},\boldsymbol{\xi})\Phi_{\boldsymbol{k\lambda}n}(\boldsymbol{r},\boldsymbol{\xi}) = \mathcal{E}_{\boldsymbol{k\lambda}n}\Phi_{\boldsymbol{k\lambda}n}(\boldsymbol{r},\boldsymbol{\xi})\,. \tag{7.15}$$

Therefore, a generalized technique that interpolates the higher-dimensional Hamiltonian $\mathcal{H}$ grants also directly access to the interpolated electronic structure of the physical Hamiltonian H of interest.

7.3 Definition and maximal localization

We establish an efficient generalization of WFs for higher-dimensional phase spaces by performing Fourier transformations of the orthogonal product states discussed above with respect to both $\boldsymbol{k}$ and $\boldsymbol{\lambda}$. The sought objects that originate from such a construction are referred to as higher-dimensional Wannier functions (HDWFs):

$$W_{\boldsymbol{R}\Xi n}(\boldsymbol{r},\boldsymbol{\xi}) = \frac{1}{N_{\boldsymbol{k}}}\frac{1}{N_{\boldsymbol{\lambda}}}\sum_{\boldsymbol{k\lambda}m} \mathrm{e}^{-\mathrm{i}\boldsymbol{k}\cdot\boldsymbol{R}}\mathrm{e}^{-\mathrm{i}\boldsymbol{\lambda}\cdot\Xi}\mathcal{U}_{mn}^{(\boldsymbol{k},\boldsymbol{\lambda})}\Phi_{\boldsymbol{k\lambda}m}(\boldsymbol{r},\boldsymbol{\xi})\,. \tag{7.16}$$

Analogously to the case of standard MLWFs, the HDWFs are labeled by an orbital index n and the direct lattice vector $\boldsymbol{R}$. However, these functions are distinguished by an additional lattice vector Ξ that is related to $\boldsymbol{\lambda}$ just like the direct lattice vector $\boldsymbol{R}$ is conjugate to the crystal momentum $\boldsymbol{k}$. The localization properties of HDWFs are mediated by the unitary gauge transformations $\mathcal{U}^{(\boldsymbol{k},\boldsymbol{\lambda})}$, and $N_{\boldsymbol{k}}$ and $N_{\boldsymbol{\lambda}}$ stand for the number of mesh points used to sample the phase space of $\boldsymbol{k}$ and $\boldsymbol{\lambda}$, respectively. Owing to the fact that the product states $|\Phi_{\boldsymbol{k\lambda}n}\rangle$ are orthogonal, the constructed orbitals $|W_{\boldsymbol{R}\Xi n}\rangle$ constitute an orthonormal basis, *i.e.*, $\langle W_{\boldsymbol{R}\Xi n}|W_{\boldsymbol{R}'\Xi' m}\rangle = \delta_{\boldsymbol{RR}'}\delta_{\Xi\Xi'}\delta_{nm}$, where the integration is performed over the supercell in the higher-dimensional real space.

7.3.1 Centers and spread in real space

To develop an initial interpretation of the orbitals $|W_{\boldsymbol{R}\boldsymbol{\Xi}n}\rangle$ given by Eq. (7.16), we begin by considering the expressions for the centers of these functions in $\boldsymbol{r}$ and $\boldsymbol{\xi}$. The centers of HDWFs in the physical real space $\boldsymbol{r}$ can be directly related to the Brillouin-zone sum of the Berry connection in crystal momentum space:

$$\langle W_{\mathbf{0}\mathbf{0}n}|\boldsymbol{r}|W_{\mathbf{0}\mathbf{0}n}\rangle = \frac{\mathrm{i}}{N_{\boldsymbol{k}}N_{\boldsymbol{\lambda}}}\sum_{\boldsymbol{k}\boldsymbol{\lambda}}\langle\phi^{(\mathrm{W})}_{\boldsymbol{k}\boldsymbol{\lambda}n}|\nabla_{\boldsymbol{k}}|\phi^{(\mathrm{W})}_{\boldsymbol{k}\boldsymbol{\lambda}n}\rangle = \frac{\mathrm{i}}{N_{\boldsymbol{k}}N_{\boldsymbol{\lambda}}}\sum_{\boldsymbol{k}\boldsymbol{\lambda}}\langle u^{(\mathrm{W})}_{\boldsymbol{k}\boldsymbol{\lambda}n}|\nabla_{\boldsymbol{k}}|u^{(\mathrm{W})}_{\boldsymbol{k}\boldsymbol{\lambda}n}\rangle\,, \tag{7.17}$$

which is the generalization of the expression for the centers of MLWFs, and it can be derived easily by taking into account the form of the Bloch-like lattice-periodic parts $|\phi^{(\mathrm{W})}_{\boldsymbol{k}\boldsymbol{\lambda}n}\rangle = \sum_m \mathcal{U}^{(\boldsymbol{k},\boldsymbol{\lambda})}_{mn}|\phi_{\boldsymbol{k}\boldsymbol{\lambda}m}\rangle$ and $|u^{(\mathrm{W})}_{\boldsymbol{k}\boldsymbol{\lambda}n}\rangle = \sum_m \mathcal{U}^{(\boldsymbol{k},\boldsymbol{\lambda})}_{mn}|u_{\boldsymbol{k}\boldsymbol{\lambda}m}\rangle$ that include the unitary gauge transformation $\mathcal{U}^{(\boldsymbol{k},\boldsymbol{\lambda})}$. Remarkably, Eq. (7.17) is independent of the auxiliary orbitals as the momentum gradient does not act on $|\rho_{\boldsymbol{\lambda}}\rangle$. We obtain similarly the centers in the auxiliary space if we start from Eq. (7.16) and evaluate the expectation value of $\boldsymbol{\xi}$ in the HDWF basis, which yields

$$\begin{aligned}\langle W_{\mathbf{0}\mathbf{0}n}|\boldsymbol{\xi}|W_{\mathbf{0}\mathbf{0}n}\rangle &= \frac{\mathrm{i}}{N_{\boldsymbol{k}}N_{\boldsymbol{\lambda}}}\sum_{\boldsymbol{k}\boldsymbol{\lambda}}\langle\phi^{(\mathrm{W})}_{\boldsymbol{k}\boldsymbol{\lambda}n}|\nabla_{\boldsymbol{\lambda}}|\phi^{(\mathrm{W})}_{\boldsymbol{k}\boldsymbol{\lambda}n}\rangle\\ &= \frac{\mathrm{i}}{N_{\boldsymbol{k}}N_{\boldsymbol{\lambda}}}\sum_{\boldsymbol{k}\boldsymbol{\lambda}}\left[\langle u^{(\mathrm{W})}_{\boldsymbol{k}\boldsymbol{\lambda}n}|\nabla_{\boldsymbol{\lambda}}|u^{(\mathrm{W})}_{\boldsymbol{k}\boldsymbol{\lambda}n}\rangle + \langle\rho_{\boldsymbol{\lambda}}|\nabla_{\boldsymbol{\lambda}}|\rho_{\boldsymbol{\lambda}}\rangle\right]\,.\end{aligned} \tag{7.18}$$

Although this expression appears to depend explicitly on the auxiliary orbitals, the according contribution $\langle\rho_{\boldsymbol{\lambda}}|\nabla_{\boldsymbol{\lambda}}|\rho_{\boldsymbol{\lambda}}\rangle$ vanishes in the deep-well limit (see Eq. (7.8)) such that

$$\langle W_{\mathbf{0}\mathbf{0}n}|\boldsymbol{\xi}|W_{\mathbf{0}\mathbf{0}n}\rangle = \frac{\mathrm{i}}{N_{\boldsymbol{k}}N_{\boldsymbol{\lambda}}}\sum_{\boldsymbol{k}\boldsymbol{\lambda}}\langle u^{(\mathrm{W})}_{\boldsymbol{k}\boldsymbol{\lambda}n}|\nabla_{\boldsymbol{\lambda}}|u^{(\mathrm{W})}_{\boldsymbol{k}\boldsymbol{\lambda}n}\rangle\,. \tag{7.19}$$

Consequently, the centers in the auxiliary space are given by the Brillouin-zone sum of the Berry connection of the Bloch-like periodic parts in the phase space of the generic parameter $\boldsymbol{\lambda}$. The expectation values for the squared position operators amount to

$$\langle W_{\mathbf{0}\mathbf{0}n}|r^2|W_{\mathbf{0}\mathbf{0}n}\rangle = \frac{-1}{N_{\boldsymbol{k}}N_{\boldsymbol{\lambda}}}\sum_{\boldsymbol{k}\boldsymbol{\lambda}}\langle\phi^{(\mathrm{W})}_{\boldsymbol{k}\boldsymbol{\lambda}n}|\nabla^2_{\boldsymbol{k}}|\phi^{(\mathrm{W})}_{\boldsymbol{k}\boldsymbol{\lambda}n}\rangle = \frac{-1}{N_{\boldsymbol{k}}N_{\boldsymbol{\lambda}}}\sum_{\boldsymbol{k}\boldsymbol{\lambda}}\langle u^{(\mathrm{W})}_{\boldsymbol{k}\boldsymbol{\lambda}n}|\nabla^2_{\boldsymbol{k}}|u^{(\mathrm{W})}_{\boldsymbol{k}\boldsymbol{\lambda}n}\rangle\,, \tag{7.20}$$

as well as

$$\begin{aligned}\langle W_{\mathbf{0}\mathbf{0}n}|\xi^2|W_{\mathbf{0}\mathbf{0}n}\rangle &= \frac{-1}{N_{\boldsymbol{k}}N_{\boldsymbol{\lambda}}}\sum_{\boldsymbol{k}\boldsymbol{\lambda}}\langle\phi^{(\mathrm{W})}_{\boldsymbol{k}\boldsymbol{\lambda}n}|\nabla^2_{\boldsymbol{\lambda}}|\phi^{(\mathrm{W})}_{\boldsymbol{k}\boldsymbol{\lambda}n}\rangle\\ &= \frac{-1}{N_{\boldsymbol{k}}N_{\boldsymbol{\lambda}}}\sum_{\boldsymbol{k}\boldsymbol{\lambda}}\left[\langle u^{(\mathrm{W})}_{\boldsymbol{k}\boldsymbol{\lambda}n}|\nabla^2_{\boldsymbol{\lambda}}|u^{(\mathrm{W})}_{\boldsymbol{k}\boldsymbol{\lambda}n}\rangle + \langle\rho_{\boldsymbol{\lambda}}|\nabla^2_{\boldsymbol{\lambda}}|\rho_{\boldsymbol{\lambda}}\rangle\right]\,.\end{aligned} \tag{7.21}$$

Contrary to the center coordinates in $\boldsymbol{\xi}$ that are independent of the auxiliary orbitals, the expectation value of ξ^2 acquires a finite contribution from the overlap $\langle\rho_{\boldsymbol{\lambda}}|\nabla^2_{\boldsymbol{\lambda}}|\rho_{\boldsymbol{\lambda}}\rangle$.

In connection with Eqs. (7.17) and (7.19) for the centers, the above expressions can be used to determine the generalized spread functional $\tilde{\Omega}$ that evaluates the spatial extent of HDWFs in the higher-dimensional real space:

$$\tilde{\Omega} = \sum_n \left(\langle W_{\mathbf{0}\mathbf{0}n}|\mathfrak{r}^2|W_{\mathbf{0}\mathbf{0}n}\rangle - \langle W_{\mathbf{0}\mathbf{0}n}|\mathfrak{r}|W_{\mathbf{0}\mathbf{0}n}\rangle^2\right)\,, \tag{7.22}$$

where we introduced the generalized position operator $\boldsymbol{\mathfrak{r}} = (\boldsymbol{r}, \boldsymbol{\xi})$ in order to simplify the notation. As we explained in Sec. 5.2, the constraint of minimal real-space spread defines the usual MLWFs unambiguously up to a global phase factor. Analogously, the unitary gauge transformations $\mathcal{U}^{(\boldsymbol{k},\boldsymbol{\lambda})}$ that enter in the definition of HDWFs, Eq. (7.16), can be fixed by imposing the condition of minimal spread $\tilde{\Omega}$ in the higher-dimensional real space. This renders the resulting states $|W_{\boldsymbol{R}\boldsymbol{\Xi}n}\rangle$ not only localized but also unique up to a global phase factor.

7.3.2 Iterative spread minimization

The procedure of maximal localization by means of the WANNIER90 program is conventionally carried out in the three-dimensional real space. When constructing the HDWFs, however, it is necessary to extend this scheme by including the auxiliary variable $\boldsymbol{\xi}$ into the picture. Therefore, we extend the WANNIER90 program to higher dimensions in order to minimize systematically the spread $\tilde{\Omega}$ given by Eq. (7.22) in the combined real space of $\boldsymbol{r}$ and $\boldsymbol{\xi}$. Owing to the auxiliary space, obviously, the centers of HDWFs possess the additional coordinates (7.19). To define the composite lattice structure in the $(\boldsymbol{r}, \boldsymbol{\xi})$-space, we employ the higher-dimensional but block-diagonal Bravais matrix

$$A = \begin{pmatrix} A_1 & 0 \\ 0 & A_2 \end{pmatrix} , \tag{7.23}$$

where A_1 denotes the usual 3×3 Bravais matrix of the solid, and the rank of A_2 is identical to the dimension of the auxiliary space $\boldsymbol{\xi}$ that we intend to study. Associated with the direct lattice defined by the Bravais matrix A is a reciprocal lattice in the higher-dimensional phase space $(\boldsymbol{k}, \boldsymbol{\lambda})$, which entangles the crystal momentum and the abstract parameter. Just like the Brillouin zone of the crystal momentum is sampled uniformly by a Monkhorst-Pack grid, the considered values of $\boldsymbol{\lambda}$ constitute an equidistant mesh. Based on the expressions (7.17)–(7.21) for the real-space properties of HDWFs, we can exploit analogous finite-difference expressions to those in Ref. [174] to evaluate the spread $\tilde{\Omega}$. However, we point out that the role of the periodic parts $|u_{\boldsymbol{k}n}\rangle$, which enter conventionally the calculation of the spread, is now played by their higher-dimensional analogs $|\phi_{\boldsymbol{k}\boldsymbol{\lambda}n}\rangle$ defined by Eq. (7.11). To apply the finite differences, we are required to set up all necessary neighbors $(\boldsymbol{k} + \boldsymbol{b}_{\boldsymbol{k}}, \boldsymbol{\lambda} + \boldsymbol{b}_{\boldsymbol{\lambda}})$ of a point $(\boldsymbol{k}, \boldsymbol{\lambda})$, where the vectors $\boldsymbol{b}_{\boldsymbol{k}}$ and $\boldsymbol{b}_{\boldsymbol{\lambda}}$ connect the two points in the higher-dimensional reciprocal space. In general, our specific choice of the Bravais matrix facilitates this step since only those neighbors with either $\boldsymbol{b}_{\boldsymbol{k}} = \boldsymbol{0}$ or $\boldsymbol{b}_{\boldsymbol{\lambda}} = \boldsymbol{0}$ need to be taken into account.

Using the overlaps $\langle \phi_{\boldsymbol{k}\boldsymbol{\lambda}m} | \phi_{\boldsymbol{k}+\boldsymbol{b}_{\boldsymbol{k}}\, \boldsymbol{\lambda}+\boldsymbol{b}_{\boldsymbol{\lambda}}\, n} \rangle$ of the lattice-periodic wave functions at neighboring points in the composite phase space $(\boldsymbol{k}, \boldsymbol{\lambda})$, we can compute the centers and spreads of HDWFs. As we select the directions of $\boldsymbol{k}$ and $\boldsymbol{\lambda}$ to be orthogonal in the higher-dimensional reciprocal lattice, the overlaps consist of two contributions:

$$M_{mn}^{(\boldsymbol{k},\boldsymbol{b})}(\boldsymbol{\lambda}) = \langle \phi_{\boldsymbol{k}\boldsymbol{\lambda}m} | \phi_{\boldsymbol{k}+\boldsymbol{b}\, \boldsymbol{\lambda}n} \rangle , \tag{7.24}$$

$$\bar{M}_{mn}^{(\boldsymbol{\lambda},\boldsymbol{b})}(\boldsymbol{k}) = \langle \phi_{\boldsymbol{k}\boldsymbol{\lambda}m} | \phi_{\boldsymbol{k}\, \boldsymbol{\lambda}+\boldsymbol{b}\, n} \rangle , \tag{7.25}$$

depending on whether we are concerned with neighboring $\boldsymbol{k}$-points for fixed values of $\boldsymbol{\lambda}$ or vice versa. Owing to the shape of the periodic states $|\phi_{\boldsymbol{k}\boldsymbol{\lambda}m}\rangle$ in terms of products, Eq. (7.11), the overlaps are simplified further to yield

$$M_{mn}^{(\boldsymbol{k},\boldsymbol{b})}(\boldsymbol{\lambda}) = \langle u_{\boldsymbol{k}\boldsymbol{\lambda}m} | u_{\boldsymbol{k}+\boldsymbol{b}\,\boldsymbol{\lambda}n} \rangle \,, \tag{7.26}$$

$$\bar{M}_{mn}^{(\boldsymbol{\lambda},\boldsymbol{b})}(\boldsymbol{k}) = \langle u_{\boldsymbol{k}\boldsymbol{\lambda}m} | u_{\boldsymbol{k}\,\boldsymbol{\lambda}+\boldsymbol{b}\,n} \rangle \langle \rho_{\boldsymbol{\lambda}} | \rho_{\boldsymbol{\lambda}+\boldsymbol{b}} \rangle = \mathcal{M}_{mn}^{(\boldsymbol{\lambda},\boldsymbol{b})}(\boldsymbol{k}) \langle \rho_{\boldsymbol{\lambda}} | \rho_{\boldsymbol{\lambda}+\boldsymbol{b}} \rangle \,, \tag{7.27}$$

where the lattice-periodic functions $|u_{\boldsymbol{k}\boldsymbol{\lambda}n}\rangle$ of the usual Bloch states and $|\rho_{\boldsymbol{\lambda}}\rangle$ of the auxiliary orbitals enter. Implementing the overlaps (7.26) within the full-potential linearized augmented-plane-wave (FLAPW) method is straightforward and can be done analogously to the procedure outlined in Ref. [180]. In contrast, the overlaps (7.27) for different values of the abstract parameter $\boldsymbol{\lambda}$ are conceptually distinct as they rely (i) on the integrals $\langle \rho_{\boldsymbol{\lambda}} | \rho_{\boldsymbol{\lambda}+\boldsymbol{b}} \rangle$, for which analytic or numerical expressions may be used, and (ii) on the overlaps $\mathcal{M}_{mn}^{(\boldsymbol{\lambda},\boldsymbol{b})}(\boldsymbol{k}) = \langle u_{\boldsymbol{k}\boldsymbol{\lambda}m} | u_{\boldsymbol{k}\,\boldsymbol{\lambda}+\boldsymbol{b}\,n} \rangle$ between periodic parts of the Bloch states. In particular, any implementation aiming at the computation of $\mathcal{M}_{mn}^{(\boldsymbol{\lambda},\boldsymbol{b})}$ depends on the physical nature that is assigned to the generic parameter $\boldsymbol{\lambda}$. We present below a comprehensive overview of the implementation of these matrix elements within the FLAPW method for the example of the magnetization direction as the parameter $\boldsymbol{\lambda}$.

Apart from the previously described overlaps, the typical projections of Bloch states onto localized trial orbitals $g_n(\boldsymbol{r}) = \langle \boldsymbol{r} | g_n \rangle$ are also replaced in the systematic construction of maximally-localized HDWFs by projections of the product states onto new trial functions $p_n(\boldsymbol{r}, \boldsymbol{\xi})$ that are localized in the higher-dimensional real space. These projections mark the starting point for minimizing the spread $\tilde{\Omega}$ iteratively. Recalling the product shape of the wave functions $|\Phi_{\boldsymbol{k}\boldsymbol{\lambda}n}\rangle$, Eq. (7.5), we make the ansatz $p_n(\boldsymbol{r}, \boldsymbol{\xi}) = g_n(\boldsymbol{r}) h(\boldsymbol{\xi})$ or $|p_n\rangle = |g_n\rangle \otimes |h\rangle$ for the trial functions to arrive at

$$A_{mn}^{(\boldsymbol{k},\boldsymbol{\lambda})} = \langle \Phi_{\boldsymbol{k}\boldsymbol{\lambda}m} | p_n \rangle = \langle \psi_{\boldsymbol{k}\boldsymbol{\lambda}m} | g_n \rangle \langle \zeta_{\boldsymbol{\lambda}} | h \rangle \,. \tag{7.28}$$

Thus, the projections onto the localized trial functions factorize into the usual projections of Bloch states and the auxiliary projection $\langle \zeta_{\boldsymbol{\lambda}} | h \rangle$. While the computation of the projections $\langle \psi_{\boldsymbol{k}\boldsymbol{\lambda}m} | g_n \rangle$ within the FLAPW method is the same as in Ref. [180], the auxiliary ingredients $\langle \zeta_{\boldsymbol{\lambda}} | h \rangle$ can be found either numerically or analytically by choosing an appropriate $|h\rangle$. In practice, we find that the convergence of the HDWFs is often insensitive to the specific choice that is made for the localized function $\langle \boldsymbol{\xi} | h \rangle$.

7.3.3 HDWFs for the magnetization direction

In the case of MLWFs, the expressions to construct within the FLAPW method the necessary ingredients $M_{mn}^{(\boldsymbol{k},\boldsymbol{b})}$ and $A_{mn}^{(\boldsymbol{k})}$ are provided in Ref. [180]. Aiming at the generation of HDWFs, we need to evaluate additionally Eq. (7.27), *i.e.*, new overlaps of the wave functions at neighboring points in the higher-dimensional phase space are required. Although the proposed scheme applies to generic periodic parameters that drive the adiabatic Hamiltonian evolution, we restrict ourselves in this thesis to realizations of this scenario where the magnetization direction specified by the angle θ plays the role of the abstract parameter. In the following, we provide the computational expressions to compute the overlaps $\langle u^{\sigma}_{\boldsymbol{k}\theta m} | u^{\sigma'}_{\boldsymbol{k}\theta+b_\theta n} \rangle$, where σ and σ' label the spin of the θ-dependent spinor wave functions $|u_{\boldsymbol{k}\theta n}\rangle$ in the corresponding local spin coordinate frame that is specified by the magnetization direction in the used second-variation scheme [73]. Therefore, we transform these overlaps at the end into the global coordinate frame with the spin-quantization axis along z according to

$$\mathcal{M}_{mn}^{(\theta,b_\theta)}(\boldsymbol{k}) = \sum_{\sigma} \langle u^{\mathrm{gl},\sigma}_{\boldsymbol{k}\theta m} | u^{\mathrm{gl},\sigma}_{\boldsymbol{k}\theta+b_\theta n} \rangle = \sum_{\sigma\sigma'} \left[\chi^\dagger(\theta)\chi(\theta+b_\theta)\right]_{\sigma\sigma'} \langle u^{\sigma}_{\boldsymbol{k}\theta m} | u^{\sigma'}_{\boldsymbol{k}\theta+b_\theta n} \rangle \,. \tag{7.29}$$

where the spinor $|u_{\boldsymbol{k}\theta n}\rangle$ that is given in the local frame was transformed to the global one via $|u^{\mathrm{gl}}_{\boldsymbol{k}\theta n}\rangle = \chi(\theta)|u_{\boldsymbol{k}\theta n}\rangle$ with $\chi(\theta)$ given by Eq. (3.42) with $\varphi = 0°$. Based on the FLAPW partitioning, the overlaps on the far right hand-side in the local frame acquire various contributions originating from different regions of real space.

Interstitial region Using the standard expansion of the wave function into plane waves with wave vector $\boldsymbol{G}$ (see also Chapter 3), we note that the expansion coefficients in the interstitial region carry now a dependence on the angle θ:

$$\psi^{\sigma}_{\boldsymbol{k}\theta n}(\boldsymbol{r}) = \frac{1}{\sqrt{V}} \sum_{\boldsymbol{G}} c^{\boldsymbol{G}\sigma}_{\boldsymbol{k}n}(\theta) \mathrm{e}^{\mathrm{i}(\boldsymbol{k}+\boldsymbol{G})\cdot\boldsymbol{r}} \,. \tag{7.30}$$

Consequently, the overlaps of the lattice-periodic parts in the local coordinate frame assume the form

$$\langle u^{\sigma}_{\boldsymbol{k}\theta m} | u^{\sigma'}_{\boldsymbol{k}\theta+b_\theta n} \rangle = \sum_{\boldsymbol{G}\boldsymbol{G}'} \left(c^{\boldsymbol{G}\sigma}_{\boldsymbol{k}m}(\theta)\right)^* c^{\boldsymbol{G}'\sigma'}_{\boldsymbol{k}n}([\theta+b_\theta])\Theta(\boldsymbol{G}'-\boldsymbol{G}) \,, \tag{7.31}$$

where the Fourier transformation $\Theta(\boldsymbol{G})$ of the step function cutting out the interstitial region has been defined in Eq. (5.31), and the neighboring point $[\theta + b_\theta]$ lies in the "first Brillouin zone" of values for θ[2]. Although the above expression is reminiscent of the implementation of the usual overlaps $M^{(\boldsymbol{k},\boldsymbol{b})}_{mn}$ [180], we point out that plane-wave coefficients to different magnetization directions are necessary to evaluate Eq. (7.31).

Muffin tins In the case of a variable magnetization direction, the coefficients in the expansion of the muffin-tin wave functions hinge on θ such that the Bloch states in the local spin frame are given by

$$\psi^{\sigma}_{\boldsymbol{k}\theta n}(\boldsymbol{r}) = \sum_{L\mu} \left[A^{\mu,\sigma}_{Ln}(\boldsymbol{k},\theta)u^{\mu,\sigma}_{l}(r_\mu) + B^{\mu,\sigma}_{Ln}(\boldsymbol{k},\theta)\dot{u}^{\mu,\sigma}_{l}(r_\mu)\right] Y_L(\hat{\boldsymbol{r}}_\mu) \,, \tag{7.32}$$

where L stands for the set of angular momentum quantum numbers (l, l_z), $\boldsymbol{r}_\mu$ is the position vector relative to the μth muffin tin, and the spinors u^{μ}_{l} and $\dot{u}^{\mu}_{l}$ are a radial solution of the spherical Hamiltonian and its energy derivative, respectively. Exploiting the orthogonality of the spherical harmonics, the overlaps between the lattice-periodic parts at different magnetization directions read

$$\begin{aligned} \langle u^{\sigma}_{\boldsymbol{k}\theta m} | u^{\sigma'}_{\boldsymbol{k}\theta+b_\theta n} \rangle = \sum_{L\mu} \Big[& \left(A^{\mu,\sigma}_{Lm}(\boldsymbol{k},\theta)\right)^* A^{\mu,\sigma'}_{Ln}(\boldsymbol{k},[\theta+b])t^{\mu,L}_{11}(\sigma,\sigma') \\ & + \left(A^{\mu,\sigma}_{Lm}(\boldsymbol{k},\theta)\right)^* B^{\mu,\sigma'}_{Ln}(\boldsymbol{k},[\theta+b])t^{\mu,L}_{12}(\sigma,\sigma') \\ & + \left(B^{\mu,\sigma}_{Lm}(\boldsymbol{k},\theta)\right)^* A^{\mu,\sigma'}_{Ln}(\boldsymbol{k},[\theta+b])t^{\mu,L}_{21}(\sigma,\sigma') \\ & + \left(B^{\mu,\sigma}_{Lm}(\boldsymbol{k},\theta)\right)^* B^{\mu,\sigma'}_{Ln}(\boldsymbol{k},[\theta+b])t^{\mu,L}_{22}(\sigma,\sigma') \Big] \,, \end{aligned} \tag{7.33}$$

---

[2] In practice, we ensure that the Bloch states are periodic in θ by choosing the latter from the interval $[0, 4\pi)$. Alternatively, it is possible to explicitly account in the Fourier transformations for the minus that the Bloch spinors acquire under a full rotation of the spin-1/2 moments.

where the coefficients t_{ij} represent θ-independent integrals of the radial solutions and their energy derivatives:

$$t_{11}^{\mu,L}(\sigma,\sigma') = \int r_\mu^2\, u_l^{\mu,\sigma}(r_\mu) u_l^{\mu,\sigma'}(r_\mu)\,\mathrm{d}r_\mu\,, \tag{7.34}$$

$$t_{12}^{\mu,L}(\sigma,\sigma') = \int r_\mu^2\, u_l^{\mu,\sigma}(r_\mu) \dot{u}_l^{\mu,\sigma'}(r_\mu)\,\mathrm{d}r_\mu\,, \tag{7.35}$$

and analogously for t_{21} and t_{22}. As compared to the implementation of the usual overlaps $M_{mn}^{(\boldsymbol{k},\boldsymbol{b})}$ [180], the calculation of the above t-integrals is computationally less expensive as they do not include the Gaunt coefficients. However, we need to contract expansion coefficients to different values of θ in order to evaluate the muffin-tin contribution to the new overlaps (7.29). If the basis set is supplemented with local orbitals (LOs), the above expressions are easily generalized.

Vacuum contribution in film calculations In the study of two-dimensional geometries using the film implementation of the FLEUR program, an additional contribution to the overlaps arises from two semi-infinite vacua [72]. The Bloch states in each of the vacua, which extend from $-\infty$ to $-D/2$ as well as $D/2$ to ∞, are represented by

$$\begin{aligned}\psi_{\boldsymbol{k}\theta n}^{\sigma}(\boldsymbol{r}) &= \sum_{\boldsymbol{G}} \Big(a_{\boldsymbol{k}}^{\boldsymbol{G}n,\sigma}(\theta) u_{\boldsymbol{k}}^{\boldsymbol{G}_\parallel,\sigma}(z) + b_{\boldsymbol{k}}^{\boldsymbol{G}n,\sigma}(\theta) \dot{u}_{\boldsymbol{k}}^{\boldsymbol{G}_\parallel,\sigma}(z) \Big)\, \mathrm{e}^{\mathrm{i}(\boldsymbol{k}+\boldsymbol{G}_\parallel)\cdot \boldsymbol{x}_\parallel} \\ &= \sum_{\boldsymbol{G}} \Psi_{\boldsymbol{k}}^{\boldsymbol{G}n,\sigma}(\theta,z)\, \mathrm{e}^{\mathrm{i}(\boldsymbol{k}+\boldsymbol{G}_\parallel)\cdot \boldsymbol{x}_\parallel}\,,\end{aligned} \tag{7.36}$$

where the function $\Psi_{\boldsymbol{k}}^{\boldsymbol{G}n}$ contains the one-dimensional solutions $u_{\boldsymbol{k}}^{\boldsymbol{G}_\parallel}$ of the Schrödinger equation in the corresponding vacuum region as well as their energy derivatives. In addition, $\boldsymbol{G} = (\boldsymbol{G}_\parallel, G_z)$ and $\boldsymbol{r} = (\boldsymbol{r}_\parallel, z)$, and $\boldsymbol{k} = (k_x, k_y, 0)$ is considered to reside in the two-dimensional Brillouin zone associated with the film plane, which is supposed to be perpendicular to the z-axis. Introducing for convenience the abbreviation

$$\beta_{\boldsymbol{k}mn}^{\boldsymbol{G}\boldsymbol{G}',\sigma\sigma'}(\theta,[\theta+b_\theta],z) = \Big(\Psi_{\boldsymbol{k}}^{\boldsymbol{G}m,\sigma}(\theta,z)\Big)^{*}\, \Psi_{\boldsymbol{k}}^{\boldsymbol{G}'n,\sigma'}([\theta+b_\theta],z)\,, \tag{7.37}$$

we arrive at the final expression for the vacuum contribution to the sought overlaps in the local spin frame:

$$\langle u_{\boldsymbol{k}\theta m}^{\sigma} | u_{\boldsymbol{k}\theta+b_\theta n}^{\sigma'} \rangle = S_\parallel \sum_{\boldsymbol{G}\boldsymbol{G}'} \delta_{\boldsymbol{G}_\parallel - \boldsymbol{G}'_\parallel} \int_{\pm\mathcal{D}/2}^{\pm\infty} \beta_{\boldsymbol{k}mn}^{\boldsymbol{G}\boldsymbol{G}',\sigma\sigma'}(\theta,[\theta+b_\theta],z)\,\mathrm{d}z\,, \tag{7.38}$$

where the area of the in-plane unit cell is denoted as $S_\parallel$. The other contribution from the second vacuum region is derived analogously. When treating one-dimensional geometries within the FLAPW methodology [185], we find similarly contributions from the corresponding vacuum region to the matrix elements (7.29).

Projections onto trial functions In order to generate first-guess HDWFs, the projections of the Bloch states onto localized trial orbitals g_n need to be evaluated within the FLAPW method according to Eq. (7.28). We choose these trial orbitals to be zero everywhere but near the μth muffin-tin sphere to which the corresponding first guess should be associated. The angular character of the trial functions is controlled via the coefficients in the expansion $g_n(\boldsymbol{r}) = \sum_L c_{Ln}\tilde{u}_l(r_\mu)Y_L(\hat{\boldsymbol{r}}_\mu)$, and the radial function $\tilde{u}_l$ can be chosen, *e.g.*, as the first-principles states u_l^μ of the radial Schrödinger equation. If the orthogonality of the spherical harmonics is exploited, the necessary projections amount to

$$\begin{aligned}\langle\psi_{\boldsymbol{k}\theta m}|g_n\rangle = \sum_{L\sigma}\Bigg[&(A^{\mu,\sigma}_{Lm}(\boldsymbol{k},\theta))^*\, c^\sigma_{Ln}\int r_\mu^2\, u_l^{\mu,\sigma}(r_\mu)\tilde{u}_l^\sigma(r_\mu)\,\mathrm{d}r_\mu \\ &+ (B^{\mu,\sigma}_{Lm}(\boldsymbol{k},\theta))^*\, c^\sigma_{Ln}\int r_\mu^2\, \dot{u}_l^{\mu,\sigma}(r_\mu)\tilde{u}_l^\sigma(r_\mu)\,\mathrm{d}r_\mu\Bigg]\,.\end{aligned} \tag{7.39}$$

Apart from the explicit θ-dependence of the expansion coefficients, these computational expressions are analogous to those provided in Ref. [180] for the usual MLWFs.

7.4 Higher-dimensional Wannier interpolation

By separating explicitly the real-space positions $\boldsymbol{r}$ and $\boldsymbol{\xi}$, the direct lattice vectors $\boldsymbol{R}$ and Ξ, and the variables $\boldsymbol{k}$ and $\boldsymbol{\lambda}$ in reciprocal space, so far, we emphasized the conceptual differences that arise from integrating an abstract parameter into the Wannier formalism. In the remainder of this chapter, however, we adopt a simplified notation (i) to imitate for clarity the well-known terminology of the standard WFs, and (ii) to stress the strong formal analogies between a higher-dimensional Wannier interpolation based on HDWFs (see Fig. 7.2) and the conventional interpolation technique.

For this purpose, we introduce the following quantities in higher dimensions:

$$\boldsymbol{\mathfrak{K}} = (\boldsymbol{k},\boldsymbol{\lambda})\,, \qquad \boldsymbol{\mathfrak{r}} = (\boldsymbol{r},\boldsymbol{\xi})\,, \qquad \boldsymbol{\mathfrak{R}} = (\boldsymbol{R},\Xi) \tag{7.40}$$

as the generalized momentum vector $\boldsymbol{\mathfrak{K}}$, the generalized position vector $\boldsymbol{\mathfrak{r}}$, and the generalized lattice vector $\boldsymbol{\mathfrak{R}}$, respectively. If we define in addition $N_{\boldsymbol{\mathfrak{K}}} = N_{\boldsymbol{k}}N_{\boldsymbol{\lambda}}$, the definition (7.16) of HDWFs assumes the compact form

$$W_{\boldsymbol{\mathfrak{R}}n}(\boldsymbol{\mathfrak{r}}) = \frac{1}{N_{\boldsymbol{\mathfrak{K}}}}\sum_{\boldsymbol{\mathfrak{K}}m}\mathrm{e}^{-\mathrm{i}\boldsymbol{\mathfrak{K}}\cdot\boldsymbol{\mathfrak{R}}}\,\mathcal{U}^{(\boldsymbol{\mathfrak{K}})}_{mn}\Phi_{\boldsymbol{\mathfrak{K}}m}(\boldsymbol{\mathfrak{r}})\,, \tag{7.41}$$

which is formally identical to the definition of MLWFs although it should be kept in mind that the key ingredients are fundamentally different for the two cases.

7.4.1 Multiparameter Hamiltonian

After generating a single set of HDWFs via the adapted procedure of maximal localization, we can calculate the periodic parts of Bloch-like functions by inverting the above Fourier transformation:

$$|\phi^{(\mathrm{W})}_{\boldsymbol{\mathfrak{K}}n}\rangle = \sum_{\boldsymbol{\mathfrak{R}}}\mathrm{e}^{-\mathrm{i}\boldsymbol{\mathfrak{K}}\cdot(\boldsymbol{\mathfrak{r}}-\boldsymbol{\mathfrak{R}})}|W_{\boldsymbol{\mathfrak{R}}n}\rangle = |u^{(\mathrm{W})}_{\boldsymbol{\mathfrak{K}}n}\rangle\otimes|\rho_{\boldsymbol{\lambda}}\rangle\,, \tag{7.42}$$

which belong to the so-called Wannier gauge as indicated by the superscript "W". Inside of the energy window that is spanned by the constructed HDWFs, the single-particle Hamiltonian H describing the electronic system of interest can be interpolated

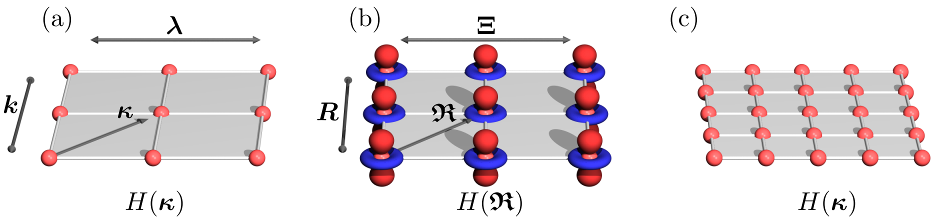

Figure 7.2: Scheme of the higher-dimensional Wannier interpolation. (a) Initially, the electronic structure is known on a coarse mesh of few $\boldsymbol{\mathfrak{K}}$-points, where the variable $\boldsymbol{\mathfrak{K}} = (\boldsymbol{k}, \boldsymbol{\lambda})$ encompasses the crystal momentum $\boldsymbol{k}$ and the abstract parameter $\boldsymbol{\lambda}$. (b) Based on this information, we construct a set of higher-dimensional Wannier functions that are localized at positions $\boldsymbol{\mathfrak{R}} = (\boldsymbol{R}, \boldsymbol{\Xi})$ in the extended real space. (c) Using the generalized hoppings $H(\boldsymbol{\mathfrak{R}})$, we establish by means of an inverse Fourier transformation an efficient but accurate interpolation of the Hamiltonian onto a much denser $\boldsymbol{\mathfrak{K}}$-grid.

with respect to $\boldsymbol{\mathfrak{K}}$. As in the usual method, the matrix elements of H in the basis of HDWFs initiate the higher-dimensional Wannier interpolation (see Fig. 7.2):

$$H_{nm}(\boldsymbol{\mathfrak{R}}) = \langle W_{\boldsymbol{0}n}|H|W_{\boldsymbol{\mathfrak{R}}m}\rangle = \frac{1}{N_{\boldsymbol{\mathfrak{K}}}}\sum_{\boldsymbol{\mathfrak{K}}\ell} \mathrm{e}^{-\mathrm{i}\boldsymbol{\mathfrak{K}}\cdot\boldsymbol{\mathfrak{R}}} \left(\mathcal{U}^{(\boldsymbol{\mathfrak{K}})}_{\ell n}\right)^{*} \mathcal{E}_{\boldsymbol{\mathfrak{K}}\ell}\,\mathcal{U}^{(\boldsymbol{\mathfrak{K}})}_{\ell m} , \tag{7.43}$$

where the $\boldsymbol{\mathfrak{K}}$-sum is over the *ab initio* mesh that underlies the maximal-localization procedure. These generalized hopping elements decay rapidly with the distance $|\boldsymbol{\mathfrak{R}}|$, and depend further solely on the difference vector connecting the two HDWFs:

$$\langle W_{\boldsymbol{\mathfrak{R}}'n}|H|W_{\boldsymbol{\mathfrak{R}}m}\rangle = \langle W_{\boldsymbol{0}n}|H|W_{\boldsymbol{\mathfrak{R}}-\boldsymbol{\mathfrak{R}}'m}\rangle = H_{nm}(\boldsymbol{\mathfrak{R}} - \boldsymbol{\mathfrak{R}}') . \tag{7.44}$$

Since the hoppings $H_{nm}(\boldsymbol{\mathfrak{R}})$ converge quickly with the number of mesh points, they can be calculated from the electronic structure known on a relatively coarse grid of $\boldsymbol{\mathfrak{K}}$-points. Through an inverse Fourier transformation one obtains a particularly efficient interpolation of the Hamiltonian at any desired point $\boldsymbol{\mathfrak{K}}$ in the higher-dimensional phase space, even though this point might originally not be contained in the coarse mesh used for constructing the set of HDWFs:

$$H^{(\mathrm{W})}_{nm}(\boldsymbol{\mathfrak{K}}) = \langle \phi^{(\mathrm{W})}_{\boldsymbol{\mathfrak{K}}n}|H_{\boldsymbol{k}}|\phi^{(\mathrm{W})}_{\boldsymbol{\mathfrak{K}}m}\rangle = \sum_{\boldsymbol{\mathfrak{R}}} \mathrm{e}^{\mathrm{i}\boldsymbol{\mathfrak{K}}\cdot\boldsymbol{\mathfrak{R}}}\langle W_{\boldsymbol{0}n}|H|W_{\boldsymbol{\mathfrak{R}}m}\rangle . \tag{7.45}$$

Due to the strong localization of the HDWFs in real space, only few lattice vectors $\boldsymbol{\mathfrak{R}}$ need to be considered in the summation. The interpolated band energies are readily accessible after the Hamiltonian matrix (7.45) was diagonalized using an appropriate unitary matrix $V^{(\boldsymbol{\mathfrak{K}})}$ such that

$$H^{(\mathrm{H})}_{nm}(\boldsymbol{\mathfrak{K}}) = \left[\left(V^{(\boldsymbol{\mathfrak{K}})}\right)^{\dagger} H^{(\mathrm{W})}(\boldsymbol{\mathfrak{K}})\, V^{(\boldsymbol{\mathfrak{K}})}\right]_{nm} = \mathcal{E}_{\boldsymbol{\mathfrak{K}}n}\delta_{nm} . \tag{7.46}$$

Similarly, the periodic parts of the interpolated wave functions assume the form

$$|\phi^{(\mathrm{H})}_{\boldsymbol{\mathfrak{K}}n}\rangle = \sum_{m} |\phi^{(\mathrm{W})}_{\boldsymbol{\mathfrak{K}}m}\rangle V^{(\boldsymbol{\mathfrak{K}})}_{mn} = |u^{(\mathrm{H})}_{\boldsymbol{\mathfrak{K}}n}\rangle \otimes |\rho_{\boldsymbol{\lambda}}\rangle , \tag{7.47}$$

where the superscript "H" denotes the so-called Hamiltonian gauge, in which the matrix of the interpolated Hamiltonian becomes diagonal.

7.4.2 Pure and mixed Berry curvatures

Beyond the interpolation of the electronic structure, our generalized technique based on HDWFs grants the pure Berry curvatures $\Omega^{\boldsymbol{kk}}$ and $\Omega^{\boldsymbol{\lambda\lambda}}$ as well as the mixed Berry curvatures $\Omega^{\boldsymbol{k\lambda}}$ and $\Omega^{\boldsymbol{\lambda k}}$, all of which determine the general Berry curvature tensor (4.38). Thereby, the generalized interpolation contributes to a complete characterization of the geometry of the underlying higher-dimensional phase space. The scheme that we propose to calculate these geometric objects is rather analogous to the conventional approach for the momentum-space Berry curvature [183] in that all quantities are eventually evaluated under the Hamiltonian gauge. While the method in Ref. [183] is restricted to the phase space of crystal momentum, however, we are able to study by means of the higher-dimensional interpolation the aforementioned (otherwise hidden) Berry curvatures that drive intriguing geometric phenomena, for example, the antidamping spin-orbit torques (4.52) in inversion-asymmetric magnets. In addition, the anisotropy of transport properties such as the anomalous Hall conductivity is readily available as a beneficial "side effect" of our general approach.

To begin with, we consider the well-known expression of the Berry curvature matrix

$$\begin{aligned}\Omega^{(\mathrm{H})}_{nm,\alpha\beta}(\boldsymbol{\mathfrak{K}}) &= \partial_\alpha A^{(\mathrm{H})}_{nm,\beta}(\boldsymbol{\mathfrak{K}}) - \partial_\beta A^{(\mathrm{H})}_{nm,\alpha}(\boldsymbol{\mathfrak{K}}) \\ &= -2\mathrm{Im}\langle \partial_\alpha u^{(\mathrm{H})}_{\boldsymbol{\mathfrak{K}}n} | \partial_\beta u^{(\mathrm{H})}_{\boldsymbol{\mathfrak{K}}m}\rangle\,,\end{aligned}\tag{7.48}$$

where $A^{(\mathrm{H})}_{nm,\alpha}(\boldsymbol{\mathfrak{K}}) = \mathrm{i}\langle u^{(\mathrm{H})}_{\boldsymbol{\mathfrak{K}}n} | \partial_\alpha u^{(\mathrm{H})}_{\boldsymbol{\mathfrak{K}}m}\rangle$ is the Berry connection matrix of the lattice-periodic parts $|u^{(\mathrm{H})}_{\boldsymbol{\mathfrak{K}}n}\rangle$ of the Bloch states, and $\partial_\alpha = \partial/\partial\mathfrak{K}_\alpha$ with $\mathfrak{K}_\alpha$ as αth entry of $\boldsymbol{\mathfrak{K}}$. The total Berry curvature of all occupied states is locally gauge-invariant and given by

$$\Omega_{\alpha\beta}(\boldsymbol{\mathfrak{K}}) = \sum_n f^{(\mathrm{H})}_{\boldsymbol{\mathfrak{K}}n} \Omega^{(\mathrm{H})}_{nn,\alpha\beta}(\boldsymbol{\mathfrak{K}})\,,\tag{7.49}$$

where the occupation numbers $f^{(\mathrm{H})}_{\boldsymbol{\mathfrak{K}}n}$ are either zero or one at zero temperature. On the one hand, pure Berry curvatures are obtained if α and β refer to the same parameter type. For instance, we recover from Eq. (7.49) the pure momentum Berry curvature that gives rise to the anomalous Hall effect if $\alpha = k_i$ and $\beta = k_j$. On the other hand, if α and β refer to distinct variable types, we obtain mixed Berry curvatures. These geometric objects determine, *e.g.*, magneto-electric coupling effects in clean materials with broken inversion symmetry [28,237], given that the abstract parameter $\boldsymbol{\lambda}$ in the Hamiltonian plays the role of the magnetization direction $\hat{\boldsymbol{m}}$, Eq. (4.52).

The total Berry curvature (7.49) can be rewritten by evaluating the derivative of the wave functions $|u^{(\mathrm{H})}_{\boldsymbol{\mathfrak{K}}n}\rangle$ that are defined through Eq. (7.47):

$$|\partial_\alpha u^{(\mathrm{H})}_{\boldsymbol{\mathfrak{K}}n}\rangle = \sum_m |\partial_\alpha u^{(\mathrm{W})}_{\boldsymbol{\mathfrak{K}}m}\rangle V^{(\boldsymbol{\mathfrak{K}})}_{mn} + \sum_m |u^{(\mathrm{W})}_{\boldsymbol{\mathfrak{K}}m}\rangle \left(\partial_\alpha V^{(\boldsymbol{\mathfrak{K}})}_{mn}\right)\,.\tag{7.50}$$

Next, we introduce for every matrix $\mathcal{O}$ the abbreviation $\bar{\mathcal{O}}^{(\mathrm{H})} = V^\dagger \mathcal{O}^{(\mathrm{W})} V$, which we utilize to reformulate the second term above since $\partial_\alpha V^{(\boldsymbol{\mathfrak{K}})} = V^{(\boldsymbol{\mathfrak{K}})} D^{(\mathrm{H})}_\alpha(\boldsymbol{\mathfrak{K}})$ where

$$D^{(\mathrm{H})}_{mn,\alpha}(\boldsymbol{\mathfrak{K}}) = \begin{cases} \dfrac{\bar{H}^{(\mathrm{H})}_{mn,\alpha}}{\mathcal{E}_{\boldsymbol{\mathfrak{K}}n} - \mathcal{E}_{\boldsymbol{\mathfrak{K}}m}} & \text{, if } n \neq m \\ 0 & \text{, if } n = m \end{cases}\,,\tag{7.51}$$

which follows from standard perturbation theory with respect to α. In the previous definition $\bar{H}^{(\mathrm{H})}_\alpha = V^\dagger \partial_\alpha H^{(\mathrm{W})} V$ with $H^{(\mathrm{W})}$ given by Eq. (7.45). As a consequence, we arrive at an alternative expression for Eq. (7.50):

$$|\partial_\alpha u^{(\mathrm{H})}_{\boldsymbol{\mathfrak{K}}n}\rangle = \sum_m |\partial_\alpha u^{(\mathrm{W})}_{\boldsymbol{\mathfrak{K}}m}\rangle V^{(\boldsymbol{\mathfrak{K}})}_{mn} + \sum_m |u^{(\mathrm{H})}_{\boldsymbol{\mathfrak{K}}m}\rangle D^{(\mathrm{H})}_{mn,\alpha}(\boldsymbol{\mathfrak{K}}) \,. \tag{7.52}$$

The adopted simplified notation renders the wave-function derivatives formally identical to Eq. (26) of Ref. [183], which provides derivatives with respect to the crystal momentum only. However, we emphasize that the above equation is generalized to the higher-dimensional case, and thus it enables us to compute on an equal footing the response of the wave functions upon changing the abstract parameter $\boldsymbol{\lambda}$. Based on Eq. (7.52), we may carry out similar algebra as in Ref. [183] using the relation

$$A^{(\mathrm{H})}_{nm,\alpha}(\boldsymbol{\mathfrak{K}}) = \bar{A}^{(\mathrm{H})}_{nm,\alpha}(\boldsymbol{\mathfrak{K}}) + \mathrm{i} D^{(\mathrm{H})}_{nm,\alpha}(\boldsymbol{\mathfrak{K}}) \tag{7.53}$$

to obtain the final result for the $\boldsymbol{\mathfrak{K}}$-dependent Berry curvature of all occupied states:

$$\begin{aligned}\Omega_{\alpha\beta}(\boldsymbol{\mathfrak{K}}) = {} & \sum_n f^{(\mathrm{H})}_{\boldsymbol{\mathfrak{K}}n} \bar{\Omega}^{(\mathrm{H})}_{nn,\alpha\beta} + \mathrm{i} \sum_{nm} (f^{(\mathrm{H})}_{\boldsymbol{\mathfrak{K}}m} - f^{(\mathrm{H})}_{\boldsymbol{\mathfrak{K}}n}) D^{(\mathrm{H})}_{nm,\alpha} D^{(\mathrm{H})}_{mn,\beta} \\ & + \sum_{nm} (f^{(\mathrm{H})}_{\boldsymbol{\mathfrak{K}}m} - f^{(\mathrm{H})}_{\boldsymbol{\mathfrak{K}}n}) \left[D^{(\mathrm{H})}_{nm,\alpha} \bar{A}^{(\mathrm{H})}_{mn,\beta} - D^{(\mathrm{H})}_{nm,\beta} \bar{A}^{(\mathrm{H})}_{mn,\alpha} \right] ,\end{aligned} \tag{7.54}$$

which grants access to pure or mixed Berry curvatures, depending on the explicit physical nature of the variables that are associated with the labels α and β.

Except for the occupation numbers, all quantities that enter Eq. (7.54) are first calculated in the Wannier gauge and then rotated using the unitary transformation $V^{(\boldsymbol{\mathfrak{K}})}$ that diagonalizes the interpolated Hamiltonian. Thus, in order to evaluate by means of the higher-dimensional Wannier interpolation $\bar{\Omega}^{(\mathrm{H})}_{\alpha\beta}(\boldsymbol{\mathfrak{K}})$, $\bar{A}^{(\mathrm{H})}_\alpha(\boldsymbol{\mathfrak{K}})$, and $D^{(\mathrm{H})}_\alpha(\boldsymbol{\mathfrak{K}})$, the corresponding quantities are needed first in the Wannier gauge. From Eqs. (7.42) and (7.45), and from the condition[3] $\langle \rho_{\boldsymbol{\lambda}} | \partial_\alpha \rho_{\boldsymbol{\lambda}} \rangle = 0$, it follows that

$$H^{(\mathrm{W})}_{nm,\alpha}(\boldsymbol{\mathfrak{K}}) = \sum_{\boldsymbol{\mathfrak{R}}} \mathrm{i} \mathfrak{R}_\alpha \mathrm{e}^{\mathrm{i}\boldsymbol{\mathfrak{K}}\cdot\boldsymbol{\mathfrak{R}}} \langle W_{\mathbf{0}n} | H | W_{\boldsymbol{\mathfrak{R}}m} \rangle \,, \tag{7.55}$$

$$A^{(\mathrm{W})}_{nm,\alpha}(\boldsymbol{\mathfrak{K}}) = \sum_{\boldsymbol{\mathfrak{R}}} \mathrm{e}^{\mathrm{i}\boldsymbol{\mathfrak{K}}\cdot\boldsymbol{\mathfrak{R}}} \langle W_{\mathbf{0}n} | \mathfrak{r}_\alpha | W_{\boldsymbol{\mathfrak{R}}m} \rangle \,, \tag{7.56}$$

$$\Omega^{(\mathrm{W})}_{nm,\alpha\beta}(\boldsymbol{\mathfrak{K}}) = \sum_{\boldsymbol{\mathfrak{R}}} \mathrm{i} \mathrm{e}^{\mathrm{i}\boldsymbol{\mathfrak{K}}\cdot\boldsymbol{\mathfrak{R}}} \left[\mathfrak{R}_\alpha \langle W_{\mathbf{0}n} | \mathfrak{r}_\beta | W_{\boldsymbol{\mathfrak{R}}m} \rangle - \mathfrak{R}_\beta \langle W_{\mathbf{0}n} | \mathfrak{r}_\alpha | W_{\boldsymbol{\mathfrak{R}}m} \rangle \right] \,. \tag{7.57}$$

Clearly, the hoppings $\langle W_{\mathbf{0}n} | H | W_{\boldsymbol{\mathfrak{R}}m} \rangle$ and the matrix elements of the generalized position operator in the HDWF basis, $\langle W_{\mathbf{0}n} | \mathfrak{r}_\alpha | W_{\boldsymbol{\mathfrak{R}}m} \rangle$, are required to determine the sought quantities. These ingredients are obtained by inverting Eqs. (7.45) and (7.56) on the coarse *ab initio* mesh. While the hoppings relate to the band energies according to Eq. (7.43), the matrix elements of the higher-dimensional position operator amount to

$$\langle W_{\mathbf{0}n} | \mathfrak{r}_\alpha | W_{\boldsymbol{\mathfrak{R}}m} \rangle = \frac{\mathrm{i}}{N_{\boldsymbol{\mathfrak{K}}}} \sum_{\boldsymbol{\mathfrak{K}}} \mathrm{e}^{-\mathrm{i}\boldsymbol{\mathfrak{K}}\cdot\boldsymbol{\mathfrak{R}}} \langle \phi^{(\mathrm{W})}_{\boldsymbol{\mathfrak{K}}n} | \partial_\alpha \phi^{(\mathrm{W})}_{\boldsymbol{\mathfrak{K}}m} \rangle \,. \tag{7.58}$$

---

[3] Recall that $\langle \rho_{\boldsymbol{\lambda}} | \partial_{\boldsymbol{k}} | \rho_{\boldsymbol{\lambda}} \rangle = 0$ trivially, and $\langle \rho_{\boldsymbol{\lambda}} | \partial_{\boldsymbol{\lambda}} | \rho_{\boldsymbol{\lambda}} \rangle = 0$ can be achieved by proper choice of the auxiliary orbitals, *e.g.*, by considering the deep-well limit, Eq. (7.9).

Using for the wave-function derivative in Eq. (7.58) the finite-difference formula [174]

$$|\partial_\alpha \phi^{(\mathrm{W})}_{\boldsymbol{\mathfrak{K}}m}\rangle = \sum_{\boldsymbol{b}} w_b b_\alpha \left(|\phi^{(\mathrm{W})}_{\boldsymbol{\mathfrak{K}}+\boldsymbol{b}m}\rangle - |\phi^{(\mathrm{W})}_{\boldsymbol{\mathfrak{K}}m}\rangle \right) + O(b^2)\,, \tag{7.59}$$

where $\boldsymbol{b}$ connects neighboring $\boldsymbol{\mathfrak{K}}$-points and w_b are appropriately chosen weights, we realize that the higher-dimensional positions (7.58) along the αth direction are determined by the overlaps at neighboring grid points $\boldsymbol{\mathfrak{K}}$ and $\boldsymbol{\mathfrak{K}}+\boldsymbol{b}$:

$$\begin{aligned}\langle W_{\mathbf{0}n}|\mathfrak{r}_\alpha|W_{\boldsymbol{\mathfrak{R}}m}\rangle &= \frac{\mathrm{i}}{N_{\boldsymbol{\mathfrak{K}}}} \sum_{\boldsymbol{\mathfrak{K}}\boldsymbol{b}} \mathrm{e}^{-\mathrm{i}\boldsymbol{\mathfrak{K}}\cdot\boldsymbol{\mathfrak{R}}} w_b b_\alpha \left[\langle \phi^{(\mathrm{W})}_{\boldsymbol{\mathfrak{K}}n} | \phi^{(\mathrm{W})}_{\boldsymbol{\mathfrak{K}}+\boldsymbol{b}m}\rangle - \delta_{nm} \right] \\ &= \frac{\mathrm{i}}{N_{\boldsymbol{\mathfrak{K}}}} \sum_{\boldsymbol{\mathfrak{K}}\boldsymbol{b}} \mathrm{e}^{-\mathrm{i}\boldsymbol{\mathfrak{K}}\cdot\boldsymbol{\mathfrak{R}}} w_b b_\alpha \left[\left\{ \left(\mathcal{U}^{(\boldsymbol{\mathfrak{K}})}\right)^\dagger M^{(\boldsymbol{\mathfrak{K}},\boldsymbol{b})} \mathcal{U}^{(\boldsymbol{\mathfrak{K}}+\boldsymbol{b})} \right\}_{nm} - \delta_{nm} \right] ,\end{aligned} \tag{7.60}$$

where $M^{(\boldsymbol{\mathfrak{K}},\boldsymbol{b})}_{nm} = \langle \phi_{\boldsymbol{\mathfrak{K}}n} | \phi_{\boldsymbol{\mathfrak{K}}+\boldsymbol{b}m}\rangle$ denotes the overlap of the *ab initio* wave functions $|\phi_{\boldsymbol{\mathfrak{K}}n}\rangle$, which constitute the key objects in the construction of maximally-localized HDWFs.

7.4.3 Spiralization tensor

Considering now situations where the abstract parameter $\boldsymbol{\lambda}$ is the magnetization direction $\hat{\boldsymbol{m}}$, we apply the higher-dimensional Wannier interpolation to extract the DMI spiralization, Eq. (4.58), by resorting to the analogies with the orbital magnetization noted earlier. The orbital magnetization of periodic systems at zero temperature can be evaluated based on a gauge-invariant formulation of the usual Wannier interpolation [184], which we generalize here to calculate the spiralization D_{ij} from HDWFs. To begin with, we decompose the spiralization D_{ij} into a local circulation D^{lc}_{ij} and an itinerant circulation D^{ic}_{ij} that read

$$D^{\mathrm{lc}}_{ij} = \frac{\hat{\boldsymbol{e}}_i}{NV} \cdot \mathrm{Im} \sum_{\boldsymbol{k}n}^{\mathrm{occ}} \hat{\boldsymbol{m}} \times \left\langle \frac{\partial u_{\boldsymbol{\mathfrak{K}}n}}{\partial \hat{\boldsymbol{m}}} \middle| H_{\boldsymbol{k}} - \mathcal{E}_{\mathrm{F}} \middle| \frac{\partial u_{\boldsymbol{\mathfrak{K}}n}}{\partial k_j} \right\rangle, \tag{7.61}$$

$$D^{\mathrm{ic}}_{ij} = \frac{\hat{\boldsymbol{e}}_i}{NV} \cdot \mathrm{Im} \sum_{\boldsymbol{k}n}^{\mathrm{occ}} \hat{\boldsymbol{m}} \times \left\langle \frac{\partial u_{\boldsymbol{\mathfrak{K}}n}}{\partial \hat{\boldsymbol{m}}} \middle| \mathcal{E}_{\boldsymbol{\mathfrak{K}}n} - \mathcal{E}_{\mathrm{F}} \middle| \frac{\partial u_{\boldsymbol{\mathfrak{K}}n}}{\partial k_j} \right\rangle, \tag{7.62}$$

such that $D_{ij} = D^{\mathrm{lc}}_{ij} + D^{\mathrm{ic}}_{ij}$. After introducing the operator $\mathcal{P}(\boldsymbol{\mathfrak{K}}) = \sum_n^{\mathrm{occ}} |u_{\boldsymbol{\mathfrak{K}}n}\rangle\langle u_{\boldsymbol{\mathfrak{K}}n}|$ and its complement $\mathcal{Q}(\boldsymbol{\mathfrak{K}}) = 1 - \mathcal{P}(\boldsymbol{\mathfrak{K}})$ that project onto the manifold of all occupied and unoccupied states, respectively, we may define the “geometric” objects[4]

$$\mathcal{F}_{\alpha\beta}(\boldsymbol{\mathfrak{K}}) = \mathrm{Tr}\left[(\partial_\alpha \mathcal{P})\mathcal{Q}(\partial_\beta \mathcal{P})\right] , \tag{7.63}$$

$$\mathcal{G}_{\alpha\beta}(\boldsymbol{\mathfrak{K}}) = \mathrm{Tr}\left[(\partial_\alpha \mathcal{P})\mathcal{Q}H_{\boldsymbol{k}}\mathcal{Q}(\partial_\beta \mathcal{P})\right] , \tag{7.64}$$

$$\mathcal{H}_{\alpha\beta}(\boldsymbol{\mathfrak{K}}) = \mathrm{Tr}\left[H_{\boldsymbol{k}}(\partial_\alpha \mathcal{P})\mathcal{Q}(\partial_\beta \mathcal{P})\right] , \tag{7.65}$$

where the dependence of $\mathcal{P}$ and $\mathcal{Q}$ on $\boldsymbol{\mathfrak{K}}$ is implied, α and β denote possibly distinct types of phase-space variables, and Tr denotes the trace over the full electronic Hilbert

---

[4] As both $\mathcal{G}_{\alpha\beta}$ and $\mathcal{H}_{\alpha\beta}$ rely explicitly on the Hamiltonian $H_{\boldsymbol{k}}$, only the term $\mathcal{F}_{\alpha\beta}$ related to the Berry curvature is a strictly geometric property of the underlying phase space.

space of all states. Since the trace is invariant under unitary basis transformations, the above quantities are gauge-invariant.

As in the case of the orbital magnetization [184], the two contributions (7.61) and (7.62) of the spiralization can be rewritten as ground-state properties that are individually gauge-invariant:

$$D_{ij}^{\mathrm{lc}} = \frac{\hat{\boldsymbol{e}}_i}{NV} \cdot \mathrm{Im} \sum_{\boldsymbol{k}} \hat{\boldsymbol{m}} \times \left(\boldsymbol{\mathcal{G}}_{\hat{\boldsymbol{m}} k_j} - \mathcal{E}_{\mathrm{F}} \boldsymbol{\mathcal{F}}_{\hat{\boldsymbol{m}} k_j} \right) \, , \tag{7.66}$$

$$D_{ij}^{\mathrm{ic}} = \frac{\hat{\boldsymbol{e}}_i}{NV} \cdot \mathrm{Im} \sum_{\boldsymbol{k}} \hat{\boldsymbol{m}} \times \left(\boldsymbol{\mathcal{H}}_{\hat{\boldsymbol{m}} k_j} - \mathcal{E}_{\mathrm{F}} \boldsymbol{\mathcal{F}}_{\hat{\boldsymbol{m}} k_j} \right) \, , \tag{7.67}$$

where the short-hand vector notation $\boldsymbol{\mathcal{F}}_{\hat{\boldsymbol{m}} k_j}$, for instance, stands for the geometric quantity of Eq. (7.63) with $\partial_\alpha = \partial_{\hat{\boldsymbol{m}}}$ being the gradient with respect to the magnetization direction $\hat{\boldsymbol{m}}$ and $\partial_\beta = \partial_{k_j}$ as the derivative in the jth component of the crystal momentum. Consequently, $\boldsymbol{\mathcal{F}}_{\hat{\boldsymbol{m}} k_j}$ mediates the mixed Berry curvature $\Omega^{\hat{\boldsymbol{m}}\boldsymbol{k}}$ in the higher-dimensional phase space, and we remark in passing that this framework provides an alternative expression to compute the torkance (4.52), which quantifies the antidamping SOTs:

$$\tau_{ij} = \frac{2e}{N} \hat{\boldsymbol{e}}_i \cdot \mathrm{Im} \sum_{\boldsymbol{k}} \hat{\boldsymbol{m}} \times \boldsymbol{\mathcal{F}}_{\hat{\boldsymbol{m}} k_j} \, . \tag{7.68}$$

Using that $\mathrm{Im}\,\mathrm{Tr}\left[(\partial_\alpha \mathcal{P})\mathcal{P}(\partial_\beta \mathcal{P})\right] = 0$ and plugging the definition (7.63) into Eq. (7.68), we easily verify that the above formula is indeed identical to Eq. (4.52). Similarly, we can prove that the sum of Eqs. (7.66) and (7.67) is identical to the expression for the DMI in the modern theory, Eq. (4.58).

So far, we did not specify any gauge choice (*i.e.*, no superscript was given to the wave functions) under which $\mathcal{F}_{\alpha\beta}$, $\mathcal{G}_{\alpha\beta}$, and $\mathcal{H}_{\alpha\beta}$ are evaluated. Even though these phase-space quantities are in principle gauge-invariant, it is most convenient to calculate them from wave functions in the Wannier gauge (with "W" as superscript). Then, the projection operator onto the manifold spanned by the M Bloch-like states in the Wannier gauge, Eq. (7.42), assumes the form $\mathcal{P} = \sum_{nm}^{M} |\phi_{\boldsymbol{\mathfrak{K}}n}^{(\mathrm{W})}\rangle f_{nm}^{(\mathrm{W})} \langle \phi_{\boldsymbol{\mathfrak{K}}m}^{(\mathrm{W})}|$, where the non-diagonal matrix $f^{(\mathrm{W})}$ is obtained by transforming the diagonal occupation matrix $f^{(\mathrm{H})}$ into the Wannier gauge via the Hermitian conjugate of $V^{(\boldsymbol{\mathfrak{K}})}$. We introduce also $g^{(\mathrm{W})} = 1 - f^{(\mathrm{W})}$, where "1" stands for the identity matrix in the considered M-dimensional subspace. In strong formal analogy to the derivations in Ref. [184] for the orbital magnetization, we arrive at the following expressions for the phase-space objects that underlie the DMI spiralization:

$$\begin{aligned} \mathrm{Im}\, \mathcal{F}_{\alpha\beta} = &- \frac{1}{2} \mathrm{Re}\,\mathrm{tr} \left[f^{(\mathrm{W})} \Omega_{\alpha\beta}^{(\mathrm{W})} \right] \\ &+ \mathrm{Im}\,\mathrm{tr} \left[f^{(\mathrm{W})} A_\alpha^{(\mathrm{W})} g^{(\mathrm{W})} J_\beta^{(\mathrm{W})} + f^{(\mathrm{W})} J_\alpha^{(\mathrm{W})} g^{(\mathrm{W})} A_\beta^{(\mathrm{W})} \right] \\ &+ \mathrm{Im}\,\mathrm{tr} \left[f^{(\mathrm{W})} J_\alpha^{(\mathrm{W})} g^{(\mathrm{W})} J_\beta^{(\mathrm{W})} \right] \, , \end{aligned} \tag{7.69}$$

$$\begin{aligned}\operatorname{Im}\mathcal{G}_{\alpha\beta} = &-\frac{1}{2}\operatorname{Re}\operatorname{tr}\left[f^{(\mathrm{W})}\Lambda^{(\mathrm{W})}_{\alpha\beta}\right] + \operatorname{Im}\operatorname{tr}\left[f^{(\mathrm{W})}H^{(\mathrm{W})}f^{(\mathrm{W})}A^{(\mathrm{W})}_{\alpha}f^{(\mathrm{W})}A^{(\mathrm{W})}_{\beta}\right]\\ &+\operatorname{Im}\operatorname{tr}\left[f^{(\mathrm{W})}(J^{(\mathrm{W})}_{\alpha}g^{(\mathrm{W})}B^{(\mathrm{W})}_{\beta} - J^{(\mathrm{W})}_{\beta}g^{(\mathrm{W})}B^{(\mathrm{W})}_{\alpha})\right]\\ &+\operatorname{Im}\operatorname{tr}\left[f^{(\mathrm{W})}J^{(\mathrm{W})}_{\alpha}g^{(\mathrm{W})}H^{(\mathrm{W})}g^{(\mathrm{W})}J^{(\mathrm{W})}_{\beta}\right]\,, \end{aligned}\tag{7.70}$$

$$\begin{aligned}\operatorname{Im}\mathcal{H}_{\alpha\beta} = &-\frac{1}{2}\operatorname{Re}\operatorname{tr}\left[f^{(\mathrm{W})}H^{(\mathrm{W})}f^{(\mathrm{W})}\Omega^{(\mathrm{W})}_{\alpha\beta}\right] - \operatorname{Im}\operatorname{tr}\left[f^{(\mathrm{W})}H^{(\mathrm{W})}f^{(\mathrm{W})}A^{(\mathrm{W})}_{\alpha}f^{(\mathrm{W})}A^{(\mathrm{W})}_{\beta}\right]\\ &+\operatorname{Im}\operatorname{tr}\left[f^{(\mathrm{W})}H^{(\mathrm{W})}f^{(\mathrm{W})}\left(A^{(\mathrm{W})}_{\alpha}g^{(\mathrm{W})}J^{(\mathrm{W})}_{\beta} + J^{(\mathrm{W})}_{\alpha}g^{(\mathrm{W})}A^{(\mathrm{W})}_{\beta}\right)\right]\\ &+\operatorname{Im}\operatorname{tr}\left[f^{(\mathrm{W})}H^{(\mathrm{W})}f^{(\mathrm{W})}J^{(\mathrm{W})}_{\alpha}g^{(\mathrm{W})}J^{(\mathrm{W})}_{\beta}\right]\,. \end{aligned}\tag{7.71}$$

Here, all ingredients depend on $\boldsymbol{\mathfrak{K}}$, and tr stands for the trace over the Bloch-like states, which is distinct from the trace Tr that underlies Eqs. (7.63)–(7.65).

The relevant matrices $H^{(\mathrm{W})}$, $A^{(\mathrm{W})}_{\alpha}$, and $\Omega^{(\mathrm{W})}_{\alpha\beta}$ in the Wannier gauge have already been defined by Eqs. (7.45), (7.56), and (7.57), respectively, based on the generalized hoppings and position elements of the HDWFs. Additionally, the above expressions contain the matrix objects $J^{(\mathrm{W})}_{\alpha} = \mathrm{i}VD^{(\mathrm{H})}_{\alpha}V^{\dagger}$, where $D^{(\mathrm{H})}_{\alpha}$ is given by Eq. (7.51), as well as further matrices that enter only in the computation of $\operatorname{Im}\mathcal{G}_{\alpha\beta}$:

$$B^{(\mathrm{W})}_{nm,\alpha} = \sum_{\boldsymbol{\mathfrak{R}}} \mathrm{e}^{\mathrm{i}\boldsymbol{\mathfrak{K}}\cdot\boldsymbol{\mathfrak{R}}}\langle W_{\mathbf{0}n}|H\mathfrak{r}'_{\alpha}|W_{\boldsymbol{\mathfrak{R}}m}\rangle\,, \tag{7.72}$$

where $\mathfrak{r}' = \mathfrak{r} - \boldsymbol{\mathfrak{R}}$, and $\Lambda^{(\mathrm{W})}_{\alpha\beta} = \mathrm{i}\left[C^{(\mathrm{W})}_{\alpha\beta} - C^{(\mathrm{W})\dagger}_{\alpha\beta}\right]$ with

$$C^{(\mathrm{W})}_{nm,\alpha\beta} = \sum_{\boldsymbol{\mathfrak{R}}} \mathrm{e}^{\mathrm{i}\boldsymbol{\mathfrak{K}}\cdot\boldsymbol{\mathfrak{R}}}\langle W_{\mathbf{0}n}|\mathfrak{r}_{\alpha}H\mathfrak{r}'_{\beta}|W_{\boldsymbol{\mathfrak{R}}m}\rangle\,. \tag{7.73}$$

Within the present formalism, the DMI spiralization can be evaluated in periodic systems at the expense of extra matrix elements of $H\mathfrak{r}'$ and $\mathfrak{r}H\mathfrak{r}'$ in the basis of HDWFs that are necessary to perform the higher-dimensional Wannier interpolation. This is in contrast to the interpolation of generic Berry curvatures discussed previously, where such information is not needed. By inverting the Fourier transformations in Eqs. (7.72) and (7.73) on the coarse *ab initio* mesh of $\boldsymbol{\mathfrak{K}}$-points, we arrive at explicit expressions for the sought matrix elements:

$$\langle W_{\mathbf{0}n}|H\mathfrak{r}'_{\alpha}|W_{\boldsymbol{\mathfrak{R}}m}\rangle = \frac{\mathrm{i}}{N_{\boldsymbol{\mathfrak{K}}}}\sum_{\boldsymbol{\mathfrak{K}}} \mathrm{e}^{-\mathrm{i}\boldsymbol{\mathfrak{K}}\cdot\boldsymbol{\mathfrak{R}}}\langle \phi^{(\mathrm{W})}_{\boldsymbol{\mathfrak{K}}n}|H_{\boldsymbol{k}}|\partial_{\alpha}\phi^{(\mathrm{W})}_{\boldsymbol{\mathfrak{K}}m}\rangle\,, \tag{7.74}$$

$$\langle W_{\mathbf{0}n}|\mathfrak{r}_{\alpha}H\mathfrak{r}'_{\beta}|W_{\boldsymbol{\mathfrak{R}}m}\rangle = \frac{1}{N_{\boldsymbol{\mathfrak{K}}}}\sum_{\boldsymbol{\mathfrak{K}}} \mathrm{e}^{-\mathrm{i}\boldsymbol{\mathfrak{K}}\cdot\boldsymbol{\mathfrak{R}}}\langle \partial_{\alpha}\phi^{(\mathrm{W})}_{\boldsymbol{\mathfrak{K}}n}|H_{\boldsymbol{k}}|\partial_{\beta}\phi^{(\mathrm{W})}_{\boldsymbol{\mathfrak{K}}m}\rangle\,. \tag{7.75}$$

We employ the finite-difference formula (7.59) to express the derivatives of the wave functions, and we realize that Eq. (7.74) is determined by the band energies and the overlaps $M^{(\boldsymbol{\mathfrak{K}},\boldsymbol{b})}_{nm} = \langle\phi_{\boldsymbol{\mathfrak{K}}n}|\phi_{\boldsymbol{\mathfrak{K}}+\boldsymbol{b}m}\rangle$, *i.e.*, information that is already available at the stage of generating HDWFs. However, the matrix elements of $\mathfrak{r}\hat{H}\mathfrak{r}'$ given by Eq. (7.75) rely on new information encoded in the integrals $Z^{(\boldsymbol{\mathfrak{K}},\boldsymbol{b}_1,\boldsymbol{b}_2)}_{nm} = \langle\phi_{\boldsymbol{\mathfrak{K}}+\boldsymbol{b}_1n}|H_{\boldsymbol{k}}|\phi_{\boldsymbol{\mathfrak{K}}+\boldsymbol{b}_2m}\rangle$ of the Hamiltonian at $\boldsymbol{\mathfrak{K}}$ in between states at neighboring points $\boldsymbol{\mathfrak{K}}+\boldsymbol{b}_1$ and $\boldsymbol{\mathfrak{K}}+\boldsymbol{b}_2$. Although these quantities do not enter in the construction of HDWFs, they are important in the scheme as they allow us to perform the higher-dimensional Wannier interpolation of the DMI spiralization. Therefore, we discuss in the following the implementation of these matrix elements in the FLAPW method.

7.4.4 Spiralization within FLAPW

In close formal analogy to the discussion in Section 5.3.4, we outline briefly the computational expressions for evaluating the matrix elements $\langle u_{\boldsymbol{k}+\boldsymbol{b}\theta n}|H_{\boldsymbol{k}\theta}|u_{\boldsymbol{k}\theta+b_\theta m}\rangle$ within the FLAPW method. These matrix elements of the Hamiltonian at $(\boldsymbol{k},\theta)$ between states at neighboring phase-space points $(\boldsymbol{k}+\boldsymbol{b},\theta)$ and $(\boldsymbol{k},\theta+b_\theta)$ are important ingredients in the higher-dimensional Wannier interpolation of the spiralization according to its modern Berry phase theory. Here, $|u_{\boldsymbol{k}\theta n}\rangle$ denote the lattice-periodic eigenstates of $H_{\boldsymbol{k}\theta}=\mathrm{e}^{-\mathrm{i}\boldsymbol{k}\cdot\boldsymbol{r}}H(\theta)\mathrm{e}^{\mathrm{i}\boldsymbol{k}\cdot\boldsymbol{r}}$ with $H(\theta)$ as the Hamiltonian for the given magnetization direction specified by θ. Using the Bloch states $|\psi_{\boldsymbol{k}\theta n}\rangle=\mathrm{e}^{\mathrm{i}\boldsymbol{k}\cdot\boldsymbol{r}}|u_{\boldsymbol{k}\theta n}\rangle$, we arrive at

$$\langle u_{\boldsymbol{k}+\boldsymbol{b}\theta n}|H_{\boldsymbol{k}\theta}|u_{\boldsymbol{k}\theta+b_\theta m}\rangle=\langle\psi_{[\boldsymbol{k}+\boldsymbol{b}]\theta n}|\mathrm{e}^{\mathrm{i}\boldsymbol{b}\cdot\boldsymbol{r}}H(\theta)|\psi_{\boldsymbol{k}\theta+b_\theta m}\rangle\,, \tag{7.76}$$

which is different from Eq. (5.27) as only a single phase arising from $\boldsymbol{b}$ enters in the above equation. Following the notation of Section 5.3.4, we introduce $\boldsymbol{G}(\boldsymbol{k})$ to shift the crystal momentum $\boldsymbol{k}$ into the first Brillouin zone, *i.e.*, $[\boldsymbol{k}]=\boldsymbol{k}-\boldsymbol{G}(\boldsymbol{k})$.

Interstitial region The contribution to Eq. (7.76) that results from the interstitial region is derived similarly as in Section 5.3.4, and the final expression is in fact formally identical to Eq. (5.30) except for minor modifications:

$$\langle u_{\boldsymbol{k}+\boldsymbol{b}\theta n}|H_{\boldsymbol{k}\theta}|u_{\boldsymbol{k}\theta+b_\theta m}\rangle=\sum_{\boldsymbol{G}\boldsymbol{G}'}\left(c^{\boldsymbol{G}}_{\boldsymbol{k}+\boldsymbol{b}_1 n}(\theta)\right)^*c^{\boldsymbol{G}'}_{\boldsymbol{k}m}(\theta+b_\theta)\left\{\frac{\boldsymbol{\mathcal{K}}^2+\boldsymbol{\mathcal{K}}'^2}{4}\Theta(\boldsymbol{\mathcal{G}})+V(\boldsymbol{\mathcal{G}})\right\}\,, \tag{7.77}$$

where $V(\boldsymbol{\mathcal{G}})$ and $\Theta(\boldsymbol{\mathcal{G}})$ are the Fourier transformations of the potential and the step function, respectively, and the plane-wave vectors $\boldsymbol{G}$ and $\boldsymbol{G}'$ enter in the abbreviations $\boldsymbol{\mathcal{K}}=\boldsymbol{k}+\boldsymbol{G}-\boldsymbol{G}(\boldsymbol{k}+\boldsymbol{b}_1)$, $\boldsymbol{\mathcal{K}}'=\boldsymbol{k}+\boldsymbol{G}'$, and $\boldsymbol{\mathcal{G}}=\boldsymbol{\mathcal{K}}'-\boldsymbol{\mathcal{K}}$. Note that $\boldsymbol{\mathcal{K}}'$ is defined differently than in Section 5.3.4.

Muffin tins Based on the specific form of the spinor wave functions in the muffin tins (see also Chapter 3), the matrix elements (7.76) assume the form

$$\begin{aligned}\langle u_{\boldsymbol{k}+\boldsymbol{b}_1\theta n}|H_{\boldsymbol{k}\theta}|u_{\boldsymbol{k}\theta+b_\theta m}\rangle=\sum_{LL'}\sum_{\mu}\Big\{&\left(A^\mu_{Ln}(\boldsymbol{k}+\boldsymbol{b}_1,\theta)\right)^*A^\mu_{L'm}(\boldsymbol{k},\theta+b_\theta)I^{\mu,uu}_{LL'}(\boldsymbol{b}_1,\boldsymbol{b}_2)\\&+\left(A^\mu_{Ln}(\boldsymbol{k}+\boldsymbol{b}_1,\theta)\right)^*B^\mu_{L'm}(\boldsymbol{k},\theta+b_\theta)I^{\mu,u\dot{u}}_{LL'}(\boldsymbol{b}_1,\boldsymbol{b}_2)\\&+\left(B^\mu_{Ln}(\boldsymbol{k}+\boldsymbol{b}_1,\theta)\right)^*A^\mu_{L'm}(\boldsymbol{k},\theta+b_\theta)I^{\mu,\dot{u}u}_{LL'}(\boldsymbol{b}_1,\boldsymbol{b}_2)\\&+\left(B^\mu_{Ln}(\boldsymbol{k}+\boldsymbol{b}_1,\theta)\right)^*B^\mu_{L'm}(\boldsymbol{k},\theta+b_\theta)I^{\mu,\dot{u}\dot{u}}_{LL'}(\boldsymbol{b}_1,\boldsymbol{b}_2)\Big\}\,,\end{aligned} \tag{7.78}$$

where the I-coefficients

$$I^{\mu,uu}_{LL'}(\boldsymbol{b})=\int Y^*_L(\hat{\boldsymbol{r}}_\mu)\mathrm{e}^{\mathrm{i}\boldsymbol{b}\cdot\boldsymbol{r}}u^\mu_l(r_\mu)H(\boldsymbol{r}_\mu)Y_{L'}(\hat{\boldsymbol{r}}_\mu)u^\mu_{l'}(r_\mu)\,\mathrm{d}\boldsymbol{r}_\mu\,, \tag{7.79}$$

$$I^{\mu,u\dot{u}}_{LL'}(\boldsymbol{b})=\int Y^*_L(\hat{\boldsymbol{r}}_\mu)\mathrm{e}^{\mathrm{i}\boldsymbol{b}\cdot\boldsymbol{r}}u^\mu_l(r_\mu)H(\boldsymbol{r}_\mu)Y_{L'}(\hat{\boldsymbol{r}}_\mu)\dot{u}^\mu_{l'}(r_\mu)\,\mathrm{d}\boldsymbol{r}_\mu\,, \tag{7.80}$$

are defined analogously to Section 5.3.4 but they contain only one phase factor due to $\boldsymbol{b}$ (instead of two phases stemming from $\boldsymbol{b}_1$ and $\boldsymbol{b}_2$ in Section 5.3.4). Exploiting again the Rayleigh expansion of the plane-wave factor and introducing the Gaunt coefficients, we arrive at the final expression

$$\begin{aligned} I^{\mu,uu}_{LL'}(\boldsymbol{b}) = 4\pi \mathrm{e}^{-\mathrm{i}\boldsymbol{b}\cdot\boldsymbol{\tau}_\mu} \sum_{\bar{L}} (-1)^{\bar{l}} \mathrm{i}^{\bar{l}} Y_{\bar{L}}(\hat{\boldsymbol{b}}) \sum_{\mathcal{L}} G_{\mathcal{L}L\bar{L}} \\ \times \int Y^*_{\mathcal{L}}(\hat{\boldsymbol{r}}_\mu) u^\mu_l(r_\mu) j_{\bar{l}}(br_\mu) H(\boldsymbol{r}_\mu) Y_{L'}(\hat{\boldsymbol{r}}_\mu) u^\mu_{l'}(r_\mu)\, \mathrm{d}\boldsymbol{r}_\mu\,, \end{aligned} \tag{7.81}$$

and analogously for all other I-integrals. As the original expression includes just a single phase factor $\mathrm{e}^{\mathrm{i}\boldsymbol{b}\cdot\boldsymbol{r}}$, only one Gaunt coefficient appears and the evaluation of the muffin-tin contribution to the matrix elements (7.76) is much less expensive than the according task in the calculation of orbital magnetism.

Spherical muffin-tin Hamiltonian Since the spherically averaged potential and the kinetic energy couple only spherical harmonics to the same angular momentum, we arrive at the following contribution arising from the spherical Hamiltonian:

$$\begin{aligned} I^{\mu,uu}_{LL'}(\boldsymbol{b}) = 4\pi \mathrm{e}^{-\mathrm{i}\boldsymbol{b}\cdot\boldsymbol{\tau}_\mu} \sum_{\bar{L}} (-1)^{\bar{l}} \mathrm{i}^{\bar{l}} Y_{\bar{L}}(\hat{\boldsymbol{b}}) \sum_{\mathcal{L}} G_{\mathcal{L}L\bar{L}} \delta_{L'\mathcal{L}} \\ \times \int r^2_\mu\, u^\mu_l(r_\mu) j_{\bar{l}}(br_\mu) H_\ell(r_\mu) u^\mu_{l'}(r_\mu)\, \mathrm{d}r_\mu\,, \end{aligned} \tag{7.82}$$

where the angular momentum ℓ enters in the set of quantum numbers $\mathcal{L}$. Evidently, the spherical contribution is independent of the magnetization direction as long as the spherical potential does not depend on θ, which holds for calculations that resort to the magnetic force theorem. As in the case of Section 5.3.4, the above radial integrals are symmetrized by applying half of H_ℓ to the right and half of it to the left.

Non-spherical muffin-tin Hamiltonian The contribution from the non-spherical part V_l of the scalar potential amounts to

$$\begin{aligned} I^{\mu,uu}_{LL'}(\boldsymbol{b}) = 4\pi \mathrm{e}^{-\mathrm{i}\boldsymbol{b}\cdot\boldsymbol{\tau}_\mu} \sum_{\bar{L}} (-1)^{\bar{l}} \mathrm{i}^{\bar{l}} Y_{\bar{L}}(\hat{\boldsymbol{b}}) \sum_{\mathcal{L}} \sum_{\tilde{L}}^{\tilde{l}\neq 0} G_{\mathcal{L}L\bar{L}} G_{\mathcal{L}L'\tilde{L}} \\ \times \int r^2_\mu\, u^\mu_l(r_\mu) j_{\bar{l}}(br_\mu) V_{\tilde{l}}(r_\mu) u^\mu_{l'}(r_\mu)\, \mathrm{d}r_\mu\,, \end{aligned} \tag{7.83}$$

which is also independent of θ as in the case of the spherical muffin-tin Hamiltonian.

Contribution from the spin-orbit interaction Coupling only spherical harmonics of the same angular momentum, the spin-orbit interaction contributes the following term to the I-coefficients that are necessary to evaluate Eq. (7.76):

$$\begin{aligned} I^{\mu,uu}_{LL'}(\boldsymbol{b}) = 4\pi \mathrm{e}^{-\mathrm{i}\boldsymbol{b}\cdot\boldsymbol{\tau}_\mu} \sum_{\bar{L}} (-1)^{\bar{l}} \mathrm{i}^{\bar{l}} Y_{\bar{L}}(\hat{\boldsymbol{b}}) \sum_{\mathcal{L}} G_{\mathcal{L}L\bar{L}} \delta_{L'\mathcal{L}} \left[\boldsymbol{L}\cdot\boldsymbol{S}\right]^{\sigma\sigma'}_{\mathcal{L}L'} \\ \times \int r^2_\mu\, u^\mu_l(r_\mu) j_{\bar{l}}(br_\mu) V_{\mathrm{so}}(r_\mu) u^\mu_{l'}(r_\mu)\, \mathrm{d}r_\mu\,, \end{aligned} \tag{7.84}$$

where we used the same definitions as in Section 5.3.4. While this expression appears to be independent of the magnetization direction at first sight, in fact, it relies implicitly on the angle θ since both $\boldsymbol{L}$ (locked to the lattice) and $\boldsymbol{S}$ (locked to the magnetization direction) need to be referred to within a common frame. Consequently, the spin-orbit part of the I-coefficients has to be recalculated for every magnetization direction.

Vacuum contribution in film calculations In analogy to Section 5.3.4, the vacuum contribution for truly two-dimensional geometries reads

$$\begin{aligned}\langle u_{\boldsymbol{k}+\boldsymbol{b}\theta n}|H_{\boldsymbol{k}\theta}|u_{\boldsymbol{k}\theta+b_\theta m}\rangle = \sum_{\boldsymbol{G}\boldsymbol{G}'} &\left(a^{\boldsymbol{G}n}_{\boldsymbol{k}+\boldsymbol{b}}(\theta)\right)^* a^{\boldsymbol{G}'m}_{\boldsymbol{k}}(\theta+b_\theta)\mathcal{I}^{uu}_{\boldsymbol{G}_\parallel\boldsymbol{G}'_\parallel}(\boldsymbol{b}) \\ &+ \left(a^{\boldsymbol{G}n}_{\boldsymbol{k}+\boldsymbol{b}}(\theta)\right)^* b^{\boldsymbol{G}'m}_{\boldsymbol{k}}(\theta+b_\theta)\mathcal{I}^{u\dot{u}}_{\boldsymbol{G}_\parallel\boldsymbol{G}'_\parallel}(\boldsymbol{b}) \\ &+ \left(b^{\boldsymbol{G}n}_{\boldsymbol{k}+\boldsymbol{b}}(\theta)\right)^* a^{\boldsymbol{G}'m}_{\boldsymbol{k}}(\theta+b_\theta)\mathcal{I}^{\dot{u}u}_{\boldsymbol{G}_\parallel\boldsymbol{G}'_\parallel}(\boldsymbol{b}) \\ &+ \left(b^{\boldsymbol{G}n}_{\boldsymbol{k}+\boldsymbol{b}}(\theta)\right)^* b^{\boldsymbol{G}'m}_{\boldsymbol{k}}(\theta+b_\theta)\mathcal{I}^{\dot{u}\dot{u}}_{\boldsymbol{G}_\parallel\boldsymbol{G}'_\parallel}(\boldsymbol{b}) \,,\end{aligned} \tag{7.85}$$

where we introduced the magnetization-independent coefficient

$$\mathcal{I}^{uu}_{\boldsymbol{G}_\parallel\boldsymbol{G}'_\parallel}(\boldsymbol{b}) = S_\parallel \left[\delta_{\boldsymbol{g}_\parallel\boldsymbol{g}'_\parallel} I_1^{uu} + I_2^{uu}\right] \,, \tag{7.86}$$

and analogously for all other $\mathcal{I}$-integrals. Again, $S_\parallel$ is the area of the in-plane unit cell, $\boldsymbol{g}_\parallel = \boldsymbol{G}_\parallel + \boldsymbol{k} - \boldsymbol{G}_\parallel(\boldsymbol{k}+\boldsymbol{b})$, and $\boldsymbol{g}'_\parallel = \boldsymbol{G}'_\parallel + \boldsymbol{k}$, which is different from the definition used previously in Section 5.3.4. The factors I_1 and I_2 are defined by integrals of the vacuum Hamiltonian and the wave functions with an additional phase:

$$I_1^{uu} = \int_{\pm D/2}^{\pm\infty} u_{\boldsymbol{G}_\parallel}(\boldsymbol{k}+\boldsymbol{b}, z)\mathrm{e}^{\mathrm{i}G_z(\boldsymbol{k}+\boldsymbol{b})z} h(z) u_{\boldsymbol{G}'_\parallel}(\boldsymbol{k}, z)\,\mathrm{d}z\,, \tag{7.87}$$

$$I_2^{uu} = \int_{\pm D/2}^{\pm\infty} u_{\boldsymbol{G}_\parallel}(\boldsymbol{k}+\boldsymbol{b}, z)\mathrm{e}^{\mathrm{i}G_z(\boldsymbol{k}+\boldsymbol{b})z} V_{\boldsymbol{g}_z-\boldsymbol{g}'_z}(z) u_{\boldsymbol{G}'_\parallel}(\boldsymbol{k}, z)\,\mathrm{d}z\,. \tag{7.88}$$

Transformation to the global coordinate frame Eventually, to be consistent with the construction of HDWFs for the magnetization direction, we aim at the matrix elements (7.76) but given in the global coordinate frame with the spin-quantization axis along z, *i.e.*, $\langle u^{\mathrm{gl}}_{\boldsymbol{k}+\boldsymbol{b}\theta n}|H^{\mathrm{gl}}_{\boldsymbol{k}\theta}|u^{\mathrm{gl}}_{\boldsymbol{k}\theta+b_\theta m}\rangle$, where the superscript "gl" indicates that these quantities are given with respect to a global coordinate frame oriented along the z-axis. However, when reading in at each magnetization direction the potential and the eigenvectors, these quantities are usually referred to in a local coordinate frame defined by the corresponding magnetization direction (here θ). Thus, the expressions provided in the previous paragraphs are given in the local frame, rendering the following transformation obligatory:

$$\begin{aligned}\langle u^{\mathrm{gl}}_{\boldsymbol{k}+\boldsymbol{b}\theta n}|H^{\mathrm{gl}}_{\boldsymbol{k}\theta}|u^{\mathrm{gl}}_{\boldsymbol{k}\theta+b_\theta m}\rangle &= \langle u_{\boldsymbol{k}+\boldsymbol{b}\theta n}|\chi^\dagger(\theta)\chi(\theta)H_{\boldsymbol{k}\theta}\chi^\dagger(\theta)\chi(\theta+b_\theta)|u_{\boldsymbol{k}\theta+b_\theta m}\rangle \\ &= \langle u_{\boldsymbol{k}+\boldsymbol{b}\theta n}|H_{\boldsymbol{k}\theta}\chi(b_\theta)|u_{\boldsymbol{k}\theta+b_\theta m}\rangle\,.\end{aligned} \tag{7.89}$$

where the quantities in the last line are referred to in the local coordinate frame determined by θ or $\theta + b_\theta$, and the unitary matrix $\chi(\theta)$ is the transformation defined by Eq. (3.42) with $\varphi = 0°$, *i.e.*,

$$\chi(\theta) = \begin{pmatrix} \cos\frac{\theta}{2} & -\sin\frac{\theta}{2} \\ \sin\frac{\theta}{2} & \cos\frac{\theta}{2} \end{pmatrix}\,. \tag{7.90}$$

This matrix transforms a spinor wave function with spin components σ from the local frame specified by θ to the global frame oriented along the z-axis, which results in

$$\sum_{\sigma\sigma'}\langle u^{\mathrm{gl},\sigma}_{\boldsymbol{k}+\boldsymbol{b}\theta n}|H^{\mathrm{gl},\sigma\sigma'}_{\boldsymbol{k}\theta}|u^{\mathrm{gl},\sigma'}_{\boldsymbol{k}\theta+b_\theta m}\rangle = \sum_{\sigma\sigma'\sigma''}\langle u^{\sigma}_{\boldsymbol{k}+\boldsymbol{b}\theta n}|H^{\sigma\sigma'}_{\boldsymbol{k}\theta}\chi^{\sigma'\sigma''}(b_\theta)|u^{\sigma''}_{\boldsymbol{k}\theta+b_\theta m}\rangle\,. \tag{7.91}$$

7.4.5 Velocity and torque operator

An alternative approach towards the torkance τ_{ij} and the spiralization D_{ij} is to interpolate explicitly the matrix elements of the velocity operator $\hbar^{-1}\partial_{\boldsymbol{k}} H_{\boldsymbol{k}}$ and the torque operator $\hat{\boldsymbol{m}} \times \partial_{\hat{\boldsymbol{m}}} H$, followed by evaluating Eqs. (4.52) and (4.58) on the basis of these quantities. The higher-dimensional Wannier interpolation is ideally suited to achieve this goal since derivatives of the Hamiltonian with respect to the crystal momentum and the magnetization direction are treated accurately on an equal footing. That is, we need to evaluate the matrix elements $\langle u^{(\mathrm{H})}_{\mathfrak{K}n} | \partial_\alpha H_{\boldsymbol{k}} | u^{(\mathrm{H})}_{\mathfrak{K}m} \rangle$ in the Hamiltonian gauge, where ∂_α denotes the variation either in the crystal momentum or in the additional parameter $\boldsymbol{\lambda} = \hat{\boldsymbol{m}}$, which stands for the magnetization direction in this case. By taking into account the Hellmann-Feynman theorem and Eq. (7.53), it follows that

$$\langle u^{(\mathrm{H})}_{\mathfrak{K}n} | \partial_\alpha H_{\boldsymbol{k}} | u^{(\mathrm{H})}_{\mathfrak{K}m} \rangle = \bar{H}^{(\mathrm{H})}_{nm,\alpha} - \mathrm{i}(\mathcal{E}_{\mathfrak{K}m} - \mathcal{E}_{\mathfrak{K}n}) \bar{A}^{(\mathrm{H})}_{nm,\alpha} \,. \tag{7.92}$$

Building onto this expression for the matrix elements of the general adiabatic interaction $\partial_\alpha H_{\boldsymbol{k}}$, the interpolated velocity (where $\partial_\alpha = \partial_{\boldsymbol{k}}$) assumes the form

$$\hbar \boldsymbol{v}_{nm}(\mathfrak{K}) = \langle u^{(\mathrm{H})}_{\mathfrak{K}n} | \partial_{\boldsymbol{k}} H_{\boldsymbol{k}} | u^{(\mathrm{H})}_{\mathfrak{K}m} \rangle = \bar{H}^{(\mathrm{H})}_{nm,\boldsymbol{k}} - \mathrm{i}(\mathcal{E}_{\mathfrak{K}m} - \mathcal{E}_{\mathfrak{K}n}) \bar{A}^{(\mathrm{H})}_{nm,\boldsymbol{k}} \,, \tag{7.93}$$

and analogously for the torque operator (where $\partial_\alpha = \partial_{\hat{\boldsymbol{m}}}$):

$$\begin{aligned} \boldsymbol{\mathcal{T}}_{nm}(\mathfrak{K}) &= \left\langle u^{(\mathrm{H})}_{\mathfrak{K}n} \middle| \hat{\boldsymbol{m}} \times \frac{\partial H}{\partial \hat{\boldsymbol{m}}} \middle| u^{(\mathrm{H})}_{\mathfrak{K}m} \right\rangle = \hat{\boldsymbol{m}} \times \left[\bar{H}^{(\mathrm{H})}_{nm,\hat{\boldsymbol{m}}} - \mathrm{i}(\mathcal{E}_{\mathfrak{K}m} - \mathcal{E}_{\mathfrak{K}n}) \bar{A}^{(\mathrm{H})}_{nm,\hat{\boldsymbol{m}}} \right] \\ &= \left[\bar{H}^{(\mathrm{H})}_{nm,\theta} - \mathrm{i}(\mathcal{E}_{\mathfrak{K}m} - \mathcal{E}_{\mathfrak{K}n}) \bar{A}^{(\mathrm{H})}_{nm,\theta} \right] \hat{\boldsymbol{e}}_\varphi - \frac{1}{\sin\theta} \left[\bar{H}^{(\mathrm{H})}_{nm,\varphi} - \mathrm{i}(\mathcal{E}_{\mathfrak{K}m} - \mathcal{E}_{\mathfrak{K}n}) \bar{A}^{(\mathrm{H})}_{nm,\varphi} \right] \hat{\boldsymbol{e}}_\theta \,, \end{aligned} \tag{7.94}$$

where we defined $\hat{\boldsymbol{m}}$ in spherical coordinates as $\hat{\boldsymbol{m}} = (\cos\varphi \sin\theta, \sin\varphi \sin\theta, \cos\theta)$.

Remarkably, the higher-dimensional Wannier interpolation of velocity and torque operators is possible using solely the generalized hoppings (7.43) and the position elements (7.58) in the basis of HDWFs, which are also the key ingredients for interpolating Berry curvatures. In contrast to the interpolation technique for the DMI spiralization that is presented above, information on the operators $H\mathfrak{r}'$ and $\mathfrak{r}H\mathfrak{r}'$ is not required. Nevertheless, we find that D_{ij} obtained through this approach agrees well with the full scheme discussed before, which interpolates the DMI spiralization formally analogously to the Berry phase theory of orbital magnetism.

Chapter 8

Spin-orbit torques and the Dzyaloshinskii-Moriya interaction in metallic heterostructures

Contents

By applying the previously developed formalism to the magnetization direction $\hat{\boldsymbol{m}}$, we elucidate in this chapter the microscopic origin and the magnitude of spin-orbit torques (SOTs) and Dzyaloshinskii-Moriya interaction (DMI) in ferromagnetic heterostructures that lack inversion symmetry. In particular, we verify the predictive power of the higher-dimensional Wannier interpolation by comparing the calculated anisotropy of the considered phenomena in Mn/W(001) to an equivalent but more cumbersome approach. Additionally, we scrutinize the correlations of torques and chiral exchange interactions with the electronic structure in Co-based trilayers that constitute an ideal playground to tailor the DMI, for instance, by means of alloying. Based on our methodology, we easily extract the anisotropy of the SOTs with the magnetization direction and outline its general consequences for controlling the dynamical properties of magnetic skyrmions.

Some of the results presented in Section 8.2 have already been published:

J.-P. Hanke, F. Freimuth, S. Blügel, and Y. Mokrousov
J. Phys. Soc. Jpn. **87***, 041010 (2018)*

8.1 Chiral magnet Mn/W(001)

While the concept of the higher-dimensional Wannier interpolation applies to any set of generic parameters $\boldsymbol{\lambda}$ that drive the adiabatic Hamiltonian evolution, we devote the rest of this thesis to the special but highly relevant situation where the abstract parameter is the magnetization direction $\hat{\boldsymbol{m}} = (\cos\varphi\sin\theta, \sin\varphi\sin\theta, \cos\theta)$. In order to confirm that our method operates correctly and facilitates the accurate prediction of spin torques and chiral exchange interactions based on their Berry phase theory, at first, we revisit the ferromagnetic Mn monolayer on the (001) surface of a W substrate, Fig. 6.2(a), which we studied already from the viewpoint of orbital magnetism. Appendix A.2 summarizes the computational details of our first-principles calculations of the spin-orbit torques (SOTs) and the Dzyaloshinskii-Moriya interaction (DMI) in Mn/W(001) based on higher-dimensional Wannier functions (HDWFs).

Figure 6.2(b) illustrates the complex electronic structure of the perpendicularly magnetized ferromagnet along high-symmetry directions of the square-shaped Bril-

	64^2	128^2	256^2	512^2	1024^2
τ_{yx} (ea_0)	0.8081	0.8897	0.8675	0.8622	0.8623
D_{yx} $(\mathrm{meV}a_0/\mathrm{uc})$	51.14	45.08	45.50	45.28	45.37

Table 8.1: Convergence of the torkance τ_{yx} and the spiralization D_{yx} with the number of $\boldsymbol{k}$-points that sample the Brillouin zone in the higher-dimensional Wannier interpolation in clean Mn/W(001) with perpendicular magnetization. The in-plane unit cell containing ten atoms is denoted as "uc".

louin zone. The magneto-crystalline anisotropy in the metallic heterostructure promotes the direction perpendicular to the film as the easy axis. If the magnetization is normal to the film plane, the four-fold rotational symmetry associated with the particular surface orientation of the bcc substrate dictates an antisymmetric tensor shape for the even torkance and the spiralization, whereas the odd torkance is proportional to the identity matrix[1]:

$$\tau^{\text{even}} = \begin{pmatrix} 0 & -\tau_{yx} \\ \tau_{yx} & 0 \end{pmatrix} , \qquad \tau^{\text{odd}} = \begin{pmatrix} \tau_{yy} & 0 \\ 0 & \tau_{yy} \end{pmatrix} , \qquad D = \begin{pmatrix} 0 & -D_{yx} \\ D_{yx} & 0 \end{pmatrix} . \tag{8.1}$$

Rooting in the electronic structure, the three quantities τ_{yx}, τ_{yy}, and D_{yx} are thus sufficient to characterize uniquely the SOTs and the DMI in perpendicularly magnetized Mn/W(001). However, the structure of the torkance tensor assumes a more general shape for an arbitrary magnetization direction that breaks the rotational symmetry of the crystal. On the other hand, the overall form of the spiralization tensor is always determined by the symmetries of the crystal lattice, irrespective of $\hat{\boldsymbol{m}}$.

Since the entries of torkance and spiralization tensors originate from integrals over the Brillouin zone of momentum space, in the beginning, we comment on the convergence of these Berry phase properties with respect to the number of $\boldsymbol{k}$-points that are employed in the higher-dimensional Wannier interpolation. As suggested by the results in Table 8.1, the spiralization converges more quickly with the number of mesh points than τ_{yx} in the clean limit, which alludes to the possibility of estimating roughly D_{yx} directly from the first-principles calculation of the electronic structure on a coarse grid [28]. Drawing analogies with Berry phase effects that originate from the current-current correlation, we note that this behavior is reminiscent of the orbital magnetization (OM) that is described adequately already for relatively small sizes of the interpolation mesh [184]. In order to obtain well-converged values for both torkance and spiralization, we choose an interpolation $\boldsymbol{k}$-mesh of 1024×1024 points, which guarantees high accuracy.

Employing the higher-dimensional Wannier interpolation, we present in Fig. 8.1 the dependence of torkance and spiralization in Mn/W(001) on disorder as mediated by the constant band broadening Γ. Additionally, the individual contributions from the two terms in Eq. (4.61) are depicted in the case of D_{yx}. While the odd torkance τ_{yy} diverges in the clean limit, Eq. (4.51), the even torkance τ_{yx} and the spiralization D_{yx} amount to constant intrinsic values for small Γ, stemming from scattering-independent geometrical properties of the underlying complex phase space, see Eqs. (4.52) and (4.58). Although the magnitude of these phenomena reduces generally with increasing Γ and vanishes eventually for strong disorder, the spiralization

---

[1] This statement holds always if the system exhibits an n-fold rotational symmetry with $n > 2$.

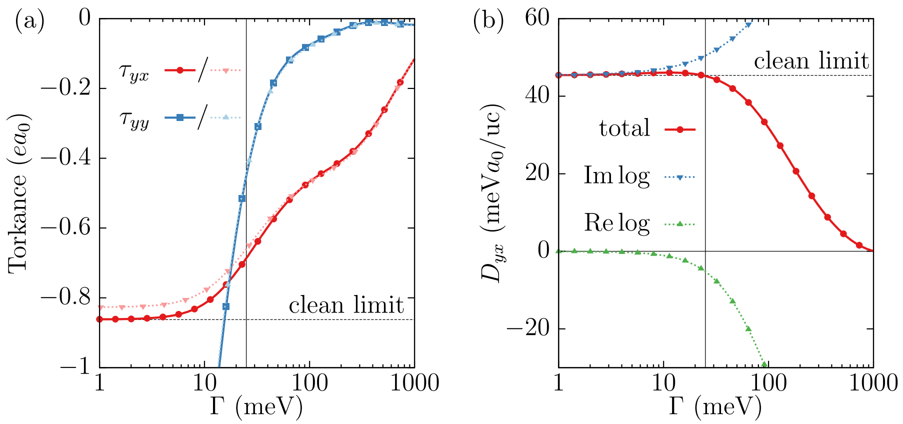

Figure 8.1: Dependence of (a) the torkance and (b) the spiralization on the constant band broadening Γ applied to the electronic structure of Mn/W(001). The behavior of τ_{yx} and τ_{yy} (dark solid lines) is compared in (a) to the disorder dependence obtained in Ref. [133] (light dotted lines). Additionally, the spiralization in (b) is decomposed into the two contributions entering Eq. (4.61), which are labeled accordingly as "Im log" and "Re log". Dashed horizontal lines illustrate the Berry phase limit to which τ_{yx} and D_{yx} converge for $\Gamma \to 0$.

D_{yx} in Mn/W(001) is particularly robust with respect to moderate disorder, keeping its intrinsic value up to at least $\Gamma = 25\,\text{meV}$. If the band broadening is increased further, the two terms that contribute to D_{yx} in Eq. (4.61) become sizable but opposite in sign, which leads to an exact cancellation for large Γ. In order to benchmark our higher-dimensional Wannier interpolation, we compare in Fig. 8.1(a) the obtained disorder dependence of τ_{yx} and τ_{yy} to an alternative approach [133] that represents the torque operator in the expressions (4.49) and (4.50) based on the ferromagnetic exchange field. Since the latter quantity is readily available in the first-principles code, the conventional Wannier interpolation is sufficient to evaluate the torkance for a fixed magnetization direction in this approach. As we show in Fig. 8.1(a), our results for the Γ-dependence of the torkance agree excellently with the obtained values from the described formalism based on the *ab initio* exchange field [133], which demonstrates that the higher-dimensional Wannier interpolation allows indeed for an accurate prediction of SOTs and DMI in metallic heterostructures.

However, when we aim at evaluating the anisotropy of current-induced torques and chiral exchange interactions with respect to the magnetization direction, the higher-dimensional Wannier interpolation is advantageous as it grants efficient access to the torkance and the spiralization at any desired magnetization direction based on just a single set of HDWFs. Considering the illustrative case of $\varphi = 0°$, we display in Fig. 8.2(a,b) the behavior of τ_{yx}, τ_{yy}, and D_{yx} in Mn/W(001) upon varying the polar angle that determines the magnetization direction $\hat{\boldsymbol{m}} = (\sin\theta, 0, \cos\theta)$. In the clean system without any disorder, both torkance and spiralization exhibit a prominent anisotropy with θ, where the non-monotonic dependence of τ_{yx} on the magnetic orientation is particularly complex. Additionally, we compare our results for D_{yx} to values [238] obtained within the above exchange-field approach that necessitates the

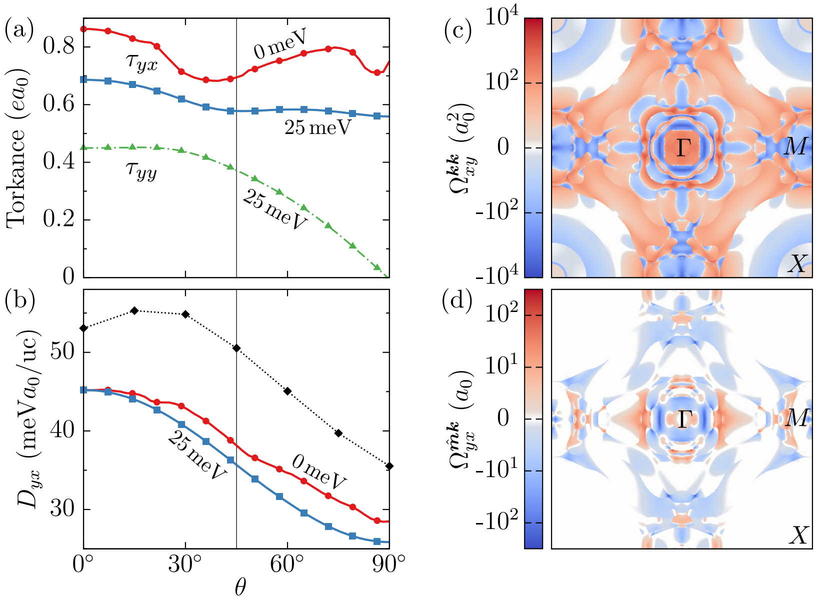

Figure 8.2: Anisotropy of (a) torkance and (b) spiralization with respect to the magnetization direction $\hat{\boldsymbol{m}} = (\sin\theta, 0, \cos\theta)$ in Mn/W(001). While τ_{yx} and D_{yx} are shown in the clean limit as well as for $\Gamma = 25\,\text{meV}$, the anisotropy of τ_{yy} is studied only for moderate disorder. The behavior of D_{yx} is compared in (b) to data points (black diamonds) each of which was extracted from a separate set of maximally-localized Wannier functions [238]. (c,d) Distribution of momentum Berry curvature $\Omega^{\boldsymbol{kk}}_{xy}$ and mixed Berry curvature $\Omega^{\hat{\boldsymbol{m}}\boldsymbol{k}}_{yx}$ throughout the Brillouin zone for an out-of-plane magnetization.

construction of individual sets of maximally-localized Wannier functions (MLWFs) for every magnetization direction, rendering the calculation for many angles θ cumbersome and time-consuming. Irrespective of an overall shift, our prediction based on the generalized interpolation scheme follows qualitatively the global trend of the conventional exchange-field approach, which proves that the higher-dimensional Wannier interpolation facilitates the accurate evaluation of anisotropic Berry phase properties.

We contrast further in Fig. 8.2(c,d) the reciprocal-space distribution of the momentum Berry curvature $\Omega^{\boldsymbol{kk}}_{xy}$ that underlies the intrinsic anomalous Hall effect and the mixed Berry curvature $\Omega^{\hat{\boldsymbol{m}}\boldsymbol{k}}_{yx}$, which gives rise to the antidamping SOT in perpendicularly magnetized Mn/W(001). While $\Omega^{\boldsymbol{kk}}_{xy}$ follows the rotational symmetry originating from the specific (001) surface orientation of the bcc substrate, the behavior of the mixed curvature of all occupied states is naturally distinct as it contains the variation of the wave function only with respect to one of the momentum coordinates. Moreover, although both quantities exhibit characteristic features due to the Fermi surface, the Berry curvature of momentum space reveals a much more rich texture as compared to the curvature of the higher-dimensional phase space of crystal momentum and magnetization direction.

Incorporating the constant broadening $\Gamma = 25\,\text{meV}$ of the energy bands, finally, we elucidate the role of decent disorder for the dependence of spiralization and torkance on the magnetization direction, Fig. 8.2(a,b). While the anisotropy curves are primarily smoothened, the magnitude of τ_{yx} is significantly flattened as compared to the clean limit. Figure 8.2(a) presents further the behavior of the torkance τ_{yy} with varying θ, which is generally smaller in magnitude than τ_{yx} and considerably robust if the magnetization is tilted only slightly away from the out-of-plane direction. As the metallic heterostructure is symmetric with respect to reflections at the plane perpendicular to the magnetization direction if $\theta = 90°$, the torkance τ_{yy} vanishes in the case of $\hat{\boldsymbol{m}}$ lying in the film plane.

In conclusion, providing a powerful tool to determine the anisotropy of current-induced spin torques and chiral exchange interactions with respect to the magnetization direction, the framework of HDWFs enables us to efficiently predict these phenomena in complex magnets based on the first-principles electronic structure. Moreover, the generic method is ideally suited to investigate the behavior of other electronic, magnetic, or transport effects, *e.g.*, the Gilbert damping that relates to the torque-torque correlation function [239, 240].

8.2 Co-based trilayer systems

Recently, the interfacial DMI was shown to be tunable in magnetic heterostructures of Co sandwiched between different heavy metals such as Pt and Ir [241–243], holding therefore bright prospects for the observation of small magnetic skyrmions at room temperature. In this context, current-induced SOTs can be envisaged to provide an efficient means for controlling and manipulating the dynamical properties of such chiral nano-scale objects. While the symmetric system Pt/Co/Pt exhibits locally chiral exchange interactions that are of equal magnitude but opposite in sign at the two interfaces, the manifestation of a non-zero DMI in Ir/Co/Pt or Au/Co/Pt is often interpreted from the perspective of *additive* interfacial contributions to the chiral exchange interaction (see, *e.g.*, [242]). Starting from the first-principles electronic structure, we elucidate in the following the microscopic origin of DMI and SOTs in thin Co-based multilayers, where we scrutinize the anisotropy of these phenomena with respect to the magnetization direction. In particular, using the advanced Wannier interpolation (see Chapter 7), we evaluate the Berry phase expressions of spiralization and torkance in the alloyed materials $\mathrm{Ir}_\delta\mathrm{Pt}_{1-\delta}$/Co/Pt and $\mathrm{Au}_\gamma\mathrm{Pt}_{1-\gamma}$/Co/Pt with the crystal structure as illustrated in Fig. 8.4(a). Based on the virtual crystal approximation (VCA), we vary the compositions δ and γ of the overlayer, and analyze their effect on DMI and SOTs. A comprehensive overview of the computational parameters that underlie the first-principles calculations are provided in Appendix A.6.

8.2.1 Dependence on the overlayer composition

Figure 8.3 presents the complex electronic structure of the three stoichiometric compounds (a) Ir/Co/Pt, (b) Pt/Co/Pt, and (c) Au/Co/Pt in the vicinity of the Fermi level along the high-symmetry lines of the hexagonal Brillouin zone. At this stage, the magnetization direction is always oriented perpendicular to the film plane of the ferromagnetic heterostructures. While the band structure of the symmetric compound Pt/Co/Pt is identical for $+\boldsymbol{k}$ and $-\boldsymbol{k}$, the absence of spatial inversion symmetry renders the band dispersions of Ir/Co/Pt and Au/Co/Pt intrinsically distinct around

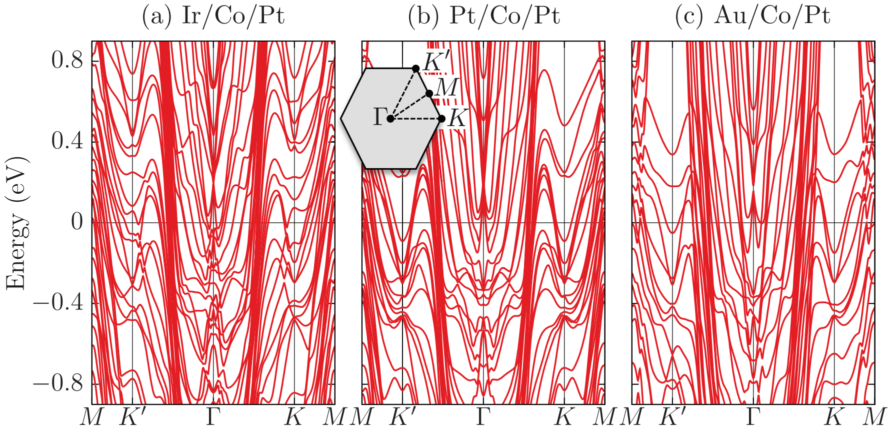

Figure 8.3: Electronic band structure along the high-symmetry lines of the hexagonal Brillouin zone (see inset of the middle panel) in the three stoichiometric heterostructures of (a) Ir/Co/Pt, (b) Pt/Co/Pt, and (c) Au/Co/Pt. The energy scale is relative to the corresponding Fermi level. In all of these cases, the Co layer is magnetized perpendicular to the film plane, which corresponds to the polar angle $\theta = 0$.

the two valleys K and K'.

Due to the three-fold rotational symmetry around the axis normal to the magnetic trilayers lacking inversions, the shape of the response tensors D and τ that characterize spiralization and torkance, respectively, is dictated by Eq. (8.1), *i.e.*, the only non-trivial entries amount to D_{yx}, τ_{yx}^{even}, and τ_{yy}^{odd}. Figure 8.4(b) illustrates the variation of D_{yx} upon tuning the composition ratio of the Pt overlayers by substitutional doping either with Ir (controlled by δ) or with Au (mediated by γ). Strikingly, the DMI spiralization exhibits an intricate non-monotonic behavior when changing the alloy composition, and even inverts its sign for moderate doping with Ir near $\delta = 0.25$. We proclaim these doped systems as promising materials for experiments to investigate in more detail. Turning to the regime of strong doping instead, we find that the magnitude of D_{yx} is comparable in the two limiting cases $\delta \approx 1$ and $\gamma \approx 1$ even though the compounds with Au-rich overlayers reveal larger values of the spiralization as compared to the Ir complements. Principally, our results for the perpendicularly magnetized heterostructures demonstrate that an adequate engineering of the electronic structure, *e.g.*, via doping provides an efficient tool to design magnitude and sign of the chiral exchange interaction in inversion-asymmetric heterostructures. Revealing the complex oscillatory correlation of the intrinsic torkance with the composition ratio, Figure 8.7(a) shows that τ_{yx} is appreciably more sensitive to fine chemical changes of the overlayers in the clean limit as compared to the spiralization. Clearly, including the effect of disorder by means of the constant band broadening $\Gamma = 25\,\text{meV}$ smoothens generally the curves of both spiralization and torkance in Figs. 8.4(b) and 8.7(a), respectively. However, while disorder hardly affects the qualitative behavior of D_{yx} and preserves the overall trend in τ_{yx}, the latter quantity is altered notably on a quantitative level. Remarkably, the even torkance τ_{yx} is almost the same for the Ir-rich and Au-rich compounds with moderate disorder

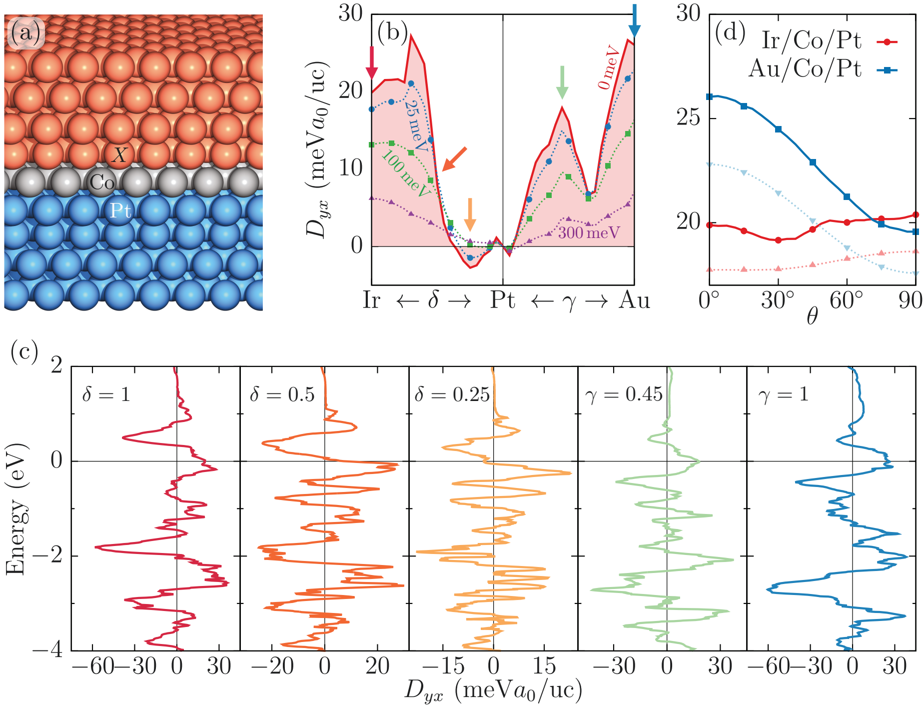

Figure 8.4: (a) Crystal structure of the Co-based heterostructures comprising the Pt substrate, the Co monolayer, and the overlayers X. (b) Spiralization D_{yx} for varying overlayer composition in Ir$_\delta$Pt$_{1-\delta}$/Co/Pt and Au$_\gamma$Pt$_{1-\gamma}$/Co/Pt, respectively, where the magnetization is perpendicular to the film plane. While the solid red curve corresponds to the clean limit, the dotted lines include the effect of disorder due to a finite broadening Γ of the energy bands by 25 meV, 100 meV, and 300 meV. The spiralization is given in units of meVa_0/uc, where "uc" stands for the in-plane unit cell. (c) Energy dependence of D_{yx} in the clean limit for the different alloy concentrations that are marked in (b) by correspondingly colored arrows. The energy scale is relative to the according Fermi level. (d) Anisotropy of D_{yx} with respect to the magnetization direction represented by the polar angle θ in the compounds Ir/Co/Pt and Au/Co/Pt for $\Gamma = 0$ meV (solid lines) and $\Gamma = 25$ meV (dotted lines).

whereas the odd torkance τ_{yy} is opposite in sign for the two cases, and its magnitude exceeds thoroughly the one of τ_{yx} (see inset of Fig. 8.7(a)).

Utilizing the constant-Γ model, we present in Fig. 8.5 the disorder dependence of torkance and spiralization in the perpendicularly magnetized compounds Ir/Co/Pt and Au/Co/Pt. While both the even torkance τ_{yx} and the spiralization D_{yx} reach constant intrinsic values in the regime of weak disorder, Eqs. (4.52) and (4.58), the odd torkance τ_{yy} diverges like $1/\Gamma$ in the clean limit as evident from Eq. (4.51). Strikingly, increasing the disorder enhances initially the even torkance in Ir/Co/Pt before it tends to zero for larger values of Γ as in the case of all of the studied quantities.

In order to trace fingerprints of the underlying electronic structure that manifest eventually in the chiral exchange interaction, we display in Fig. 8.4(c) how the spi-

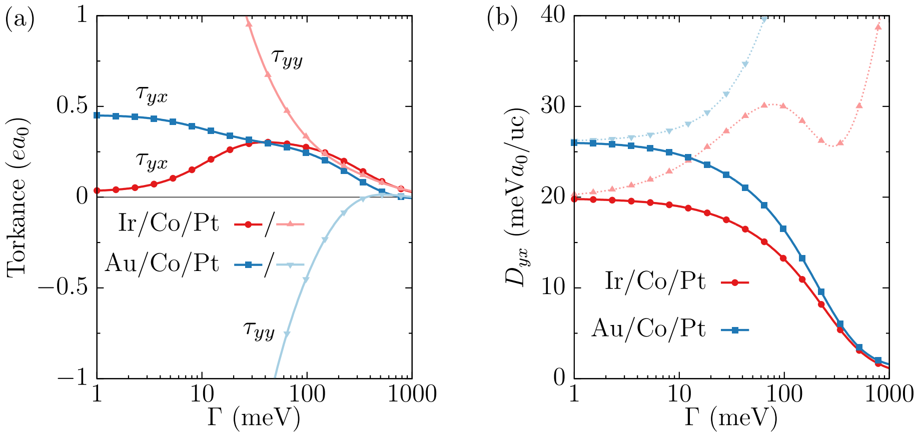

Figure 8.5: Behavior of (a) torkance and (b) spiralization with increasing band broadening Γ in the compounds Ir/Co/Pt (red) and Au/Co/Pt (blue) with perpendicular magnetization. In panel (a), dark and light colors are used to illustrate the even torkance τ_{yx} and the odd torkance τ_{yy}, respectively. In addition to the dependence of D_{yx}, we depict in (b) the contribution proportional to the imaginary part of the logarithm in Eq. (4.61) using dotted lines.

ralization D_{yx} varies with the position of the Fermi level in selected compounds. The predicted rapidly oscillating energy dependence is strongly reminiscent of the behavior of the anomalous Hall conductivity and the OM in thin magnetic films (see, *e.g.*, the results for Mn/W(001) in Chapter 6). As the states of d orbital character are well-known to play a crucial role for the physics of DMI in the considered transition metals [244], we can ascribe the peak structure in Fig. 8.4(c) to the positions of the $3d$ states of Co and the $5d$ states of the heavy metals as well as to their mutual hybridization. In particular, since the relevant heavy-metal states with strong spin-orbit coupling are located at smaller energies when altering the overlayers from Ir over Pt to Au, also the characteristic features of the spiralization D_{yx} shift towards lower energies. Due to the hybridization of these d orbitals with other available states, the elaborate energy dependence of DMI is modified further. At energies higher than 1 eV above the actual Fermi level, the important d states are typically not accessible, which leads to a strong suppression of the spiralization.

In order to uncover the microscopic origin of antidamping SOTs and DMI in the Co-based trilayers, we map out in Fig. 8.6 the distributions of the mixed Berry curvature $\Omega_{yx}^{\hat{m}\boldsymbol{k}}$ of all occupied bands, Eq. (4.41), and the momentum-resolved contributions to the spiralization D_{yx} in the hexagonal Brillouin zone. Since these quantities relate to the torque-velocity correlation, which differentiates only with respect to a single component of the Bloch vector, both violate naturally the rotational symmetries of the considered compounds (a) Ir/Co/Pt, (b) Pt/Co/Pt, and (c) Au/Co/Pt in momentum space. Consequently, the obtained distributions at $+\boldsymbol{k}$ and $-\boldsymbol{k}$ are intrinsically different and not at all linked by crystalline symmetries in general. However, the privileged case of Pt/Co/Pt is an exception as the sustained inversion symmetry renders the mixed Berry curvature and the spiralization exactly opposite in sign at $\pm\boldsymbol{k}$, which manifests in a consistent cancellation and thus no net SOT and DMI. While

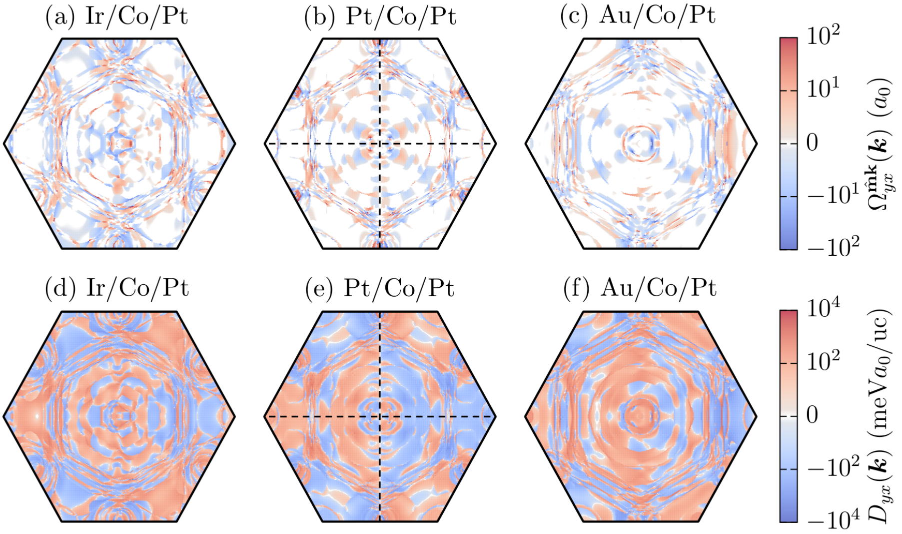

Figure 8.6: Distribution of the mixed Berry curvature $\Omega_{yx}^{\hat{m}\boldsymbol{k}}$ (top) and the Dzyaloshinskii-Moriya spiralization D_{yx} (bottom) of all occupied bands in the hexagonal Brillouin zone for the three stoichiometric heterostructures (a,d) Ir/Co/Pt, (b,e) Pt/Co/Pt, and (c,f) Au/Co/Pt. The Co monolayer in these thin films is perpendicularly magnetized. In the labels, a_0 denotes Bohr's radius and "uc" stands for the in-plane unit cell. Note the logarithmic color scale.

the mixed Berry curvature is sharply peaked in narrow regions owing to its strong sensitivity to fine electronic-structure details, the distribution of D_{yx} reveals a richer structure comprising important background contributions from broad regions of the Brillouin zone. Nevertheless, the total DMI spiralization is determined by an integral that contains as well rapidly altering large contributions at specific locations in momentum space, which opens an intriguing perspective to promote drastic changes of the net spiralization by inducing a non-equilibrium population of the electronic states using electric fields or charge currents.

8.2.2 Anisotropy with the magnetization direction

One of the major advantages of the Berry phase theory of SOT and DMI is the readily available dependence of the corresponding response tensors – *i.e.*, the torkance and the spiralization – on the magnetic orientation of the ferromagnet. Being deliberately designed for this purpose, the higher-dimensional Wannier interpolation (see Chapter 7) is ideally suited to extract efficiently this anisotropy with respect to the magnetization direction $\hat{\boldsymbol{m}} = (\cos\varphi\sin\theta, \sin\varphi\sin\theta, \cos\theta)$. While the spiralization and the even torkance are antisymmetric tensors if the magnetization is oriented perpendicular to the film plane of the considered heterostructures, Eq. (8.1), this is not valid anymore if $\hat{\boldsymbol{m}}$ points into an arbitrary direction.

When keeping the azimuthal angle fixed to $\varphi = 0°$, we find that the three tensor elements D_{yx}, τ_{yx}^{even}, and τ_{yy}^{odd} constitute by far the most important contributions to

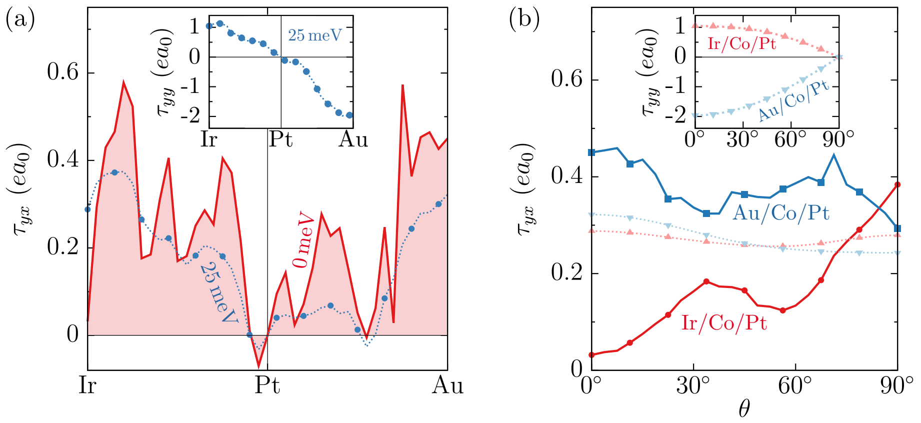

Figure 8.7: (a) Dependence of the even torkance τ_{xy} on the overlayer composition in perpendicularly magnetized Co-based trilayers in the clean limit (red solid line) and for $\Gamma = 25\,\text{meV}$ (blue dotted line). In the latter case of decent disorder, the variation of the odd torkance τ_{yy} is shown in the inset. (b) Red and blue lines illustrate the anisotropy of τ_{yx} with respect to the magnetization direction in Ir/Co/Pt and Au/Co/Pt, respectively, for $\Gamma = 0\,\text{meV}$ (dark solid) and $\Gamma = 25\,\text{meV}$ (light dotted). The inset reveals the behavior of τ_{yy} in the moderately disordered compounds.

the effects in the Co-based trilayers even if the magnetization is tilted. Tuning the remaining free angle θ, we display in Figs. 8.4(d) and 8.7(b) the dependence of these non-trivial tensor entries on the magnetization direction in the two considered compounds Ir/Co/Pt and Au/Co/Pt. Despite the fact that the DMI spiralization varies with θ in both materials, its anisotropy is much more pronounced in the Au/Co/Pt system as compared to the case of the Ir overlayers. In the former heterostructure, the original value of $D_{yx} = 26\,\text{meV}a_0/\text{uc}$ at $\theta = 0°$ is fairly diminished by about one quarter to $20\,\text{meV}a_0/\text{uc}$ upon rotating the magnetization direction into the film plane. Regarding the anisotropy of the torkance shown in Fig. 8.7(b), the magnitude of τ_{yx} evolves only moderately with the polar angle θ in Au/Co/Pt. In sharp contrast, the intrinsic torkance is prominently anisotropic in Ir/Co/Pt, where it rises from a negligible value to as much as $0.4\,ea_0$ if the magnetization direction resides in the film plane. While including disorder effects via the constant band broadening $\Gamma = 25\,\text{meV}$ merely modifies the curve of the DMI spiralization except for a small shift, the susceptibility of the intrinsic torkance to subtle changes of the electronic structure manifests in a particularly reduced anisotropy of τ_{yx} in both compounds. As a consequence, the moderately disordered trilayers feature an almost isotropic τ_{yx} on the order of $0.3\,ea_0$. The scattering-dependent contribution τ_{yy}, however, varies strongly with the magnetization direction and vanishes eventually once the magnetic moments are oriented in-plane due to the reflection symmetry at the plane perpendicular to $\hat{\boldsymbol{m}}$.

As uncovered in Fig. 8.7(b) by the efficient higher-dimensional Wannier interpolation of the electronic structure, the torkance reveals a complex dependence on the magnetic orientation of the Co layer in the considered two-dimensional heterostructures. This anisotropy of SOTs in trilayers with broken inversion symmetry plays generally an important role for controlling and tailoring the dynamical properties of magnetic skyrmions in these sytems. In particular, the anti-damping SOT has been shown to drive the dynamics of chiral skyrmions in interfacial film systems. Consequently, precise knowledge of the local variation of the torkance with magnetization direction is rendered crucial to evaluate accurately the forces that enter in the semiclassical equations of motion of these chiral objects (see, *e.g.*, Ref. [245]).

Chapter 9

Topology for electrical magnetization control in complex magnets

Contents

Uncovering the deep connections between electrical control of magnetism and topology, we describe in this chapter how the emergence of band crossings, or, monopoles in the electronic structure can amplify magneto-electric coupling effects in metallic and insulating phases of magnetic materials. Drawing close analogies with the quantum anomalous Hall effect, we lay out the concept of "mixed" Weyl semimetals that provide the most natural interpretation of enhanced spin-orbit torques (SOTs) rooting in the non-trivial topology of the complex phase space of crystal momentum and magnetization direction. As a proof of principle, we construct a simple tight-binding model of a mixed Weyl semimetal that displays a strong electric-field response if magnetic monopoles emerge in the underlying phase space. Using advanced density functional theory methods, we then identify magnetically doped Graphene and functionalized bismuth films as promising realizations of this class of materials from first principles. Strikingly, these insulating ferromagnets reveal much larger SOTs as compared to conventional metallic heterostructures, and pave thus the road towards low-dissipation magnetization control by electric fields.

The results presented in this chapter have already been published:

J.-P. Hanke, F. Freimuth, C. Niu, S. Blügel, and Y. Mokrousov
Nature Communications **8***, 1479 (2017)*

9.1 Prelude

Switching the magnetization with ultralow power consumption by electrically induced spin-orbit torques (SOTs) is of outstanding relevance for designing and operating future information devices that follow the fundamental principles of spintronics. In particular, owing to their robustness against disorder details [133], the antidamping torques are perceived to hold promises for switching the magnetization reliably.

While these torques are of intrinsically geometric origin in clean systems (see Chapter 4), basic research on the electrical control of magnetism started to reach out to topological condensed matter only recently – for instance, highly efficient magnetization switching was achieved in metallic systems of magnetically doped topological insulators [246]. Although in the latter conducting materials large torques can be generated, this electric-field response does not root in the global topological properties of these overall trivial systems. Ever since the discovery of the quantum anomalous Hall effect in magnetic insulators has revolutionized and unified our understanding of elementary properties, many transport phenomena in insulating magnets are naturally interpreted based on the non-trivial topology in momentum space [19, 102, 103]. By bridging analogously the field of electrical magnetization control by SOTs and the domain of topological spintronics, in the following, we promote the ubiquitous arguments of topology for designing magneto-electric coupling phenomena in magnetic insulators in the absence of longitudinal dissipative charge currents.

To optimize the performance of magnetization switching in spintronic devices by electrically induced SOTs, Fig. 9.1(a,b), insights into the microscopic origin of the most vital contributions to the electric-field response are crucial. In this respect, it is particularly rewarding to draw an analogy between the antidamping torque rooting in the mixed Berry curvature $\Omega^{\hat{\boldsymbol{m}}\boldsymbol{k}}$ and the intrinsic anomalous Hall effect as determined by the momentum Berry curvature $\Omega^{\boldsymbol{k}\boldsymbol{k}}$. Both of these Berry curvatures are components of the general curvature tensor $\boldsymbol{\Omega}$ in the complex phase space combining the crystal momentum $\boldsymbol{k}$ and the magnetization direction $\hat{\boldsymbol{m}}$ [26, 133]. As we motivated in Chapter 4, important sources or sinks of the momentum Berry curvature $\Omega^{\boldsymbol{k}\boldsymbol{k}}$ are degeneracies, *i.e.*, points where at least two bands cross, which are also referred to as *magnetic monopoles* in momentum space [82]. Following the very same rationale in the case of current-induced torques, band crossings in the composite phase space can be anticipated to manifest locally in a large mixed Berry curvature $\Omega^{\hat{\boldsymbol{m}}\boldsymbol{k}}$, which in turn yields the dominant microscopic contribution to the torkance and the spiralization given by Eqs. (4.52) and (4.58), respectively. Therefore, materials that exhibit such magnetic monopoles near the Fermi level can be expected to display profoundly large SOTs and Dzyaloshinskii-Moriya interaction (DMI).

9.2 Mixed Weyl semimetals

In the field of topological condensed matter [247, 248], the recent advances in realizing Chern insulators that exhibit the quantum anomalous Hall effect have been striking [102, 103]. Similarly, the material class of topological semimetals raised lately to great eminence due to their exceptional properties stemming from monopoles in momentum space. Amid these halfmetallic systems are the three-dimensional magnetic *Weyl semimetals*, which host gapless low-energy excitations with linear dispersion – so-called *Weyl fermions* – close to non-degenerate band crossings at generic $\boldsymbol{k}$-points [249–252]. Acting as sources of the Berry curvature $\Omega^{\boldsymbol{k}\boldsymbol{k}}$, these degeneracies are also known as *Weyl points*. Conventionally, the Weyl fermions are described by the Weyl Hamiltonian $H_{\mathrm{w}} = \sum_i v_i k_i \sigma_i$, where $\boldsymbol{\sigma} = (\sigma_x, \sigma_y, \sigma_z)$ is the vector of Pauli matrices, and v_i are coefficients of the band dispersion. In addition to the current intensive ventures in predicting new type-I and type-II Weyl semimetals in nature [251–253], scrutinizing the stability and symmetry protection of the Weyl

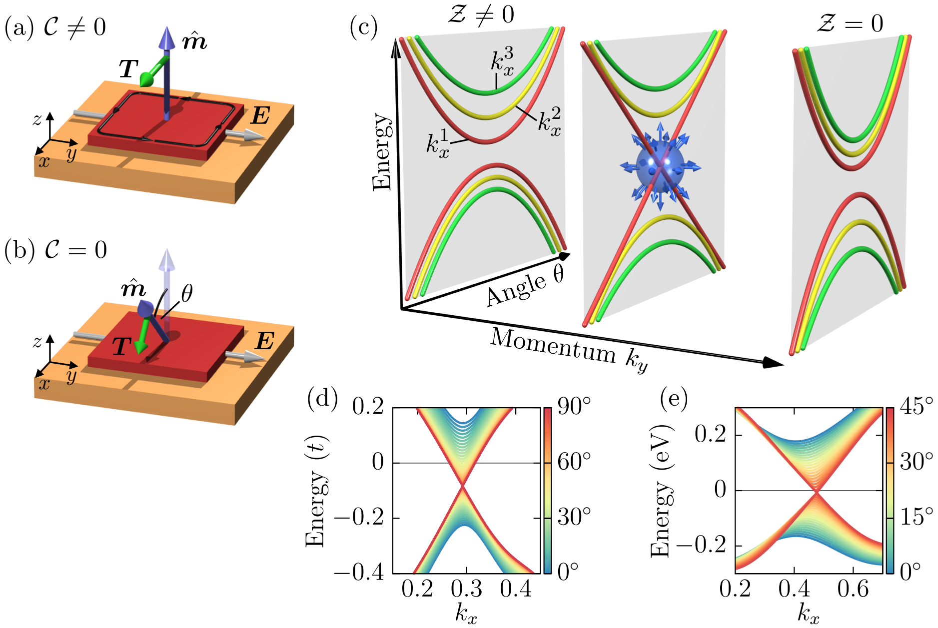

Figure 9.1: Emergence of mixed Weyl points in the complex phase space of crystal momentum and magnetization direction. (a) If an electric field $\boldsymbol{E}$ is applied, the magnetization $\hat{\boldsymbol{m}}$ of a topologically non-trivial insulator is subject to the antidamping torque $\boldsymbol{T}$. (b) The resulting reorientation of $\hat{\boldsymbol{m}}$ by an angle θ can trigger a topological phase transition to the trivial insulator. (c) Schematic evolution of two energy bands in the complex phase space, where colors represent different values of k_x. If we tune k_y, the electronic structure displays a monopole as signalized by the change of the mixed Chern number $\mathcal{Z}$. Indeed, such crossing points are observed in (d) the model of magnetically doped graphene with hopping t and atomic distance a, and (e) the functionalized bismuth film, where colors indicate the magnetization direction $\hat{\boldsymbol{m}} = (\sin\theta, 0, \cos\theta)$ in both cases. The value of k_y is fixed to (d) $k_y = 0.41 \cdot 4\pi/(3a)$ and (e) $k_y = 0.19$ in internal units.

points and uncovering exotic transport properties of the Weyl semimetallic phase are subjects of ever-growing research interest [254].

In order to lay the firm ground for an interpretation of magneto-electric effects using universal arguments of topology, we aim at generalizing the notion of the Weyl point to the case of the complex phase space of crystal momentum and magnetization direction. By replacing formally one of the momentum variables (k_z) in the usual Weyl Hamiltonian with the magnetization direction[1] as specified by an angle θ, we introduce the concept of a *mixed Weyl semimetal*, where crystal momentum and magnetization are entangled. As a result, the low-energy behavior of the system in this complex phase space is described by $H_{\text{mw}} = v_x k_x \sigma_x + v_y k_y \sigma_y + v_\theta \theta \sigma_z$, where θ is the angle that the magnetization direction $\hat{\boldsymbol{m}} = (\sin\theta, 0, \cos\theta)$ encloses with the

---

[1] At this stage, we restrict ourselves to the case of a fixed azimuthal angle $\varphi = 0$.

z-axis. Including explicitly the angle θ endows a mixed Weyl semimetal with distinct physical properties – while it is insulating for general directions of the magnetization, it features band crossings at the Fermi level for special values of θ. These values are determined either by the symmetries of the magnet or by the interplay of spin-orbit coupling and exchange interaction in low-symmetric situations. As illustrated in Fig. 9.1(c), a mixed Weyl semimetal as described by the new Weyl Hamiltonian H_{mw} hosts *ergo* magnetic monopoles, or, *mixed Weyl points* that give rise to prominent contributions to the Berry curvatures $\Omega^{\boldsymbol{kk}}$ and $\Omega^{\hat{\boldsymbol{m}}\boldsymbol{k}}$ in the complex phase space of $\boldsymbol{k}$ and θ. In analogy to conventional Weyl semimetals [249], we can classify the underlying topology and detect such magnetic monopoles by tracking the flux of the mixed Berry curvature through planes of constant k_y as given by the integer *mixed Chern number* $\mathcal{Z} = 1/(2\pi)\int \Omega_{yx}^{\hat{\boldsymbol{m}}\boldsymbol{k}}\mathrm{d}\theta\mathrm{d}k_x$, Fig. 9.1(c). Alternatively, we can identify the topological structure of these degeneracies based on their *monopole charge*, which is the flux of the Berry curvature field through a closed two-dimensional surface that encompasses one of the monopoles[2]. Utilizing the dynamical magnetization in topologically non-trivial materials, we demonstrate here the existence of mixed Weyl semimetals and focus on the implications of the corresponding monopoles for magneto-electric coupling phenomena. In particular, we uncover that a strong electric-field response due to the magnetic monopoles in mixed Weyl semimetals is invaluable in paving the road towards low-dissipation magnetization control by SOTs [255].

9.3 Tight-binding considerations

To scrutinize the nature of emergent monopoles in the complex phase space of magnets, we begin with a tight-binding model of magnetically doped graphene [101]:

$$\begin{aligned} H = &- t\sum_{\langle ij\rangle}\sum_{\alpha} c_{i\alpha}^{\dagger}c_{j\alpha} + \mathrm{i}t_{\mathrm{so}}\sum_{\langle ij\rangle}\sum_{\alpha\beta}\hat{\boldsymbol{e}}_z\cdot(\boldsymbol{\sigma}\times\boldsymbol{d}_{ij})_{\alpha\beta}c_{i\alpha}^{\dagger}c_{j\beta} \\ &+ \lambda\sum_{i}\sum_{\alpha\beta}(\hat{\boldsymbol{m}}\cdot\boldsymbol{\sigma})_{\alpha\beta}c_{i\alpha}^{\dagger}c_{i\beta} - \lambda_{\mathrm{nl}}\sum_{\langle ij\rangle}\sum_{\alpha\beta}(\hat{\boldsymbol{m}}\cdot\boldsymbol{\sigma})_{\alpha\beta}c_{i\alpha}^{\dagger}c_{j\beta}\,, \end{aligned} \tag{9.1}$$

which is depicted in Fig. 9.2(a). Here, $c_{i\alpha}^{\dagger}$ ($c_{i\alpha}$) denotes the creation (annihilation) of an electron with spin α at the ith lattice site, $\langle ...\rangle$ restricts the corresponding sums to nearest neighbors, and the unit vector $\boldsymbol{d}_{ij}$ points from j to i. Apart from the usual hopping with amplitude t, the first line in Eq. (9.1) contains the Rashba spin-orbit coupling of strength t_{so} originating from the surface potential gradient of the substrate. The remaining two terms in Eq. (9.1) are the exchange energy due to the local (λ) and non-local (λ_{nl}) exchange interaction between spin and magnetization. Depending on the magnetic orientation $\hat{\boldsymbol{m}}$, the non-local exchange describes a hopping process during which the spin can flip. Introducing four orthonormal basis states on the bipartite honeycomb lattice, we represent this tight-binding model with $t_{\mathrm{so}} = 0.3\,t$, $\lambda = 0.1\,t$, and $\lambda_{\mathrm{nl}} = 0.4\,t$ as a 4×4 matrix that is diagonalized at every $\boldsymbol{k}$-point to obtain the electronic and topological properties.

---

[2] The concept of a monopole charge relies on working with an at least three-dimensional phase space as spanned by k_x, k_y, and θ. Thus, if the magnetization direction is not taken into account, the monopole charge is ill-defined in any two-dimensional system.

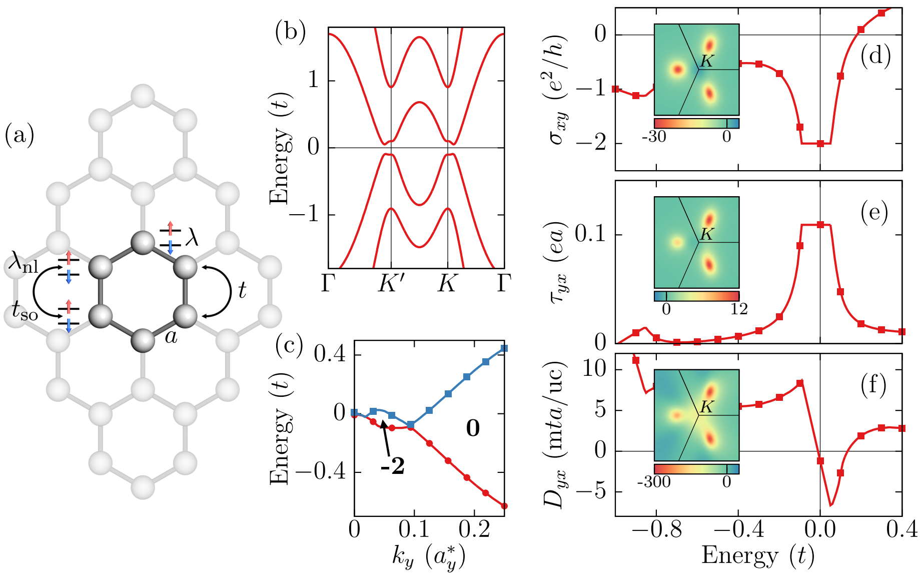

Figure 9.2: Model of magnetically doped graphene. (a) Sketch of the tight-binding model and the parameters therein. (b) Band structure with out-of-plane magnetization and $t_{\mathrm{so}} = 0.3\,t$, $\lambda = 0.1\,t$, $\lambda_{\mathrm{nl}} = 0.4\,t$. (c) Evolution of the valence band top (red circles) and conduction band bottom (blue squares) with k_y, where the depicted gap closing occurs for $\theta = -90°$ and $\boldsymbol{k} = (0.71a_x^*, 0.09a_y^*)$ with $a_x^* = 2\pi/(\sqrt{3}a)$ and $a_y^* = 4\pi/(3a)$. Bold integers denote the mixed Chern number $\mathcal{Z}$ in the insulating regions. (d)–(f) Energy dependence of the anomalous Hall conductivity $\sigma_{xy} = \mathcal{C}e^2/h = e^2/(2\pi h)\int \Omega_{xy}^{\boldsymbol{kk}} \mathrm{d}k_x \mathrm{d}k_y$, the torkance τ_{yx}, and the spiralization D_{yx}, respectively, for an out-of-plane magnetization. Insets show the corresponding momentum-space distributions summed over all occupied states in the vicinity of the K-point.

Monitoring the variation of the mixed Chern number $\mathcal{Z}$ with k_y, we evidence first that the above model hosts indeed a mixed Weyl semimetallic state. As presented in Fig. 9.2(c), the topological index $\mathcal{Z}$ changes from -2 to 0 at a certain value of k_y, heralding thereby the emergence of a band crossing in the complex phase space that carries a topological charge of $+2$. While this band crossing appears near the K'-point off any high-symmetry line for $\theta = -90°$, another monopole of opposite charge is located close to the K-point if the magnetization is oriented in-plane along the $+x$-direction (see Fig. 9.1(d)). The fact that the quantum anomalous Hall effect emerges not only for $\theta = 0°$ [101], Fig. 9.2(d), but over a broad range of magnetization directions can be viewed as a key manifestation of the magnetic monopoles serving as sources of the curvature $\Omega^{\boldsymbol{kk}}$. In addition, large contributions to the mixed Berry curvature $\Omega^{\hat{\boldsymbol{m}}\boldsymbol{k}}$ in the vicinity of one of the monopoles are visible in the momentum-space distributions of the torkance and the spiralization shown in the insets of Figs. 9.2(e) and 9.2(f), respectively. For an out-of-plane magnetization ($\theta = 0°$), the dominant microscopic contribution to the phenomena roots in an avoided band crossing along the line ΓK – a residue of the Weyl point in the extended phase space. As the expression for the mixed Berry curvature hinges only on the derivative of the wave function with respect to one of the components of the Bloch wave vector (see Eq. (4.39)), the symmetry between k_x and k_y in the distributions of torkance and spiralization is broken naturally.

Stemming from the momentum-space distribution driven by the monopole, the energy dependence of the torkance τ_{yx} in Fig. 9.2(e) reveals a modest size of $0.1\,ea$ in the insulating region (with a as interatomic distance), which remains constant through the global band gap. Contrary to the integer Chern numbers $\mathcal{C}$ and $\mathcal{Z}$, the height of the torkance plateau in Fig. 9.2(e) is, however, sensitive to details of the electronic structure such as model parameters and magnetization direction, *i.e.*, the torkance τ_{yx} is not guaranteed to be quantized to a robust value. Because of their intimate relation in the Berry phase theory [28, 123], the constant torkance implies a linear variation of the spiralization D_{yx} in the gap, changing from $8\,\mathrm{m}ta/\mathrm{uc}$ to $-6\,\mathrm{m}ta/\mathrm{uc}$ as shown in Fig. 9.2(f), where “uc” refers to the in-plane unit cell of two atoms.

9.4 First-principles theory

9.4.1 Magnetically doped Graphene

In order to identify realizations of the characteristic model predictions above, we investigate from *ab initio* systems of graphene decorated by transition-metal adatoms, Fig. 9.4(a). As we discussed in Chapter 6, the complex hybridization of graphene p states with transition-metal d states mediated by spin-orbit coupling renders these systems one of the prototypical material classes that accommodate the quantum anomalous Hall effect [186, 256–259]. Details on the first-principles calculations are provided in Appendix A.3. Within the topologically non-trivial band gap of these materials with the magnetization perpendicular to the graphene plane, depending on the transition-metal adatom, both torkance and spiralization can attain vast magnitudes that originate from mixed Weyl points in the combined phase space. In the case of W deposited in a 4×4-geometry on graphene, for instance, we predict an eminently large value for the torkance of $\tau_{yx} = -2.9\,ea_0$ (with a_0 being Bohr’s radius), and the spiralization D_{yx} ranges from $-5\,\mathrm{meV}a_0/\mathrm{uc}$ to $60\,\mathrm{meV}a_0/\mathrm{uc}$, Fig. 9.4(b–e). Thereby, both monopole-driven phenomena surpass utterly the conventional values that are obtained in metallic magnetic heterostructures [28, 133] and non-centrosymmetric bulk magnets [167]. Since the details of the electronic structure can affect the value of the torkance plateau in the gapped regions, when replacing W with other transition metals such as Ir, we find that the magnitude of SOT and DMI can be tailored according to our calculations.

9.4.2 Functionalized bismuth bilayer

Alluding ultimately to room-temperature applications in spintronics, we aim at realizing pronounced magneto-electric coupling phenomena in magnetic insulators that display a larger band gap as compared to the above examples. For this purpose, we consider a semi-hydrogenated Bi(111) bilayer as shown in Fig. 9.3(a), which constitutes a notable prototype of functionalized insulators that exhibit non-trivial topological properties and phases [259]. Below, we uncover that the semi-hydrogenated bismuth bilayer is a mixed Weyl semimetal with complex topology in the compos-

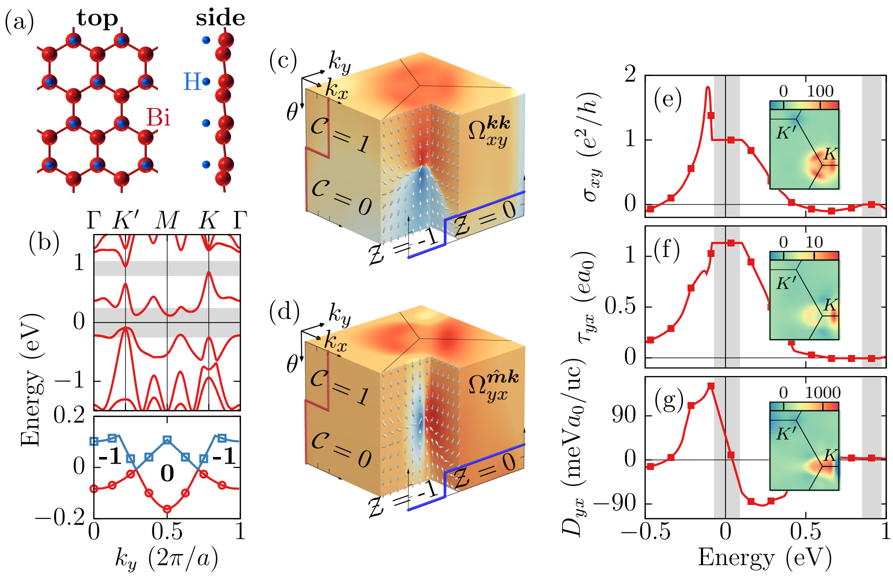

Figure 9.3: Magneto-electric properties of a mixed Weyl semimetal. (a) Top and side view of the semi-hydrogenated Bi(111) bilayer. (b) First-principles band structure for an out-of-plane magnetization, where the region of the topological band gap and the trivial one above are highlighted. Additionally, the evolution of valence band top (red circles) and conduction band bottom (blue squares) with k_y is shown. Bold integers denote the mixed Chern number $\mathcal{Z}$, and a is the in-plane lattice constant. (c,d) Distribution of momentum and mixed Berry curvatures in the complex phase space close to one of the emergent Weyl points. Gray arrows represent the direction of the curvature field $(-\Omega^{\hat{\boldsymbol{m}}\boldsymbol{k}}_{yy}, \Omega^{\hat{\boldsymbol{m}}\boldsymbol{k}}_{yx}, \Omega^{\boldsymbol{kk}}_{xy})$, and a logarithmic color scale is used to display two of its components, where dark red (dark blue) denotes large positive (negative) values. (e)–(g) Energy dependence of σ_{xy}, τ_{yx}, and D_{yx} for a perpendicularly magnetized film. Insets show the microscopic contributions in momentum space near the inequivalent valleys K and K'.

ite phase space of the crystal momentum $\boldsymbol{k}$ and the magnetization direction θ. If the magnetization is perpendicular to the film plane, the system is a valley-polarized quantum anomalous Hall insulator [260] with a magnetic moment of $1.0\,\mu_\mathrm{B}$ per unit cell, a large band gap of 0.18 eV at the Fermi energy, and a prominent asymmetry between the valleys K and K' depicted in Fig. 9.3(b). Appendix A.7 provides the computational details that underlie our first-principles calculations.

By analyzing in Fig. 9.3(b) how the mixed Chern number $\mathcal{Z}$ evolves with k_y, we discover two magnetic monopoles of opposite charge ±1 that emerge right at the transitions between the two topologically inequivalent phases that are distinguished by the topological index $\mathcal{Z} = -1$ or $\mathcal{Z} = 0$. These crossing points and their topological charges in the composite phase space could be extracted equivalently from monitoring the evolution of the usual Chern number $\mathcal{C}$ with varying magnetization direction. Strikingly, the monopoles occur at generic phase-space points near the valley K for $\theta = 43^\circ$ (see Fig. 9.1(e)) and close to the K'-point for $\theta = 180^\circ - 43^\circ = 137^\circ$, respectively, which implies that the charge-neutral pair of mixed Weyl points is formed by monopoles located at different magnetization directions. Thus, in sharp contrast to their traditional cousins realized in three spatial dimensions, two-dimensional mixed Weyl semimetals can host a single metallic point at the phase transition. As presented in Fig. 9.3(c,d), the existence of such mixed Weyl points in the electronic structure impacts drastically the shape of the general Berry curvature $\boldsymbol{\Omega}$ in their vicinity, which becomes obvious when representing $\boldsymbol{\Omega}$ as a vector field in the complex phase space. Displaying characteristic sign changes when moving through the monopoles in phase space, the singular behavior of the Berry curvature encourages us to interpret the mixed Weyl points as sources or drains of $\boldsymbol{\Omega}$. If the magnetization is oriented out of the plane, the non-trivial topology of the electronic structure in momentum space results in the quantization of $\mathcal{C}$ to +1, Fig. 9.3(e), which is primarily due to large positive contributions near K, where the energy bands approach each other. The energy dependence of the torkance and the spiralization in the insulating magnet, shown in Figs. 9.3(f) and 9.3(g), herald the sublime magnitudes of these phenomena of the order of $1.1\, ea_0$ for τ_{yx} and $50\,\mathrm{meV}a_0/\mathrm{uc}$ for D_{yx}, surpassing by far the typical magnitudes of these effects in magnetic metallic materials [28, 133, 167].

9.4.3 Torque due to magnetic anisotropy

Before turning to a clear proof that the predicted magneto-electric phenomena root indeed in mixed Weyl points, we comment on the role of the magnetic anisotropy energy for the studied effects. Our calculations reveal that magnetically doped graphene favors an in-plane magnetization while an out-of-plane orientation is preferred in the functionalized bismuth film. In both cases, the respective magnetic state is stabilized by a magnetic anisotropy barrier that is comparable to the values of the order of 1 meV in metallic heterostructures such as Co/Pt.

If $\hat{\boldsymbol{m}}$ is not aligned with the easy axis (or lies outside of the easy plane), the magnetization is subject to an additional *magnetic anisotropy torque* [133] due to the magnetic anisotropy energy. However, the qualitative behavior of this torque is completely different from the electrically induced antidamping SOT since the former roots not in the geometry of the complex phase space, thus being not responsive to the mixed Weyl points. By performing explicit calculations, we estimate that for the example of the functionalized bismuth film with $\theta = 30^\circ$ the magnitude of the antidamping SOT is larger than the magnetic anisotropy torque if the applied in-plane electric field exceeds the rather small value of $5\,\mathrm{mV/Å}$. To tailor the exact relation between the magnetic anisotropy torque and the antidamping SOT, one can thus either tune the magnitude of the applied in-plane electric field, or adapt the strength of the magnetic anisotropy energy by applying an out-of-plane electric field [186].

9.5 Nature of the electric-field response

At this stage, the key question arises whether the striking magnitude of the SOT in the considered magnetic insulators can be ascribed unambiguously to the presence of the mixed Weyl semimetallic state. We address this point in the following by explicitly unfolding the utter relevance of the emergent magnetic monopoles in giving rise to a pronounced magneto-electric response. First, when removing the mixed

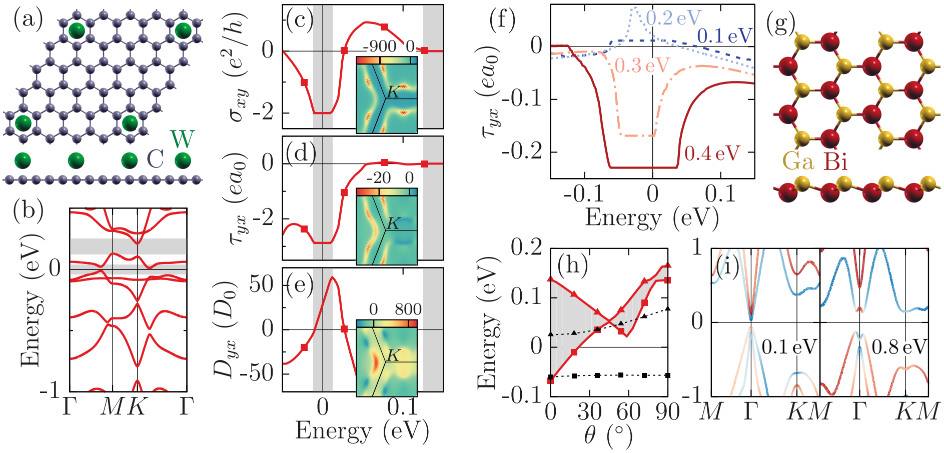

Figure 9.4: Monopole-driven spin-orbit torques in mixed Weyl semimetals. (a) Crystal structure of graphene decorated by W adatoms. (b) First-principles band structure of the perpendicularly magnetized film. The topologically non-trivial gap around the Fermi level and the trivial gap above are highlighted. (c)–(e) Energy dependence of anomalous Hall conductivity σ_{xy}, torkance τ_{yx}, and spiralization D_{yx}, respectively. In the latter case, the unit D_0 stands for meVa_0 per unit cell. Insets show the microscopic contributions in momentum space near the K-point. (f) Energy dependence of the torkance τ_{yx} in a GaBi film upon applying an exchange field $\boldsymbol{B} = B_0(\sin\theta, 0, \cos\theta)$ perpendicular to the film plane, where the numbers denote B_0. (g) Crystal structure of the system. (h) Evolution of valence band top (squares) and conduction band bottom (triangles) with varying θ for $B_0 = 0.1\,\mathrm{eV}$ (black dashed lines) and $B_0 = 0.8\,\mathrm{eV}$ (red solid lines). (i) Band structures for $\theta = 0°$ and two different values of B_0, where colors illustrate the spin polarization normal to the film.

Weyl points from the electronic structure of the tight-binding model (9.1), *e.g.*, by including an intrinsic (on-site) spin-orbit coupling term, we confirm that the electric-field response is strongly diminished in the insulating phase, which identifies the monopoles as unique origin of large SOTs and DMI. To confirm this statement also in the presented first-principles results, secondly, we study the electric-field response within the topologically trivial gaps above the Fermi level that are highlighted in Figs. 9.3(b) and 9.4(b). Since no mixed Weyl points manifest in the corresponding energy regions, where the gaps remain opened for any value of θ, we obtain a greatly suppressed magnitude of the antidamping torkance τ_{yx} as evident from Figs. 9.3(f) and 9.4(d).

Finally, we clearly promote the exceptional role of these distinct points by considering an educational example of a thin film of GaBi with triangular lattice structure, Fig. 9.4(g). The computational parameters of our electronic-structure calculations are summarized in Appendix A.8. As the original system is a non-magnetic trivial insulator, we artificially apply on top the exchange field $\boldsymbol{B} = B_0(\sin\theta, 0, \cos\theta)$ to trigger a topological phase transition as the field strength B_0 is tuned in the exchange term $\boldsymbol{B}\cdot\boldsymbol{\sigma}$. While varying B_0 we carefully follow the evolution of the hybrid system from a trivial magnetic insulator for $|B_0| \leq 0.2\,\mathrm{eV}$ to a mixed Weyl semimetal as signalized by the emergence of magnetic monopoles in the electronic structure. The quantum anomalous Hall effect accompanies the latter phase over a finite range of directions θ, *e.g.*, if the exchange field is perpendicular to the film plane as shown in Fig. 9.4(h,i). Comparing in Fig. 9.4(f) the electric-field response for these two distinct phases, we identify drastic changes in sign and magnitude of the torkance τ_{yx} with the transition from the topologically trivial insulator to the mixed Weyl semimetal hosting monopoles near the Γ-point for generic directions θ. This demonstrates uniquely the crucial importance of emergent mixed Weyl points in inducing large magneto-electric coupling effects in topologically non-trivial magnetic insulators.

9.6 Discussion and outlook

Since mixed Weyl semimetals manifest an intricate interplay between the magnetization direction and the topology in momentum space, magnetization switching via antidamping torques can mediate topological phase transitions in these systems from a Chern insulator to a trivial magnetic insulator as illustrated in Fig. 9.1(a,b). The case of the functionalized bismuth film serves as an ideal example, where the material turns from a Chern insulator into a trivial magnetic insulator with a band gap of 0.25 eV if the magnetization lies in the film plane. Nevertheless, the resulting antidamping torkance in this trivial state is still very large, and also the DMI exhibits a strong variation within the gap due to the presence of mixed Weyl points in the complex phase space, Fig. 9.5(a). Therefore, we propose in particular quantum anomalous Hall systems fabricated to date [103, 261–263] as promising candidates for the experimental search and realization of large magneto-electric response and topological phase transitions. Strikingly, mixed Weyl semimetals that consolidate a prominent electric-field response and a large energy gap (such as, *e.g.*, functionalized bismuth films) hold extremely auspicious prospects for room-temperature applications of magneto-electric coupling effects in low-dissipation[3] magnetization control – a topic that is under ongoing intensive scrutiny (see, *e.g.*, Refs. [255, 264, 265]). While a large antidamping SOT in magnetic metallic bilayers (*e.g.*, Co/Pt) stems primarily from the spin Hall effect due to the strong spin-orbit interaction in the non-magnetic substrate [145], the sizable SOT in the insulating phase of mixed Weyl semimetals is of profoundly different origin. As this effect is driven by the presence of magnetic monopoles rather than the spin-orbit coupling itself, mixed Weyl semimetals open the intriguing perspective to achieve pronounced magneto-electric responses even in materials consisting of light atoms with weak spin-orbit interaction.

Analogously to transport effects and SOTs, the phenomenon of orbital magnetism is prominently susceptible to the mixed Weyl points in the electronic structure, owing to its intimate relation to the Berry curvature in momentum space. In the functionalized bismuth film, for example, the magnitude of the $\boldsymbol{k}$-resolved out-of-plane OM in Fig. 9.5(b) amounts to colossal values of as much as $\pm 10\,\mu_{\mathrm{B}}/\mathrm{uc}$ close to the monopole. Although the integral of these competing local contributions over the neighborhood of a single mixed Weyl point almost vanishes in equilibrium, these monopoles may manifest in a particularly large current-induced OM if an electric field $\boldsymbol{E}$ is used to

---

[3] Here, "low-dissipation" refers to the vastly suppressed Ohmic losses in insulating systems as compared to metallic magnets.

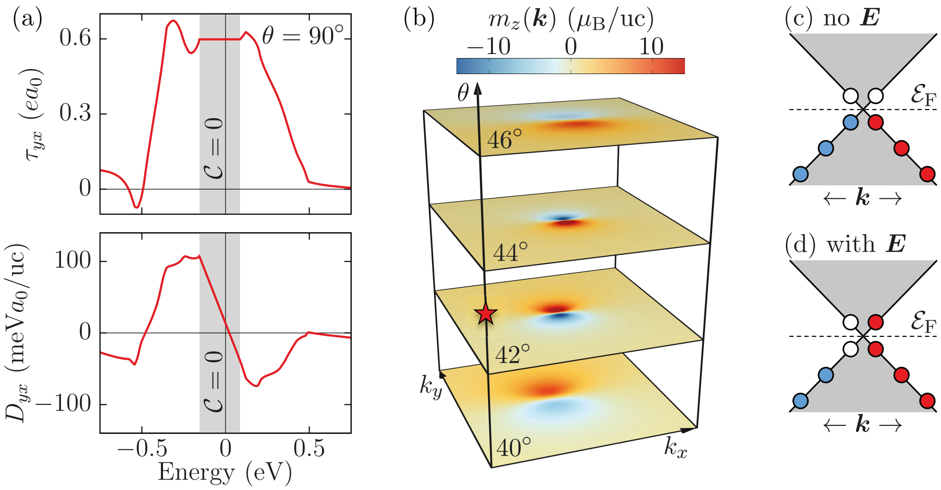

Figure 9.5: (a) Energy dependence of τ_{yx} and D_{yx} in the functionalized bismuth film for an in-plane magnetization direction, where the shaded region illustrates the topologically trivial energy gap around the Fermi level. (b) Momentum-space distribution of the out-of-plane orbital magnetization (orbital magnetization (OM)) close to the mixed Weyl point that appears for $\theta = 43°$ (star). (c) In equilibrium, the states with positive (red) and negative (blue) local contributions to the OM are occupied equally, and open circles denote unoccupied states. (d) This population can be modified by an applied electric field $\boldsymbol{E}$ to induce a large net OM.

repopulate the electronic states around the Fermi level as illustrated in Fig. 9.5(c,d). Stemming from the complex geometry of the extended phase space, such monopole-driven orbital Edelstein effect can have momentous consequences, especially for phenomena that are associated with the orbital moment at the Fermi surface such as the gyrotropic magnetic effect [128].

In the examples that we studied here, the non-trivial topology of the mixed Weyl semimetals results in a DMI that takes values from broad range when passing the band gap, which implies that proper electronic-structure engineering enables us to tailor both strength and sign of the DMI in a given system. Exploiting such versatility by doping or by applying strain could help to stabilize chiral magnetic structures like magnetic skyrmions in insulating ferromagnets. In addition, very large antidamping SOT in such textured materials would lay out exciting avenues to manipulate and control the dynamical properties of chiral objects by magneto-electric coupling effects under minimal energy consumption.

At this stage, we emphasize the overall significance of the discussed magnetic monopoles in the complex phase space, which do not only govern the electric-field response in insulating magnets but contribute also in metals, where they are hidden, however, in the background of myriad energy bands crossing the Fermi level. In analogy to the (non-quantized) anomalous Hall effect in metals, this renders the analysis of SOT and DMI particularly tedious, owing to the competing effects associated with the metallic bands. Furthermore, the reachable magnitude of response phenomena is limited as compared to magnetic insulators since the reachable electric-field strength in metals is typically much smaller. Strikingly, the emergent Weyl points in the electronic structure could provide an alternative explanation for the strong SOT in magnetically doped topological insulators (see, *e.g.*, Ref. [246]), which is ascribed so far to the peculiar spin-momentum locking of the helical surface states of the topological insulator constituting a highly efficient source of spin currents.

Up next, we discuss the relevance of the outlined Berry phase physics for antiferromagnets, where the reliable switching of the staggered magnetization by means of current-induced spin torques has been demonstrated only lately [14]. Here, we focus on antiferromagnets that reveal the combined symmetry of time reversal and spatial inversion, for which the phenomenon of SOT is intimately related to the physics of *Dirac fermions* as doubly-degenerate elementary excitations with linear dispersion [266, 267]. Similarly to the suggested notion of mixed Weyl semimetals, we anticipate that the concept of *mixed Dirac semimetals* in the complex phase space of crystal momentum and staggered magnetization direction will become invaluable for grasping the microscopic origins of SOTs in insulating antiferromagnets. Adopting the very same viewpoint that we formulated above for ferromagnets, emergent monopoles (*mixed Dirac points*) in the degenerate electronic structure of antiferromagnets can be expected to form the leading sources or sinks of the according general non-Abelian Berry curvature. Analogously to the spin Berry curvature for quantum spin Hall insulators and Dirac semimetals [268–270], the mixed band-diagonal components of this curvature tensor manifest in sublattice-dependent antidamping SOTs. Based on this rewarding microscopic understanding, applying the principles of electronic-structure engineering for topological properties that rely on the staggered magnetization could advance the use of pronounced magneto-electric response in insulating antiferromagnets.

In order to conclude our pioneering expedition for the complex topology of the combined phase space of the crystal momentum and the magnetization direction $\hat{\boldsymbol{m}} = (\cos\varphi\sin\theta, \sin\varphi\sin\theta, \cos\theta)$, we elucidate briefly the influence of the azimuthal angle φ that was set to zero so far. As an illustrative example, we start from the mixed Weyl points in the functionalized bismuth film and study their dynamical behavior in the four-dimensional space $(k_x, k_y, \theta, \varphi)$ as the magnetization direction is varied. Following this procedure, we realize that these monopoles are robust but move along a closed line through the combined phase space as shown in Fig. 9.6, which reminds us of the physics of topological nodal-line semimetals discussed, *e.g.*, in Refs. [271, 272]. Therefore, it is tempting to refer to these loops as *mixed nodal lines* that are characterized by a non-trivial topological Berry phase around them. Uncovering the effect of these intriguing mixed nodal lines on transport, magnetic properties, and magneto-electric coupling is left for future studies.

In conclusion, accounting for the response of the electronic structure to the dynamical magnetization holds bright promises for understanding and designing various geometrical phenomena in insulating and metallic magnets such as strong magneto-electric effects, magneto-crystalline anisotropy, magnetic damping, and prominent current-induced orbital magnetism. The developed technique of generalized Wannier interpolation is optimally adapted to describe efficiently these phenomena originating from the complex geometry of the underlying higher-dimensional phase space.

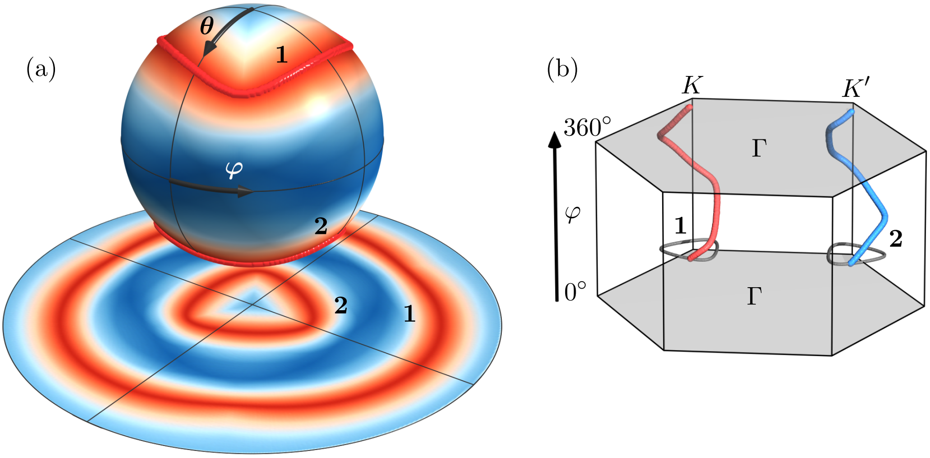

Figure 9.6: Mixed nodal lines in the functionalized bismuth film. (a) The global band gap evolves with the magnetization direction $\hat{\boldsymbol{m}} = (\cos\varphi\sin\theta, \sin\varphi\sin\theta, \cos\theta)$ as indicated by the colors ranging from red (no gap) to blue (finite gap). The energy gap vanishes along two closed loops in the upper (1) and lower (2) hemisphere, respectively, and the topological Berry phase is non-trivial around these two mixed nodal lines. (b) These loops can be understood as mixed Weyl points that are dragged around either K (1, red) or K' (2, blue) in the hexagonal Brillouin zone as φ varies and θ is adapted accordingly. Solid gray lines denote projections of these nodal lines to the plane.

Chapter 10

Summary and conclusions

In the current work, we have presented a comprehensive first-principles analysis of geometric phenomena in complex magnetic systems based on the accurate full-potential linearized augmented-plane-wave (FLAPW) method. In order to unify the efficient description of anomalous charge transport, orbital magnetism, electrically induced spin torques, and chiral exchange interactions, the Jülich density functional theory code FLEUR has been supplemented by newly developed computational methods.

By implementing and applying a Wannier-based interpolation scheme for the orbital magnetization (OM) according to a recent Berry phase theory, we identified in the first part of this thesis the key role of the so-called modern theory for the reliable treatment of orbital magnetism in density functional theory. While the modern theory of OM was suggested so far to provide only non-critical corrections to orbital magnetism as compared to a simple yet routinely employed atom-centered approximation (ACA), we demonstrated that the predictive power of the latter approach is limited to elementary bulk ferromagnets. When dealing with orbital magnetism in material classes that are under extensive scrutiny in today's spintronics such as magnetic heterostructures and topologically complex systems, however, we showed that the OM is described qualitatively only within the rigorous Berry phase theory. For example, the ACA breaks down completely in Chern insulators, for which the underlying non-trivial topology in momentum space manifests in an OM that varies linearly with energy as predicted correctly by the modern theory. Thus, our results substantiate unambiguously the use of the complete but computationally challenging Berry phase formalism, and emphasize additionally the relevance of this modern theory in order to link to experiments on orbital magnetism in novel spintronic devices. Since most *ab initio* frameworks of density functional theory still resort to the simple ACA, we further anticipate that our general conclusions will eventually motivate efforts for implementing the Berry phase approach in other electronic-structure codes as well.

The emergence of a spontaneous orbital moment in the crystal field of a periodic solid is typically ascribed to the spin-orbit interaction, which breaks the degeneracy between left- and right-circulating charge currents. Going beyond this well-known and widely accepted explanation of orbital magnetism in ferromagnets, we promoted the unconventional phenomenon of topological orbital magnetism that manifests even in the absence of spin-orbit coupling due to the complex arrangement of spins in noncollinear magnets. In these systems, the effect of the chiral spin texture is mapped to a fictitious magnetic field that manipulates the electrons' motion and lifts ultimately the quenching of the orbital moment in the crystal field. Considering as prototypes bulk and film antiferromagnets with $3\boldsymbol{Q}$ spin structure, we pioneered the comprehensive analysis of topological orbital magnetism, investigated the accompanying topological Hall effect, and correlated the phenomena with the first-principles electronic structure. While the direction of the OM is determined solely by the symmetry of the studied materials, its magnitude relies on the scalar spin chirality as determined by the non-trivial spin texture. Being tunable by means of adequate engineering of the electronic structure as uncovered by our calculations, the topological OM can amount to remarkably sizable values of as much as $-1.6\,\mu_{\mathrm{B}}$ per unit cell in the case of the two-dimensional antiferromagnet Mn/Cu(111), which puts the considered systems on one level with conventional ferromagnets. As a consequence, these spin-compensated magnets are prototypical examples of a new class of materials coined topological orbital ferromagnets, *i.e.*, systems for which the macroscopic magnetization is purely due to the orbital magnetism that is present without any reference to the spin-orbit interaction or electron-electron correlations. Originating from the chiral spin texture, the resulting topological orbital moments are rather robust, which holds intriguing promises to use them as fundamental operational units and reliable information carriers in the burgeoning field of chiral orbitronics. Finally, we proposed potential material realizations based on an analysis of the corresponding magnetic point groups, and outlined a protocol to detect topological orbital magnetism in experiments on magnetic circular dichroism.

Developing the new formalism of higher-dimensional Wannier functions (HDWFs), we established in the second part of this thesis an accurate but efficient Wannier interpolation of Hamiltonians that depend on a set of abstract parameters besides the crystal momentum. Since this generalized interpolation scheme resembles formally the usual technique based on maximally-localized Wannier functions (MLWFs), the former is directly accessible to the large community of physicists that employ routinely the conventional Wannier interpolation. The scope of scientific problems to which our advanced method can be applied is particularly broad, including but not limited to the computation of exchange constants, the efficient description of anisotropic transport effects, and the accurate evaluation of magneto-electric coupling phenomena. In this thesis, we focused on spin-orbit torques (SOTs) and the Dzyaloshinskii-Moriya interaction (DMI) in ferromagnetic systems, both of which are interpreted naturally as geometric responses in the curved phase space of crystal momentum and magnetization direction. Given this setting, we elucidated the FLAPW implementation of the necessary first-principles input for constructing HDWFs, and specified also the higher-dimensional Wannier interpolation for the Berry phase theory of torkance and spiralization.

We verified that our advanced *ab initio* scheme interpolates torkance and spiralization accurately, and facilitates moreover the calculation of the anisotropy of these Berry phase properties with the magnetization direction as compared to an alternative but cumbersome approach based on the exchange field. Additionally, our technique was applied to unravel efficiently the microscopic origins of the studied phenomena of SOT and DMI as well as their mutual connection in metallic heterostructures. Scrutinizing as highly relevant example the system of a Co monolayer on Pt(111) covered by alloyed overlayers of $5d$ transition metals, we discovered a complex non-monotonic dependence of the spiralization on the composition ratio. Remarkably, we predicted characteristic sign changes of the spiralization under moderate doping of the Pt overlayer with Ir, which constitute thus promising systems for experiments to study in more detail. Ultimately, we outlined the consequences of the prominently anisotropic spin torques in the Co-based heterostructures on the dynamical properties of chiral magnetic skyrmions. As demonstrated by our first-principles calculations exploiting the valuable higher-dimensional Wannier interpolation, proper electronic-structure engineering constitutes overall an auspicious tool to tailor SOTs and DMI as well as their anisotropy in complex metallic magnets.

When topology as a branch of mathematics reached out to the field of physics, our understanding of many elementary solid-state phenomena was revolutionized, manifesting eventually in a classification of matter based on global geometrical properties of the underlying momentum space. Following analogous logic, we proposed in this thesis to utilize the ubiquitous arguments of topology to explain prominent magneto-electric phenomena and magnetization switching in insulating ferromagnets. In particular, we introduced the concept of mixed Weyl semimetals, for which the combined phase space of crystal momentum and magnetization direction hosts magnetic monopoles that manifest in large antidamping torques and DMI. Using a tight-binding model and first-principles calculations of realistic materials based on the developed technique of HDWFs, we confirmed our theoretical ideas and identified unambiguously the key role of the emergent monopoles. Strikingly, the magnitude of electrically induced spin torques in the insulating phase of the considered mixed Weyl semimetals can easily exceed the size of SOTs in the conventional metallic heterostructures studied before. This opens fascinating perspectives for designing the electric-field control of magnetism in novel low-dissipation spintronic devices that may operate ultimately even at room temperature owing to the decent bulk band gap in these materials. Moreover, efficient magnetization switching by large antidamping torques can mediate topological phase transitions owing to the complex interplay of magnetization direction and topology in mixed Weyl semimetals. Our pioneering first-principles expedition to the higher-dimensional phase space entangling Bloch wave vector and magnetization direction was complemented by an assessment of the importance of the suggested concepts for controlling magnetism or generating spin currents in insulating antiferromagnets, metals, and doped topological insulators. Eventually, we discovered that the geometric phenomenon of orbital magnetism is enhanced locally in the vicinity of the magnetic monopoles, which can manifest in a prominent non-equilibrium OM due to external electric fields or charge currents.

In conclusion, this thesis has combined developments of versatile computational methods for density functional theory with applications in spin-orbitronics to advance the understanding of fundamental properties of complex magnetic systems, and to predict new emergent phenomena based on the universal arguments of topology.

Appendices

Appendix A

Computational details

In the following, we present the computational details of our self-consistent density functional calculations that were performed within the FLAPW code FLEUR [74]. After converging initially the electronic charge density with the computational parameters chosen to guarantee predictive power, we collected information on the wave functions and the band energies on a coarse grid that samples the Brillouin zone. Depending on whether we construct MLWFs or HDWFs, we forwarded this information as input either to the conventional WANNIER90 program [273] or to our generalized version of the code. In a final post-processing step, the resulting tight-binding functions were used to achieve an efficient but accurate Wannier interpolation of the considered electronic properties on a dense mesh.

In most of the calculations, we employed the generalized gradient approximation (GGA) based on the functional by Perdew, Burke, and Ernzerhof (PBE) [52], unless stated explicitly. Conventionally, the temperature smearing of the Fermi-Dirac distribution that enters the evaluation of the Fermi energy was set to 1 mHtr. The MLWFs were constructed from the wave-function information on a uniform mesh of $8\times 8\times 8$ (bulk) or 8×8 (film) $\boldsymbol{k}$-points sampling the full Brillouin zone. Additionally, we considered 8 different angles θ in $[0^\circ, 360^\circ)$ when we aimed at generating HDWFs. To interpolate the Brillouin-zone integrals to high accuracy, we used a dense $\boldsymbol{k}$-mesh of $200\times 200\times 200$ (bulk) and 1024×1024 (film) points when invoking the Wannier interpolation. The developed technique based on HDWFs allows us to determine these integrals for any desired value of θ.

A.1 Elementary bulk ferromagnets

When assessing orbital magnetism in the elementary bulk ferromagnets, we used the lattice constant $5.417\,a_0$ (with a_0 as Bohr's radius) for bcc Fe, $6.662\,a_0$ for fcc Ni, and the lattice parameters $a = 4.718\,a_0$ and $c = 7.617\,a_0$ for hcp Co. In the case of Fe and Co, the plane-wave cutoff was chosen as $4.5\,a_0^{-1}$ and the muffin-tin radius was $2.28\,a_0$, whereas these parameters were $3.7\,a_0^{-1}$ and $2.29\,a_0$ for Ni. In order to disentangle 18 MLWFs from 30 Bloch states, we utilized three d orbitals and six sp^3d^2 hybrid orbitals per spin direction as first-guess projections. The frozen window extended up to 5 eV above the Fermi level in Fe, and 10 eV above the Fermi energy in Co and Ni.

A.2 Mn/W(001)

In our first-principles study of the chiral magnet Mn/W(001) with a square in-plane unit cell, we adopted the structural parameters from Ref. [274] with the lattice constant $5.981\,a_0$. The spacing between Mn and the first W layer was $2.85\,a_0$, and subsequent W layers had an interlayer distance of $2.99\,a_0$. We chose a plane-wave cutoff of $4.1\,a_0^{-1}$, and the muffin-tin radii of Mn and W were both set to $2.42\,a_0$. To generate 180 MLWFs (or HDWFs) out of 252 energy bands, three d orbitals and six

sp^3d^2 hybrids were used a trial orbitals, and the upper bound of the frozen window was set to 2 eV above the Fermi level.

A.3 Magnetically doped graphene

When decorating graphene with various magnetic transition-metal adatoms, we employed the atomic coordinates and computational parameters from Ref. [186]. In the case of W adatoms placed in a hexagonal 4×4 geometry at the hollow sites of graphene, the in-plane lattice constant was $18.643\, a_0$, and the buckling amounted to $\Delta z = 3.288\, a_0$. The plane-wave cutoff was chosen as $4.0\, a_0^{-1}$, and the muffin-tin radii of W and C were $2.7\, a_0$ and $1.2\, a_0$, respectively. Using nine trial functions per spin on each transition-metal adatom (s, p, and d orbitals) and three sp^2 hybrids on C, we generated 82 MLWFs or HDWFs from the electronic structure obtained on a coarse 6×6 $\boldsymbol{k}$-mesh (supplemented by 8 different angles in the higher-dimensional framework). The frozen window stretched up to 4 eV above the Fermi energy.

Similarly, we used in the case of Ir adatoms a 2×2 geometry with the lattice constant $9.321\, a_0$, a buckling of $\Delta z = 3.383\, a_0$, and a coarse mesh of 8×8 $\boldsymbol{k}$-points to generate the tight-binding representation.

A.4 Mn/Cu(111)

Non-collinear calculations of the Mn monolayer at the lattice constant of Cu(111) with the antiferromagnetic $3\boldsymbol{Q}$ spin texture [208] were performed within the local density approximation (LDA) using a parametrization due to Moruzzi, Janak, and Williams [275]. The interatomic distance on the triangular lattice was chosen as $4.830\, a_0$, the plane-wave cutoff was $4.0\, a_0^{-1}$, and a muffin-tin radius of $2.29\, a_0$ was used. Starting from three d orbitals and six sp^3d^2 hybrids, we generated 72 MLWFs out of 102 Bloch states with a frozen window up to about 5 eV above the Fermi energy. When including in addition 5 atomic layers of the Cu(111) substrate with an interlayer distance of the order of $4.0\, a_0$ and a muffin-tin radius of $2.29\, a_0$, we constructed 432 MLWFs from 604 energy bands.

A.5 γ-FeMn

We modeled the cubic system with imposed $3\boldsymbol{Q}$ spin structure as hexagonal (111) planes in ABC stacking such that strain modifies the interlayer spacing between different (111) planes. To account phenomenologically the Poisson effect, *i.e.*, the transverse strain response to axial strain, we included lateral lattice modifications via the Poisson ratio $\nu = 0.27$. In the unstrained case, the cubic crystal has a lattice constant of $6.862\, a_0$, which changes under strain as indicated in the main text. The plane-wave cutoff was $3.8\, a_0^{-1}$, and we further used a muffin-tin radius of $2.29\, a_0$ of the constituents. Adopting the virtual crystal approximation (VCA) [235], we occupied the lattice sites by virtual atoms that interpolate between the physical properties of Fe and Mn, depending on the composition ratio. Finally, we projected onto 9 trial functions (three d and six sp^3d^2 hybrids) per atom and spin direction in order to extract 72 MLWF from 102 energy bands, where the frozen window extend up to 5 eV above the Fermi energy.

A.6 Co-based trilayers

Starting from the experimental lattice parameters for hexagonal Pt/Co/Pt with an in-plane lattice constant of $5.211\,a_0$, we relaxed the two interface layers and kept the resulting atomic positions fixed even when doping the Pt overlayer with Ir or Au. Apart from the Co layer where the muffin-tin radius was set to $2.23\,a_0$, we chose the muffin-tin radii of all atoms as $2.29\,a_0$, and used $4.0\,a_0^{-1}$ as plane-wave cutoff. Although exchange and correlation effects were treated by a revised PBE functional [276], we verified that similar results can be obtained when using LDA as parametrized, *e.g.*, by Vosko, Wilk, and Nusair [48]. To account for the effect of substitutional alloying of the top Pt layers with Ir or Au, we employed the simple technique of VCA [235]. Using projections onto d_{xy}, d_{yz}, d_{xz}, and sp^3d^2, we applied our extension of the WANNIER90 program [273] to compute a single set of 162 HDWFs from a manifold of 228 Bloch states, with the upper bound of the frozen window at about 2 eV above the Fermi level.

A.7 Semi-hydrogenated Bi(111) bilayer

The hexagonal in-plane unit cell of the H-functionalized bismuth bilayer had a lattice constant of $10.315\,a_0$. We chose a plane-wave cutoff of $3.8\,a_0^{-1}$, and the muffin-tin radii of H and Bi were $1.21\,a_0$ and $2.80\,a_0$, respectively. Using s-like trial functions on hydrogen and p orbitals on bismuth, we generated 14 HDWFs out of 28 Bloch bands, where the frozen window extended up to 2 eV above the Fermi energy. We obtained the mixed Chern number discussed in Chapter 9 by integrating the mixed Berry curvature $\Omega_{yx}^{\hat{\boldsymbol{m}}\boldsymbol{k}}$ on a uniform mesh of 1024 k_x-values and 512 angles θ in $[0°, 360°)$.

A.8 GaBi film with an exchange field

The hexagonal lattice of the intrinsically non-magnetic GaBi film with an in-plane lattice constant of $8.543\,a_0$ shares the crystalline symmetries of the functionalized bismuth bilayer. In the former case, we employed $4.0\,a_0^{-1}$ as plane-wave cutoff and chose a muffin-tin radius of $2.45\,a_0$ for both Ga and Bi. We used projections onto s and p orbitals on these atom types and a frozen window 2 eV higher than the Fermi level in order to extract iteratively 16 MLWF from a group of 32 energy bands. After computing the matrix elements of the vector $\boldsymbol{\sigma}$ of Pauli matrices in this Wannier basis, we added to the constructed tight-binding Hamiltonian an according exchange term $\boldsymbol{B}\cdot\boldsymbol{\sigma}$ to study the dependence of the electronic structure on the direction of the exchange field $\boldsymbol{B}$.

Appendix B

Dzyaloshinskii-Moriya interaction and disorder

In order to derive the dependence of the Dzyaloshinskii-Moriya interaction (DMI) on the constant band broadening Γ that models disorder, we start from the Kubo linear-response expression of the DMI spiralization tensor [28]:

$$D_{ij} = \frac{1}{hV} \int_{-\infty}^{\mathcal{E}_\mathrm{F}} (\mathcal{E} - \mathcal{E}_\mathrm{F}) \operatorname{Re}\operatorname{Tr} \left\langle \mathcal{T}_i G^\mathrm{R}(\mathcal{E}) v_j \frac{\mathrm{d}G^\mathrm{R}(\mathcal{E})}{\mathrm{d}\mathcal{E}} - T_i \frac{\mathrm{d}G^\mathrm{R}(\mathcal{E})}{\mathrm{d}\mathcal{E}} v_j G^\mathrm{R}(\mathcal{E}) \right\rangle \mathrm{d}\mathcal{E} \,, \tag{B.1}$$

where $G^\mathrm{R}(\mathcal{E}) = \hbar/(\mathcal{E} - H + \mathrm{i}\eta)$ is the retarded Green function of the single-particle Hamiltonian H, and $\eta > 0$ is small. Using the eigenstate representation and replacing η with the band broadening Γ, we arrive at

$$\begin{aligned} D_{ij} &= \frac{1}{hV} \frac{1}{N_{\boldsymbol{k}}} \int_{-\infty}^{\mathcal{E}_\mathrm{F}} (\mathcal{E} - \mathcal{E}_\mathrm{F}) \operatorname{Re} \sum_{\boldsymbol{k}nm} \mathcal{T}_{nm,i} v_{mn,j} \left[G_m^\mathrm{R}(\mathcal{E}) \frac{\mathrm{d}G_n^\mathrm{R}(\mathcal{E})}{\mathrm{d}\mathcal{E}} - (n \leftrightarrow m) \right] \mathrm{d}\mathcal{E} \\ &= \frac{\hbar}{2\pi V} \frac{1}{N_{\boldsymbol{k}}} \operatorname{Re} \sum_{\boldsymbol{k}nm} \mathcal{T}_{nm,i} v_{mn,j} \int_{-\infty}^{\mathcal{E}_\mathrm{F}} \frac{(\mathcal{E} - \mathcal{E}_\mathrm{F})(\mathcal{E}_{\boldsymbol{k}m} - \mathcal{E}_{\boldsymbol{k}n})}{(\mathcal{E} - \mathcal{E}_{\boldsymbol{k}n} + \mathrm{i}\Gamma)^2 (\mathcal{E} - \mathcal{E}_{\boldsymbol{k}m} + \mathrm{i}\Gamma)^2} \mathrm{d}\mathcal{E} \\ &= \frac{\hbar}{2\pi V} \frac{1}{N_{\boldsymbol{k}}} \operatorname{Re} \sum_{\boldsymbol{k}nm} \mathcal{T}_{nm,i} v_{mn,j} \mathcal{Y}_{nm}(\Gamma) \,, \end{aligned} \tag{B.2}$$

where $\mathcal{T}_{nm,i} = \langle u_{\boldsymbol{k}n} | \mathcal{T}_i | u_{\boldsymbol{k}m} \rangle$ and $v_{mn,j} = \langle u_{\boldsymbol{k}m} | v_j | u_{\boldsymbol{k}n} \rangle$ denote the matrix elements of torque and velocity operator, respectively, and $G_n^\mathrm{R}(\mathcal{E}) = \hbar/(\mathcal{E} - \mathcal{E}_{\boldsymbol{k}n} + \mathrm{i}\Gamma)$ with the band energy $\mathcal{E}_{\boldsymbol{k}n}$. The abbreviation $\mathcal{Y}_{nm}(\Gamma)$ stands for the Γ-dependent energy integration that yields for $n \neq m$

$$\begin{aligned} \mathcal{Y}_{nm}(\Gamma) &= \int_{-\infty}^{\mathcal{E}_\mathrm{F}} \frac{(\mathcal{E} - \mathcal{E}_\mathrm{F})(\mathcal{E}_{\boldsymbol{k}m} - \mathcal{E}_{\boldsymbol{k}n})}{(\mathcal{E} - \mathcal{E}_{\boldsymbol{k}n} + \mathrm{i}\Gamma)^2 (\mathcal{E} - \mathcal{E}_{\boldsymbol{k}m} + \mathrm{i}\Gamma)^2} \mathrm{d}\mathcal{E} \\ &= \frac{2}{\mathcal{E}_{\boldsymbol{k}m} - \mathcal{E}_{\boldsymbol{k}n}} - \frac{\mathcal{E}_{\boldsymbol{k}n} + \mathcal{E}_{\boldsymbol{k}m} - 2(\mathcal{E}_\mathrm{F} + \mathrm{i}\Gamma)}{(\mathcal{E}_{\boldsymbol{k}n} - \mathcal{E}_{\boldsymbol{k}m})^2} \log \frac{\mathcal{E}_{\boldsymbol{k}m} - \mathcal{E}_\mathrm{F} - \mathrm{i}\Gamma}{\mathcal{E}_{\boldsymbol{k}n} - \mathcal{E}_\mathrm{F} - \mathrm{i}\Gamma} \\ &= \frac{2}{\mathcal{E}_{\boldsymbol{k}m} - \mathcal{E}_{\boldsymbol{k}n}} - \frac{\mathcal{E}_{\boldsymbol{k}n} + \mathcal{E}_{\boldsymbol{k}m} - 2(\mathcal{E}_\mathrm{F} + \mathrm{i}\Gamma)}{(\mathcal{E}_{\boldsymbol{k}n} - \mathcal{E}_{\boldsymbol{k}m})^2} \mathcal{L}_{nm}(\Gamma) \,. \end{aligned} \tag{B.3}$$

Here, we introduced $\mathcal{L}_{nm}(\Gamma)$ for the complex logarithm:

$$\mathcal{L}_{nm}(\Gamma) = \log \frac{\mathcal{E}_{\boldsymbol{k}m} - \mathcal{E}_\mathrm{F} - \mathrm{i}\Gamma}{\mathcal{E}_{\boldsymbol{k}n} - \mathcal{E}_\mathrm{F} - \mathrm{i}\Gamma} \,. \tag{B.4}$$

Obviously, both $\mathcal{Y}_{nm}(\Gamma)$ and $\mathcal{L}_{nm}(\Gamma)$ reverse sign if n and m are interchanged, *i.e.*, they constitute antisymmetric matrices. In combination with the fact that the imaginary part of $\mathcal{T}_{nm,i} v_{mn,j}$ also changes sign while $\operatorname{Re}[\mathcal{T}_{nm,i} v_{mn,j}]$ is invariant under permutations of n and m, it follows that

$$D_{ij} = -\frac{\hbar}{2\pi V} \frac{1}{N_{\boldsymbol{k}}} \sum_{\boldsymbol{k}nm} \operatorname{Im}[\mathcal{T}_{nm,i} v_{mn,j}] \operatorname{Im}\mathcal{Y}_{nm}(\Gamma) \,. \tag{B.5}$$

Since the imaginary part of $\mathcal{Y}_{nm}(\Gamma)$ amounts to

$$\mathrm{Im}\mathcal{Y}_{nm}(\Gamma) = -\frac{\mathcal{E}_{\boldsymbol{k}n} + \mathcal{E}_{\boldsymbol{k}m} - 2\mathcal{E}_{\mathrm{F}}}{(\mathcal{E}_{\boldsymbol{k}n} - \mathcal{E}_{\boldsymbol{k}m})^2}\mathrm{Im}\mathcal{L}_{nm}(\Gamma) + \frac{2\Gamma}{(\mathcal{E}_{\boldsymbol{k}n} - \mathcal{E}_{\boldsymbol{k}m})^2}\mathrm{Re}\mathcal{L}_{nm}(\Gamma)\,, \tag{B.6}$$

we arrive at the final expression for the disorder dependence of the DMI spiralization tensor in the case of a constant band broadening Γ:

$$\begin{aligned} D_{ij} = {} & \frac{\hbar}{2\pi V}\frac{1}{N_{\boldsymbol{k}}}\sum_{\boldsymbol{k}n}\sum_{m\neq n}\mathrm{Im}\left[\mathcal{T}_{nm,i}v_{mn,j}\right] \\ & \times\left[\frac{\mathcal{E}_{\boldsymbol{k}n} + \mathcal{E}_{\boldsymbol{k}m} - 2\mathcal{E}_{\mathrm{F}}}{(\mathcal{E}_{\boldsymbol{k}n} - \mathcal{E}_{\boldsymbol{k}m})^2}\mathrm{Im}\mathcal{L}_{nm}(\Gamma) - \frac{2\Gamma}{(\mathcal{E}_{\boldsymbol{k}n} - \mathcal{E}_{\boldsymbol{k}m})^2}\mathrm{Re}\mathcal{L}_{nm}(\Gamma)\right]\,, \end{aligned} \tag{B.7}$$

which coincides with Eq. (4.61) of the main text when taking into account Eq. (B.4).

In the clean limit of $\Gamma \to 0^+$, the second part in Eq. (B.6) vanishes. In order to evaluate the remaining term, we represent the logarithm of the complex argument as

$$\log\frac{\mathcal{E}_{\boldsymbol{k}m} - \mathcal{E}_{\mathrm{F}} - \mathrm{i}\Gamma}{\mathcal{E}_{\boldsymbol{k}n} - \mathcal{E}_{\mathrm{F}} - \mathrm{i}\Gamma} = \log\left(\alpha + \mathrm{i}\beta\right) = \log\left(r\mathrm{e}^{\mathrm{i}\phi}\right)\,, \tag{B.8}$$

with the absolute value $r = \sqrt{\alpha^2 + \beta^2}$, the phase $\phi = \mathrm{Arg}(\alpha + \mathrm{i}\beta)$, and

$$\alpha = \frac{\mathcal{E}_{\mathrm{F}}^2 - \mathcal{E}_{\mathrm{F}}\mathcal{E}_{\boldsymbol{k}m} - \mathcal{E}_{\mathrm{F}}\mathcal{E}_{\boldsymbol{k}n} + \mathcal{E}_{\boldsymbol{k}m}\mathcal{E}_{\boldsymbol{k}n} + \Gamma^2}{(\mathcal{E}_{\boldsymbol{k}n} - \mathcal{E}_{\mathrm{F}})^2 + \Gamma^2} \longrightarrow \frac{(\mathcal{E}_{\mathrm{F}} - \mathcal{E}_{\boldsymbol{k}m})}{(\mathcal{E}_{\mathrm{F}} - \mathcal{E}_{\boldsymbol{k}n})}\,, \tag{B.9}$$

$$\beta = \Gamma\frac{\mathcal{E}_{\boldsymbol{k}m} - \mathcal{E}_{\boldsymbol{k}n}}{(\mathcal{E}_{\boldsymbol{k}n} - \mathcal{E}_{\mathrm{F}})^2 + \Gamma^2} \longrightarrow \Gamma\frac{\mathcal{E}_{\boldsymbol{k}m} - \mathcal{E}_{\boldsymbol{k}n}}{(\mathcal{E}_{\boldsymbol{k}n} - \mathcal{E}_{\mathrm{F}})^2}\,, \tag{B.10}$$

where we consider Γ to be small but still finite. The relevant non-zero contributions to $\mathrm{Im}\mathcal{L}_{nm}(\Gamma)$ in the clean limit (for which $\beta \to 0$) originate from the two different cases $\phi = \arctan(\beta/\alpha) + \pi$ if $\alpha < 0, \beta \geq 0$, and $\phi = \arctan(\beta/\alpha) - \pi$ if $\alpha < 0, \beta < 0$, which translates to

$$\mathrm{Im}\log\left(\alpha + \mathrm{i}\beta\right) = \phi \longrightarrow \begin{cases} +\pi & \text{if } n \text{ occupied and } m \text{ unoccupied,} \\ -\pi & \text{if } m \text{ occupied and } n \text{ unoccupied,} \\ 0 & \text{otherwise.} \end{cases} \tag{B.11}$$

Using additionally that $\mathrm{Im}\left[\mathcal{T}_{nm,i}v_{mn,j}\right]$ changes sign if n and m are interchanged, we end up with an overall factor 2π in the DMI spiralization such that

$$\begin{aligned} D_{ij} &= \frac{\hbar}{2\pi V}\frac{1}{N_{\boldsymbol{k}}}2\pi\sum_{n}^{\mathrm{occ}}\sum_{m}^{\mathrm{unocc}}\mathrm{Im}\left[\mathcal{T}_{nm,i}v_{mn,j}\right]\frac{\mathcal{E}_{\boldsymbol{k}n} + \mathcal{E}_{\boldsymbol{k}m} - 2\mathcal{E}_{\mathrm{F}}}{(\mathcal{E}_{\boldsymbol{k}n} - \mathcal{E}_{\boldsymbol{k}m})^2} \\ &= \frac{\hbar}{V}\frac{1}{N_{\boldsymbol{k}}}\sum_{n}^{\mathrm{occ}}\sum_{m}^{\mathrm{unocc}}\mathrm{Im}\left[\mathcal{T}_{nm,i}v_{mn,j}\right]\left\{\frac{-1}{\mathcal{E}_{\boldsymbol{k}n} - \mathcal{E}_{\boldsymbol{k}m}} + 2\frac{\mathcal{E}_{\boldsymbol{k}n} - \mathcal{E}_{\mathrm{F}}}{(\mathcal{E}_{\boldsymbol{k}n} - \mathcal{E}_{\boldsymbol{k}m})^2}\right\}\,, \end{aligned} \tag{B.12}$$

which is equivalent to Eq. (4.58) of the main text if the summation over m is modified to run over all states $m \neq n$. However, the contributions where both n and m are occupied cancel out.

List of Figures

List of Tables

List of Abbreviations

ACA	atom-centered approximation
APW	augmented-plane-wave
DFT	density functional theory
DMI	Dzyaloshinskii-Moriya interaction
FLAPW	full-potential linearized augmented-plane-wave
GGA	generalized gradient approximation
GMR	giant magnetoresistance
HDWF	higher-dimensional Wannier function
KKR	Kohn-Korringa-Rostoker
LAPW	linearized augmented-plane-wave
LCAO	linear combination of atomic orbitals
LDA	local density approximation
LO	local orbital
LSDA	local spin density approximation
MLWF	maximally-localized Wannier function
MRAM	magnetoresistive random-access memory
OM	orbital magnetization
PBE	Perdew, Burke, and Ernzerhof
SIC	self-interaction correction
SOT	spin-orbit torque
STT	spin-transfer torque
TMR	tunneling magnetoresistance
VCA	virtual crystal approximation
WF	Wannier function
XMCD	X-ray magnetic circular dichroism

Bibliography

[1] Binasch, G., Grünberg, P., Saurenbach, F. & Zinn, W. Enhanced magnetoresistance in layered magnetic structures with antiferromagnetic interlayer exchange. *Phys. Rev. B* **39**, 4828–4830 (1989).

[2] Baibich, M. N. *et al.* Giant magnetoresistance of (001)Fe/(001)Cr magnetic superlattices. *Phys. Rev. Lett.* **61**, 2472–2475 (1988).

[3] Julliere, M. Tunneling between ferromagnetic films. *Phys. Lett. A* **54**, 225–226 (1975).

[4] Miyazaki, T. & Tezuka, N. Giant magnetic tunneling effect in Fe/Al_2O_3/Fe junction. *J. Magn. Magn. Mater.* **139**, L231 – L234 (1995).

[5] Moodera, J. S., Kinder, L. R., Wong, T. M. & Meservey, R. Large magnetoresistance at room temperature in ferromagnetic thin film tunnel junctions. *Phys. Rev. Lett.* **74**, 3273–3276 (1995).

[6] Slonczewski, J. Current-driven excitation of magnetic multilayers. *J. Magn. Magn. Mater.* **159**, L1–L7 (1996).

[7] Berger, L. Emission of spin waves by a magnetic multilayer traversed by a current. *Phys. Rev. B* **54**, 9353–9358 (1996).

[8] Parkin, S. S. P., Hayashi, M. & Thomas, L. Magnetic domain-wall racetrack memory. *Science* **320**, 190–194 (2008).

[9] Kent, A. D. & Worledge, D. C. A new spin on magnetic memories. *Nat. Nanotechnol.* **10**, 187–191 (2015).

[10] Parkin, S. & Yang, S.-H. Memory on the racetrack. *Nat. Nanotechnol.* **10**, 195–198 (2015).

[11] Matsukura, F., Tokura, Y. & Ohno, H. Control of magnetism by electric fields. *Nat. Nanotechnol.* **10**, 209–220 (2015).

[12] Miron, I. M. *et al.* Perpendicular switching of a single ferromagnetic layer induced by in-plane current injection. *Nature* **476**, 189–193 (2011).

[13] Liu, L., Lee, O., Gudmundsen, T., Ralph, D. & Buhrman, R. Current-induced switching of perpendicularly magnetized magnetic layers using spin torque from the spin Hall effect. *Phys. Rev. Lett.* **109**, 96602 (2012).

[14] Wadley, P. *et al.* Electrical switching of an antiferromagnet. *Science* **351**, 587–590 (2016).

[15] Dzyaloshinsky, I. A thermodynamic theory of “weak” ferromagnetism of antiferromagnetics. *J. Phys. Chem. Solids* **4**, 241–255 (1958).

[16] Moria, T. Anisotropic Superexchange Iteraction and Weak Ferromagnetism. *Phys. Rev.* **120**, 91–98 (1960).

[17] Fert, A., Cros, V. & Sampaio, J. Skyrmions on the track. *Nat. Nanotechnol.* **8**, 152–156 (2013).

[18] Thouless, D. J., Kohmoto, M., Nightingale, M. P. & Den Nijs, M. Quantized Hall conductance in a two-Dimensional periodic potential. *Phys. Rev. Lett.* **49**, 405–408 (1982).

[19] Haldane, F. D. M. Model for a Quantum Hall Effect without Landau Levels: Condensed-Matter Realization of the Parity Anomaly. *Phys. Rev. Lett.* **61**, 2015–2018 (1988).

[20] Pancharatnam, S. Generalized theory of interference, and its applications. In *Proc. Indian Acad. Sci. - Sect. A*, vol. 44, 247–262 (Springer India, 1956).

[21] Berry, M. V. Quantal Phase Factors Accompanying Adiabatic Changes. *Proc. R. Soc. A Math. Phys. Eng. Sci.* **392**, 45–57 (1984).

[22] King-Smith, R. D. & Vanderbilt, D. Theory of Polatization of Crystalline Solids. *Phys. Rev. B* **47**, 1651 (1993).

[23] Resta, R. Macroscopic polarization in crystaline dielectrics the geometric approach. *Rev. Mod. Phys.* **66**, 899 (1994).

[24] Thonhauser, T., Ceresoli, D., Vanderbilt, D. & Resta, R. Orbital magnetization in periodic insulators. *Phys. Rev. Lett.* **95**, 137205 (2005).

[25] Ceresoli, D., Thonhauser, T., Vanderbilt, D. & Resta, R. Orbital magnetization in crystalline solids: Multi-band insulators, Chern insulators, and metals. *Phys. Rev. B* **74**, 24408 (2006).

[26] Xiao, D., Shi, J. & Niu, Q. Berry phase correction to electron density of states in solids. *Phys. Rev. Lett.* **95**, 137204 (2005).

[27] Shi, J., Vignale, G., Xiao, D. & Niu, Q. Quantum theory of orbital magnetization and its generalization to interacting systems. *Phys. Rev. Lett.* **99**, 197202 (2007).

[28] Freimuth, F., Blügel, S. & Mokrousov, Y. Berry phase theory of Dzyaloshinskii-Moriya interaction and spin-orbit torques. *J. Phys. Condens. Matter* **26**, 104202 (2014).

[29] Hohenberg, P. & Kohn, W. Inhomogeneous Electron Gas. *Phys. Rev.* **136**, B864 (1964).

[30] Kohn, W. & Sham, L. J. Self-consistend equations including exchange and correlation effects. *Phys. Rev.* **140**, 1133–1138 (1965).

[31] Wannier, G. H. The structure of electronic excitation levels in insulating crystals. *Phys. Rev.* **52**, 191–197 (1937).

[32] Schrödinger, E. Quantisierung als Eigenwertproblem. *Ann. Phys.* **385**, 437–490 (1926).

[33] Born, M. & Oppenheimer, R. Zur Quantentheorie der Moleküle. *Ann. Phys.* **389**, 457–484 (1927).

[34] Dirac, P. A. M. Quantum mechanics of many-electron systems. In *P. R. Soc. Lond. A - Conta.*, vol. 123, 714–733 (JSTOR, 1929).

[35] Slater, J. C. A Simplification of the Hartree-Fock-Method. *Phys. Rev.* **3**, 385–390 (1951).

[36] Sakurai, J. J. & Tuan, S. F. *Modern Quantum Mechanics* (Addison-Wesley, 1994).

[37] Hartree, D. R. The Wave Mechanics of an Atom with a non-Coulomb Central Field. Part III. Term Values and Intensities in Series in Optical Spectra. In *Math. Proc. Cambridge Philos. Soc.*, vol. 24, 426 (Cambridge Univ. Press, 1928).

[38] Fock, V. Näherungsmethode zur Lösung des quantenmechanischen Mehrkörperproblems. *Z. Phys.* **61**, 126–148 (1930).

[39] Thomas, L. H. The calculation of atomic fields. In *Math. Proc. Cambridge Philos. Soc.*, vol. 23, 542 (Cambridge Univ. Press, 1927).

[40] Fermi, E. Application of statistical gas methods to electronic systems. *Atti della R. Accad. Naz. dei Lincei* **6**, 602–607 (1927).

[41] Fermi, E. Eine statistische Methode zur Bestimmung einiger Eigenschaften des Atoms und ihre Anwendung auf das Periodensystem der Elemente. *Z. Phys.* **48**, 73–79 (1928).

[42] Bloch, F. Bemerkung zur Elektronentheorie des Ferromagnetismus und der elektrischen Leitfähigkeit. *Z. Phys.* **57**, 545–555 (1929).

[43] Dirac, P. A. M. Note on Exchange Phenomena in the Thomas Atom. In *Math. Proc. Cambridge Philos. Soc.*, vol. 26, 376 (Cambridge Univ. Press, 1930).

[44] Engel, E. & Dreizler, R. M. *Density Functional Theory: An Advanced Course* (Springer, 2011).

[45] von Barth, U. & Hedin, L. A local exchange-correlation potential for the spin polarized case. i. *J. Phys. C Solid State Phys.* **5**, 1629 (1972).

[46] Gunnarsson, O. & Lundqvist, B. I. Exchange and correlation in atoms, molecules, and solids by the spin-density-functional formalism. *Phys. Rev. B* **13**, 4274–4298 (1976).

[47] Ceperley, D. M. & Alder, B. J. Ground State of the Electron Gas by a Stochastic Method. *Phys. Rev. Lett.* **45**, 566–569 (1980).

[48] Vosko, S. H., Wilk, L. & Nusair, M. Accurate spin-dependent electron liquid correlation energies for local spin density calculations: a critical analysis. *Can. J. Phys.* **58**, 1200–1211 (1980).

[49] Perdew, J. P. & Zunger, A. Self-interaction correction to density-functional approximations for many-electron systems. *Phys. Rev. B* **23**, 5048–5079 (1981).

[50] Jones, R. O. & Gunnarsson, O. The density functional formalism, its applications and prospects. *Rev. Mod. Phys.* **61**, 689–746 (1989).

[51] Parr, R. G., Yang, W. & Weitao, Y. *Density-Functional Theory of Atoms and Molecules* (Oxford Univ. Press, 1994).

[52] Perdew, J., Burke, K. & Ernzerhof, M. Generalized gradient approximation made simple. *Phys. Rev. Lett.* **77**, 3865 (1996).

[53] Anisimov, V. I., Antropov, V. P., Liechtenstein, A. I., Gubanov, V. A. & Postnikov, A. V. Electronic structure and magnetic properties of 3d impurities in ferromagnetic metals. *Phys. Rev. B* **37**, 5598–5602 (1988).

[54] Anisimov, V. I., Zaanen, J. & Andersen, O. K. Band theory and Mott insulators: Hubbard U instead of Stoner I. *Phys. Rev. B* **44**, 943–954 (1991).

[55] Anisimov, V. I., Solovyev, I. V., Korotin, M. A., Czyżyk, M. T. & Sawatzky, G. A. Density-functional theory and NiO photoemission spectra. *Phys. Rev. B* **48**, 16929–16934 (1993).

[56] Solovyev, I. V., Dederichs, P. H. & Anisimov, V. I. Corrected atomic limit in the local-density approximation and the electronic structure of d impurities in Rb. *Phys. Rev. B* **50**, 16861–16871 (1994).

[57] Cococcioni, M. & de Gironcoli, S. Linear response approach to the calculation of the effective interaction parameters in the LDA+U method. *Phys. Rev. B* **71**, 35105 (2005).

[58] Kulik, H. J., Cococcioni, M., Scherlis, D. A. & Marzari, N. Density Functional Theory in Transition-Metal Chemistry: A Self-Consistent Hubbard U Approach. *Phys. Rev. Lett.* **97**, 103001 (2006).

[59] Şaşıoğlu, E., Friedrich, C. & Blügel, S. Effective Coulomb interaction in transition metals from constrained random-phase approximation. *Phys. Rev. B* **83**, 121101 (2011).

[60] Städele, M., Majewski, J. A., Vogl, P. & Görling, A. Exact Kohn-Sham Exchange Potential in Semiconductors. *Phys. Rev. Lett.* **79**, 2089–2092 (1997).

[61] Bloch, F. Über die Quantenmechanik der Elektronen in Kristallgittern. *Z. Phys.* **52**, 555–600 (1929).

[62] Slater, J. C. Wave Functions in a Periodic Potential. *Phys. Rev.* **51**, 846 – 851 (1937).

[63] Andersen, O. K. Linear methods in band theory. *Phys. Rev. B* **12**, 3060–3083 (1975).

[64] Koelling, D. D. & Arbman, G. O. Use of energy derivative of the radial solution in an augmented plane wave method: application to copper. *J. Phys. F Met. Phys.* **5**, 2041 (1975).

[65] Singh, D. Ground-state properties of lanthanum: Treatment of extended-core states. *Phys. Rev. B* **43**, 6388 (1991).

[66] Krasovskii, E. E. & Schattke, W. The extended-LAPW-based k·p method for complex band structure calculations. *Solid State Commun.* **93**, 775–779 (1995).

[67] Sjöstedt, E., Nordström, L. & Singh, D. J. An alternative way of linearizing the augmented plane-wave method. *Solid State Commun.* **114**, 15–20 (2000).

[68] Hamann, D. R. Semiconductor Charge Densities with Hard-Core and Soft-Core Pseudopotentials. *Phys. Rev. Lett.* **42**, 662–665 (1979).

[69] Wimmer, E., Krakauer, H., Weinert, M. & Freeman, A. J. Full-potential self-consistent linearized-augmented-plane-wave method for calculating the electronic structure of molecules and surfaces: O2 molecule. *Phys. Rev. B* **24**, 864–875 (1981).

[70] Weinert, M. Solution of Poisson's equation: Beyond Ewald-type methods. *J. Math. Phys.* **22**, 2433–2439 (1981).

[71] Weinert, M., Wimmer, E. & Freeman, A. J. Total-energy all-electron density functional method for bulk solids and surfaces. *Phys. Rev. B* **26**, 4571–4578 (1982).

[72] Krakauer, H., Posternak, M. & Freeman, A. Linearized augmented plane-wave method for the electronic band structure of thin films. *Phys. Rev. B* **19**, 1706–1719 (1979).

[73] Li, C., Freeman, A., Jansen, H. & Fu, C. Magnetic anisotropy in low-dimensional ferromagnetic systems: Fe monolayers on Ag (001), Au (001), and Pd (001) substrates. *Phys. Rev. B* **42**, 5433–5442 (1990).

[74] See http://www.flapw.de.

[75] Kurz, P. *Non-Collinear Magnetism at Surfaces and in Ultrathin Films.* Ph.D. thesis, RWTH Aachen (2000).

[76] Nordström, L. & Singh, D. J. Noncollinear Intra-atomic Magnetism. *Phys. Rev. Lett.* **76**, 4420–4423 (1996).

[77] Berry, M. Anticipations of the geometric phase. *Phys. Today* **43**, 34–40 (1990).

[78] Bernevig, B. A. & Hughes, T. L. *Topological insulators and topological superconductors* (Princeton University Press, 2013).

[79] Wilczek, F. & Zee, A. Appearance of gauge structure in simple dynamical systems. *Phys. Rev. Lett.* **52**, 2111–2114 (1984).

[80] Tomita, A. & Chiao, R. Observation of Berry's Topological Phase by Use of an Optical Fiber. *Phys. Rev. Lett.* **57**, 937–940 (1986).

[81] Hannay, J. H. Angle variable holonomy in adiabatic excursion of an integrable Hamiltonian. *J. Phys. A. Math. Gen.* **18**, 221–230 (1985).

[82] Fang, Z. The Anomalous Hall Effect and Magnetic Monopoles in Momentum Space. *Science* **302**, 92–95 (2003).

[83] Solem, J. C. & Biedenharn, L. C. Understanding geometrical phases in quantum mechanics: An elementary example. *Found. Phys.* **23**, 185–195 (1993).

[84] Dirac, P. A. M. Quantised Singularities in the Electromagnetic Field. In *Proc. R. Soc. A Math. Phys. Eng. Sci.*, vol. 133, 60–72 (The Royal Society, 1931).

[85] Aharonov, Y. & Bohm, D. Significance of Electromagnetic Potentials in the Quantum Theory. *Phys. Rev.* **115**, 485–491 (1959).

[86] Bohm, A., Mostafazadeh, A., Koizumi, H., Niu, Q. & Zwanziger, J. *The Geometric Phase in Quantum Systems: Foundations, Mathematical Concepts, and Applications in Molecular and Condensed Matter Physics* (Springer Science & Business Media, 2003).

[87] Hall, E. H. On a New Action of the Magnet on Electric Currents. *Am. J. Math.* **2**, 287 (1879).

[88] Ando, T., Matsumoto, Y. & Uemura, Y. Theory of Hall Effect in a Two-Dimensional Electron System. *J. Phys. Soc. Japan* **39**, 279–288 (1975).

[89] Klitzing, K. v., Dorda, G. & Pepper, M. New method for high-accuracy determination of the fine-structure constant based on quantized hall resistance. *Phys. Rev. Lett.* **45**, 494–497 (1980).

[90] Laughlin, R. B. Quantized Hall conductivity in two dimensions. *Phys. Rev. B* **23**, 5632–5633 (1981).

[91] Laughlin, R. B. Anomalous quantum Hall effect: An incompressible quantum fluid with fractionally charged excitations. *Phys. Rev. Lett.* **50**, 1395–1398 (1983).

[92] Hall, E. H. On the "Rotational Coefficient" in nickel and cobalt. *Philos. Mag.* **12**, 157–172 (1881).

[93] Jungwirth, T., Niu, Q. & MacDonald, A. H. Anomalous Hall Effect in Ferromagnetic Semiconductors. *Phys. Rev. Lett.* **88**, 207208 (2002).

[94] Onoda, M. & Nagaosa, N. Topological Nature of Anomalous Hall Effect in Ferromagnets. *J. Phys. Soc. Japan* **71**, 19–22 (2002).

[95] Nagaosa, N. Anomalous Hall Effect –A New Perspective–. *J. Phys. Soc. Japan* **75**, 42001 (2006).

[96] Nagaosa, N., Sinova, J., Onoda, S., MacDonald, A. H. & Ong, N. P. Anomalous Hall effect. *Rev. Mod. Phys.* **82**, 1539–1592 (2010).

[97] Lowitzer, S., Ködderitzsch, D. & Ebert, H. Coherent description of the intrinsic and extrinsic anomalous Hall effect in disordered alloys on an ab-initio level. *Phys. Rev. Lett.* **105**, 266604 (2010).

[98] Weischenberg, J., Freimuth, F., Sinova, J., Blügel, S. & Mokrousov, Y. Ab Initio Theory of the Scattering-Independent Anomalous Hall Effect. *Phys. Rev. Lett.* **107**, 106601 (2011).

[99] Xiao, D., Chang, M.-C. & Niu, Q. Berry Phase Effects on Electronic Properties. *Rev. Mod. Phys.* **82**, 1959 (2009).

[100] Karplus, R. & Luttinger, J. M. Hall Effect in Ferromagnetics. *Phys. Rev.* **95**, 1154–1160 (1954).

[101] Qiao, Z. *et al.* Quantum Anomalous Hall Effect in Graphene from Rashba and Exchange Effects. *Phys. Rev. B* **82**, 161414 (2010).

[102] Yu, R. *et al.* Quantized anomalous Hall effect in magnetic topological insulators. *Science* **329**, 61–4 (2010).

[103] Chang, C.-Z. *et al.* Experimental Observation of the Quantum Anomalous Hall Effect in a Magnetic Topological Insulator. *Science* **340**, 167–170 (2013).

[104] Dyakonov, M. I. & Perel, V. I. Current-induced spin orientation of electrons in semiconductors. *Phys. Lett. A* **35**, 459–460 (1971).

[105] Dyakonov, M. I. & Perel, V. I. Possibility of orienting electron spins with current. *JETP Lett.* **13**, 467–469 (1971).

[106] Mong, R. S. K., Essin, A. M. & Moore, J. E. Antiferromagnetic topological insulators. *Phys. Rev. B* **81**, 245209 (2010).

[107] Sinova, J., Valenzuela, S. O., Wunderlich, J., Back, C. H. & Jungwirth, T. Spin Hall effects. *Rev. Mod. Phys.* **87**, 1213–1260 (2015).

[108] Taylor, J. W. *et al.* Temperature dependence of the spin and orbital magnetization density in $Sm_{0.982}Gd_{0.018}Al_2$ around the spin-orbital compensation point. *Phys. Rev. B* **66**, 161319(R) (2002).

[109] Gotsis, H. J. & Mazin, I. Ferromagnetism and spin-orbital compensation in Sm intermetallics. *Phys. Rev. B* **68**, 224427 (2003).

[110] Qiao, S. *et al.* Direct evidence of ferromagnetism without net magnetization observed by x-ray magnetic circular dichroism. *Phys. Rev. B* **70**, 134418 (2004).

[111] Xiao, D., Yao, Y., Fang, Z. & Niu, Q. Berry phase effect in anomalous thermoelectric transport. *Phys. Rev. Lett.* **97**, 26603 (2006).

[112] Murakami, S. Quantum Spin Hall Effect and Enhanced Magnetic Response by Spin-Orbit Coupling. *Phys. Rev. Lett.* **97**, 236805 (2006).

[113] Xiao, D., Yao, W. & Niu, Q. Valley-contrasting physics in graphene: Magnetic moment and topological transport. *Phys. Rev. Lett.* **99**, 236809 (2007).

[114] Wang, X., Vanderbilt, D., Yates, J. R. & Souza, I. Fermi-surface calculation of the anomalous Hall conductivity. *Phys. Rev. B* **76**, 195109 (2007).

[115] Malashevich, A., Souza, I., Coh, S. & Vanderbilt, D. Theory of orbital magnetoelectric response. *New J. Phys.* **12**, 53032 (2010).

[116] Essin, A. M., Moore, J. E. & Vanderbilt, D. Magnetoelectric polarizability and axion electrodynamics in crystalline insulators. *Phys. Rev. Lett.* **102**, 146805 (2009).

[117] Essin, A. M., Turner, A. M., Moore, J. E. & Vanderbilt, D. Orbital magnetoelectric coupling in band insulators. *Phys. Rev. B* **81**, 205104 (2010).

[118] Vleck, J. H. On the Anisotroyy of Cubic Ferromagnetic Crystals. *Phys. Rev.* **1076**, 385–401 (1937).

[119] Meyer, A. J. P. & Asch, G. Experimental g' and g Values of Fe, Co, Ni, and Their Alloys. *J. Appl. Phys.* **32**, S330 (1961).

[120] Thole, B. T., Carra, P., Sette, F. & van der Laan, G. X-Ray Circular-Dichroism as a Probe of Orbital Magnetization. *Phys. Rev. Lett.* **68**, 1943–1946 (1992).

[121] Carra, P., Thole, B. T., Altarelli, M. & Wang, X. X-Ray Circular Dichroism and Local Magnetic Fields. *Phys. Rev. Lett.* **70**, 694–697 (1993).

[122] Chen, C. T. *et al.* Experimental confirmation of the X-ray magnetic circular dichroism sum rules for iron and cobalt. *Phys. Rev. Lett.* **75**, 152–155 (1995).

[123] Thonhauser, T. Theory of Orbital Magnetization in Solids. *Int. J. Mod. Phys. B* **25**, 1429 (2011).

[124] Resta, R. Electrical polarization and orbital magnetization: the modern theories. *J. Phys. Condens. Matter* **22**, 123201 (2010).

[125] Aryasetiawan, F. & Karlsson, K. Modern theory of orbital magnetic moment in solids. *J. Phys. Chem. Solids* (2017).

[126] Nikolaev, S. A. & Solovyev, I. V. Orbital magnetization of insulating perovskite transition-metal oxides with a net ferromagnetic moment in the ground state. *Phys. Rev. B* **89**, 64428 (2014).

[127] Souza, I. & Vanderbilt, D. Dichroic f-sum rule and the orbital magnetization of crystals. *Phys. Rev. B* **77**, 054438 (2008).

[128] Zhong, S., Moore, J. E. & Souza, I. Gyrotropic Magnetic Effect and the Magnetic Moment on the Fermi Surface. *Phys. Rev. Lett.* **116**, 077201 (2016).

[129] Yoda, T., Yokoyama, T. & Murakami, S. Current-induced orbital and spin magnetizations in crystals with helical structure. *Sci. Rep.* **5**, 12024 (2015).

[130] Bernevig, B. A., Hughes, T. L. & Zhang, S. C. Orbitronics: The intrinsic orbital current in p-doped silicon. *Phys. Rev. Lett.* **95**, 066601 (2005).

[131] Kontani, H., Tanaka, T., Hirashima, D. S., Yamada, K. & Inoue, J. Giant orbital Hall effect in transition metals: Origin of large spin and anomalous Hall effects. *Phys. Rev. Lett.* **102**, 016601 (2009).

[132] Freimuth, F., Bamler, R., Mokrousov, Y. & Rosch, A. Phase-space Berry phases in chiral magnets: Dzyaloshinskii-Moriya interaction and the charge of skyrmions. *Phys. Rev. B* **88**, 214409 (2013).

[133] Freimuth, F., Blügel, S. & Mokrousov, Y. Spin-orbit torques in Co/Pt (111) and Mn/W (001) magnetic bilayers from first principles. *Phys. Rev. B* **90**, 174423 (2014).

[134] Li, Z. & Zhang, S. Domain-wall dynamics and spin-wave excitations with spin-transfer torques. *Phys. Rev. Lett.* **92**, 207203 (2004).

[135] Stiles, M. D. & Zangwill, A. Anatomy of spin-transfer torque. *Phys. Rev. B* **66**, 144071–1440714 (2002).

[136] Ralph, D. C. & Stiles, M. D. Spin transfer torques. *J. Magn. Magn. Mater.* **320**, 1190–1216 (2008).

[137] Urban, R., Woltersdorf, G. & Heinrich, B. Gilbert Damping in Single and Multilayer Ultrathin Films: Role of Interfaces in Nonlocal Spin Dynamics. *Phys. Rev. Lett.* **87**, 217204 (2001).

[138] Mizukami, S., Ando, Y. & Miyazaki, T. Effect of spin diffusion on Gilbert damping for a very thin permalloy layer in Cu/permalloy/Cu/Pt films. *Phys. Rev. B* **66**, 1044131–1044139 (2002).

[139] Tserkovnyak, Y., Brataas, A. & Bauer, G. E. W. Enhanced Gilbert Damping in Thin Ferromagnetic Films. *Phys. Rev. Lett.* **88**, 117601 (2002).

[140] Tserkovnyak, Y., Brataas, A. & Bauer, G. E. W. Spin pumping and magnetization dynamics in metallic multilayers. *Phys. Rev. B* **66**, 224403 (2002).

[141] Gambardella, P. & Miron, I. M. Current-induced spin-orbit torques. *Philos. Trans. R. Soc. A Math. Phys. Eng. Sci.* **369**, 3175–3197 (2011).

[142] Chernyshov, A. *et al.* Evidence for reversible control of magnetization in a ferromagnetic material by means of spin–orbit magnetic field. *Nat. Phys.* **5**, 656–659 (2009).

[143] Miron, I. M. *et al.* Current-driven spin torque induced by the Rashba effect in a ferromagnetic metal layer. *Nat. Mater.* **9**, 230–234 (2010).

[144] Miron, I. M. *et al.* Fast current-induced domain-wall motion controlled by the Rashba effect. *Nat. Mater.* **10**, 419–423 (2011).

[145] Garello, K. *et al.* Symmetry and magnitude of spin–orbit torques in ferromagnetic heterostructures. *Nat. Nanotechnol.* **8**, 587–593 (2013).

[146] Mahan, G. D. *Many-particle physics* (Springer Science & Business Media, 2013).

[147] Bastin, A., Lewiner, C., Betbeder-matibet, O. & Nozieres, P. Quantum oscillations of the Hall effect of a fermion gas with random impurity scattering. *J. Phys. Chem. Solids* **32**, 1811–1824 (1971).

[148] Bode, M. *et al.* Chiral magnetic order at surfaces driven by inversion asymmetry. *Nature* **447**, 190–193 (2007).

[149] Bogdanov, A. & Yablonskii, D. Thermodynamically stable “vortices” in magnetically ordered crystals. The mixed state of magnets. *Zh. Eksp. Teor. Fiz* **95**, 178 (1989).

[150] Neubauer, A. *et al.* Topological Hall effect in the A-phase of MnSi. *Phys. Rev. Lett.* **102**, 2–5 (2009).

[151] Kanazawa, N. *et al.* Large topological Hall effect in a short-period helimagnet MnGe. *Phys. Rev. Lett.* **106**, 156603 (2011).

[152] Tretiakov, O. A. & Abanov, A. Current driven magnetization dynamics in ferromagnetic nanowires with a Dzyaloshinskii-Moriya interaction. *Phys. Rev. Lett.* **105**, 157201 (2010).

[153] Thiaville, A., Rohart, S., Jué, É., Cros, V. & Fert, A. Dynamics of Dzyaloshinskii domain walls in ultrathin magnetic films. *Europhysics Lett.* **100**, 57002 (2012).

[154] Haazen, P. P. J. *et al.* Domain wall depinning governed by the spin Hall effect. *Nat. Mater.* **12**, 299–303 (2013).

[155] Ryu, K.-S., Thomas, L., Yang, S.-H. & Parkin, S. Chiral spin torque at magnetic domain walls. *Nat. Nanotechnol.* **8**, 527–533 (2013).

[156] Emori, S., Bauer, U., Ahn, S.-M., Martinez, E. & Beach, G. S. D. Current-driven dynamics of chiral ferromagnetic domain walls. *Nat. Mater.* **12**, 611–616 (2013).

[157] Heide, M., Bihlmayer, G. & Blügel, S. Dzyaloshinskii-Moriya interaction accounting for the orientation of magnetic domains in ultrathin films: Fe/W(110). *Phys. Rev. B* **78**, 140403 (2008).

[158] Ferriani, P. *et al.* Atomic-scale Spin spiral with a unique rotational sense: Mn monolayer on W(001). *Phys. Rev. Lett.* **101**, 27201 (2008).

[159] Heide, M., Bihlmayer, G. & Blügel, S. Describing Dzyaloshinskii-Moriya spirals from first principles. *Phys. B Condens. Matter* **404**, 2678–2683 (2009).

[160] Zimmermann, B., Heide, M., Bihlmayer, G. & Blügel, S. First-principles analysis of a homochiral cycloidal magnetic structure in a monolayer Cr on W(110). *Phys. Rev. B* **90**, 115427 (2014).

[161] Schweflinghaus, B., Zimmermann, B., Heide, M., Bihlmayer, G. & Blügel, S. Role of Dzyaloshinskii-Moriya interaction for magnetism in transition-metal chains at Pt step edges. *Phys. Rev. B* **94**, 024403 (2016).

[162] Koretsune, T., Nagaosa, N. & Arita, R. Control of Dzyaloshinskii-Moriya interaction in $\mathrm{Mn}_{1-x}\mathrm{Fe}_x\mathrm{Ge}$: a first-principles study. *Sci. Rep.* **5**, 13302 (2015).

[163] Kikuchi, T., Koretsune, T., Arita, R. & Tatara, G. Dzyaloshinskii-Moriya Interaction as a Consequence of a Doppler Shift due to Spin-Orbit-Induced Intrinsic Spin Current. *Phys. Rev. Lett.* **116**, 247201 (2016).

[164] Katsnelson, M. I., Kvashnin, Y. O., Mazurenko, V. V. & Lichtenstein, A. I. Correlated band theory of spin and orbital contributions to Dzyaloshinskii-Moriya interactions. *Phys. Rev. B* **82**, 100403 (2010).

[165] Mankovsky, S. & Ebert, H. An accurate scheme to calculate the interatomic Dzyaloshinskii-Moriya interaction parameters. *Phys. Rev. B* **96**, 104416 (2017).

[166] Franz, C. *et al.* Real-space and reciprocal-space Berry phases in the Hall effect of $\mathrm{Mn}_{1-x}\mathrm{Fe}_x\mathrm{Si}$. *Phys. Rev. Lett.* **112**, 186601 (2014).

[167] Gayles, J. *et al.* Dzyaloshinskii-Moriya Interaction and Hall Effects in the Skyrmion Phase of $\mathrm{Mn}_{1-x}\mathrm{Fe}_x\mathrm{Ge}$. *Phys. Rev. Lett.* **115**, 36602 (2015).

[168] Marzari, N., Mostofi, A. A., Yates, J. R., Souza, I. & Vanderbilt, D. Maximally localized Wannier functions: Theory and applications. *Rev. Mod. Phys.* **84**, 1419–1475 (2012).

[169] Kohn, W. Analytic properties of Block waves and Wannier functions. *Phys. Rev.* **115**, 809 (1959).

[170] Cloizeaux, J. D. Analytical properties of n-dimensional energy bands and wannier functions. *Phys. Rev.* **135**, A698–A707 (1964).

[171] Nenciu, G. Existence of the exponentially localised Wannier functions. *Commun. Math. Phys.* **91**, 81–85 (1983).

[172] He, L. & Vanderbilt, D. Exponential decay properties of Wannier functions and related quantities. *Phys. Rev. Lett.* **86**, 5341–5344 (2001).

[173] Brouder, C., Panati, G., Calandra, M., Mourougane, C. & Marzari, N. Exponential localization of Wannier functions in insulators. *Phys. Rev. Lett.* **98**, 46402 (2007).

[174] Marzari, N. & Vanderbilt, D. Maximally-localized generalized Wannier functions for composite energy bands. *Phys. Rev. B* **56**, 12847 (1997).

[175] Souza, I., Marzari, N. & Vanderbilt, D. Maximally-localized Wannier functions for entangled energy bands. *Phys. Rev. B* **65**, 35109 (2001).

[176] Foster, J. M. & Boys, S. F. Canonical configurational interaction procedure. *Rev. Mod. Phys.* **32**, 300–302 (1960).

[177] Boys, S. Localized orbitals and localized adjustment functions. *Quantum Theory Atoms, Mol. Solid State, A Tribut. to John C. Slater* 253 (1966).

[178] Blount, E. I. Formalism of Band Theory. *Solid State Phys.* **13**, 306–373 (1962).

[179] Mostofi, A. A. Wannier90: A tool for obtaining maximally-localised Wannier functions. *Comput. Phys. Commun.* **178**, 685–699 (2008).

[180] Freimuth, F., Mokrousov, Y., Wortmann, D., Heinze, S. & Blügel, S. Maximally localized Wannier functions within the FLAPW formalism. *Phys. Rev. B* **78**, 35120 (2008).

[181] Sakuma, R. Symmetry-adapted Wannier functions in the maximal localization procedure. *Phys. Rev. B* **87**, 235109 (2013).

[182] Slater, J. C. & Koster, G. F. Simplified LCAO method for the periodic potential problem. *Phys. Rev.* **94**, 1498–1524 (1954).

[183] Wang, X., Yates, J. R., Souza, I. & Vanderbilt, D. Ab initio calculation of the anomalous Hall conductivity by Wannier interpolation. *Phys. Rev. B* **74**, 195118 (2006).

[184] Lopez, M. G., Vanderbilt, D., Thonhauser, T. & Souza, I. Wannier-based calculation of the orbital magnetization in crystals. *Phys. Rev. B* **85**, 014435 (2012).

[185] Mokrousov, Y., Bihlmayer, G. & Blügel, S. Full-potential linearized augmented plane-wave method for one-dimensional systems: Gold nanowire and iron monowires in a gold tube. *Phys. Rev. B* **72**, 45402 (2005).

[186] Zhang, H., Lazo, C., Blügel, S., Heinze, S. & Mokrousov, Y. Electrically tunable quantum anomalous Hall effect in 5d transition-metal adatoms on graphene. *Phys. Rev. Lett.* **108**, 56802 (2011).

[187] Ohgushi, K., Murakami, S. & Nagaosa, N. Spin anisotropy and quantum Hall effect in the kagomé lattice: Chiral spin state based on a ferromagnet. *Phys. Rev. B* **62**, R6065–R6068 (2000).

[188] Taguchi, Y., Oohara, Y., Yoshizawa, H., Nagaosa, N. & Tokura, Y. Spin chirality, Berry phase and anomalous Hall effect in a frustrated ferromagnet. *Science* **291**, 2573–2576 (2001).

[189] Shindou, R. & Nagaosa, N. Orbital Ferromagnetism and Anomalous Hall Effect in Antiferromagnets on the Distorted fcc Lattice. *Phys. Rev. Lett.* **87**, 116801 (2001).

[190] Hoffmann, M. *et al.* Topological orbital magnetization and emergent Hall effect of an atomic-scale spin lattice at a surface. *Phys. Rev. B* **92**, 020401(R) (2015).

[191] dos Santos Dias, M., Bouaziz, J., Bouhassoune, M., Blügel, S. & Lounis, S. Chirality-driven orbital magnetic moments as a new probe for topological magnetic structures. *Nat. Commun.* **7**, 13613 (2016).

[192] Bruno, P., Dugaev, V. & Taillefumier, M. Topological Hall Effect in Magnetic Nanostructures. *Phys. Rev. Lett.* **93**, 58–59 (2012).

[193] Huang, S. X. & Chien, C. L. Extended skyrmion phase in epitaxial FeGe (111) thin films. *Phys. Rev. Lett.* **108**, 267201 (2012).

[194] Brown, P. J., Forsyth, J. B., Nunez, V. & Tasset, F. The low-temperature antiferromagnetic structure of Mn_5Si_3 revised in the light of neutron polarimetry. *J. Phys. Condens. Matter* **4**, 10025 (1992).

[195] Sürgers, C., Fischer, G., Winkel, P. & Löhneysen, H. v. Large topological Hall effect in the non-collinear phase of an antiferromagnet. *Nat. Commun.* **5**, 3400 (2014).

[196] Sürgers, C., Kittler, W., Wolf, T. & Löhneysen, H. v. Anomalous Hall effect in the noncollinear antiferromagnet Mn_5Si_3. *AIP Adv.* **6**, 055604 (2016).

[197] Bak, P. Two-dimensionally modulated magnetic structure of neodymium, commensurate-commensurate transitions in CeSb, and the devil's staircase. *J. Appl. Phys.* **50**, 1970–1974 (1979).

[198] Forgan, F. M. The magnetic structure of neodymium below 20K: a first-principles mean field theory for two-dimensionally modulated spin patterns in an antiferromagnet. *J. Phys. F Met. Phys.* **12**, 779 (1982).

[199] McEwen, K. A. & Walker, M. B. Free-energy analysis of the single-q and double-q magnetic structures of neodymium. *Phys. Rev. B* **34**, 1781–1783 (1986).

[200] Forgan, E. M., Gibbons, E. P., McEwen, K. A. & Fort, D. Observation of a Quadruple-q Magnetic Structure in Neodymium. *Phys. Rev. Lett.* **62**, 470–473 (1989).

[201] Bertaut, E., Fruchart, D., Bouchaud, J. & Fruchart, R. Diffraction neutronique de Mn_3GaN. *Solid State Commun.* **6**, 251–256 (1968).

[202] Gomonay, O. Berry-phase effects and electronic dynamics in a noncollinear antiferromagnetic texture. *Phys. Rev. B* **91**, 144421 (2015).

[203] Chen, H., Niu, Q. & Macdonald, A. H. Anomalous Hall effect arising from noncollinear antiferromagnetism. *Phys. Rev. Lett.* **112**, 017205 (2014).

[204] Kübler, J. & Felser, C. Non-collinear antiferromagnets and the anomalous Hall effect. *Europhysics Lett.* **108**, 67001 (2014).

[205] Nakatsuji, S., Kiyohara, N. & Higo, T. Large anomalous Hall effect in a non-collinear antiferromagnet at room temperature. *Nature* **527**, 212 (2015).

[206] Nayak, A. K. *et al.* Large anomalous Hall effect driven by non-vanishing Berry curvature in non-collinear antiferromagnetic Mn_3Ge. *Sci. Adv.* **2**, e1501870–e1501870 (2015).

[207] Zhang, Y. *et al.* Strong anisotropic anomalous Hall effect and spin Hall effect in the chiral antiferromagnetic compounds Mn_3X (X=Ge, Sn, Ga, Ir, Rh, and Pt). *Phys. Rev. B* **95**, 75128 (2017).

[208] Kurz, P., Bihlmayer, G., Hirai, K. & Blügel, S. Three-Dimensional Spin Structure on a Two-Dimensional Lattice: Mn/Cu(111). *Phys. Rev. Lett.* **86**, 1106–1109 (2001).

[209] Penc, K. & Läuchli, A. M. Spin nematic phases in quantum spin systems. In *Introd. to Frustrated Magn.*, 331–362 (Springer, 2011).

[210] Menzel, M. *et al.* Information transfer by vector spin chirality in finite magnetic chains. *Phys. Rev. Lett.* **108**, 197204 (2012).

[211] Kouvel, J. & Kasper, J. Long-range antiferromagnetism in disordered Fe-Ni-Mn alloys. *J. Phys. Chem. Solids* **24**, 529–536 (1963).

[212] Endoh, Y. & Ishikawa, Y. Antiferromagnetism of γ Iron Manganes AlIoys. *J. Phys. Soc. Japan* **30**, 1614 (1971).

[213] Kübler, J., Höck, K.-H., Sticht, J. & Williams, A. R. Density functional Theory of Magnetism. *J. Phys. F Met. Phys.* **18**, 469–483 (1988).

[214] Schulthess, T. C., Butler, W. H., Stocks, G. M., Maat, S. & Mankey, G. J. Non-collinear magnetism in substitutionally disordered face-centered-cubic FeMn. *J. Appl. Phys.* **85**, 4842 (1999).

[215] Sakuma, A. First-principles study on the non-collinear magnetic structures of disordered alloys. *J. Phys. Soc. Japan* **69**, 3072–3083 (2000).

[216] Peng, W. Y. & Zhang, J. H. Magnetostriction studies in an antiferromagnetic polycrystalline $Mn_{42}Fe_{58}$ alloy. *Appl. Phys. Lett.* **89** (2006).

[217] He, A., Ma, T., Zhang, J., Luo, W. & Yan, M. Antiferromagnetic $Mn_{50}Fe_{50}$ wire with large magnetostriction. *J. Magn. Magn. Mater.* **321**, 3778–3781 (2009).

[218] Kang, Y., Chang, Y. S., He, W., Cai, J. W. & Kang, S. S. Strong modification of intrinsic spin Hall effect in FeMn with antiferromagnetic order formation. *RSC Adv.* **6**, 93491–93495 (2016).

[219] http://www.cryst.ehu.es.

[220] Aroyo, M. I. *et al.* Bilbao Crystallographic Server: I. Databases and crystallographic computing programs. *Zeitschrift für Krist.* **221**, 15–27 (2006).

[221] Aroyo, M. I., Kirov, A., Capillas, C., Perez-Mato, J. M. & Wondratschek, H. Bilbao Crystallographic Server. II. Representations of crystallographic point groups and space groups. *Acta Crystallogr. Sect. A Found. Crystallogr.* **62**, 115–128 (2006).

[222] Shaked, H., Hastings, J. M. & Corliss, L. M. Magnetic Structure of Magnesium Chromite. *Phys. Rev. B* **1**, 3116–3124 (1970).

[223] Fruchart, D. & Bertaut, E. F. Magnetic Studies of the Metallic Perovskite-Type Compounds of Manganese. *J. Phys. Soc. Japan* **44**, 781–791 (1978).

[224] Zhou, J. *et al.* Predicted Quantum Topological Hall Effect and Noncoplanar Antiferromagnetism in $K_{0.5}RhO_2$. *Phys. Rev. Lett.* **116**, 256601 (2016).

[225] Grohol, D. *et al.* Spin chirality on a two-dimensional frustrated lattice. *Nat. Mater.* **4**, 323–328 (2005).

[226] Fernández-Diaz, M. T., Alonso, J. A., Martinez-Lope, M. J., Casais, M. T. & Garcia-Muñoz, J. L. Magnetic structure of the $HoNiO_3$ perovskite. *Phys. Rev. B* **64**, 144417 (2001).

[227] Aczel, A. A. *et al.* Coupled Nd and B′ spin ordering in the double perovskites $Nd_2NaB'O_6$ (B′=Ru, Os). *Phys. Rev. B* **88**, 14413 (2013).

[228] Volkova, O. S. *et al.* Noncollinear ferrimagnetic ground state in $Ni(NO_3)_2$. *Phys. Rev. B* **90**, 134407 (2014).

[229] Burlet, P., Rossat-Mignod, J., Troć, R. & Henkie, Z. Non-colinear magnetic structure of U_3P_4 and U_3As_4. *Solid State Commun.* **39**, 745–749 (1981).

[230] Garlea, V. O. *et al.* Magnetic and Orbital Ordering in the Spinel MnV_2O_4. *Phys. Rev. Lett.* **100**, 66404 (2008).

[231] Wiebe, C. R. *et al.* Magnetic ordering in the spin-ice candidate $Ho_2Ru_2O_7$. *Phys. Rev. Lett.* **93**, 076403 (2004).

[232] Roman, E. S. Orientation Dependence of the Anomalous Hall Effect in 3d-Ferromagnets. *Phys. Rev. Lett.* **103**, 97203 (2010).

[233] Ležaić, M., Mavropoulos, P., Bihlmayer, G. & Blügel, S. Exchange interactions and local-moment fluctuation corrections in ferromagnets at finite temperatures based on noncollinear density-functional calculations. *Phys. Rev. B* **88**, 134403 (2013).

[234] Vanderbilt, D. & King-Smith, R. Electric polariation as a bulk quantity and its relation to surface charge. *Phys. Rev. B* **48**, 4442 (1993).

[235] Bellaiche, L. & Vanderbilt, D. Virtual crystal approximation revisited: Application to dielectric and piezoelectric properties of perovskites. *Phys. Rev. B* **61**, 7877–7882 (2000).

[236] Skylaris, C.-K., Mostofi, A. A., Haynes, P. D., Diéguez, O. & Payne, M. C. Nonorthogonal generalized Wannier function pseudopotential plane-wave method. *Phys. Rev. B* **66**, 035119 (2002).

[237] Kurebayashi, H. *et al.* An antidamping spin–orbit torque originating from the Berry curvature. *Nat. Nanotechnol.* **9**, 211–217 (2014).

[238] Freimuth, F. private communication.

[239] Kamberský, V. Spin-orbital Gilbert damping in common magnetic metals. *Phys. Rev. B* **76**, 134416 (2007).

[240] Gilmore, K., Idzerda, Y. U. & Stiles, M. D. Identification of the dominant precession damping mechanism in Fe, Co, and Ni by first-principles calculations. *Phys. Rev. Lett.* **99**, 027204 (2007).

[241] Hrabec, A. *et al.* Measuring and tailoring the Dzyaloshinskii-Moriya interaction in perpendicularly magnetized thin films. *Phys. Rev. B* **90**, 020402 (2014).

[242] Moreau-Luchaire, C. *et al.* Additive interfacial chiral interaction in multilayers for stabilization of small individual skyrmions at room temperature. *Nat. Nanotechnol.* **11**, 444–448 (2016).

[243] Yang, H., Thiaville, A., Rohart, S., Fert, A. & Chshiev, M. Anatomy of Dzyaloshinskii-Moriya Interaction at Co/Pt Interfaces. *Phys. Rev. Lett.* **115**, 267210 (2015).

[244] Kashid, V. *et al.* Dzyaloshinskii-Moriya interaction and chiral magnetism in $3d$-$5d$ zigzag chains: Tight-binding model and ab initio calculations. *Phys. Rev. B* **90**, 054412 (2014).

[245] Ado, I. A., Tretiakov, O. A. & Titov, M. Microscopic theory of spin-orbit torques in two dimensions. *Phys. Rev. B* **95**, 094401 (2017).

[246] Mellnik, A. R. *et al.* Spin-transfer torque generated by a topological insulator. *Nature* **511**, 449–451 (2014).

[247] Hasan, M. & Kane, C. Colloquium: Topological insulators. *Rev. Mod. Phys.* **82**, 3045–3067 (2010).

[248] Qi, X.-L. & Zhang, S.-C. Topological insulators and superconductors. *Rev. Mod. Phys.* **83**, 1057–1110 (2011).

[249] Xu, G., Weng, H., Wang, Z., Dai, X. & Fang, Z. Chern Semimetal and the Quantized Anomalous Hall Effect in HgCr. *Phys. Rev. Lett.* **107**, 186806 (2011).

[250] Gosálbez-Martínez, D., Souza, I. & Vanderbilt, D. Chiral degeneracies and Fermi-surface Chern numbers in bcc Fe. *Phys. Rev. B* **92**, 85138 (2015).

[251] Xu, S.-Y. *et al.* Discovery of a Weyl fermion semimetal and topological Fermi arcs. *Science* **349**, 613–617 (2015).

[252] Lv, B. Q. *et al.* Experimental discovery of weyl semimetal TaAs. *Phys. Rev. X* **5**, 031013 (2015).

[253] Soluyanov, A. A. *et al.* Type-II Weyl semimetals. *Nature* **527**, 495–498 (2015).

[254] Jia, S., Xu, S.-Y. & Hasan, M. Z. Weyl semimetals, Fermi arcs and chiral anomalies. *Nat. Mater.* **15**, 1140–1144 (2016).

[255] Avci, C. O. *et al.* Current-induced switching in a magnetic insulator. *Nat. Mater.* **16**, 309–314 (2016).

[256] Ding, J., Qiao, Z., Feng, W., Yao, Y. & Niu, Q. Engineering quantum anomalous/valley Hall states in graphene via metal-atom adsorption: An ab-initio study. *Phys. Rev. B* **84**, 1–9 (2011).

[257] Acosta, C. M., Lima, M. P., Miwa, R. H., Da Silva, A. J. R. & Fazzio, A. Topological phases in triangular lattices of Ru adsorbed on graphene: Ab initio calculations. *Phys. Rev. B* **89**, 155438 (2014).

[258] Hu, J., Zhu, Z. & Wu, R. Chern half metals: A new class of topological materials to realize the quantum anomalous Hall effect. *Nano Lett.* **15**, 2074–2078 (2015).

[259] Ren, Y., Qiao, Z. & Niu, Q. Topological phases in two-dimensional materials: a review. *Reports Prog. Phys.* **79**, 066501 (2016).

[260] Niu, C. *et al.* Functionalized bismuth films: Giant gap quantum spin Hall and valley-polarized quantum anomalous Hall states. *Phys. Rev. B* **91**, 41303 (2015).

[261] Checkelsky, J. G. *et al.* Trajectory of the anomalous Hall effect towards the quantized state in a ferromagnetic topological insulator. *Nat. Phys.* **10**, 1–6 (2014).

[262] Kou, X. *et al.* Scale-Invariant Quantum Anomalous Hall Effect in Magnetic Topological Insulators. *Phys. Rev. Lett.* **113**, 1–15 (2014).

[263] Chang, C.-Z. *et al.* High-precision realization of robust quantum anomalous Hall state in a hard ferromagnetic topological insulator. *Nat. Mater.* **14**, 473–477 (2015).

[264] Chu, Y.-H. *et al.* Electric-field control of local ferromagnetism using a magnetoelectric multiferroic. *Nat. Mater.* **7**, 478–482 (2008).

[265] Chiba, D. *et al.* Magnetization vector manipulation by electric fields. *Nature* **455**, 515–518 (2008).

[266] Tang, P., Zhou, Q., Xu, G. & Zhang, S.-C. Dirac Fermions in Antiferromagnetic Semimetal. *Nat. Phys.* **12**, 1100–1104 (2016).

[267] Šmejkal, L., Železný, J., Sinova, J. & Jungwirth, T. Electric Control of Dirac Quasiparticles by Spin-Orbit Torque in an Antiferromagnet. *Phys. Rev. Lett.* **118**, 106402 (2017).

[268] Murakami, S. Phase transition between the quantum spin Hall and insulator phases in 3D: Emergence of a topological gapless phase. *New J. Phys.* **9**, 29802 (2007).

[269] Murakami, S. & Kuga, S.-i. Universal phase diagrams for the quantum spin Hall systems. *Phys. Rev. B* **78**, 165313 (2008).

[270] Yang, B.-J. & Nagaosa, N. Classification of stable three-dimensional Dirac semimetals with nontrivial topology. *Nat. Commun.* **5**, 4898 (2014).

[271] Burkov, A. A., Hook, M. D. & Balents, L. Topological nodal semimetals. *Phys. Rev. B* **84**, 235126 (2011).

[272] Fang, C., Chen, Y., Kee, H. Y. & Fu, L. Topological nodal line semimetals with and without spin-orbital coupling. *Phys. Rev. B* **92**, 081201 (2015).

[273] Mostofi, A. A. *et al.* An updated version of wannier90: A tool for obtaining maximally-localised Wannier functions. *Comput. Phys. Commun.* **185**, 2309–2310 (2014).

[274] Ferriani, P., Heinze, S., Bihlmayer, G. & Blügel, S. Unexpected trend of magnetic order of 3d transition-metal monolayers on W(001). *Phys. Rev. B* **72**, 24452 (2005).

[275] Janak, J. F., Williams, A. R. & Moruzzi, V. L. Local exchange-correlation potentials and the Fermi surface of copper. *Phys. Rev. B* **6**, 4367–4370 (1972).

[276] Zhang, Y. & Yang, W. Comment on “Generalized Gradient Approximation Made Simple”. *Phys. Rev. Lett.* **80**, 890–890 (1998).

Publications

Higher-dimensional Wannier functions of multiparameter Hamiltonians
J.-P. Hanke, F. Freimuth, S. Blügel, and Y. Mokrousov
Physical Review B **91**, 184413 (2015), Editor's suggestion

Role of Berry phase theory for describing orbital magnetism: From magnetic heterostructures to topological orbital ferromagnets
J.-P. Hanke, F. Freimuth, A. K. Nandy, H. Zhang, S. Blügel, and Y. Mokrousov
Physical Review B **94**, 121114(R) (2016)

Prototypical topological orbital ferromagnet γ-FeMn
J.-P. Hanke, F. Freimuth, S. Blügel, and Y. Mokrousov
Scientific Reports **7**, 41078 (2017)

Toward surface orbitronics: giant orbital magnetism from the orbital Rashba effect at the surface of sp-metals
D. Go, J.-P. Hanke, P. M. Buhl, F. Freimuth, G. Bihlmayer, H.-W. Lee, Y. Mokrousov, and S. Blügel
Scientific Reports **7**, 46742 (2017)

Mixed Weyl semimetals and low-dissipation magnetization control in insulators by spin-orbit torques
J.-P. Hanke, F. Freimuth, C. Niu, S. Blügel, and Y. Mokrousov
Nature Communications **8**, 1479 (2017)

Higher-dimensional Wannier interpolation for the modern theory of the Dzyaloshinskii-Moriya interaction: Application to Co-based trilayers
J.-P. Hanke, F. Freimuth, S. Blügel, and Y. Mokrousov
Journal of the Physical Society of Japan **87***, 041010 (2018)*

Antiferromagnetic dual topological insulator and topological phase transitions in two-dimensional honeycomb structures
C. Niu, J.-P. Hanke, P. M. Buhl, G. Bihlmayer, D. Wortmann, S. Blügel, and Y. Mokrousov
submitted (2017), preprint arXiv:1705.07035

Mixed topological semimetals and orbital magnetism in two-dimensional spin-orbit ferromagnets
C. Niu, J.-P. Hanke, P. M. Buhl, H. Zhang, G. Bihlmayer, D. Wortmann, S. Blügel, and Y. Mokrousov
to be submitted (2018)

Acknowledgment

Since doing a doctorate in physics is a long-term project, this research would not have been possible without the support, the patience, and the enthusiasm of many people to whom I am obliged. First of all, I would like to thank Prof. Dr. Stefan Blügel for giving me the great opportunity to conduct my Ph.D. studies in his renowned institute at the Forschungszentrum Jülich. I am grateful to him for evaluating this thesis as first referee as well as for suggesting to me many interesting ideas, not all of which I could follow during my time as a Ph.D. student. Additionally, I am indebted to Prof. Dr. Carsten Honerkamp for preparing the second opinion on the present work.

I would like to thank in particular my supervisor Prof. Dr. Yuriy Mokrousov, who has been an outstanding and committed mentor. His inspiring supervision including our frequent meetings encouraged me to develop and follow own research ideas. His way of thinking has strongly affected my attitude towards setting scientific concepts into a global context, which assisted me tremendously in writing publications and communicating research results. Furthermore, I would like to thank Dr. Frank Freimuth for numerous vivid discussions and valuable advices during my Ph.D. studies. He shared with me his expertise on the FLEUR code, Wannier functions, and spin-orbit torques, putting me in an optimal position to carry out the theoretical developments presented in this thesis. He also shared with me some of his unpublished data that allowed me to benchmark my computational method.

Over the past years, I had fruitful collaborations with Prof. Dr. Hongbin Zhang, Dr. Ashis Kumar Nandy, and Dongwook Go, which I would like to acknowledge explicitly. Moreover, I enjoyed many interesting discussions with people from the institute, including especially Dr. Chengwang Niu, Dr. Bernd Zimmermann, Dr. Manuel dos Santos Dias, Patrick Buhl, and my office mate Markus Hoffmann. These discussions covered a wide range of topics from topological materials over magnetic interactions to American football. In general, I thank all members of the Peter Grünberg Institute for creating a comfortable but stimulating atmosphere at work. Special thanks go to Ute Winkler for helping just perfectly with any administrative issues.

Finally, I am extremely grateful for the unconditional love and the support that I receive everyday from my family – in particular from my wife Katharina, my parents, and my grandparents.

Jülich, February 2018 Jan-Philipp Hanke

Band / Volume 169
Tailoring the Electronic Properties of Epitaxial Oxide Films via Strain for SAW and Neuromorphic Applications
Y. Dai (2018), VI, 133 pp
ISBN: 978-3-95806-319-8

Band / Volume 170
The electronic structure of transition metal dichalcogenides investigated by angle-resolved photoemission spectroscopy
M. Gehlmann (2018), ii, 108, XVIII pp
ISBN: 978-3-95806-324-2

Band / Volume 171
Control of neuron adhesion by metal nanoparticles
A. Q. Tran (2018), viii, 108 pp
ISBN: 978-3-95806-332-7

Band / Volume 172
Neutron Scattering
Lectures of the JCNS Laboratory Course held at Forschungszentrum Jülich and at the Heinz-Maier-Leibnitz Zentrum Garching
edited by T. Brückel, S. Förster, G. Roth, and R. Zorn (Eds.) (2018), ca 300 pp
ISBN: 978-3-95806-334-1

Band / Volume 173
Spin scattering of topologically protected electrons at defects
P. Rüßmann (2018), vii, 230 pp
ISBN: 978-3-95806-336-5

Band / Volume 174
Interfacing EuO in confined oxide and metal heterostructures
P. Lömker (2018), vi, 140 pp
ISBN: 978-3-95806-337-2

Band / Volume 175
Operando Chemistry and Electronic Structure of Electrode / Ferroelectric Interfaces
S. Gonzalez (2018), 172 pp
ISBN: 978-3-95806-341-9

Band / Volume 176
Magnetic Properties of Self-assembled Manganese Oxide and Iron Oxide Nanoparticles
Spin Structure and Composition
X. Sun (2018), ii, 178 pp
ISBN: 978-3-95806-345-7

Schriften des Forschungszentrums Jülich
Reihe Schlüsseltechnologien / Key Technologies

Band / Volume 177
Model-based reconstruction of magnetisation distributions in nanostructures from electron optical phase images
J. Caron (2018), XXI, 183 pp
ISBN: 978-3-95806-346-4

Band / Volume 178
Simultaneous dual-color imaging on single-molecule level on a Widefield microscope and applications
R. Ledesch (2018), ix, 119 pp
ISBN: 978-3-95806-348-8

Band / Volume 179
Methoden der Leitfähigkeitsuntersuchung mittels Rasterkraftmikroskop und deren Anwendung auf Barium Titanat Systeme
B. Reichenberg (2018), x, 144 pp
ISBN: 978-3-95806-350-1

Band / Volume 180
Manipulation of magnetism in iron oxide nanoparticle / $BaTiO_3$ composites and low-dimensional iron oxide nanoparticle arrays
L. Wang (2018), VI, 151 pp
ISBN: 978-3-95806-351-8

Band / Volume 181
Creating and characterizing a single molecule device for quantitative surface science
M. Green (2018), viii, 142 pp (untersch. Pag.)
ISBN: 978-3-95806-352-5

Band / Volume 182
8th Georgian-German School and Workshop in Basic Science
A. Kacharava (Ed.) erscheint nur als CD (2018)
ISBN: 978-3-95806-353-2

Band / Volume 183
Topological properties of complex magnets from an advanced *ab-initio* Wannier description
J.-P. Hanke (2018), xi, 173 pp
ISBN: 978-3-95806-357-0

Weitere ***Schriften des Verlags im Forschungszentrum Jülich*** unter
http://wwwzb1.fz-juelich.de/verlagextern1/index.asp

Schlüsseltechnologien / Key Technologies
Band / Volume 183
ISBN 978-3-95806-357-0

Mitglied der Helmholtz-Gemeinschaft

JÜLICH
Forschungszentrum